DAMAGE ASSESSMENT IN REINFORCED CONCRETE USING CONTACTLESS ULTRASOUND

BY

SU YUN HAM

DISSERTATION

Submitted in partial fulfillment of the requirements
for the degree of Doctor of Philosophy in Civil Engineering
in the Graduate College of the
University of Illinois at Urbana-Champaign, 2015

Urbana, Illinois

Doctoral Committee:

Professor John S. Popovics, Chair
Professor David A. Lange
Associate Professor Michael L. Oelze
Associate Professor Nils Rydén
Professor Richard L Weaver

ABSTRACT

The poor state of the deteriorating national infrastructure makes essential the need for implementation of non-destructive evaluation (NDE) and structural health monitoring (SHM) for existing concrete structures. Conventional contact-type ultrasonic testing (UT) methods offer efficient and useful approaches to characterize internal defects in concrete structures in a nondestructive fashion. However, the large testing areas normally associated with concrete structures make conventional ultrasonic methods extremely labor- and time-intensive. Contactless, or air-coupled, UT systems offer a solution to this limitation. In this thesis, high-performance contactless UT systems are studied, developed, implemented and verified in order to characterize several different type of damage (delamination, distributed microcracking, and rail seat deterioration) in concrete structures. The work comprises new hardware system design and testing approach development. The hardware, comprising the modified sensors and the automation/robotic scanning system, are designed and assembled by the author. The performance of the system is optimized with respect to generated pulse frequency content and energy, signal to noise ratio, and rapid data collection and scanning. Dynamic finite element method (FEM or FE) simulations of mechanical wave-based NDE methods are developed and described in order to support the system construction, theory verification, and experimental work. The FE models simulate generation and detection of air-coupled transient waves in air and wave interactions at the interface between concrete and air from internal defects and random scatterers. Next, three NDE applications with different types of damage are reported. New experimental and analytical approaches are introduced and deployed for each case, where the fully contactless UT system is used for each. The first study deploys multichannel analysis of surface waves (MASW) measurements interpreted through Lamb wave mode analysis; 3-D images are generated that make use of the Lamb wave mode jump condition in order to identify the presence of underlying delamination defects. The next application incorporates ultrasonic backscatter measurements to characterize distributed microcracking damage in concrete. Two different backscatter measurement schemes – time domain energy subtraction analysis (ESA) and spectral variance analysis (SVA) – are developed and applied through numerical simulation and experiment. The experiments are deployed using concrete samples containing well controlled artificial damage and imparted cracking damage. Both coherent and incoherent wave analyses are performed to study scatter characteristics. The backscatter energy measurements are sensitive to the presence of distributed microcracks as compared with conventional UT approaches. Also backscatter approaches provide statistically significant distinctions between damage levels in concrete. The collected backscatter data

are also applied to image and identify localized regions of damage. In the third application, surface waves are used to interrogate interfacial damage related to rail seat deterioration (RSD) in concrete rail ties. Results from the UT tests on concrete tie samples are reported, where experimental results provide clear distinction among different RSD levels. Close proximity and large-offset scan configurations, which is appropriate for application to rail structures in situ, are proposed. Finally, future efforts toward additional implementation to actual bridge, nuclear power plant, and rail-field tests are proposed based on the work reported here.

ACKNOWLEDGEMENTS

The author gratefully acknowledges the advice, support, and guidance of Dr. John Popovics during the course of this research. His assistance and trustfulness were fundamental to the achievement of the project. His understanding attitude, encouragement, and the time spent in amiable conversations made these fix years very enjoyable. He is an excellent teacher and mentor, also a good friend.

Thanks are given Hajin Choi, Steven Garret, Jeevaka Somaratna, James Bittner, Agustin Spalvier, Homin Song, and Jesus Eiras for their assistance in the experimental or numerical phase.

Sincere appreciation goes to Dr. Taekeun Oh of National Inchon University, South Korea, for a fruitful collaboration and as a co-author. Appreciation goes to Dr. Chulwoo Jung, in Pukyong National University, for helpful advice of cement chemistry. Also thanks are given to Dr. Kerry Hall, Dr. Jinying Zhu for their advice.

Dr. Michael L. Oelze of ECE department provided valuable assistance on the scattering analysis. Dr. Nils Rydén provided great assistance on MASW technique. The author is also grateful to Dr. David A. Lange for helpful and professional advice of the rail seat deterioration problem, and Dr. Richard L Weaver with great advice of his diffuse wave and incoherent scattering.

This work was carried out through support from the National Science Foundation (NSF Grant CMMI 1300546), Association of American Railroads (AAR: 2012 to 2015), American Society for Nondestructive Testing student research proposal fellowship (ASNT number: 2012-01806), and the National Cooperative Highway Research Program (NCHRP-IDEA Number 134, Program Manager: Dr. Inam Jawed).

Finally, I would like to thank my parents for their continuous support and encouragement through my life. Last, but not least, I wish to thank my wife, Jieun Kim, for her extraordinary effort, love and faith during our seven years at the University of Illinois. May God bless all of you.

TABLE OF CONTENTS

LIST OF FIGURES

CHAPTER 1 INTRODUCTION

1.1 Problem Statement

According to a 2013 report by the American Society of Civil Engineers (Geoffrey Baskir et. al. 2013), the infrastructure of the United States requires a $3.6 trillion investment to return it to suitably good condition by 2020. A significant portion of the American infrastructure is composed of concrete. Portland cement concrete is generally durable and non-combustible, but its physical properties (e.g. strength, stiffness, and permeability) are prone to degradation due to internal chemical and physical transformations that inevitably occur over time due to exposure (Naus 2009). This is significant to the health of U.S. national infrastructure due to the fact that many large critical structural systems, such as bridges, tunnels, nuclear power plants and numerous concrete rail ties, are comprised of Portland cement concrete.

For example, concrete is widely used in nuclear power generation structures, which under normal operating conditions may be exposed to aggressive environmental exposure (moisture and contaminating ions), high temperature hot spots at piping penetrations, turbine foundations and shield walls within the primary containment structure, and sustained radiation exposure (ACI 2002). The primary containment structure of conventional light water nuclear reactors could be exposed to sustained (on the order of hours to days) high temperatures and high levels of radiation in the case of adverse operation events, for example loss of cooling accident (Naus 2007). Recently, the occurrence of alkali-silica reaction (ASR) damage in concrete disrupted nuclear power plant operation in the U.S. (NRC 2011). All of the degradation mechanisms mentioned give rise to distributed micro-cracking damage in concrete, adversely affecting material mechanical strength, stiffness and permeability, and thus the resilience and sustainability of the structural system. Accurate and sensitive characterization of such damage in place enables infrastructure management agencies to apply effective maintenance procedures, accurately predict service life and monitor structural condition after an extreme event; all of these attributes promote a resilient and sustainable infrastructure and mitigate societal risk.

Another example of important concrete infrastructure is rail ties for high-speed rail systems. Increased rail service from an $8 billion national high-speed rail system could relieve traffic congestion, conserve energy, reduce pollution and offer greater accessibility to intercity travel (Zeman 2010). However, high

load and high-speed rail systems demand increased track structure stability, so the physical condition of the rail track structure must be regularly monitored in order to ensure its safe and operating efficiently. A critical component of the track structure is the crosstie that holds track gauge, transfers loads from the rails to the ballast and provides vertical, lateral, and longitudinal stability to the track structure. Traditional timber ties are being replaced with prestressed concrete ties, which are now quite common throughout the United States. The prestressed concrete offers many benefits over timber, principally greater long-term economy and better performance under heavy rail loads and high-speed traffic (Gordon 2010). But due to their relatively high initial cost, concrete ties are only economical in applications where they last longer and require less maintenance than timber ties.

Though significant progress in health monitoring and non-destructive testing of critical large concrete infrastructure systems has been made over the years (ACI 2004), rapid and effective material characterization of concrete in large critical infrastructure systems has not yet been realized. Most conventional concrete non-destructive test (NDT) methods, such as visual inspection, sounding (e.g., chain drag), pulsed microwave/Radar techniques (GPR) and infrared thermography, cannot reliably detect and characterize distributed damage in concrete (ACI 2004). X-ray radiograph and tomographic techniques show sensitivity to internal material damage but cannot be applied in the field to large structures because of practical, financial and safety concerns. Conventional mechanical wave methods, such as ultrasonic wave pulse propagation and air-coupled impact-echo, do show sensitivity to distributed damage and can be applied in the field to large structures. These methods, however, are normally not fully contactless because physical contact with the concrete is still required. This slows down testing and may cause inconsistent coupling problems. One possible solution for this problem is to eliminate the need for physical contact between the sensors and tested structure. This technique is often referred to as contactless sensing (Green 2004). An obvious advantage of this technique is that it greatly speeds up data collection in the field, allowing for rapidly processed damage detection and automatically automated scanning. Therefore, contactless ultrasonic testing (UT) could provide an effective way to describe the location, size and shape of embedded damage or flaws for evaluation of concrete structures. In addition, an effective visualization technique for concrete defects is necessary to provide reliable condition assessment to the existing concrete infrastructure. Figure 1.1 illustrates deployment concepts for the technology produced by this research effort for large scale structures.

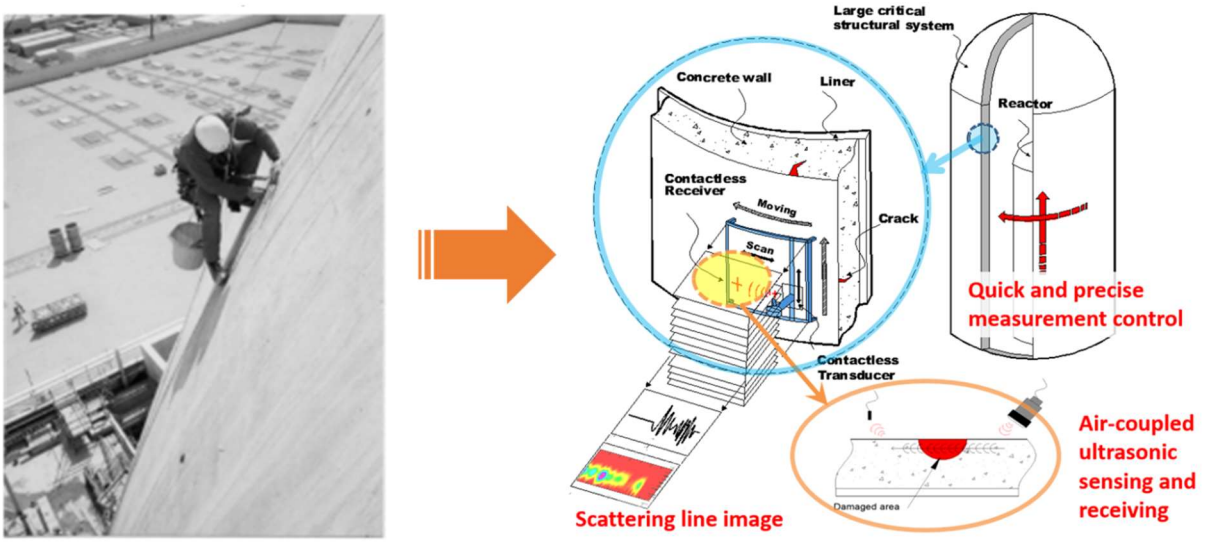

(Ham & Popovics 2015b)

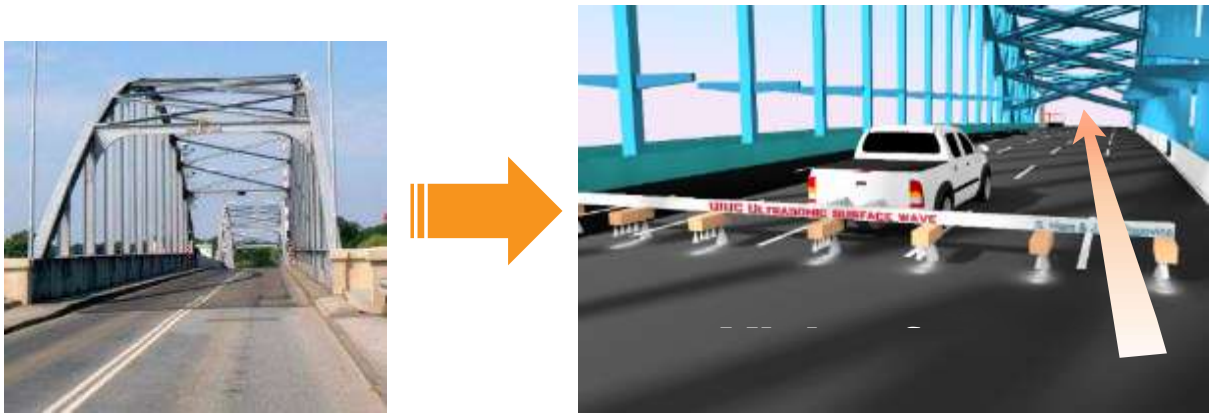

(Janberg 2013)

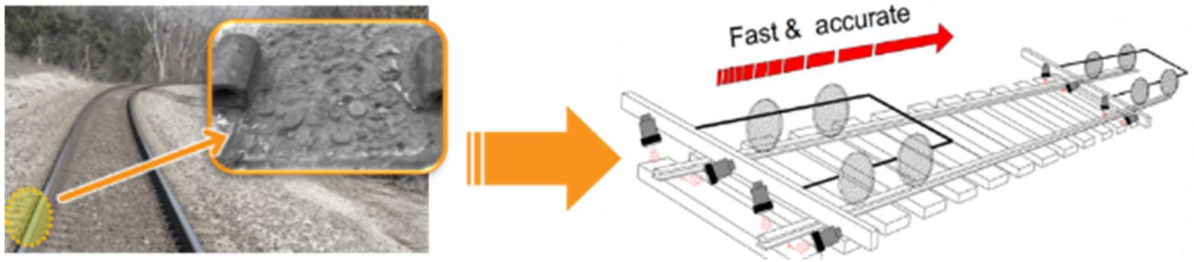

(Zeman et al. 2009) ***(Ham & Popovics 2015b).***

Figure 1.1 Illustrations of potential deployments for air-coupled ultrasonic scanning for the concrete infrastructure: (top row) nuclear power structures (Ham & Popovics 2015b), (middle row) bridge decks (Janberg 2013), (bottom row) railroad structures(Zeman et al. 2009) and (Ham & Popovics 2015b).

1.2 Objectives and Approach

The aim of this research is to characterize and visualize concrete defects using the fully contactless UT method as shown in Figure 1.2. Successful completion of the following objectives enable progress toward rapid and accurate internal imaging of damage and flaws inside concrete structures. The following specific objectives, and the corresponding approach, are offered:

1. Development and verification of cost-effective, fully air-coupled ultrasonic testing equipment

Hardware improvements and sensor optimization will be performed with regard of appropriate analysis, and maximized signal to noise ratio including development of a scanning system and contactless sensing testing configurations.

2. Numerical simulation

Efficient and accurate dynamic finite element method (FEM) simulations for air-launching and air-detecting mechanical wave-based NDE methods for concrete structures are developed and described. Parametric studies support system construction, theory verification, and experimental work.

3. Experimental verification and application

Developed contactless ultrasonic test methods are applied to samples that represent different types of critical concrete defects: delamination, distributed mircrocracking, and rail seat deterioration (RSD). Separate algorithms and testing approaches are developed with respect to each defect type and application.

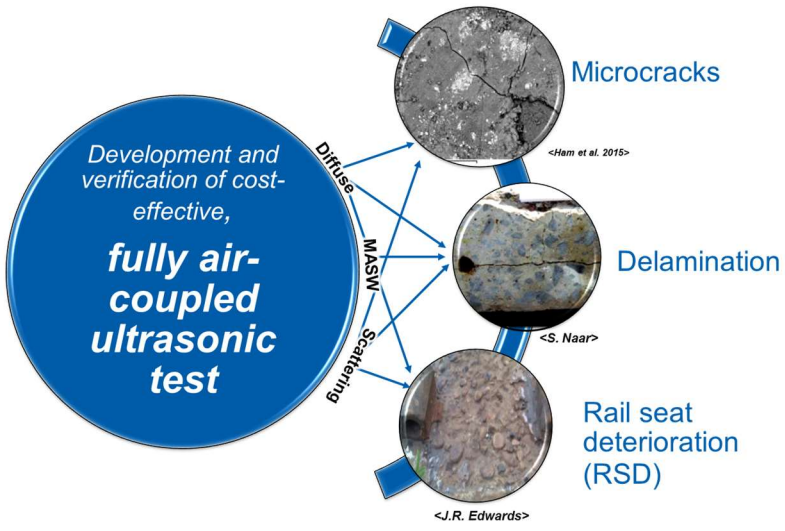

Figure 1.2 The aim of the research: to characterize and visualize concrete defects using the contactless UT method.

CHAPTER 2 BACKGROUND INFORMATION

2.1 Concrete Defects

The common types of defects in concrete structures include delamination/spalling, cracks and voids/honeycombing. Existence of such flaws in concrete severely affects durability, service life and, in some cases, the structural integrity of concrete structures.

2.1.1 Cracks

Cracks can be caused by alkali-silica reaction (ASR), thermal expansion, chemical reaction and mechanical actions such as fatigue or overloading. *ASR damage* is a reaction which occurs over time in concrete between the highly alkaline cement paste and reactive non-crystalline (amorphous) silica, found in many common aggregates (Mindess et al. 2002). *Thermal damage such as freeze thaw action occurs* in concrete that comes into contact with moisture, rendering it susceptible to damage under repeated cycles of freezing and thawing (frost attack) (Mindess et al. 2002).If there is no space for this volume expansion in a porous, water-containing material like concrete, freezing may cause distress in the concrete. *Chemical attack damage* results from carbonation, exposure to chlorides and sulfate attack. Carbonation occurs when carbon dioxide from air reacts with the calcium hydroxide in concrete to form calcium carbonate. Carbonation of concrete is a slow, continuous process progressing from the outer surface inward, slowing with increasing diffusion depth. Chloride carbonation has two effects: it increases mechanical strength of concrete, but it also decreases alkalinity, which is essential for corrosion prevention of reinforcement steel. Sulfates in solution in contact with concrete can cause chemical changes to the cement, which can cause significant microstructural effects leading to the weakening of the cement binder (chemical sulfate attack). A distinct single surface-crack is a common and significant defect that can eventually lead to failure of concrete structures. Determining the width and depth of cracks is essential to integrity assessment of concrete structures (Mindess et al. 2002).

2.1.2 Delamination (corrosion)

Delamination is a serious problem affecting the service life of reinforced slabs and concrete bridge decks. Delamination is usually occurs due to corrosion (Weyers, et al 1993). These corrosion-induced delaminations manifest as horizontal cracked planes in concrete slabs. Delamination cracking generally occurs in a top steel layer, typically 5 to 15 cm below the bridge deck surface (Scott 1999). Delamination will eventually propagate to the surface layer, causing spalling over a large area.

2.1.3 Rail Seat Deterioration (RSD) in Concrete Cross Ties

The most pressing problem for heavy haul service has been reported to be rail seat deterioration (RSD) of prestressed concrete ties (Zeman et al. 2009). This problem was especially acute for the major railroads, with their higher traffic volumes and heavier axle loads. RSD is caused by a complicated failure mechanism that involves multiple contributing factors, including lateral surface abrasions and internal hydraulic hydrostatic pressure impulses within the concrete pore fluid caused by passing train loads. These damage mechanisms eventually lead to concrete deterioration at the rail surface underneath the rail pad as shown in Figure 2.1.

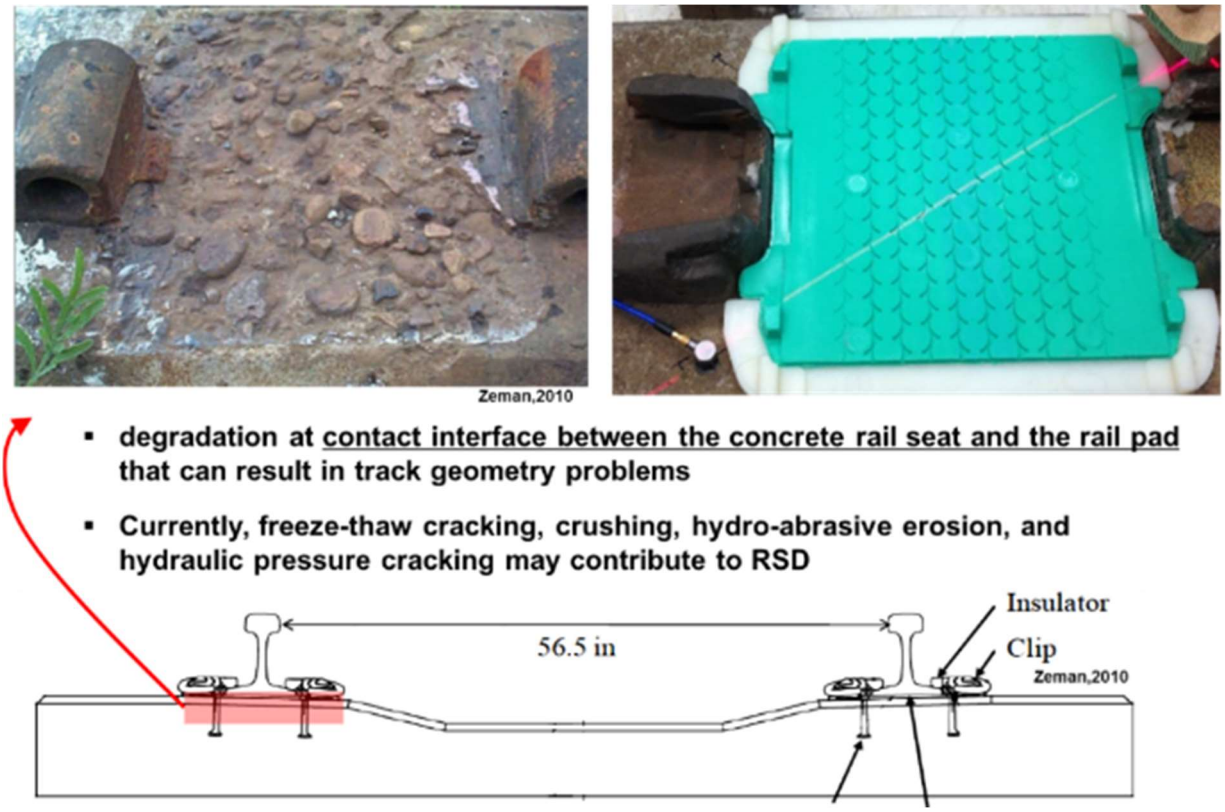

Figure 2.1 Rail seat deterioration (RSD): (top) photo with damaged sample (Zeman 2010), (top left) rail pad on damage region, and (bottom) illustration of location of RSD (Zeman 2010).

2.1.4 Voids and Honeycombing

Void and honeycombing defects are usually caused by poor consolidation of the concrete during construction. Voids, due to incomplete grouting in post-tension ducts, leave tendons vulnerable to corrosion and can eventually lead to failure of the structure.

2.2 Mechanical Wave Theory

In this chapter the fundamental concepts of stress wave propagation in elastic media are presented. It is found that the propagation of stress waves is an important factor in nondestructive tests. For more detailed derivations, the reader is encouraged to refer to one of the cited texts (Graff 1991).

2.2.1 Wave Propagation

In an elastic solid medium, there exist body waves that travel within the body wave (P- and S- waves), and surface waves (R-waves) that travel along the free surface of the materials. The P-wave velocity (C_P) in a solid depends on the mass density (ρ) and the elastic constants (E, ν) of the material throughout the concrete. Particle motion due to pressure waves is in the direction of wave propagation. P-waves are the fastest traveling waves in solids. Shear waves (S-waves) are also known as secondary, S, lateral, transverse and equivolumnal waves. Particle motion in shear waves is perpendicular to the direction of wave propagation. The speed of shear waves is always lower than that of pressure waves. The main focus of this research is to evaluate the use of surface-guided waves (also known as "Rayleigh" waves for the case of solids that are very thick with respect to the propagating wavelength) to interrogate the state of concrete. The particle motion of Rayleigh waves is elliptical and retrograde in the region close to the surface. Because they are confined to the surface of the solid, the geometric dispersion of Rayleigh waves is two-dimensional and is less than that of bulk waves (Krautkramer & Krautkramer 1990). The velocity of Rayleigh waves, C_R, at a solid-vacuum interface is approximated by the equation

$$\boldsymbol{C_R = \frac{0.87+\ .12\nu}{1+\nu}\sqrt{\frac{E}{\rho}\frac{1}{2(1+\upsilon)}}.} \qquad (2.1)$$

The relation between P-, S- and R-wave velocities are expressed by equations

$$\boldsymbol{\frac{C_s}{C_p} = \sqrt{\frac{1-2\nu}{2(1-\nu)}}} \text{ , and} \qquad (2.2)$$

$$\boldsymbol{\frac{C_R}{C_S} \approx \frac{0.87+1.12\nu}{1+\nu}} \qquad (2.3)$$

where C_p , C_S and C_R are the phase velocities of the P-, S- and R-waves, respectively, and ν refers to Poisson's ratio. C_p typically ranges from 3800 to 4500 m/s for sound concrete, and C_R from 2000 to 2700 m/s. The motion resulting from R-waves is restricted to a region near the surface and decreases exponentially in amplitude as they move away from the surface. The R-wave penetration depth is inversely related to the frequency of the wave. R-waves are easily generated in a solid by a transient point source and more readily sensed than P- and S-waves due to their large amplitude. The only

limitation in sensing R-waves is caused by the limited penetration depth; disturbances are confined to the near-surface region of thickness, approximately 2 times the wavelength, λ_R.

2.2.2 Reflection and Refraction

When a body wave (P or S) reaches an interface across which the mechanical properties of the material change, a variety of transformations occur. At the interface the wave will undergo a mode-conversion, meaning that P and S components will be present in both reflected and refracted waves, regardless of the nature of the incident wave. The amplitude of reflected and refracted waves depends on the relative acoustic impedance (Z) of the two media. In the case that the second medium exhibits higher acoustic impedance ($Z_2 > Z_1$), the reflected P-wave will be of equal sense (tension or compression). On the other hand, when the second medium has a lower Z value, as in a concrete-air boundary, there is a reversal in the amplitude sense, indicating a 180° phase change. Beyond a critical angle of incidence, θ_C, no pressure waves are transmitted into the second medium. θ_C, is defined from 90 degree perpendicular to surface. Using Snell's Law, the critical angle of reflection for the pressure mode, θ_{C1}, is

$$\boldsymbol{\theta_{C1} = arcsin\,(C_f / C_P)}, \qquad (2.4)$$

where C_f is the velocity of wave propagation in the fluid. Although the pressure amplitude is increased by transmission, the intensity of the transmitted wave is greatly reduced because of the large difference in impedance (Krautkramer & Krautkramer 1990). The transmission coefficients between a fluid and solid at oblique incidence must be derived using the acoustic analogue of the Fresnel equations for transmission at a boundary (Graff 1991). Near the critical angle of the pressure mode, a pseudo-pressure wave builds and propagates along the surface. Shear waves are primarily generated when the angle of incidence of the wave in the fluid is between the first and second critical angles, θ_{C1} and θ_{C2}. Weaker shear waves are also transmitted when the angle of incidence, θ, is greater than 0 and less than θ_{C1}. At incidences beyond θ_{C2} no waves are transmitted into the bulk of the second medium. The equation for the second critical angle is

$$\boldsymbol{\theta_{C2} = arcsin\,(C_f / C_s)}. \qquad (2.5)$$

Rayleigh waves are generated when the fluid wave is incident at an angle slightly greater than the second critical angle. This angle, θ_R, can be determined by the equation

$$\boldsymbol{\theta_R = arcsin\,(C_f / C_R)} \qquad (2.6)$$

and exists only if the shear wave velocity of the solid, C_S, is larger than the fluid wave velocity

(Krautkramer & Krautkramer 1990). Rayleigh waves leak energy in the form of pressure waves into the fluid at the same angle (Zhu et al. 2004).

2.2.3 Attenuation, Scattering, and Diffuse Waves

Mechanical and chemical effects all impose some types of micro damage to concrete. Detecting distributed microcracking prior to the extended large crack is important to monitoring concrete structures.

The energy and amplitude of an ultrasonic wave pulse decreases gradually as it propagates through a specimen. This signal "attenuation" can be used to monitor cracks and other damage in concrete as observed in a testing when the ultrasonic transducers are acoustically well-coupled to the specimen (Suaris & Fernando 1987). In general ultrasound attenuations are due to

1. scattering from the microstructure; Generally the scattering process is energy conserving- the scattered energy is not lost, but is no longer in phase with the excited wave
2. dissipation primarily from the viscoelastic loss, and
3. geometric spreading.

Scattering is a complex process dependent upon particle diameter in relation to wavelength, the number of particles per unit volume and the acoustic properties of the particles (Gaydeck, et al 1992). It is generally agreed upon that scattering is the dominant cause of ultrasonic attenuation in concrete. When the wavelength λ is much smaller than the particle size a, diffusion scattering that describes in inhomogeneous section occurs with its magnitude inversely proportional to the mean particle diameter. Stochastic scattering occurs when the particle size is approximately equal to the wavelength and is proportional to the frequency and mean particle diameter squared. When the particle size is small with respect to the wave length, $a < \frac{\lambda}{2\pi}$ ($ka < 1$), Rayleigh scattering occurs. In Rayleigh scattering, each particle acts as a spherical radiator. The contribution to the attenuation coefficient is proportional to the frequency to the fourth power, and the mean particle diameter to the third power (Gaydeck, et al 1992).

The coherent method has limitation. Large attenuation of coherent wave in concrete limits effective range of frequency (< 100 kHz); theatrically possible up to 800kHz (heavily attenuated). These wave length is too large to characterize microcracking. (Landis & Shah 1995) suggest less than 100 kHz ultrasonic signal due to large attenuation with aggregate. As shown in Figure 2.2, the experimental result

shows the scattering attenuation from aggregate is larger than fine mortar. The Coupling of absorption and scattering effects can make it difficult to link measured attenuation behavior with specific microstructure features.

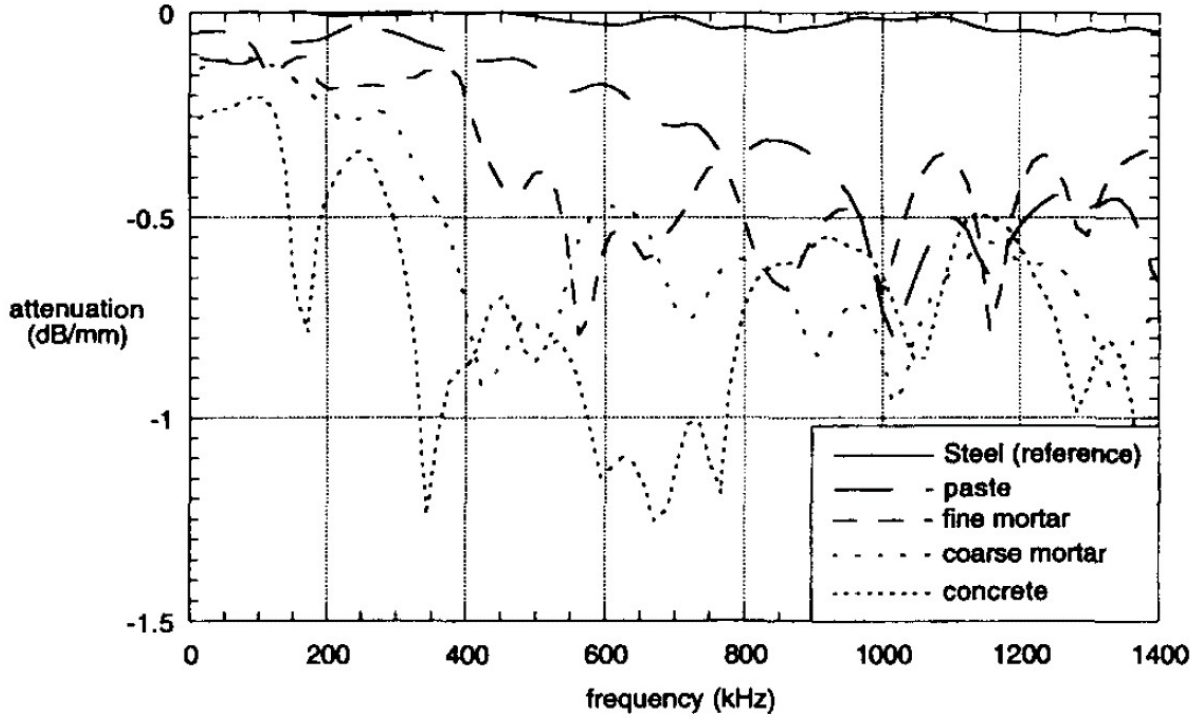

Figure 2.2 Measured ultrasonic attenuation in several specimens (Landis & Shah 1995).

Scattered ultrasonic waves in inhomogeneous media comprise a coherent (specular) part and an incoherent (diffuse) part. The coherent part as specular reflection and the incoherent as diffuse as illustrated in Figure 2.3 (Cowan et al. 1998). The coherent portion is both spatially and temporarily coherent with the incident source signal. For long wavelengths compared to the scatterers size or for small volume fractions of scatterers, the coherent portion is dominant. The coherent portion's amplitudes are significantly larger than the amplitudes of the diffuse part, so that the diffuse portion can be neglected. Attenuation is caused by energy loss (dissipation) and by scattering. Conventional ultrasonic wave NDE methods measure signal travel times and amplitudes (coherent part only) in the material, and then use ultrasonic velocity and attenuation to estimate quality of concrete

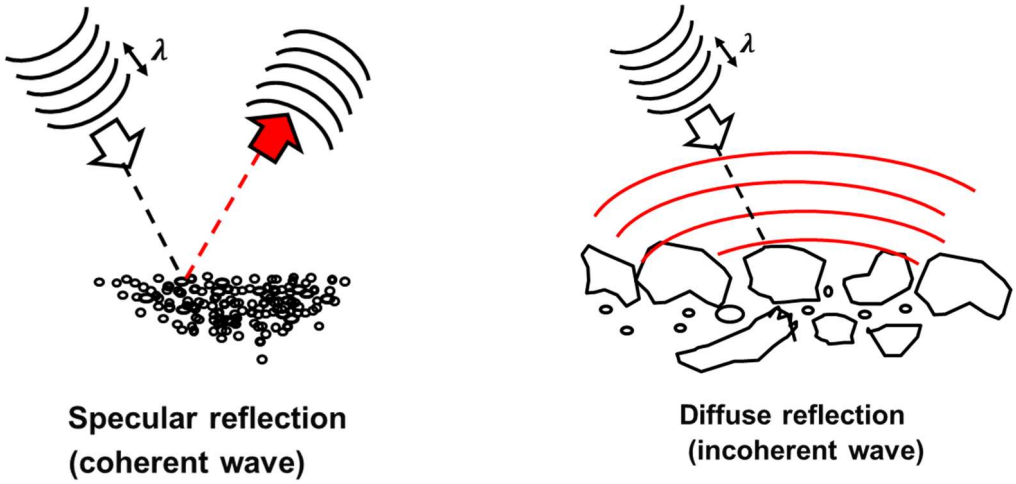

Figure 2.3 Illustration of coherent reflection (left) and diffuse reflection (right).

Diffuse field wave scattering occurs because of multiple scattering and resonance behaviors from multiple, randomly oriented scatterers (e.g. cracks) as the wave propagates through the medium. Diffusive parameters derived from the signal characteristics have been used to characterize, globally, the microstructure of materials. A Diffuse field is a wave field set up by multiple scattering (diffuse reflection), that happen after or during original coherence (Weaver & Sachse 1995). The field variables become random (it is an extremely complicated path). If the initial energy scatters many times during its path from source to receiver, it is modeled to behave as a diffusion process. It is often treated as noise, although the information it contains is a representation of microstructure of the material. This field has been used for accessing micro-scale damage in concrete (Anugonda et al. 2001). The diffuse portion of the signal is dominant in a strongly scattering material.

In Literature review, researchers have applied diffusive ultrasonic tests to concrete and have observed that contributions of the embedded aggregates in the cement matrix dominate the diffuse scattered response (Weaver 1990).; the diffuse scattered field from the aggregates obscures the scattered response from distributed micro-cracks and porosity (i.e., distributed damage) in the cement matrix (Anugonda et al. 2001; Becker et al. 2003). Although researchers have utilized the application of diffuse ultrasound to monitor applied stress (Larose & Hall 2009) and the condition of a single large macro-crack (Quiviger et al. 2012) in concrete, practical characterization of distributed damage in concrete remains difficult. Despite this, several researchers have reported some ability to distinguish distributed damage (Deroo

2009) and distributed porosity (Goueygou, Popovics, et al. 2009) in concrete using diffuse ultrasound measurements. These experiments demonstrates some significant experimental limitations (small sample size with specific geometry, need for specialized high-end laboratory equipment, etc.). Due to that, the technique has not been applied in the field.

Anugonda et al. 2001 shows ultrasound diffuse scattering in heterogeneous composition of concrete. This study considers different samples, sensing location and frequencies (but same mix design). All receiving signals are collected after 500 repetition averages. Figure 2.4(right) shows an experimental result of the fitted energy diffusion with 100 kHz excitation signal. The solid line indicates fitted diffusion equation. The error bar indicates measured fluctuation from different samples and sensing locations.

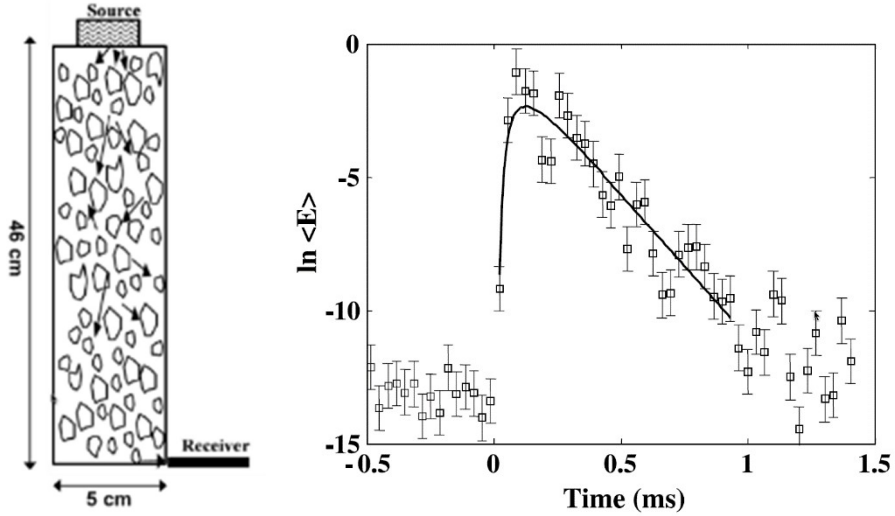

Figure 2.4 (Left) testing schematic of ultrasonic diffuse wave for 45 x 5 cm concrete sample, and (right) experimental result of energy diffusion at 100 kHz (Anugonda et al. 2001).

Figure 2.5 shows experimental data of diffusivity and dissipation. As shown in Figure 2.5 (left), data variation of diffusivity increases with decreasing frequency, while the variation of dissipation increases with increasing frequency (Figure 2.5, right). Although different samples and sensing positions are applied, these experimental results are consistent.

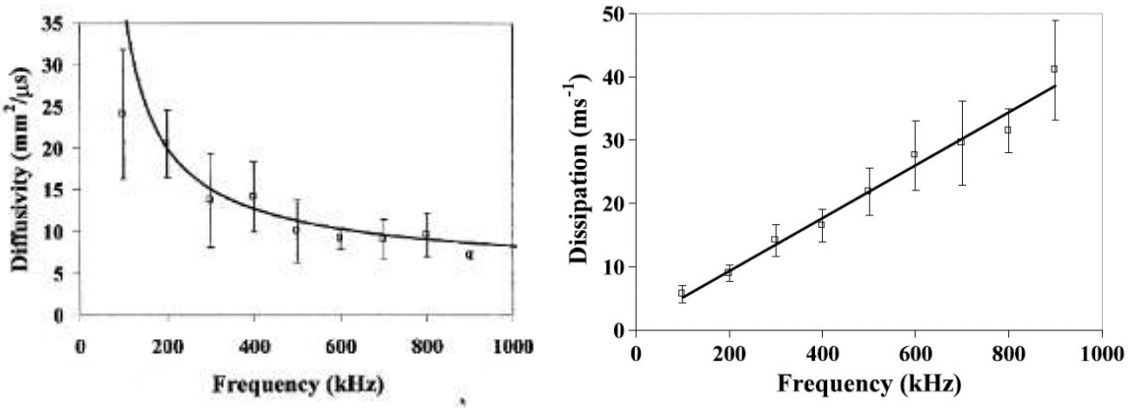

Figure 2.5 Experimental diffuse parameter data; (left) diffusivity, and (right) dissipation as a function of frequency (Anugonda et al. 2001).

Diffuse field is formed by multiply reflected waves (Lobkis & Weaver 2003). Because of random reflection, the initial arrival time of the coherent wave pulse is followed by a decaying tail, (or "coda") as shown in Figure 2.6. The coda arises from echoes whose arrival times are dependent upon features in the medium, giving rise to multiple scattering and resonance behaviors. The principal of the Coda wave analysis is comparing two signals measured at different damage levels and calculates the relative wave velocity change or time delay between them. Normally, one diffusive signal represents the response of the entire sample, because a single coherent wave path is no longer assumed. Coda wave interferometry (CWI) is detection of temporal changes in a medium by using the multiple-scattered medium as an interferometer (Snieder et al. 2002).

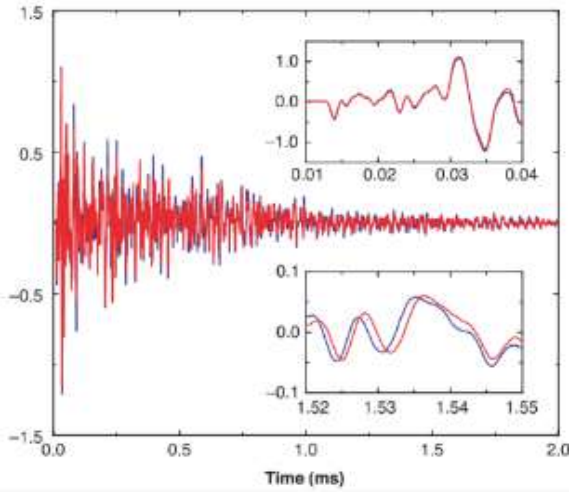

Figure 2.6 Example of waveforms recorded in a granite sample for temperatures of 45 and 50 °C, in blue and in red, respectively. The insets show details of the waveforms around the first arrival (top inset) and in the late coda (bottom inset) (Snieder et al. 2002).

Coda wave interferometry (CWI) is also used in geophysical applications such as earthquake analysis (e.g. Poupinet et al. 1984), but more recently has been applied for nondestructive testing applications for infrastructure (Shokouhi 2012; Schurr 2010). Typically, CWI measures time signal variation, for example by measuring temporal variation of crustal velocities using earthquake doublet (or pair) of microearthquakes. A pair of microearthquakes, before (M=1.7) and after (M=2.0) the Coyote Lake Earthquake (M=5.9) are studied (Poupinet et al. 1984). The doublet technique is correlated seismic noise between two receiving signal, and then analyzes small phase changes at delay time in the correlations. CWI requires, same sensor location, same source, and invariant medium properties (speed, attenuation, scattering). CWI generally is sensitive to S-wave velocity variation scattered along numerous paths through the crust. Signals are about 1ms in length. Figure 2.7 (top) shows the doublet approach using the cross spectrum, and the figure (bottom) shows delay of arrival times computed between two receiving stations, indicating fitted slope.

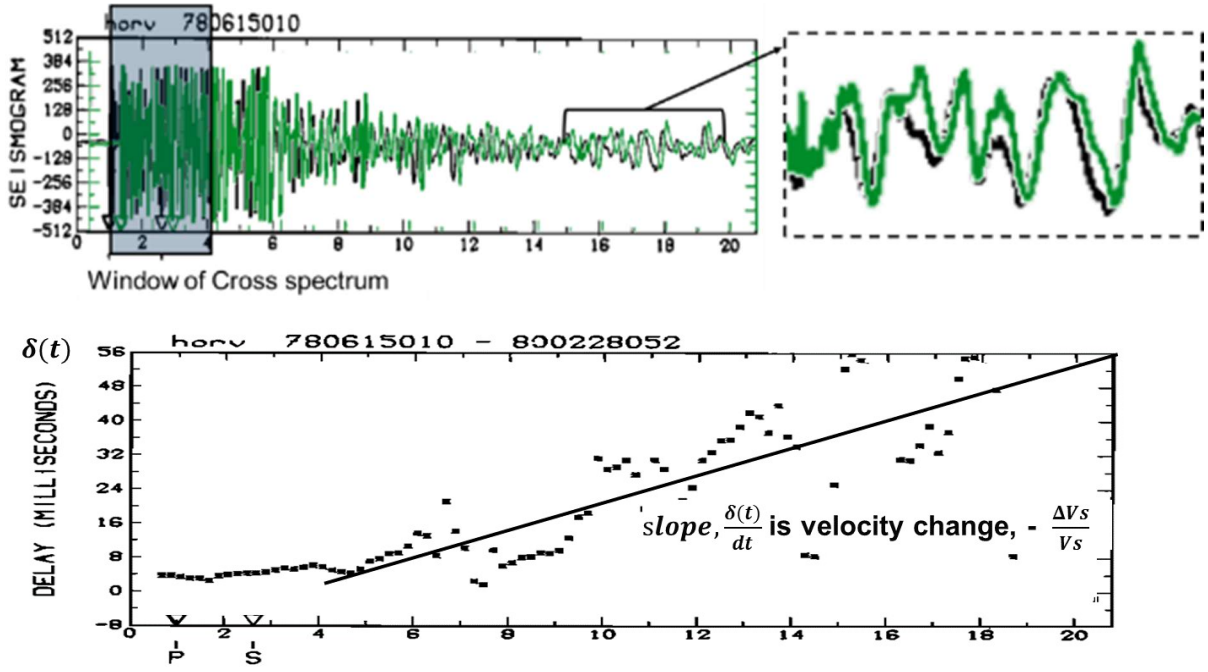

Figure 2.7 CWI with doublet approach: (top left) two doublet signals; the black signal indicates before shock and green indicates after shock. The blue shaded region indicates the window of the cross spectrum processing and (top right) zoomed in image indicating delayed signal components, and (bottom) delay of arrival times between the two signals **(Poupinet et al. 1984).**

There are other application of coda techniques (Snieder 1986). The temperature dependence of diffuse ultrasound in elastic bodies is also studied with CWI (Lobkis & Weaver 2003). Coda waves is also used

to studies stress-dependent velocity (Larose & Hall 2009).

Classical diffuse wave (or diffusivity analysis) and diffuse wave equation are explain in this section. Diffuse waves are modeled using a one-dimensional diffusion equation with dissipation (Weaver 1990; Anugonda et al. 2001; Becker et al. 2003)

$$\boldsymbol{D\frac{\partial^2}{\partial z^2}\langle E(z,t)\rangle - \frac{\partial}{\partial t}\langle E(z,t)\rangle - \sigma\langle E(z,t)\rangle = P_0\delta(z)\delta t,} \qquad (2.7)$$

where D is the ultrasonic diffusivity, σ is the energy dissipation rate, $\langle E(z,t)\rangle$ is the ultrasonic energy density as a function of time t and propagation distance z (the brackets denote the energy density over an ensemble average) $\delta(z)$ is Dirac function and P_0 is the initial energy, which is assumed to be input at time t = 0 and at z = 0. Essentially, D describes the additional "path" traveled by the propagating multiply scattered waves that give rise to additional scattered waves arriving after the direct coherent wave. The symbol, σ, describes the decay in energy of these multiply scattered waves in time. Eqn. (2.8) represents a solution to Eqn. (2.7),

$$\langle E(z,t)\rangle = P_0\frac{1}{2\sqrt{\pi Dt}}e^{\frac{-z^2}{4Dt}}e^{-\sigma t}\ , \qquad (2.8)$$

where the energy density is represented in the ultrasonic signal as a function of z and t. By examining the decay in the energy density of the signal, D and σ can be estimated through a minimization routine. Most estimators rely on taking the natural log of the energy density decay, which simplifies the extraction of D and σ as,

$$ln\langle E(z,t)\rangle = C - \frac{z^2}{4Dt} - \sigma t - 0.5lnt \qquad (2.9)$$

where *C* is

$$\frac{lnP_0}{2\sqrt{\pi D}}. \qquad (2.10)$$

The material properties are then correlated to estimates of D and σ to provide a means of characterizing materials from the decaying coda wave. The diffusion constant D is also a function of frequency, and this frequency dependence can be further exploited to provide specific information about the number density and physical characteristics of the scatterers that give rise to the coda signal (Weaver & Sachse 1995).

2.2.4 Lamb Wave Theory

Lamb waves, also known as guided plate waves, are propagating resonances which occur in free plates (Lamb 1917). The particle displacement from Lamb waves actually represent a group of wave mode types. They are formed by coupled P- and S-waves, comprising an infinite number of individual symmetrical (S) and anti-symmetric (A) solution modes, as shown in Figure 2.8. Harmonic wave propagation in along the plane direction is only possible for those combinations of frequency (f) and phase velocity (c) corresponding to standing waves in the thickness (perpendicular of wave propagation direction). These waves must obey the dispersion equation (Lamb 1917), from which dispersion curves can be calculated with

$$\frac{\tan \beta \frac{d}{2}}{\tan \alpha \frac{d}{2}} = -\left[\frac{4\alpha\beta k^2}{(k^2-\beta^2)^2}\right]^{+1} \qquad (2.11)$$

for symmetric modes and

$$\frac{\tan \beta \frac{d}{2}}{\tan \alpha \frac{d}{2}} = -\left[\frac{4\alpha\beta k^2}{(k^2-\beta^2)^2}\right]^{-1} \qquad (2.12)$$

for anti-symmetric modes where $\alpha^2 = \frac{\omega^2}{{C_p}^2} - k^2$, $\beta^2 = \frac{\omega^2}{{C_s}^2} - k^2$, ω =2πf, d =thickness, C_p = P-wave or longitudinal wave velocity, C_s = shear wave velocity, k = wavenumber = $\frac{\omega}{C_{ph}}$, $C_{ph} = phase\ velocity$.

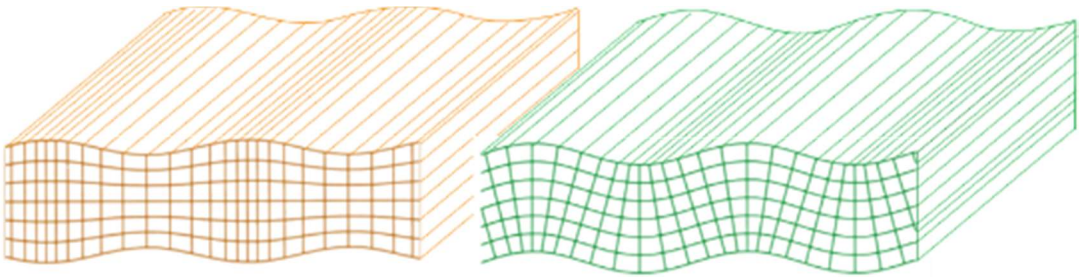

Figure 2.8 Symmetric (left) and anti-symmetric (right) mode shapes of Lamb wave.

In SH guided plane waves, the particle motion is perpendicular to wave propagating direction, and parallel to the surface of the medium. Now we consider the case of a plate having mixed boundary conditions with the Rayleigh-Lamb equation for plates. In this section, we consider P and SV waves in

the plate under conditions of plane strain. Although more complicated than the SH wave case, the results are helpful to understand a behavior of these guided waves in plate.

The potential functions, Φ and Ψ are related to u as the sum of scalar and vector potentials

$$\boldsymbol{u} = \boldsymbol{\nabla\Phi} + \boldsymbol{\nabla} \times \boldsymbol{\Psi}. \qquad (2.13)$$

Considering harmonic p waves and s waves propagating in elastic plate in x direction in Figure 2.9, the governing equations (Graff 1991) are

$$\boldsymbol{\nabla^2\Phi} = \frac{\boldsymbol{1}}{\boldsymbol{Cp}}\frac{\boldsymbol{\partial^2}}{\boldsymbol{\partial t^2}}\boldsymbol{\Phi}\ , \textit{and} \quad \boldsymbol{\nabla^2\Psi} = \frac{\boldsymbol{1}}{\boldsymbol{Cs}}\frac{\boldsymbol{\partial^2}}{\boldsymbol{\partial t^2}}\boldsymbol{\Psi}. \qquad (2.14)$$

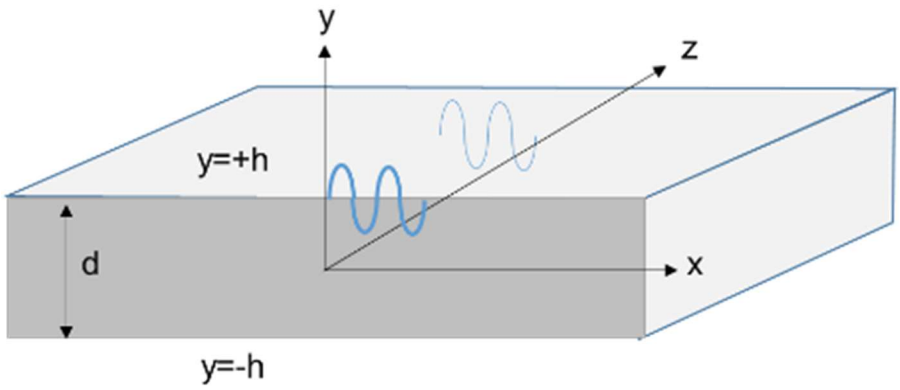

Figure 2.9 A plate with thickness d=2h.

For plane strain (z-invariant) conditions, displacements are given by

$$\boldsymbol{u_x} = \frac{\boldsymbol{\partial\varphi}}{\boldsymbol{\partial x}} + \frac{\boldsymbol{\partial\Psi_z}}{\boldsymbol{\partial y}},$$

$$\boldsymbol{u_y} = \frac{\boldsymbol{\partial\varphi}}{\boldsymbol{\partial y}} - \frac{\boldsymbol{\partial\Psi_z}}{\boldsymbol{\partial x}}, \qquad (2.15)$$

$$\textit{and,}\ \boldsymbol{u_z} = -\frac{\boldsymbol{\partial\Psi_x}}{\boldsymbol{\partial y}} + \frac{\boldsymbol{\partial\Psi_y}}{\boldsymbol{\partial y}}.$$

Also stress can be expressed in terms of the potentials as,

$$\boldsymbol{\sigma_{yx} = \mu\left(\frac{2\partial^2\varphi}{\partial x\partial y} - \frac{\partial^2\Psi}{\partial x^2} + \frac{\partial^2\varphi}{\partial y^2}\right),}$$

$$\boldsymbol{\sigma_{yy} = \lambda\left(\frac{\partial^2\varphi}{\partial x^2} + \frac{\partial^2\varphi}{\partial y^2}\right) + 2\mu\left(\frac{\partial^2\varphi}{\partial x^2} - \frac{\partial^2\Psi}{\partial x\partial y}\right).} \quad (2.16)$$

where λ and μ are known as Lame's elastic constants. μ is also known as the shear modulus. Assuming harmonic plane wave propagation in x-direction as shown in Figure 2.9, a general solution for the wave equations for harmonic plane wave propagation in the x-direction in terms of potential function is

$$\boldsymbol{\varphi(x,y) = f(y)\, e^{i(kx-\omega t)},}$$

$$\boldsymbol{\Psi(x,y) = g(y)\, e^{i(kx-\omega t)}.} \quad (2.17)$$

Substitution Eqn. (2.17) in Eqn. (2.15) gives functions f and g,

$$\boldsymbol{\frac{\partial^2}{\partial y^2} f(y) + \alpha f(y),}$$

$$\boldsymbol{\frac{\partial^2}{\partial y^2} g(y) + \beta f(y).} \quad (2.18)$$

where, α and β are functions described in Eqn. 2.12. The solution to these equations are

$$\boldsymbol{f(y) = A\sin(\alpha y) + B\cos(\alpha y),}$$

$$\boldsymbol{g(y) = C\sin(\beta y) + D\cos(\beta y).} \quad (2.19)$$

Now, before we apply the mixed boundary conditions, we consider two sets of modes: symmetric and antisymmetric modes. Substitution of Eqn. (2.19) into the wave equation Eqn. (2.15) gives

$$\boldsymbol{u_x = -ikB\cos(\alpha y) + \beta C\cos(\beta y) + ikA\sin(\alpha y) - \beta D\sin(\beta y),}$$

$$\boldsymbol{u_y = -\alpha B\sin(\alpha y) - ikC\sin(\beta y) + \alpha A\cos(\alpha y) - ikD\cos(\beta y).} \quad (2.20)$$

including A, B, C and D constants. u_x in terms of cosine terms from u_x give symmetric terms with respect to y = 0, while for u_y the B and C give antisymmetric mode. Four different cases are described in Figure 2.10. This mode shapes give us to understand how to group symmetric or antisymmetric mode.

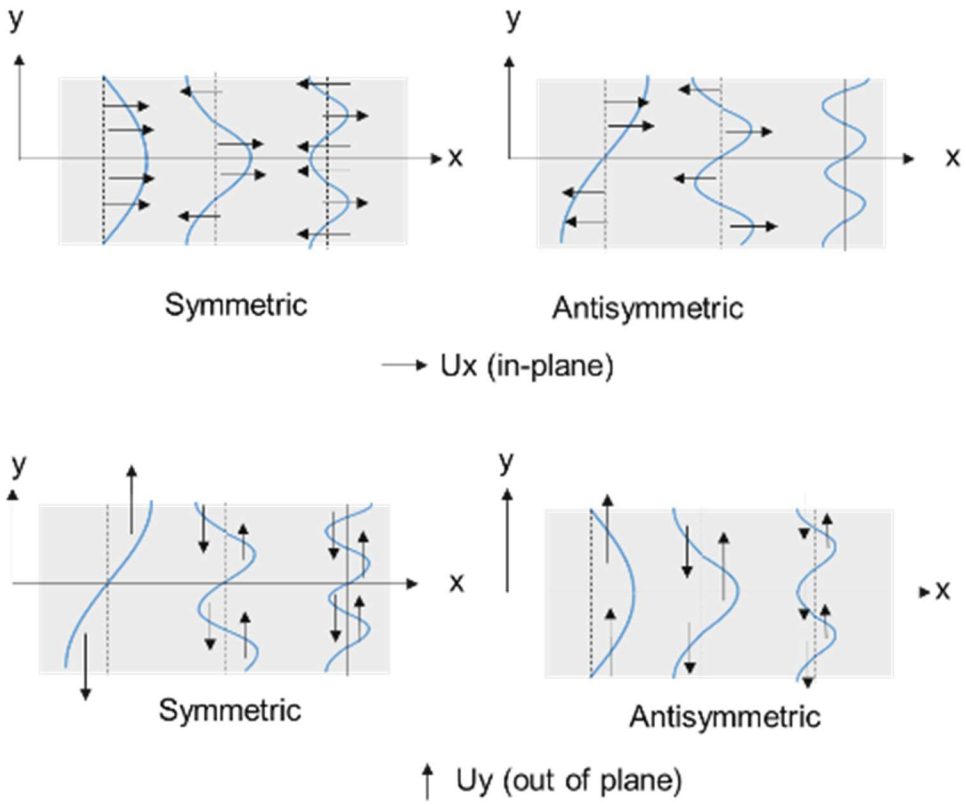

Figure 2.10 First three sets of modes for Ux (top) and Uy (bottom) displacements for symmetric (left) and anti-symmetric (right) modes.

We express the stress by

$$\sigma_{yx} = \mu\,[\,-2ik\alpha B\,\sin(\alpha y) + (k^2 - \beta^2)\,C\,\sin(\beta y)],$$

$$\sigma_{yy} = -\lambda(k^2 + \alpha^2)\,B\,\cos(\alpha y) - 2\mu[\,\alpha^2 B\cos(\alpha y) + ik\beta\,C\,\cos(\beta y)] \qquad (2.21)$$

for symmetric modes and,

$$\sigma_{yx} = \mu\,[\,-2ik\alpha\ \ \cos(\alpha y) + (k^2 - \beta^2)\,D\,\cos(\beta y)],$$

$$\sigma_{yy} = -\lambda(k^2 + \alpha^2)\,A\,\sin(\alpha y) - 2\mu[\,\alpha^2 A\,\sin(\alpha y) + ik\beta D\,\sin(\beta y)] \qquad (2.22)$$

for antisymmetric modes.

We can apply similar traction-free boundary in a plate,

$$\boldsymbol{\sigma_{yx} = \sigma_{yy} = 0 \quad at\ y = \pm h = \pm d/2.} \qquad (2.23)$$

Applying the boundary conditions will give two equations in the matrix form,

$$\begin{bmatrix} -2\mu ik\alpha\ sin(\alpha h) & \mu\left(k^2-\beta^2\right)\ sin(\beta h) \\ -\lambda\left(k^2+\alpha^2\right)cos(\alpha h) - 2\mu\alpha^2 cos(\alpha h) & -2\mu ik\beta\ cos(\beta h) \end{bmatrix} \begin{bmatrix} B \\ C \end{bmatrix} = \begin{bmatrix} 0 \\ 0 \end{bmatrix} \qquad (2.24)$$

The determinant of the matrix in Eqn. (2.24) gives one equation,

$$\frac{\mu\left(k^2-\beta^2\right)\ sin(\beta h)}{-2\mu i \quad sin(\alpha h)} = \frac{-2\mu ik \quad cos(\beta h)}{-\lambda(k^2+\alpha^2)\,cos(\alpha h) - 2\mu\alpha^2 cos(\alpha h)} \qquad (2.25)$$

for symmetric modes. From Navier's equation, Logitutunidnal (Cp) and shear wave velocity (Cs) is determined by λ, μ and the density ρ. Substituting these relations into Eqn. (2.25), we obtain Eqn. (2.11) and (2.12).

2.3 Conventional NDE Methods for Concrete Structures

2.3.1 Ultrasonic Pulse Velocity (UPV) and Ultrasonic-Echo Method

UPV tests assess the quality of concrete by measuring P-wave velocity, a given path of P-wave pulse propagation over travel time (ACI *228.2R-04*). The UPV test is easy to apply and highly successful at finding internal voids and transverse cracks. However, the need for access to both sides of a structure considerably limits the potential for wide application of this method. Moreover, wave transmission time is the only output of the UPV test and does not provide information on the depth of defects. The ultrasonic-echo method uses the arrival time of a stress wave reflected from a defect on one face of the concrete structure to monitoring deterioration (ACI *228.2R-04*). Recent advances have resulted in the improved transducer, arrays which can create a 3-D internal image of defects that may be present in a concrete element at penetration depths of up to approximately 2 m (Bishko et al. 2008).

2.3.2 Surface Wave Methods: SASW and MASW

A spectral analysis of surface waves (SASW) method is based on in-situ near-surface seismic profiling, which can provide an estimate of Young's Modulus (E) of the surface layer of a pavement as well as an estimate of thickness (Roesset et al. 1990). The R-wave velocity for each frequency component is also known as the "phase velocity". The phase velocity is calculated by the travel time between the two

receivers. The travel time is determined by measuring the phase difference of the frequency components when they arrive at the receivers, where the distance between the two receivers is known. A digitized waveform analyzer is used to determined phase information of the cross power spectrum between the two receivers for each frequency. The schematic presentation of the MASW system Multichannel analysis of surface waves (MASW) evolved from extensive studies performed by SASW investigators. They acknowledged that surface wave properties must be more complex than previously assumed, and that the two-receiver approach had clearly reached its limitation in its ability to generate analyses of greater complexity. A multiple number of receivers are deployed with even spacing along a linear survey line with receivers connected to a multicham1el recording device (seismograph). Each channel is dedicated to recording vibrations from one receiver. Recently, the author published fast MASW technique to monitor the concrete delamination using energy shift to the different mode (Ham & Popovics 2014). In addition, Schaal et al. in 2015 studied on the interaction of Rayleigh surface waves with defects in a thick aluminum plate carrying out using numerical simulations and laboratory experiments (Schaal et al. 2015).

2.3.3 Other NDT Methods

Vibration resonance tests are employed to monitor elastic constitutive properties and accrued damage in concrete samples, following a standardized test procedure (ASTM 2008b). In the procedure, the vibration of fundamental resonance modes is monitored, and the associated frequency of vibration measured with contact and contactless sensors. Dynamic elastic constants of the bulk samples are calculated from the frequency values. The specific mode of vibration, among the longitudinal, flexural and torsional families of modes, is set up by the physical testing configuration, and the frequency values of the fundamental modes are normally extracted from frequency domain signals. N.J. Carino and M. Sansalone developed the technique called impact-echo (IE) for nondestructive testing of concrete structures at the National Institute of Standards and Technology (NIST) in the 1980s. A mechanical impact is generated on the surface of the test object, and the surface responses are measured. The stress waves, which propagate into the object, undergo multiple reflections between the test surface and the internal defects (or external boundaries) of the test object. Pulsed microwave/Radar techniques (GPR) is a pulse echo method which evaluates the deterioration of a material from changes in the dielectric properties and attenuation (ASTM D6087-08). GPR uses electromagnetic waves to penetrate the pavement by transmitting the wave energy into the pavement from a moving antenna. The arrival and

strength of these echoes can then be used to calculate pavement layer thickness and other properties like moisture content. However, electromagnetic waves are disturbed by varying moisture and salt content within the concrete, thereby complicating the interpretation of RADAR images. Infrared thermography (IRT) uses solar radiation to generate thermal differentials between delaminated and sound areas of the deck (Maser R & Roddis 1990) with such an infrared camera.

2.4 Contactless Sensors

Figure 2.11 (top) shows the basic construction of a microelectromechanical system (MEMS) device. MEMS sensors vary in package type, output format and sensitivity, where the sensitivity is principally controlled by the elastic and geometric properties of the active elements (Ganji 2011). For the MEMS acoustic sensors used in this work, the active elements are composed of a fixed perforated backplate, support-body (substrate), and a thin pressure sensitive diaphragm, as shown in Figure 2.11 (bottom left). These elements are composed principally of monocrystalline silicon and produced using micro machining thin-film technology. The operation of capacitive MEMS requires an external DC bias voltage applied between the diaphragm and back plate. This typical type of sensor is called a capacitive CMOS MEMS. The CMOS (complementary metal-oxide-semiconductor) unit provides the low bias voltage to the diaphragm. The applied bias causes the diaphragm to move towards and to come in contact with the extended edges of the back plate by electrostatic attraction. Once the diaphragm contacts the extended edges of the back plate, the boundary conditions of the diaphragm are well approximated by a simply supported plate (Pedersen & McClelland 2005). This configuration provides an air gap between the diaphragm and back plate, and ensures an effective acoustic seal across the diaphragm. Air pressure variations, for example those caused by propagating acoustic waves in the air that impinge on the diaphragm, cause forced mechanical vibration of the stretched diaphragm. The CMOS unit converts the mechanical vibration to an electrical voltage output signal that is proportional to a specific sound field quantity, e.g. air pressure variation. The sensitivity and frequency bandwidth of the response are controlled by shape, thickness, and boundary conditions of the diaphragm. Figure 2.11 (bottom right) shows the frequency response of the capacitive MEMS sensors used in this work. The frequency response is fairly flat between 10 to 30 kHz, with increased sensitivity between 30 and 55 kHz. The sensitivity decreases significantly above 100 kHz (response not shown).

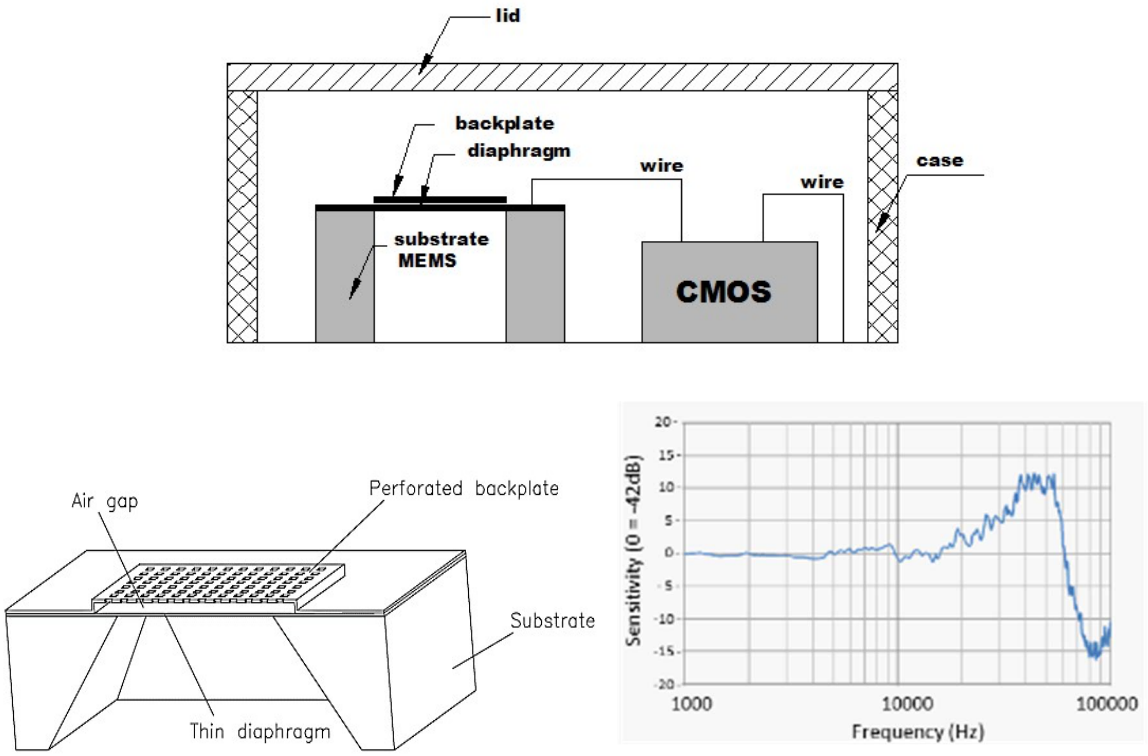

Figure 2.11 Basic construction (top) (Ham & Popovics 2015a)***, construction of active elements (bottom left) (Reproduced with permission from (Pedersen & McClelland 2005)) and frequency response (bottom right) (Reproduced with permission from(Knowles 2009)), of the type of MEMS sensor used in this work. Nominal sensor sensitivity = 7.9 mV/Pa.***

In Chapter 3, the performance of contactless MEMS sensors are evaluated with respect to those from two different contactless sensors and a contact sensor in terms of application to conventional concrete NDT methods. The two other contactless sensors are conventional microphones having distinct underlying technological bases: an electret condenser microphone (ECM) and a dynamic membrane microphone (DMM). An accelerometer is used as a contact sensor and in some cases also as reference. However the working frequency range depends on the type of microphone used; conventional DMM are limited to frequencies well below 20 kHz, while ECM can sense, in some cases, up to 80 kHz (Oh, Kee, et al. 2013). MEMS sensors show typical sensitivity of 7.9 mV/Pa at 1 kHz (Knowles 2009) and frequency range of 1 to 90 kHz (see typical range of frequency response in Figure 2.11). MEMS, ECM and accelerometers require external power and pre-amplification or circuitry, while the DMM do not. Table 2.1 compares the performance metrics of the four different sensors employed in this work. The signal to noise ratio (SNR) is calculated as the ratio of variance of total signal to variance of noise in the

signal in dB; the reported SNR values are computed from experimental data for impact-echo tests, which will be discussed subsequently. Among the air coupled sensors, MEMS demonstrate the highest sensitivity and SNR. Furthermore MEMS sensors compare favorably to the contact accelerometer; the SNR for MEMS is about half of that for conventional contact accelerometers for the tests reported here.

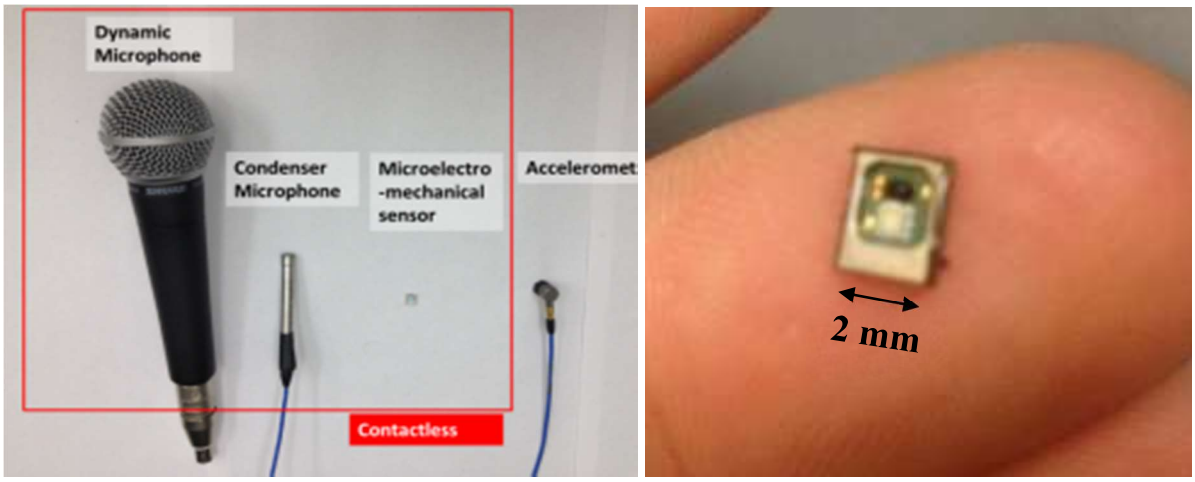

Figure 2.12 Set of tested sensors (left) and individual MEMS sensor unit (right) **(Ham & Popovics 2015a) .**

Table 2.1 Performance metrics of four sensors employed in this work (Ham & Popovics 2015a) **.**

	Sensitivity (mV/Pa) at 1 kHz	*Frequency range (kHz)*	*SNR (dB)*
Accelerometer (contact)	*1.02 mV/($\mathbf{m/s^2}$)*	*1 to 18 kHz*	*25.12*
MEMS	*7.9 (mV/Pa)*	*1 to 90 kHz*	*14.7*
ECM	*4 (mV/Pa)*	*4 to 80 kHz*	*7.04*
DMM	*1.85 (mV/Pa)*	*below 20 kHz*	*5.02*

Air-coupled ultrasonic transducers used to generate waves in air are based on one of two types of technology: a resonant piezoelectric ceramic (PZT) solid element or a capacitive membrane, which were introduced for detecting obstacles within robotic systems (Maslin 1983). PZT elements are excited with a transient electrical pulse, and then the PZT element vibrates at the natural resonant frequency. The PZT resonance emit narrower bandwidth than electrostatic type transducer which accurately emit broadband frequency by signal generator (Purnell et al. 2004). PZT transducers can be inefficient wave energy generators because the large acoustic impedance mismatch at the transducer air boundary.(Lynnworth 1965). The capacitance transducer uses a metal dielectric membrane which is

positioned with its insulating side against the surface of a rigid conducting back plate (Carr & Wykes 1993).

2.5 Signal Processing

2.5.1 Fundamental Signal Processing

Excitations (inputs) to a dynamic system progress with time, thereby producing responses (outputs), which vary with time, as well. These signals can be recorded or measured. A measured signal is referred to as a *time history.* The Fast Fourier Transform (FFT) is a discrete Fourier transform algorithm which reduces the number of computations needed for N points from $2N^2$ to 2NlgN, where lg is the base-2 logarithm. If the function to be transformed is not harmonically related to the sampling frequency, the response of an FFT looks like a sinc function (although the integrated power is still correct). Most digital signals are infinite or sufficiently large that the dataset cannot be manipulated as a whole. Sufficiently large signals are also difficult to analyze statistically because statistical calculations require all points to be available for analysis. In order to avoid these problems, engineers typically analyze small subsets of the total data through a process called windowing. Common types of windows are rectangular, Hamming, Blackman and Kaiser (Oppenheim & Schafer 2009). Digital filtering is used to attenuate signals with frequencies within some cutoff band. The actual amount of attenuation for each frequency varies from filter to filter. High-pass filters have many uses such as blocking direct current (DC) from circuitry sensitive to non-zero average voltages or RF devices. A wavelet is a mathematical function used to divide a given function or continuous-time signal into different scale components. Usually one can assign a frequency range to each scale component, which can then be studied with a resolution that matches its scale. A wavelet transform is the representation of a function by wavelets. The wavelets are scaled and translated copies (known as "daughter wavelets") of a finite-length or fast-decaying oscillating waveform (known as the "mother wavelet").

2.5.2 Short-Time-Interval Average Signal (STIS) Analysis

A short-time-interval average signal (STIS) is used for calculating signal energy density, $< E_{STIS}(f,t) >$ from experimental data. The signal using a window width (Δt) as shown in Figure 2.13 (left) equals the duration of the excited, of the square of the excited filtered signal (Weaver & Sachse 1995). The power

spectrum of each time window (Δt) is calculated. After selecting frequency windows centered at excitation frequency with frequency band width (Δf), each frequency window spectrum is integrated. Each integrated value is the energy density, < E(f,t) >. A plot of ln(E) as function of time is called as Energy diffusion, plot as shown in Figure 2.13 (right). The Energy plot can be applied to fit with Eqn. (2.7). This analysis is used in the Chapter 9.

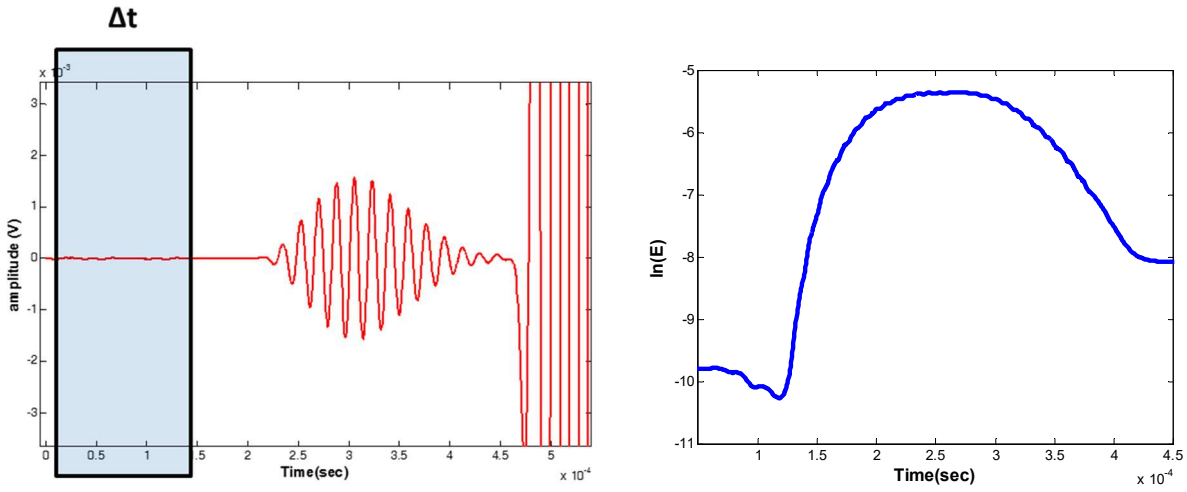

Figure 2.13 Short-time-interval average signal: (left) raw time signal with window width (Δt), and (right) short-time-interval average signal, E_{STIS}.

2.5.3 Data fusion

Data fusion analysis is subdivided into two different categories. The first is a fusion of different NDT techniques, most of which can now be automated and computer controlled in order to facilitate signal interpretation. Despite these improvements, non-destructive examinations (NDE) are usually performed by a qualified NDT inspector using NDT techniques applied on an individual basis. Because each NDT method presents different advantages and limitations, the use of more than one method is usually required to inspect a material fully. The concept of data fusion can be used to combine information from multiple NDT systems for more accurate decision-making (Gros 1997). The second category of data fusion analysis is a fusion of multiple sensors. The use of multiple sensors has numerous advantages over the use of a single sensor. A multiple-sensor device can include any instrument with several sensors of identical or dissimilar types used to measure a physical quantity. The simultaneous use of similar sensors can be very advantageous when large areas need to be covered in a short time or to assess the accuracy of the result by comparing multiple readings (Gros 1997).

2.6 Imaging

There have been many improvements to imaging technology in recent years for NDT. Imaging refers to a number of techniques looking the integrity of structures. It can be used to assist diagnosis or characterization of different structural and material conditions.

2.6.1 B-scan and C-scan images

The A-scan is single time domain signal. The B-scan presentation is a profile (cross-sectional, x-z plan) view of the test specimen. In the B-scan, the time-of-flight (travel time) of the sound pressure is displayed along the x axis, and the linear position of the transducer is displayed along the horizontal axis. The B-scan is typically produced by establishing a stacked A-scan. The C-scan presentation provides a plan-type (x-y in this case) view of the location and size of the test specimen features. The plane of the image is parallel to the scan pattern of the transducer. B- and C-scan presentations are usually produced with data from an automated data acquisition system.

2.6.2 SAFT based Images

An algorithm known as the Synthetic Aperture Focusing Technique (SAFT) has been implemented to overcome challenges experienced with B- and C-scan data for concrete. This algorithm improves resolution by coherently superimposing signals collected at multiple locations. This electively focuses the signals on each point in the image (Schickert et al. 2003). Using SAFT, researchers such as Schickert et al. have been able to construct internal images from one-sided surface scans of concrete elements (Schickert 2005). It is generally agreed that coupling and measurement tedium remain the limiting obstacle, however, recent progress has been made using arrays of point contact S-wave transducers (Mielentz 2008).

2.6.3 Tomography based Images

Tomography is the production of cross-sectional images of an object using information from projections through the object. The projections used in conventional tomography consist of velocity or attenuation measurements of ultrasonic or electromagnetic pulses transmitted through the object. The UPV tomograph was produced using the Filtered Back-projection algorithm, which is a convolution method. In order to utilize this method, the data were modified to simulate a fan-shaped data collection geometry, and straight rays from sender to receiver were assumed. This tomograph illustrates that, with sufficient measurements, the internal void can be accurately imaged. Attenuation tomographs were also attempted, but they were not published because variations in coupling made them less clear and introduced more

artifacts (Schickert 2005). There are two groups of reconstruction methods from projections: analytic, such as filtered back projection (FBP), and the iterative method such as algebraic reconstruction techniques (ART). The Analytic reconstruction methods (FBP) are efficient (fast) and elegant, but they are unable to handle complicated factors such as scatter. Until recently, filtered back projection has been used for reconstructions in x-ray CT and for most SPECT and PET reconstructions. Radon transform is used for creating images. Iterative reconstruction algorithms, on the other hand, are more versatile but less efficient. Iterative algorithms that are both fast and efficient are currently under development. With the rapid and continual advancements in computer speed and memory, iterative reconstruction algorithms will be used in more and more applications of SPECT and PET and will enable more quantitative reconstructions. The technique has already been widely used for ultrasonic imaging of concrete (Hall 2011).

CHAPTER 3 IMPROVEMENT OF CONTACTLESS SYSTEM AND VERIFICATION

In this chapter, the hardware that are used to generate and detect ultrasonic waves in concrete are described. The hardware represent a fully contactless air-coupled system, which was designed and assembled by the author. The fundamental concept and equipment configuration are shown in Figure 3.1. The equipment set comprises a computer, multi-channel data acquisition system, contactless capacitive transmitting transducer and contactless MEMS receiving transducers.

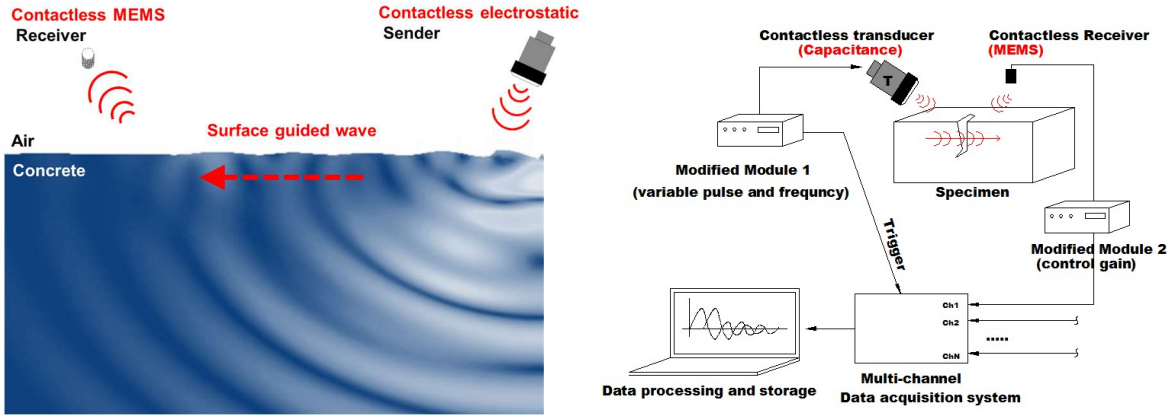

Figure 3.1 (left) Concept of fully contactless ultrasonic testing and (right) testing configuration setup (Ham & Popovics 2015b) .

The application of ultrasonic surface waves to concrete followed, allowing tests on samples with only one-sided access. In these tests, the air-coupled transducers are located on the same side of the sample, where the airborne ultrasonic energy is usually projected at the surface at some non-normal "critical" angle to promote surface wave generation. Air-coupled, contactless surface wave tests have been used in laboratory test studies to monitor porosity in small cement paste (Soltani et al. 2013), mortar (Goueygou, Lafhaj, et al. 2009), and concrete (Abraham et al. 2012; Piwakowski et al. 2012; Garnier et al. 2013) samples, and to characterize aggregate distribution in asphalt concrete (In et al. 2009). In some cases, sophisticated signal analyses schemes were employed, such as dispersion analysis with slant-stack transforms (Abraham et al. 2012) and non-linear analysis (Garnier et al. 2013), which suggest that high quality signal data can be obtained. Preliminary but limited application of air-coupled ultrasonic tests (UT) to a concrete structure in situ has been reported [15]. However, field application of air-coupled UT remains uncommon. Abraham et al. (Abraham et al. 2012), Piwakowski (Piwakowski et al. 2012) and

Garnier (Garnier et al. 2013) used the same commercial air-coupled UT hardware system, where low SNR signals and high sensitivity to the surface condition are reported for some cases.

This chapter presents work conducted to overcome key technical barriers to automated contactless UT implementation in concrete infrastructure elements. In particular, I evaluate the utility surface-guided waves for this purpose. First, I introduce and optimize a contactless UT configuration that uses low cost, high sensitive, and practical sensors so that multi-sensor arrays may be more readily deployed. The testing system produces high quality (high signal-to-noise ratio) signal data and enables reasonably large inspection lengths, e.g. greater than 0.5 m, in conventional concrete without necessitating surface preparation. I deploy the contactless UT on a pre-stressed concrete rail tie that contains realistic damage conditions to demonstrate the utility of the ultrasonic tests on concrete infrastructure elements, and then propose ultrasonic signal processing and analyses schemes appropriate for incorporation within an automated scanning system for characterizing distributed cracking damage in concrete (see Chapter 9). The findings reveal potential for extending the application air-coupled UT to concrete infrastructure elements in the field and demonstrate new testing capability for concrete structures, enabling exciting possibilities for improved automated or robotic inspection of the concrete infrastructure.

3.1 Performance Improvements to Contactless Sensing System

Hardware improvements to the contactless sender (electrostatic, capacitance transducer) and contactless receiver (MEMS sensor) are fundamental to moving forward with this work. Improved incident signals are needed to increase sensitivity and improve performance for specific applications. The contactless electrostatic transducers have great potential for performing various central-frequency, bandwidth and air pressure-level studies of input signals. The first task is to identify the usable frequency range to find optimal performance. Then various input signals will be considered including spike transients, frequency controlled tone bursts, and frequency swept chirp signals. An appropriate frequency range will be driven by the need of each test application. For example, broadband “mid-frequency” signals (10-90 kHz) are needed for MASW, enabling the creation of dispersion curves for characterizing different depths of delamination. Signals with broad frequency content may also generate more powerful data for scatter analysis and inversion. Finally, the maximum excitation pressure for the sensor needs to be established.

3.1.1 Modified Contactless Sending Transducer

The capacitive membrane transducer in our system is composed of a very thin Kapton-film membrane

(or diaphragm), vacuum-coated with metal to form a negative electrode. The thin foil is movable, and transforms electrical energy into mechanical energy (air pressure) and, conversely, mechanical energy into electrical energy. The positive electrode is the coining aluminum back plate, which also provides the resonant structure for the membrane. A DC bias is applied externally by an electronic module that uses a high voltage transformer and a bipolar junction transistor (BJT). A steel spring transfers the voltage from the back plate and holds the membrane under constant tension. Then, an AC voltage of a given frequency is applied to the membrane, which forces the film to move at the same frequency, sending out acoustic waves. When acting as a detector, the arrival of an ultrasonic wave at the membrane varies the capacitance and, in the presence of an imposed bias field, generates a dynamically varying charge upon the electrodes. As described in section 2.3, capacitance transduction provides a far better match to air (compared with PZT sensors), as the air-pocket / membrane system has a much lower acoustic impedance (Schindel et al. 1995). Our capacitive transducer with a Kapton-film membrane is commercially available and is relatively inexpensive.

The electrical excitation system, the excitation module, which comes with the commercially available capacitive package plays an important role. The module generates basically a 50 kHz 16-cycle excitation signal. A “mid-frequency” band (20-100 kHz) of ultrasonic frequencies is desired for testing concrete. In the chapter, two modified electrical excitation modules are introduced to control the pulse duration and frequency; these modules allows generation of variable pulse excitation that provides performance comparable to commercially available function generators. The first module, module A, comprises several ceramic resonators and a microchip. The module allows bandwidth and frequency control by a specific ceramic resonator. The ceramic resonator (see Figure 3.2, top left) controls the central frequency of the capacitive transducer between 30 and 80 kHz. The microchip in the module controls pulse duration. The main microchip (generic microcontroller) for the pulse control is the ATMEL Tiny45, which is controlled with an open source code communicating with a computer through the AVR ISP connector as shown Figure 3.2 (top right). The 7805 IC regulator in the module maintains a stable and constant voltage level, reducing the electric noise in the built-in commercial module. Module A is simple and easy to construct, although the pulse duration must be at least 10 cycles long owing to limited sampling resolution of the microchip. Thus it is ideal for tone burst signals at a selected central frequency.

A second module, called module B, is also used. It generates arbitrary electrical excitation signals. A generic microcontroller, such as a single–board microcontroller or PIC (Peripheral interface controller),

cannot create high frequency arbitrary waves having very low sampling rate, and as such are unsuitable for our purposes. Rather, field-programmable-gate-arrays (FPGA) shown in Figure 3.2 (bottom left) are used to generate the arbitrary signal. FPGA operate using customizable logic gates instead of writing instruction sets to the board, like a microcontroller does. The Module B FPGA uses a Papilio One board with a Spartan 3E FPGA chip. Logic gates exhibit very fast response times, in the order of nanoseconds; this is sufficient to create arbitrary pulses up to a frequency of 200 kHz. Furthermore, it is easily programmed so any waveform can be produced. Programming is carried out using Xilinx's ISE Design Suite. Although the module is more complicated in its design, it is suitable for generating arbitrary waves and chirp signals. The FPGA out signal connected to BJT in circuitry board of modified sending transducer as shown in Figure 3.2 (bottom right). More details about the circuitry are provided in A ppendix1.

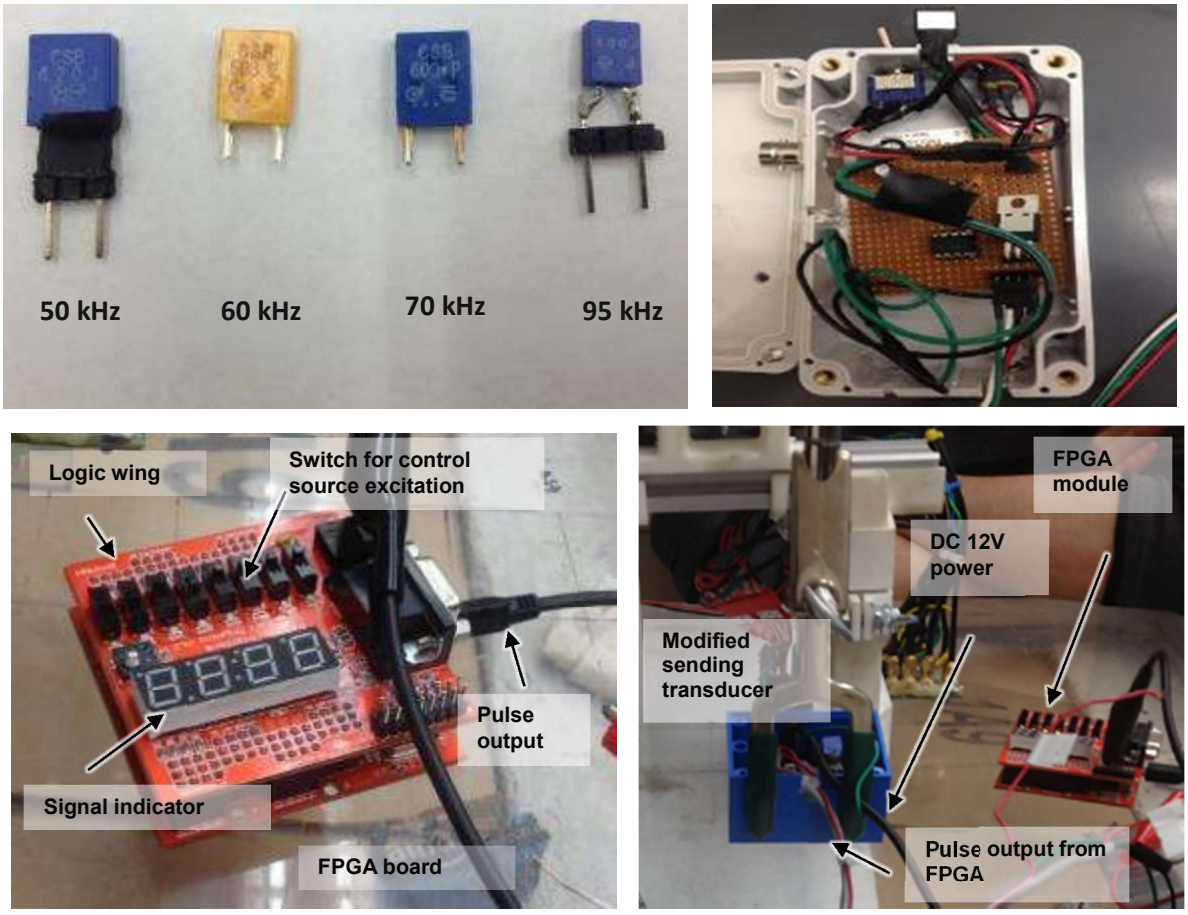

Figure 3.2 (top left) Ceramic oscillators indicating possible excited frequencies; (top right) detail of module A; (bottom left) detail of FPGA system for Module B; and (bottom right) connections for Module B.

3.1.2 Modified Contactless Receiving Transducer

Recent developments in MEMS (micro-electro-mechanical systems) sensing technology, provide an opportunity to improve our measurement capacity. MEMS are miniature, micro-machined sensors that provide a broad sensing platform across many different modalities. The advanced developments behind MEMS offer reduced power consumption, high sensitivity, reduced weight and smaller form factors, improved general performance and in varied environmental conditions and lower cost than their traditional sensing counterparts (Walraven 2003). The MEMS used in this work are a commercial product. Each individual sensor unit, shown in Figure 2, requires external electrical power (1.5 ~ 3 DC volts) and additional circuitry to operate; it is possible to purchase self-contained units where the sensor and required circuitry are already placed within a case. In the work reported here, however, basic MEMS sensor units were purchased, powered and wired by the authors in order to provide design flexibility needed to create multi-sensor arrays.

For each MEMS sensor unit, two 0.1-μF coupling capacitors were placed at the output to form a high pass filter with input resistance, and all grounds connected to the data acquisition system (DAQ) ground. The first coupling capacitor is connected between the positive (+) and the negative (–) signal out of the MEMS sensor unit. The second capacitor is placed between the positive side DAQ and the positive side of signal out. All sensors and circuitry are electrically connected and fixed by manual soldering using a micro tip, and later encased with an epoxy coating to protect the connections from physical and mechanical events. Multiple MEMS units may be incorporated into a single array set, as shown in Figure 3.3. Each sensor unit requires modest power, less than 250 μA of current at potentials between 1.5 to 3.6 V. In the work reported here, a single 1.5 V dry-cell battery (AAA or AA type) is used to provide the power for all the sensors in an array. The MEMS sensors provided consistent performance and sensitivity with the described power configuration. It is highly-integrated, having a small form factor (2 x 3 mm), and represents a cost-effective solution as compared with conventional MEMS sensors. The reduced size provides improved spatial identification of the sensed point, so better quality inspection can be performed. In addition, the CMOS MEMS sensor ($5 unit price) is far less expensive than a commercial condenser microphone ($1600 unit price), and a contact accelerometer, ($400 unit price). The MEMS sensor does not require ancillary equipment, such as an amplifier. The small size and low unit cost enables deployment of many sensors in an array.

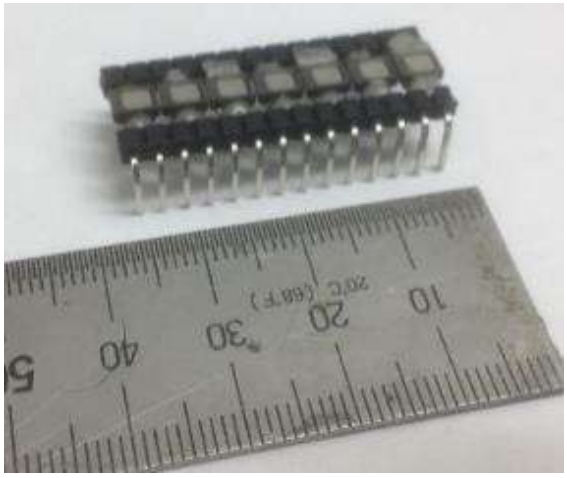

Figure 3.3 Detail of 7-element MEMS sensor array with 2-mm spacing between sensors: each MEMS unit was soldered and then coated with epoxy.

3.2 Verification and Parametric Study

3.2.1 Experimental Study of Contactless Sender

All of current research, including damage such as delamination (Chapter 5), distributed microcracks (Chapter 6), and rail seat deterioration (Chapter 7) are in need of an appropriate incident input signal with improved sensors for better analysis. Therefore, the purpose of the study is to improve a fully contactless ultrasonic system for rapid measurement of concrete structures.

The fully contactless ultrasonic testing (UT) configuration employed in this study is shown in Figure 3.4 "Height 1" indicates the distance between the concrete surface and the contactless sending transducer, and "Height 2" the distance between the surface and the contactless ultrasonic receiving transducer. The angle of incidence for the transmitter is indicated by "Angle." All test configuration parameters must be carefully controlled in order to optimize signal generation and detection. Several evaluation performance metrics with regard to signal generation are considered, including amplitude and bandwidth control, generated signal-to-noise ratio (SNR) and ease of incorporation into an automated scanning system.

All of these testing parameters is optimized value. The preliminary non-contact ultrasonic surface wave data that the author presented is very promising, but this data did reveal some limitations. For example, the generated signals were limited to a narrow band of frequencies at about 50 kHz. Ultrasonic pulses with a broader band of frequencies and controllable center frequency across our proposed "mid-

frequency" band (50-100 kHz) provide more powerful data for scatter analysis and inversion. Also higher than 50 kHz transducer allows better scattering analysis. Furthermore, the nature of the narrow-band signal masks some of the surface waves that would be associated with energy attenuation and arrival time. Thus, signal bandwidth must be increased so that the Rayleigh surface waveform is clearly districted between different characteristic concrete materials. The capacitive transducer (electrostatic transducer) sets will be electrically excited using a variety of input signals, including spike transients, frequency controlled tone bursts and frequency swept chirp signals. Several evaluation performance metrics will be considered, including amplitude and bandwidth control, generated signal-to-noise ratio (SNR) and ease of incorporation into an automated scanning system.

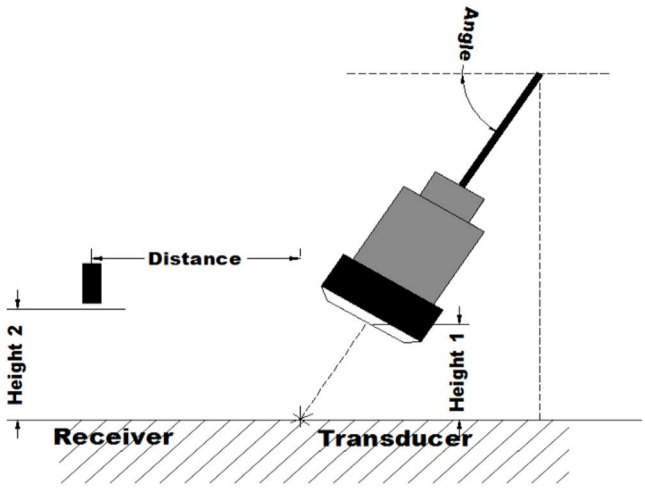

Figure 3.4 Illustration of testing configuration parameters for contactless set-up (Ham & Popovics 2015b)**.**

The contactless capacitive transmitter excites a 50 kHz tone burst 16-cycle pulse using module A. Figure 3.5 (left) shows the effect of transmitting transducer height. Both the MEMS and contact sensors are used to detect the signal at a distance of 180mm, with Height 1 varying from 2 mm to 70 mm in increments of 2.5 mm. These results indicate the highest surface air pressure amplitude at 52 mm of Height 1, as shown in Figure 3.5 (left). This coincides with the expected near-field distance for the transducer. The near-field distance (N) is approximated (Jensen et al. 2006) by

$$\mathrm{N} = \frac{D^2 F}{4 V} \tag{3.1}$$

where $D =$ diameter of the transducer, $F =$ frequncy of the transducer, and V = the velocity of sound in the material. With a 38 mm diameter transducer at 50 kHz, Eqn. (3.1) gives a near-field distance approximation of 52.6 mm.

In another test, the optimal angle of incidence for air-coupled sending transducer is studied. The sending transducer generates 50 kHz 16-cycle tone burst pulse using module A. The incident angle is changed in 2.5° increments from 72.5 to 90°, with a 180 mm distance and 52 mm for Height 1. As shown in Figure 3.5 (right), the results indicate the highest surface wave amplitude for an angle of 82.4°. This experimental result is close to the theoretical critical angle of 8° (90 ~ 81.2°), as described in section 2.2.

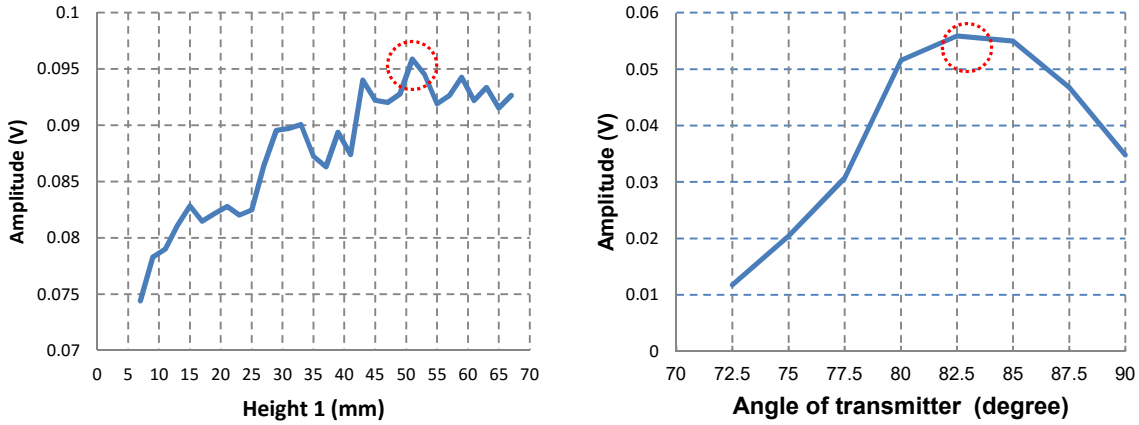

Figure 3.5 Effect of testing configuration parameters for sending transducer on amplitude of received signal with 5mm for Height 2: (left) results indicate highest received amplitude at 50 mm sending height; (right) results indicate highest received amplitude for 82 degree sending angle.

3.2.2 Experimental Study Contactless Receiver

Our study used the modified newly developed silicon-based miniature MEMS acoustic sensors from section 3.1.2 for detecting leaky ultrasonic surface waves in concrete. This particular sensing modality provides excellent sensitivity, favorable frequency bandwidth, low power consumption, small form factor (for improved spatial identification of the sensed point) and is low cost. A variety of these sensors was obtained, configured and evaluated via direct performance comparison to traditional microphones and capacitive sensors, using a consistent air-coupled ultrasonic source for tests on concrete samples.

3.2.2.1 Surface Wave Velocity Analysis

The ultrasonic surface wave results collected with MEMS from the PMMA sample. Preliminary tests were carried out to verify contactless sensor consistency in terms of amplitude and time of flight, where the seven-sensor MEMS array is oriented perpendicular to the direction of surface wave propagation.

The sensor array has 2 mm spacing between the sensor elements, and the center sensor element, indicated by 0 mm offset illustrated in Figure 3.3 was aligned with the approximate center of the propagating wave beam field. Although there are slight offset distances between the sensor elements, the distances between the ultrasonic sending transducer and all seven receiving sensors are approximately 180 mm. Thus similar time signals, in terms of amplitude and phase, are expected from all sensors. The results in Figure 3.6 that the contactless MEMS sensors provide very consistent performance across the sensor array, showing the clear arrival of the surface wave pulse slightly after the expected S-wave arrival time for PMMA. These results also indicate the potential of contactless MEMS sensors for reliable wave amplitude (attenuation) measurements that are free from sensor coupling and surface condition variations that are expected with contact sensors.

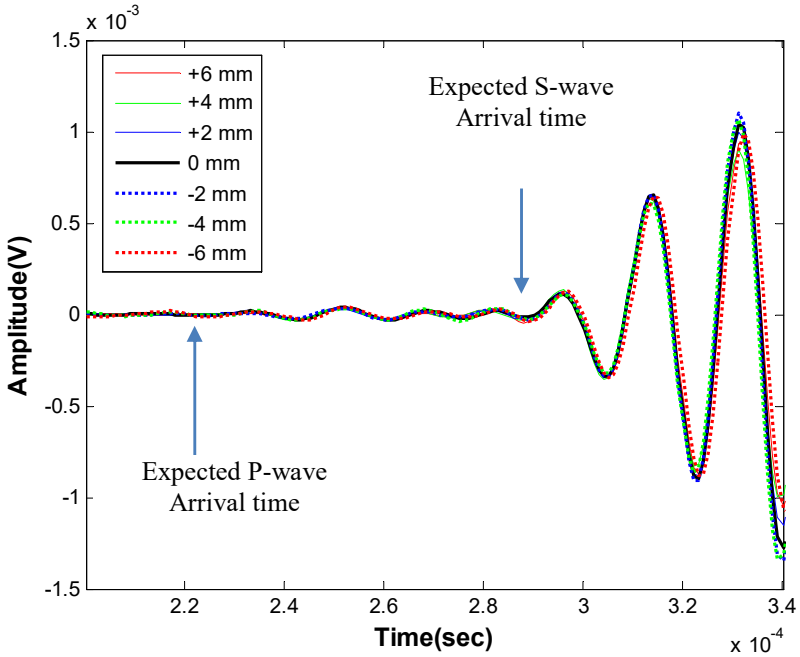

Figure 3.6 Time signals obtained from MEMS array perpendicular to surface wave propagation on PMMA; seven sensors are spaced 2mm apart in the array.

Ultrasonic surface wave velocity can be measured when the axis of the MEMS array is oriented to be parallel to the direction of wave propagation. In this case, it is expected that the arrival time of each seven sensors to consistently increase with increasing sensor offset distance. The results are shown in Figure 3.7 (left). Clear pulse arrivals with increasing delay time are seen. The pulse arrival times are plotted against sensor offset distance in Figure 3.7 (right), showing a strong linear relation between the two. The slope of a line fit to the data indicates a pulse group velocity of 1233 m/s, which agrees very

well with the expected surface wave speed for PMMA. The results demonstrate that the air-coupled test configuration reliably and consistently monitors propagating surface wave characteristics from a known solid sample.

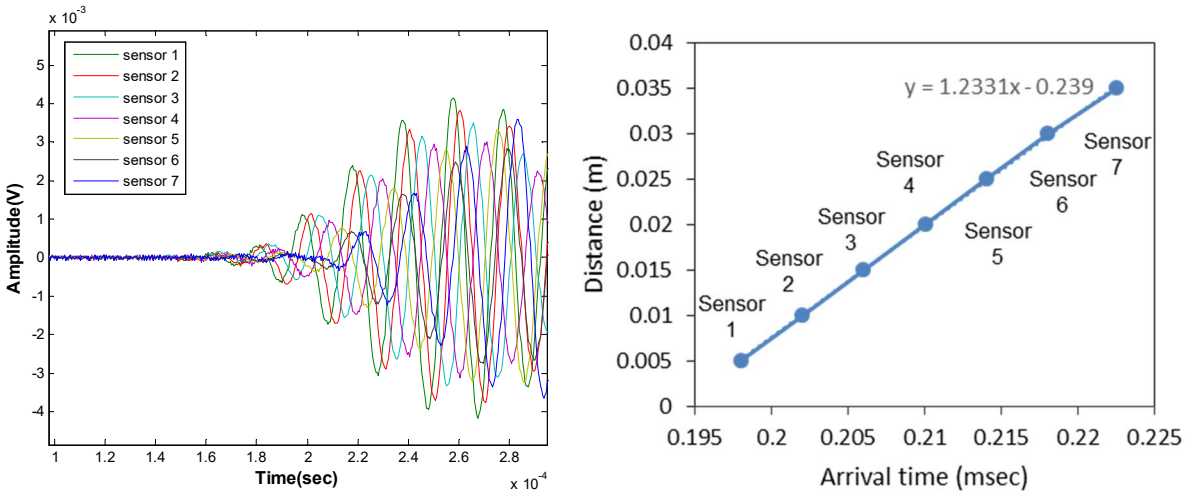

Figure 3.7 Ultrasonic surface wave signals collected with sensor array along wave path on PMMA; time signals (left) and presentation surface wave arrival time (right).

Figure 3.8 shows results from the ultrasonic surface wave test configuration applied to concrete using the MEMS sensor array and a contact accelerometer. Figure 3.8 (left) shows time domain signals from the contact sensors and (right) from contactless MEMS. Both sets of signals show similar shape, although the amplitudes from the contact sensors are much larger, as expected. Figure 3.8 plots the determined pulse arrival time against the sensor offset distance using the data as shown in Figure 3.8. Again, the arrival time and sensor offset show a strong linear relation, although the data sets show a consistent lateral offset, owing to the air gap of the contactless MEMS sensors above concrete surface. Regardless of the offset, the slopes of the fit lines should indicate surface wave group velocity. The dataset for the contact sensors, indicated by blue points, shows a surface wave velocity of approximately 2350 m/s, while that from the MEMS sensors shows approximately 2380 m/s. Although the data show more variation than that obtained from PMMA, the slope values show good agreement with each other and are reasonable values for mature concrete. The results suggest that reliable and accurate surface wave velocity data are obtained using the fully contactless ultrasonic configuration.

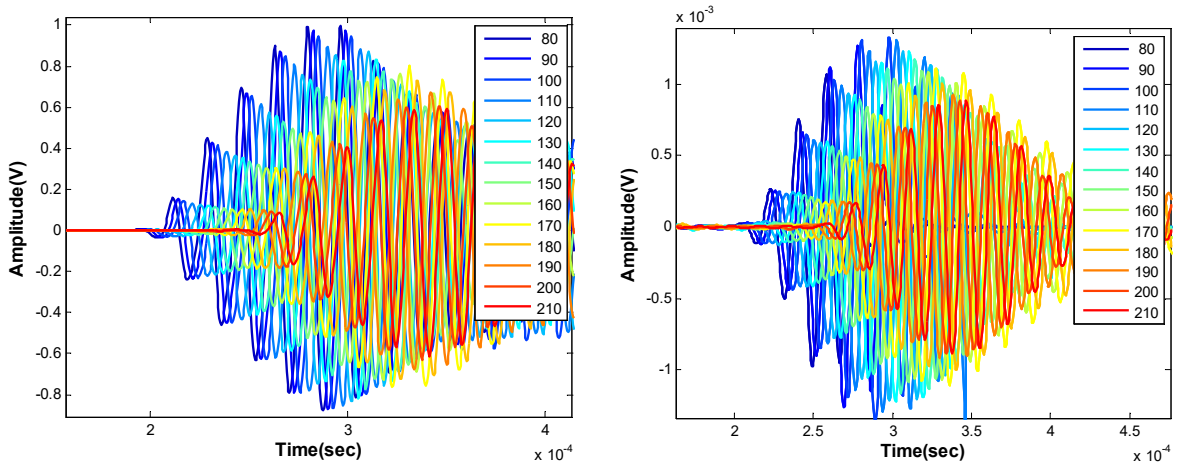

Figure 3.8 Ultrasonic surface wave time signals collected with sensor aligned along wave path on concrete; contact accelerometer (left) and with noncontact MEMS (right). The numbers in legend indicates distance between a sender and a receiver (cm).

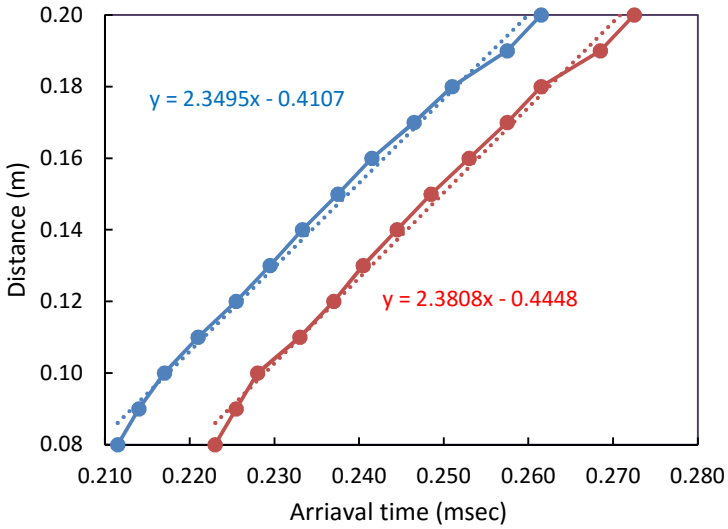

Figure 3.9 Presentation of surface wave arrival times derived from data shown Figure 3.8; contact accelerometers shown with blue and contactless MEMS with red. The slope of the fit lines indicates surface wave group velocity for each data set.

3.2.2.2 Signal Consistency

A comparison test is needed in order to understand how the air-coupled sensors operate with respect to other existing ones. The performance of a variety of ultrasonic receivers, including an air coupled MEMS sensor, an electret condenser microphone (ECM), a dynamic microphone, and a contact accelerometer, are studied using a consistent air-coupled ultrasonic sending configuration over a concrete sample. The

contact sensor is a PCB 352C15 accelerometer with nominal 10 mV/g sensitivity, flat (±3 dB) frequency response from 0.35 Hz to 25 kHz, and resonance greater than 50 kHz. An AC capacitive transducer, excited with a 50 kHz, 16-cycle tone burst signal with module A, was positioned at an 82.5° angle of incidence and 52 mm height from the surface. The offset distance between transmitter and receivers is 280 mm. The results are shown in Figure 3.10. The largest signal amplitude is provided by the contact accelerometer. The signal amplitude of the MEMS receiving transducer is approximately 1/6 that of the contact sensor, and the condenser microphone shows much smaller signal amplitude, approximately 51 times lower than that obtained by the contact sensor. The dynamic microphone did not detect the surface wave signal; this was expected as the frequency range of those sensors extends only up to 20 kHz. The surface wave velocity in the concrete was 2150 m/s, and the acoustic wave velocity in the air, measured from arrival of direct acoustic wave, was 343 m/s. In the experiment result, the MEMS sensor shows an excellent signal-to-noise ratio (SNR) at 34.4 dB, while the condenser microphone shows 2.02 dB at 50 kHz. The contact accelerometer exhibits highest SNR, 61.2 dB with 50 kHz. The SNR is calculated as the ratio of variance of total signal to variance of noise in the signal.

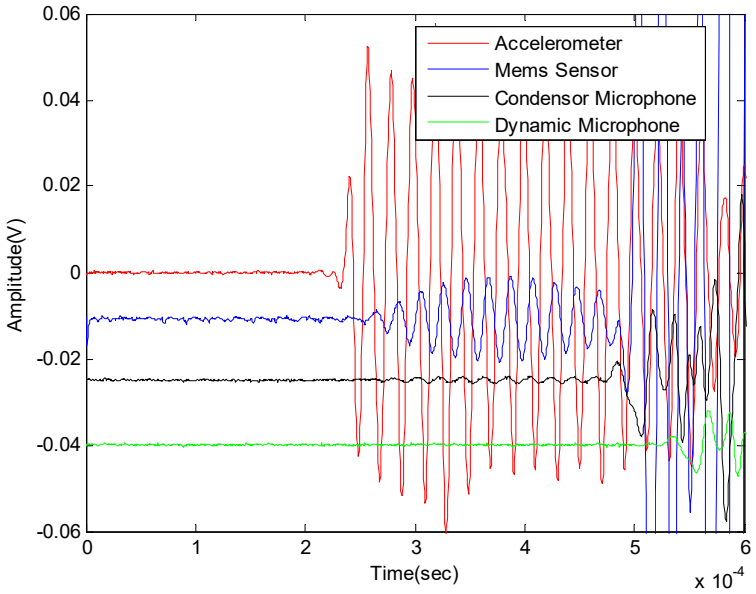

Figure 3.10 Comparison of received signals from different receiver types for a consistent source.

An important ultrasonic testing performance issue is the consistency of the measured surface wave signal. Figure 3.11 (left) shows signals generated with the air coupled capacitive transducer under 50 kHz, 10-cycle toneburst excitation with module A and collected by a single contact accelerometer. The source distance is 280mm. While maintaining consistent air-coupled surface wave generation, the

accelerometer was attached then detached three times, successively, at the same position on a concrete sample. The results indicate the contact sensor does not provide consistent signal amplitude, as the signal amplitude varies significantly owing only to the coupling condition of the contact sensor. Figure 3.11 (right) shows signals collected from two different contactless MEMS receiving transducers over the same position on a concrete sample. The MEMS sensors show much more consistent surface wave signals, in contrast to the other sensors, which show higher variation. This suggests a notable benefit for contactless sensors within sensing arrays in a scanning system, where wave amplitude data are needed for example in signal attenuation measurements.

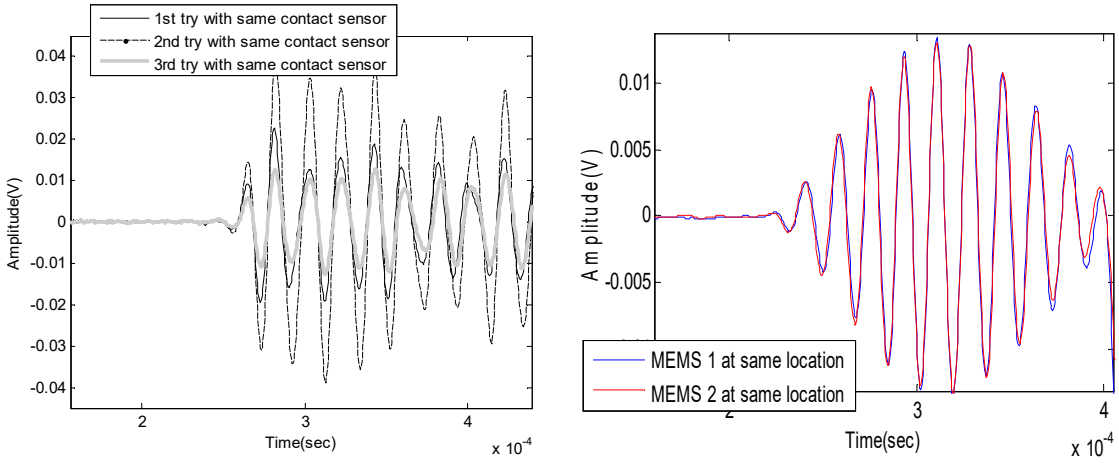

Figure 3.11 Illustration of sensor coupling consistency with regard to signal amplitude: (left) signals collected by a single contact accelerometer attached (using wax coupling) and detached three times at same position on a concrete sample using a consistent wave source, and (right) signals from two different contactless MEMS receiving transducers at the same position on a concrete sample.

3.3 Design and Implementation of Scanning System

The driving concept for implementation of this system is to enable performing cost-effective inspection: one-sided, air-coupled ultrasound techniques carried out from a moving platform.

3.3.1 Signal Improvement

Increasing the sensitivity of the received signals is also important. Minimizing ambient and electric noise will contribute to an increased SNR. Minimization of ambient noise will be accomplished by using multiple insulation baffle layers and improving electric ground, and using shield cable (or metal mesh enclosure). In previous tests the field data showed high levels of electronic noise. The 50 kHz magnetic

field shielding properties of various cable configurations were measured and compared by Ott in 1976. The hardware will be reconfigured to include shielded coax cable throughout, replacing the existing parallel cable.

The direct acoustic wave problem will be addressed with a double layer baffle wall, as shown in Figure 3.12, and by arrangement of the sender and receiver. Other proposed work requires an auto-positioning robot scanning system with multi-array sensors.

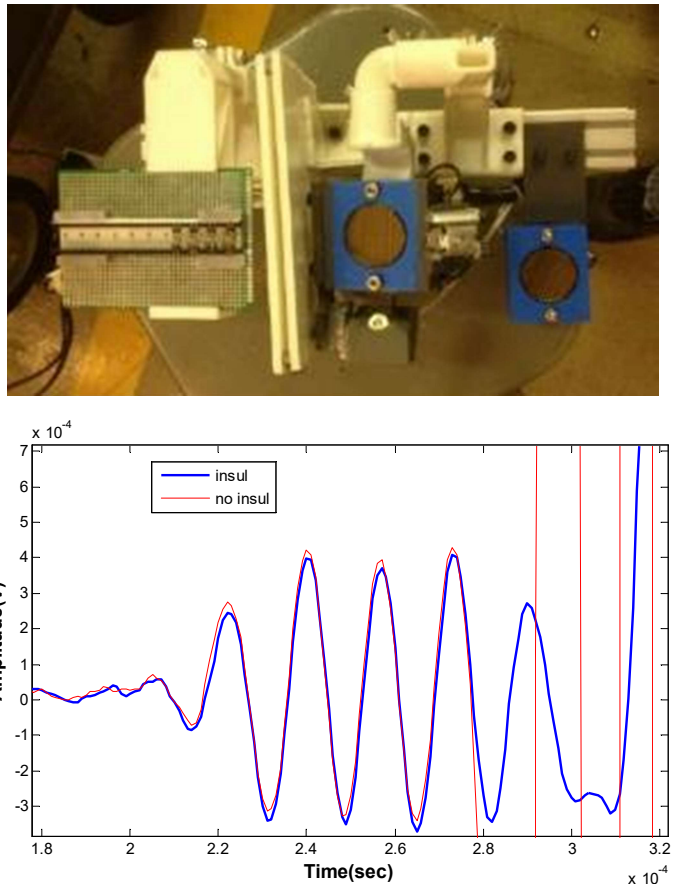

Figure 3.12 Effect of double layered baffle wall; (top) a photo of contactless ultrasonic system with a baffle wall between sender and receivers, and (bottom) plot of time signals indicating that "insul" signal is with baffle wall in place and "no insul" without the baffle wall.

3.3.2 Control System: Automated Testing Frame and Robotic Scanner

The proposed work requires individual and specific testing configurations. For example, a multi-array of sensors and receivers and 4-D axial scanning (x, y, z and φ angle) system is proposed for the wave scatter analysis. Several problems need to be overcome with the test configurations, namely

inhomogeneous material nature, long wavelength, sample size and geometry, and interference from direct acoustic waves

A large amount of consistent and reliable (in terms of spatial position) fully contactless ultrasonic data must be collected in order to quantify spatial resolution of the system and to evaluate scanning and imaging suitability. For this study, the author designed and constructed a testing frame robot, shown in Figure 3.13 that incorporates the air-coupled sending and receiving hardware. The auto scanning system (Figure 3.13 top left) provides precise, automated sensor positioning in the space above the concrete surface, achieving controlled sensor angle and height throughout the scanning process. This frame is part of an automated testing system that includes all necessary power, control, signal excitation, data acquisition and data storage capabilities. The auto test frame is designed to work with the proposed test samples and, furthermore, is adjustable and configurable to scan large-scale concrete samples or structures. The testing system was assembled in our laboratory using commercially available components and materials at reasonable cost.

A small 3-D printed frame (Figure 3.13, top right) is used to hold sending and receiving transducers. This small frame has light weight and allows accurate transducer positioning, incident angle and height. Once sufficient data sets are obtained, imaging protocols, for example signal parameter mapping, spectral signal stacking, and tomography, are then employed in order to build up amplitude attenuation images of the test samples.

The robotic scanner is based upon a similar concept of utilizing an automated frame, as described above. The main purpose of the robot mobile system is for use in high-speed generation of large-scale structural analyses such as bridge decks or slabs. With a multi-array mount system, this robot apparatus enables inspection of a variety of cracks, such as delamination, via the MASW method.

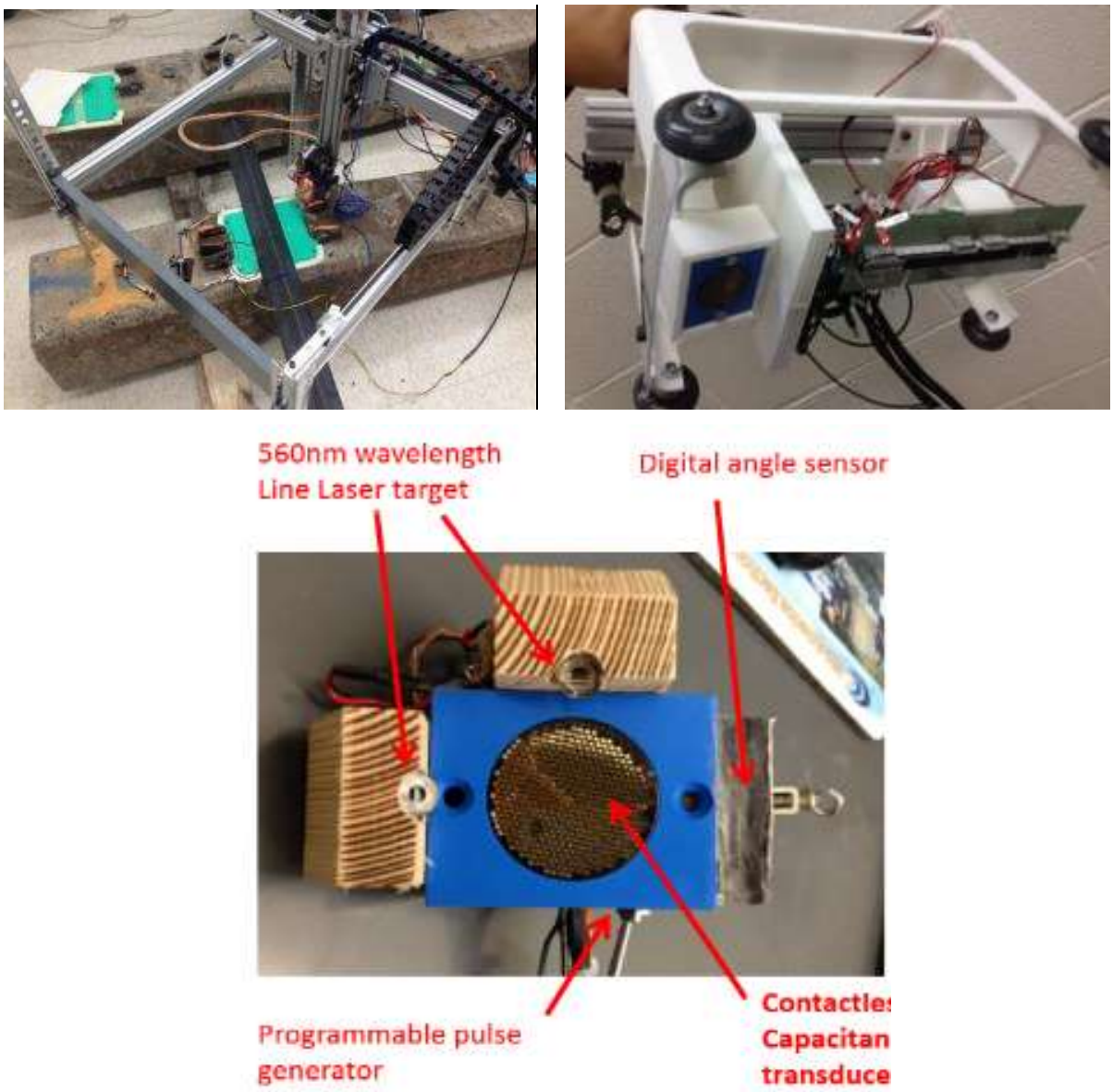

Figure 3.13 Photo of developed air-coupled scanner system: (top left) application of fixed scanning system to a concrete element, (top right) 3-D printed hand-scanner, and (bottom) detail of transmitting transducer.

3.3.3 Vision for Automated Inspection of Large Concrete Structures

Here the possible designs for air-coupled ultrasonic testing prototypes to deploy the technology and data interpretation scheme for the different damage mechanisms will be conceived (but not built). There are several types of conceivable scanning systems that could be of great use in nondestructive inspection of

large structures. First of all, robotic scanning systems can be deployed on bridge decks. Climbing robotics systems are appropriate for inspecting massive, difficult to access structures such as nuclear power plants and dams. Automatic scanning frames would provide new capability for completely contactless ultrasonic interrogation of concrete, which would enable improved health monitoring of large critical structural systems such as nuclear power plant structures. These fundamental UT scanning method will contribute tremendously through continuous advanced application in conjunction with other technologies.

3.3.4 Application to Rough Surfaces

Another important testing characteristic is the application to rough material surfaces. The condition of concrete surfaces in the field can be variable, and ultrasonic systems should obtain viable signals regardless of surface condition. The surface roughness condition (surface spatial characteristics) can affect the ability to generate ultrasound in the material through two different phenomena: scattering of ultrasound and physical coupling of the active surface of the sending sensor to the material. Surface mounted sensors are affected principally by the latter effect, whereas air-coupled sensors are affected principally by the former. The air-coupled capacitive transducer, excited with 50 kHz, 16-cycle toneburst excitation with module A, was applied to concrete surfaces with three different roughness conditions that reasonably span the expected range for concrete structures. The source distance is 380mm. The surface roughness is quantified by estimated average vertical spatial variation across the tested area, ranging from 0mm to 7 mm. As shown in Figure 3.14, our ultrasonic system provides clear viable signals for all the surface conditions, although the signal amplitude decreases as the surface roughness increases. The observed amplitude variation is most likely caused by incident ultrasound scattering from the surface, but this effect is moderate because the ultrasonic wavelength is about one order of magnitude larger than the characteristic roughness sizes. Because this air-coupled system is not meaningfully affected by the physical sensor-surface coupling problem, it may be applied effectively regardless of surface roughness condition.

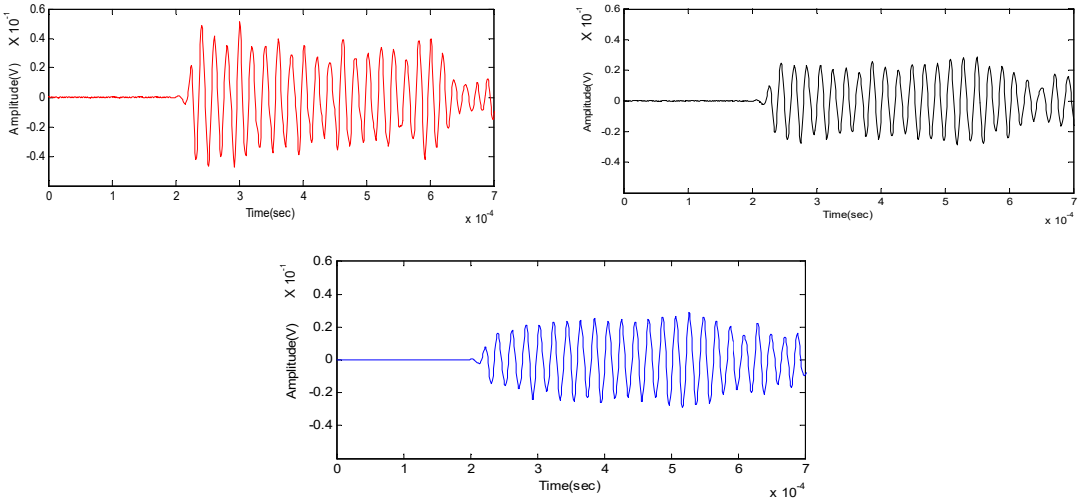

Figure 3.14 Air-coupled surface wave signals obtained from different surface roughness conditions in concrete: (top left) smooth (0 mm), (top right) medium level (2 mm average vertical roughness), and (bottom) extremely rough (5 mm average vertical roughness) (Ham & Popovics 2015b).

CHAPTER 4 FINITE ELEMENT MODEL DESCRIPTION

This chapter describes the models for dynamic finite element (FE) simulations, the results of which are shown in Chapters 5, 6, and 7. The FE simulation results are used to guide and to confirm our experimental and theoretical results. All finite models are created using the pre-processing/post-processing software, Hyperworks (Altair Engineering Inc., Troy, MI). The FE models are executed by ABAQUS (Dassault, Waltham, MA) software. Detail about the FE models are described in each section.

4.1 FE Model for Air-Coupled Generation and Detection of Surface Waves

This section describes how the fully air-coupled system, comprising non-contact sender and non-contact receivers are simulated using dynamic FE models. Previously, the author simulated the fluid / solid interaction for a solid half-space subjected to transient point excitation at the solid surface (Oh et al. 2012). That dynamic explicit FE model assumed room temperature air (V_p = 343 m/s, ρ = 1.21 kg/m^3) and solid medium that represents normal strength concrete (V_p=4000 m/s, ρ = 2400 kg/m^3, ν=0.2), assuming a linear elastic, homogeneous, and isotropic material behavior. Those findings revealed that gradually graded FE mesh spacing, increasing gradually from 0.5 mm (nearby loading point) to 2.5mm, provided accurate simulations but with reasonably low computation cost. Also, an integration time step of 1 μs with explicit analysis is needed to ensure accurate responses for the transient loads applied that simulate impact events. Figure 4.1 shows the cross-sectional snapshot image of the pressure field at 0.45 ms after the application of the impact event. The half-circle in the upper half-plane represents the acoustic wave front in the fluid, and the inclined fronts in the fluid medium represent strongly generated leaky Rayleigh wave fronts, which are tangent to the half circle at the leaky angle direction. The leaky Rayleigh wave front is separable in time from the subsequent fluid acoustic wave fronts. The Rayleigh wave in concrete is also observed, which behaves similarly to the ordinary Rayleigh wave (solid-vacuum case), and it attenuates exponentially with increasing depth within the solid.

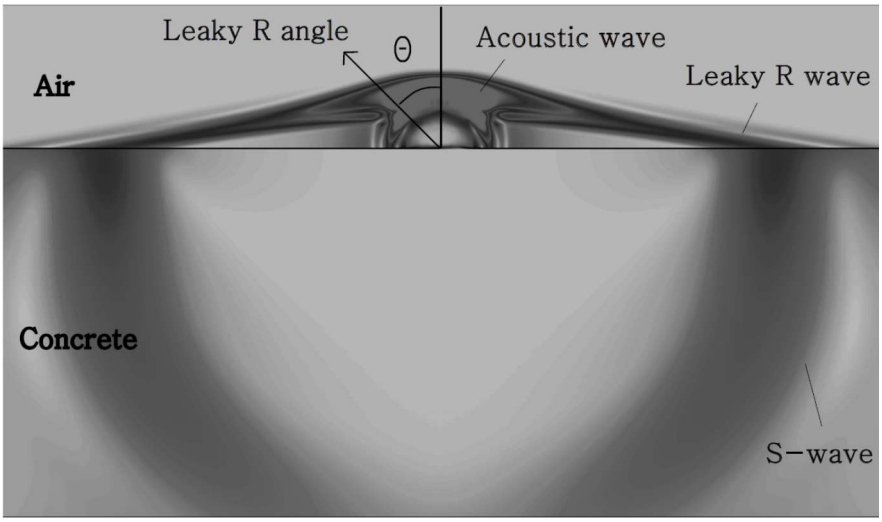

Figure 4.1 Pressure field snapshot in air and concrete medium at t = 0.45 ms after application of point load transient event on the concrete surface. Image data computed by FE simulation data (Oh et al. 2012).

In this thesis, air-launched (air-coupled or contactless) ultrasonic waves are used instead of transient point loads (impact events). Thus new appropriate FE simulations were developed to mimic the fully air coupled testing configuration developed and employed in the work. Figure 4.2 describes illustrates the new modelling approach, where FE model configuration and stress fields showing example wave-material interaction is shown. That dynamic FE model assumed room temperature air (V_p = 343 m/s, ρ = 1.21 kg/m^3) and solid medium that represents normal strength concrete (V_p=4000 m/s, ρ = 2400 kg/m^3, ν=0.2), assuming a linear elastic, homogeneous, and isotropic material behavior. The FE plain strain (PE4R) element within the ABAQUS platform was implemented with graded mesh from 1 mm nodal element length. The total length of the concrete specimen was 6000 mm, and the thickness was 500 mm as shown in Figure 4.2 (top). The excitation signal was a normal transient loading event was applied at elements on the surface of the fluid model. The excitation signal is a 16-cycle toneburst pulse with 50 kHz center frequency collected from actual our transducer. The model in Figure 4.2, simulates an air-coupled sending transducer at 80 degree incident angle, where angle is measured with respect to the plane of the solid surface. The sender (transmitter) applies distributed pressure to a fixed spatial area on the angled surface of an elastic fluid. As a first approximation, the incident acoustic beam is assumed to be a collimated beam, where the traction distribution is so applied onto the element surface. The transducer angle is simulated the change in phase of the acoustic rays travelling from the transmitter to the surface. The angled air-launched ultrasonic excitation allows control of the incident angle on a

surface and to generate directional surface waves. This model allows various parametric study for verification and simulation of the actual contactless UT transducer.

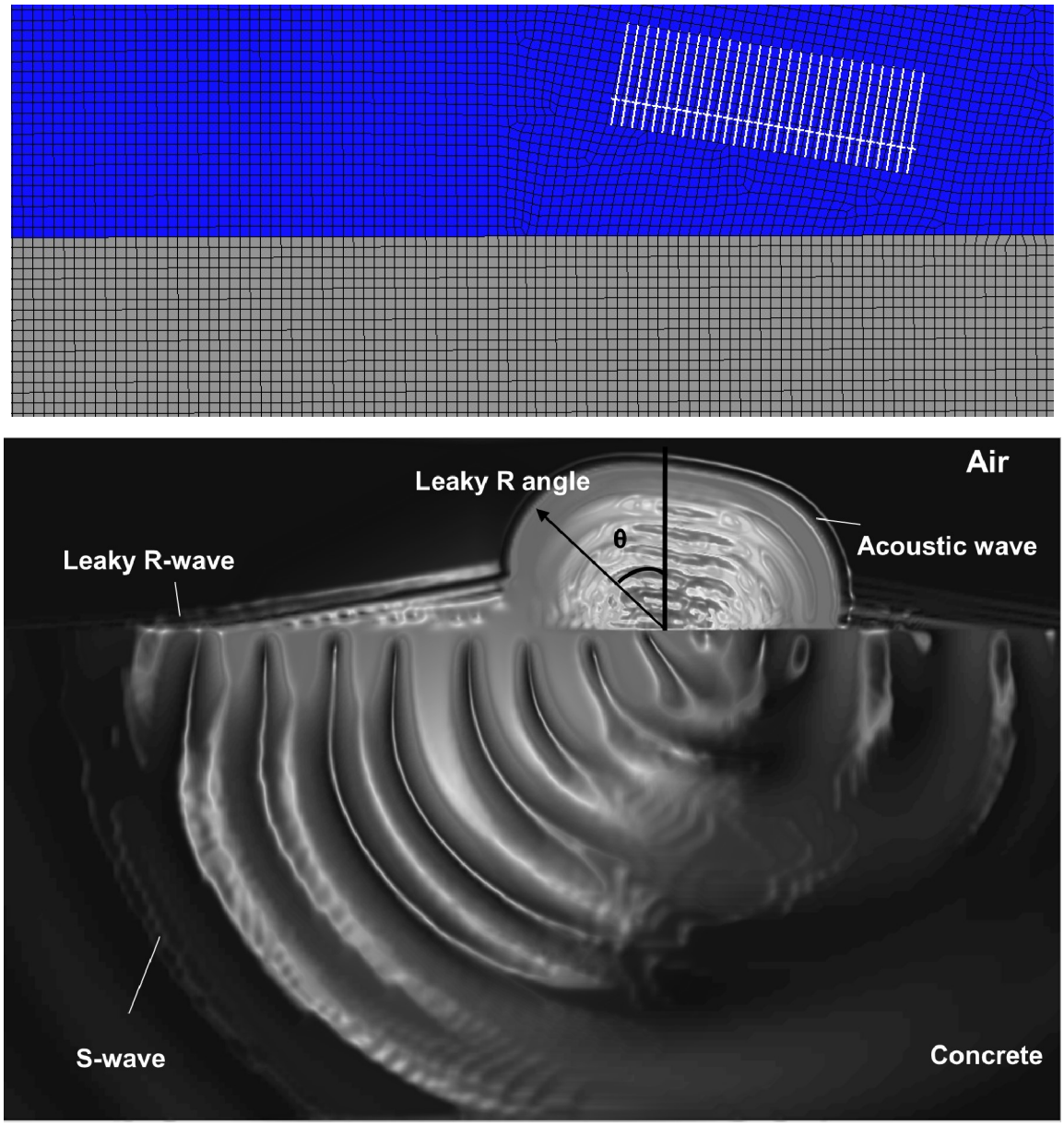

Figure 4.2 ***FE ABAQUS 1mm mesh model to simulate air launched ultrasonic surface waves into concrete. Concrete properties: ρ = 2400kg/m^3, v = 0.2, E= 35570 MPa, C_p = 4058 m/s; Fluid (air) properties: ρ =1 kg/m^3, C_p = 343 m/s. (top) and pressure wave field snapshot at 1.2 x 10^{-4}seconds showing leaky R-wave, S-wave, and acoustic wave fronts (bottom). Bright shades indicate the highest pressure; image created with FE simulation data.***

4.2 FE Model for Lamb Wave Analysis

This section describes how the behavior of air-launched surface-guided and Lamb wave are simulated using FE models. The results from this model is reported in Chapter 5 of the thesis. The ABAQUS plain strain model (PE4R) was implemented with a graded mesh from 1 to 2.5 mm nodal length in the solid. The model configuration is shown in Figure 4.3. 1 mm sized mesh were used to simulate air (mesh not shown in the figure). The total length of the concrete simulation was 6000 mm, and the thickness was 260 mm. The model configuration simulates the laboratory slab sample and testing setup used in the experiments. A broadband chirp signal was applied, in order to generate a dispersion curve with reasonably broad frequency content needed for the deployed MASW analysis. An integration time step of 1 μs with an explicit solver were used in the analysis. The excitation signal is a chirp signal having meaningful frequency content from 10 to 90 kHz; detail of the excitation signal is shown in Figure 4.*4*. Delamination damage within each region is simulated by air elements. Thirteen contactless listening positions were located every 30 mm in the air above the solid surface, where transient air pressure values were recorded. This FE model was used to simulate air-coupled, contactless ultrasonic wave propagation in concrete considering the effects of incident angle of the sender, defect depth (plate thickness), and number and position of receiving sensors. Delamination areas were simulated as air-filled with a single layer thickness.

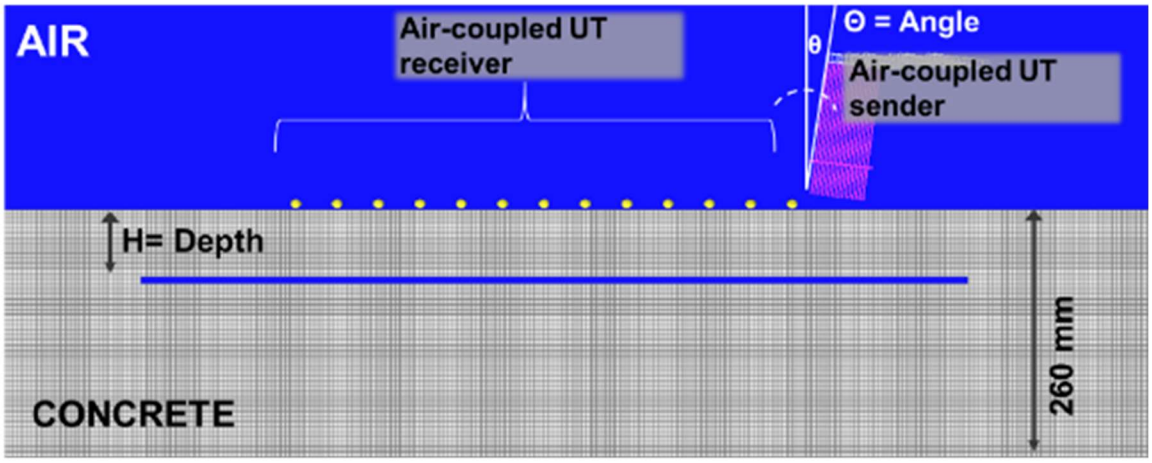

Figure 4.3 ***FE model used to simulate air-coupled, contactless ultrasonic testing in concrete to investigate the effect of incident angle, defect depth (plate thickness), and number of sensors. Concrete properties: ρ = 2400kg/m^3, v = 0.2, E= 35570 MPa, C_p = 4058 m/s; Fluid (air) properties: ρ =1 kg/m^3, C_p = 343 m/s.***

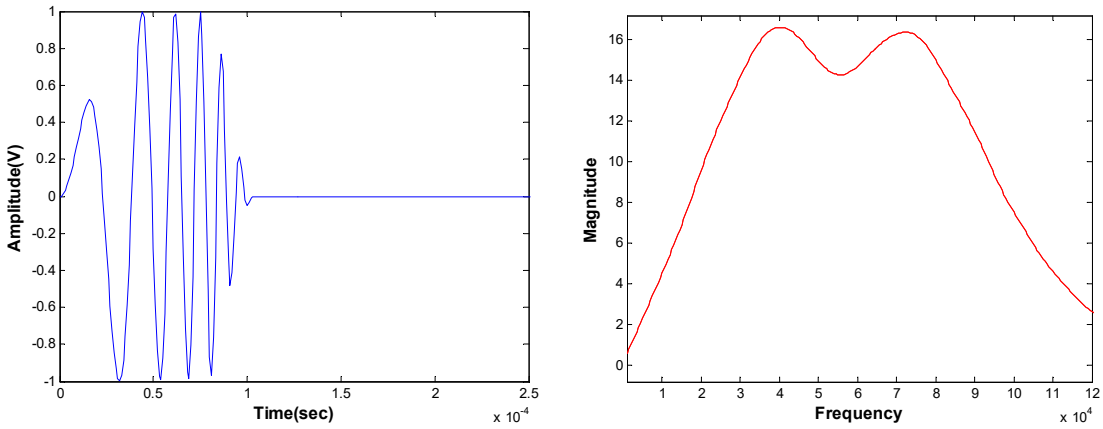

Figure 4.4 ***Chirp signal: (left) chirp signal with time duration of 100 microseconds and (right) frequency content of the shown chirp signal.***

4.3 FE Model for Microcracking Damage Analysis

This section describes how distributed micro-damage in concrete is simulated using FE models. Two different studies were carried out with this model: varying levels of damage, and varying positions of damage. The results from these models are analyzed and discussed in Chapters 6 and 7.

4.3.1 Extent of Microcracking Damage

FE was used to simulate the influence of distributed microcracks on air-launched ultrasonic surface wave signals generated by the testing configuration. The ABAQUS plain strain (PE4R) element was implemented with graded mesh from 1 to 2.5 mm nodal element length. The total length of the simulation was 2000 mm, and the thickness was 500 mm, as shown in Figure 4.5. The explicit integration method was used with a time step of 1 μs. The excitation signal is a 16-cycle toneburst pulse with 50 kHz center frequency. This input simulates the air-launched sending transducer used in the experiments. The assumed material properties are described in Figure 4.5. All receiver and sender positions simulate the actual experimental configuration; for example, the triple acoustic barrier (triple baffle layer) positioned between the sender and receivers to delay the arrival and amplitude of the direct acoustic wave is included in the simulation. Two types of model output are recorded: out-of-plane acceleration (noted as Accel 1, Accel 2, and Accel 3) at the solid surface and pressure (noted as MEMS 1, MEMS 2, and MEMS 3) in air above the surface. The red box in Figure 4.5 indicates the location of a specific damage region. The generated time signals have sufficient duration (600 microseconds) in order to capture both coherent pulse and incoherent scattered field information.

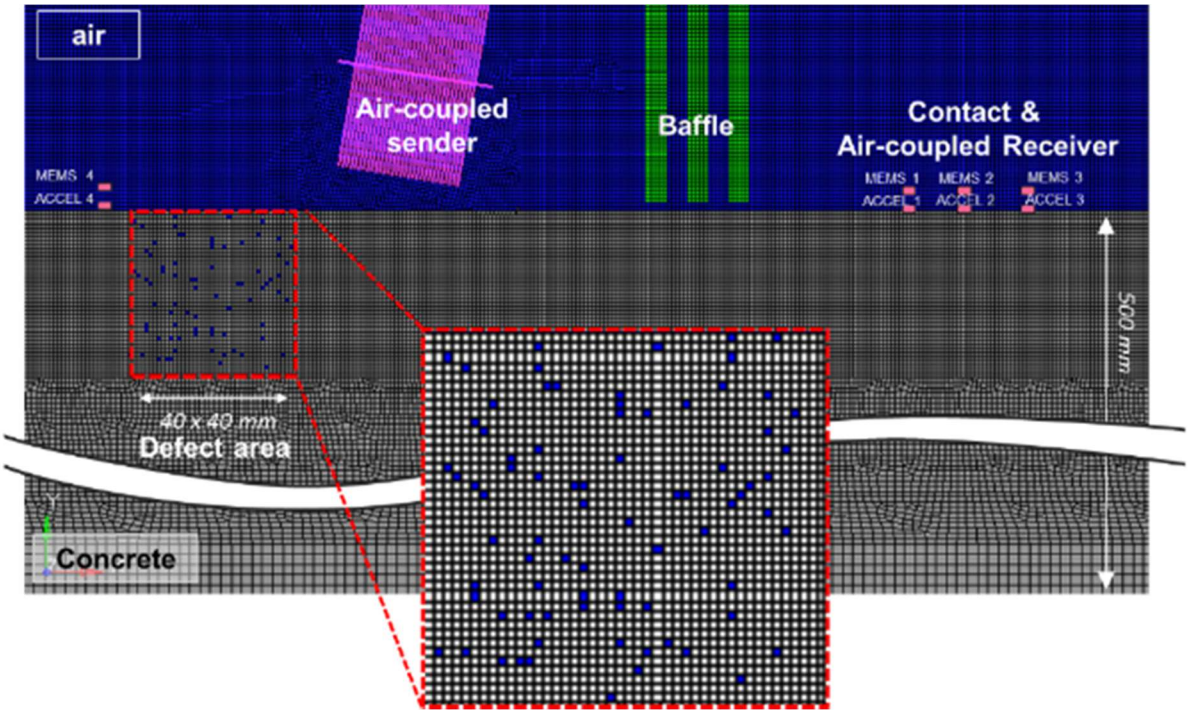

Figure 4.5 FE model used to simulate air-coupled UT configuration for investigating the effect distributed microcracking in concrete. The figure shows simulated 4% damage level where microcracks are simulated by air elements indicated by blue dots. Concrete properties: ρ = 2400kg/m3, ν = 0.2, E= 35570 MPa, C_p = 4058 m/s; Fluid (air) properties: ρ =1 kg/m3, C_p = 343 m/s.

The damage pattern within each specific region are generated randomly, but within 1 mm fixed grid. The distributed microcracking damage within each region is simulated by replacing a solid element in the mesh with an air element. The air element properties are ρ =1 kg/m^3 and C_p = 343 m/s. Five different extents of microcracking damage (0, 1, 2, 4, and 8 % volume void fraction) are used, where the damage percentage indicates amount of solid elements replaced with air elements in a specific region. As shown in Figure 4.*6*, the damage assignment procedure has several steps. Each sample sets constitutes ten different randomly distributed damage patterns at each prescribed damage level in order to simulate ten different surface wave paths from the same damage levels. Therefore, each model (each damage level) shows, at random, ten different scatter behaviors. The models are created using the Matlab random number generator (pseudorandom numbers). The random numbers determine certain node positions within the 40 x 40 mm area. The random numbered matrix in the FEA input file creates damage positions within an element group.

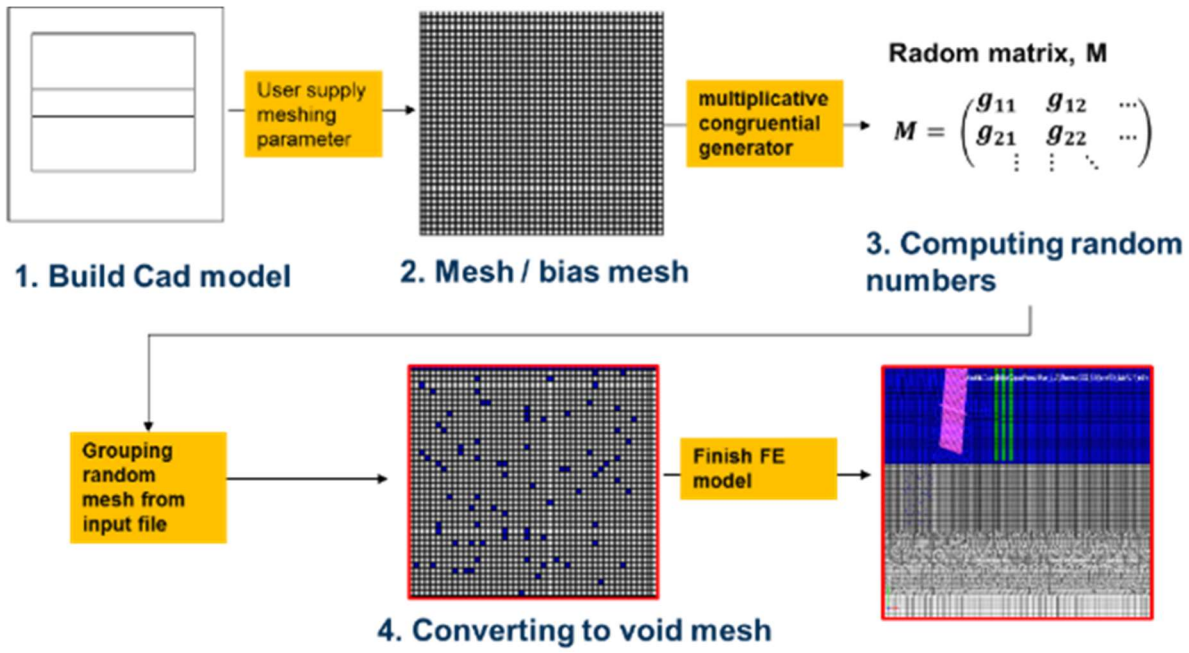

Figure 4.6 ***Illustration of FE model development process to consider random simulated damage.***

4.3.2 Location of Microcracking Damage

Dynamic FE was used to simulate the influence of the location of distributed microcracks regions on air-launched ultrasonic surface wave signals produced by the testing configuration. The model design and details are the same as described in section 4.3.1. The scanning positions are moved at every 40 mm distance. The response signals from nine different damage positions, relative to the position of the sender and receiver set, were studied from L1 to L9, as shown in Figure 4.7. In this study, each area contained 4 % damage by volume. As in the previous study, the simulated microcracking damage was randomly configured within the damage volume, where ten sets of damage configuration were considered from each position.

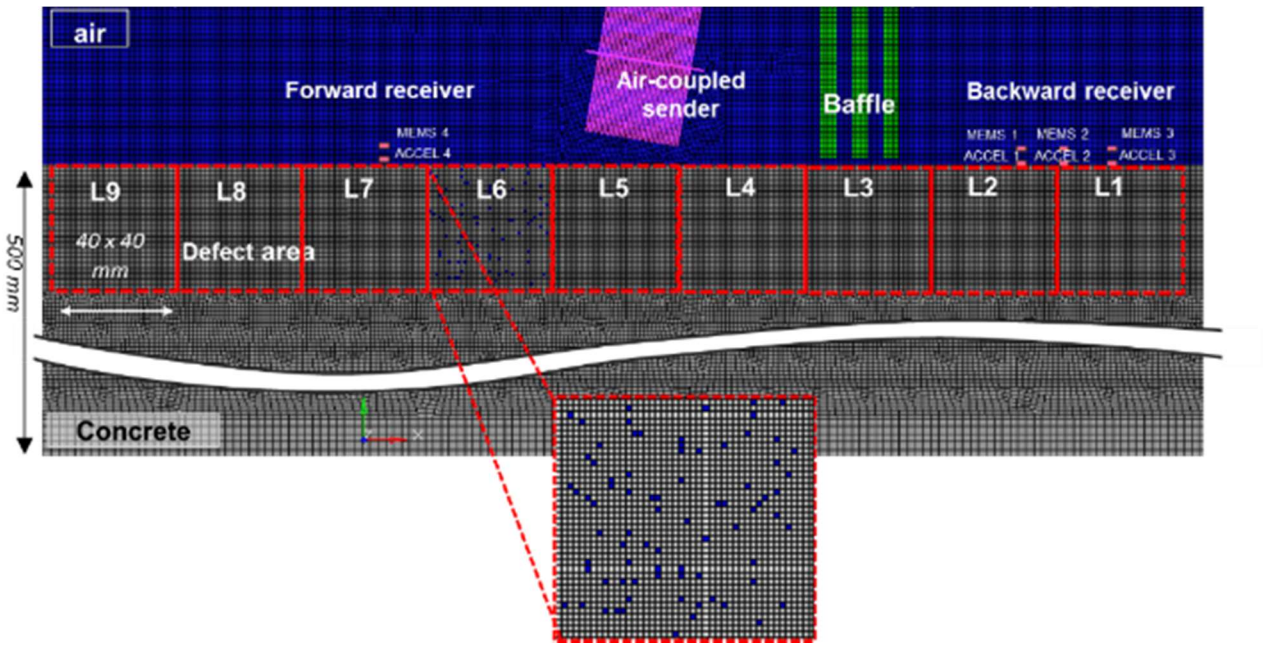

Figure 4.7 ***FE model used to simulate air- coupled ultrasonic testing configuration to investigate the effect of location (L1 to L9) of distributed microcracking damage. Concrete properties: ρ = 2400kg/m^3, v = 0.2, E= 35570 MPa, C_p = 4058 m/s; Fluid (air) properties: ρ =1 kg/m^3, C_p = 343 m/s.***

4.3.3 Eigenmode Analysis

In a separate, stand-alone study, dynamic FE was used to understand the effects of localized damage on the vibration response of prismatic samples. Real damage can occur in distinct locations; for example, one surface of a sample can experience more damage than other surfaces or areas. The results of the eigenvalue analysis described here will be compare with backscatter energy result in section 7.2. For the analysis, the FE continuum 3-D 8-node (C3D8R) element within the ABAQUS platform was used. An explicit analysis was implemented with a mesh with 5 having nodal element length. The total length of the simulated concrete prism was 500 mm, and the thickness and width were 150 mm. Specifically, the 3-D model simulates concrete sample "C", as reported in the Chapters 6 and 7. Three different cases were considered. The first model considers the behavior of an undamaged prism sample. The second model, referred to as type 1, considers the case where one surface (top surface, S1) of the sample exhibits more damage. The damage is simulated by a zone of material elastic modulus reduced by 20% with 15 mm thickness. And the third study, type 2, considers damaged zones on two opposing surfaces of the prism, with 20% and 10%, respectively, reduced modulus zones. The FE mesh models used for tasks 1 and 2 are shown in Figure 4.*8*. The testing model results are discussed in Section 7.2.4.

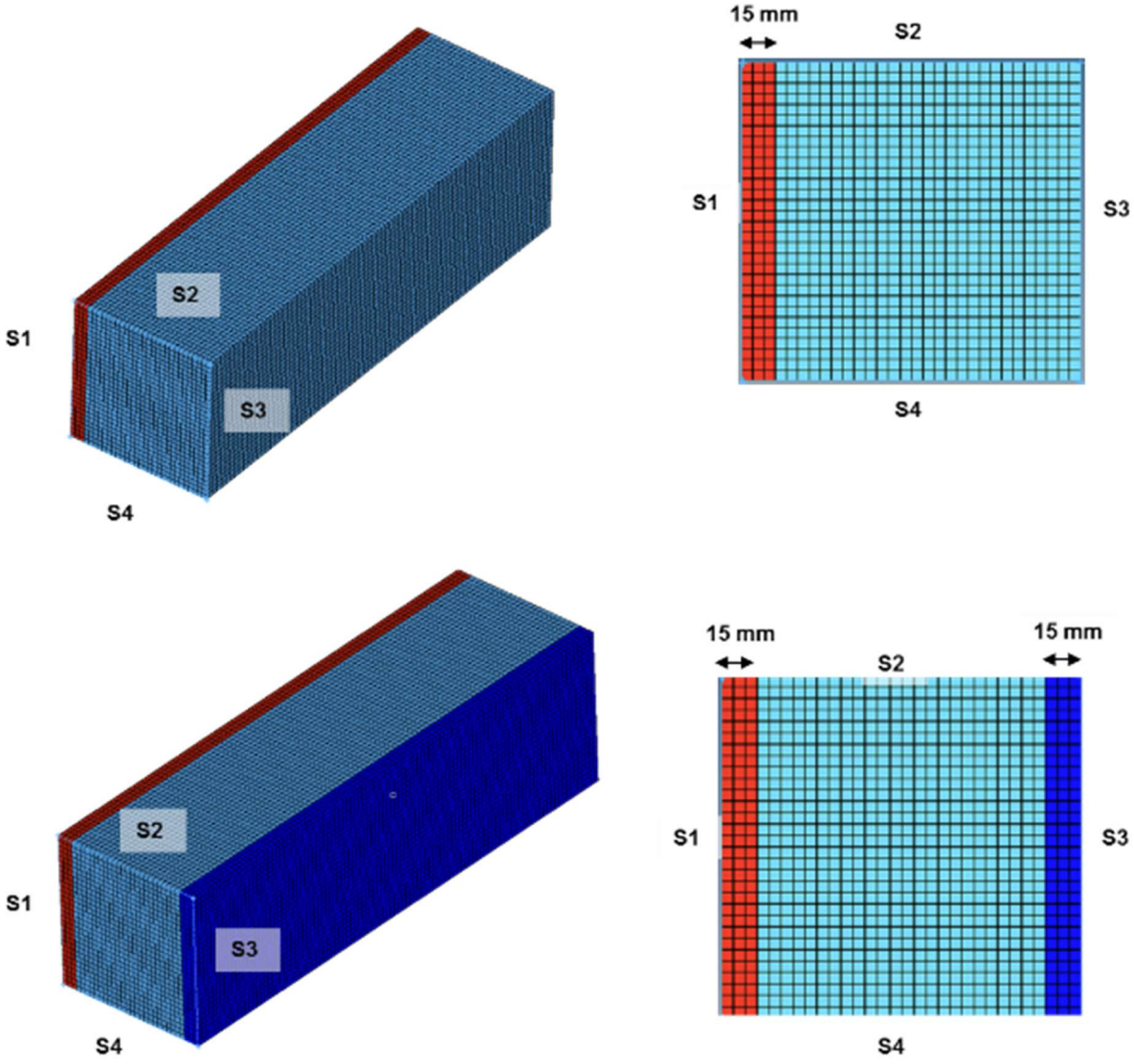

Figure 4.8 ***3-D FE model used in Eigenmode analysis to simulate the effects of distributed microcrack damage on vibration properties. : (top) model with one surface damaged, and (bottom) model with two surfaces damaged. Base concrete properties: ρ = 2400kg/m^3, v = 0.2, E= 35570 MPa, C_p = 4058 m/s. S1 indicates top surface, S3 is bottom surface, and S2 and 4 are side surfaces.***

CHAPTER 5 REFINEMENT AND APPLICATION OF THE MASW METHOD

5.1 Theory of MASW Testing for Delamination Detection

The MASW technique with fully air-coupled (contactless) ultrasound holds excellent potential for characterizing thin layer structures with Lamb wave modes (Rydèn & Lowe 2004). Presented here is a new application using the MASW technique for detecting delamination, which are assumed to have plate-like geometry. The objective of the Chapter 5 is to demonstrate experimental results using MASW analysis, and to compare those results with analytical and numerical Lamb wave interpretations, as illustrated in Figure 5.1.

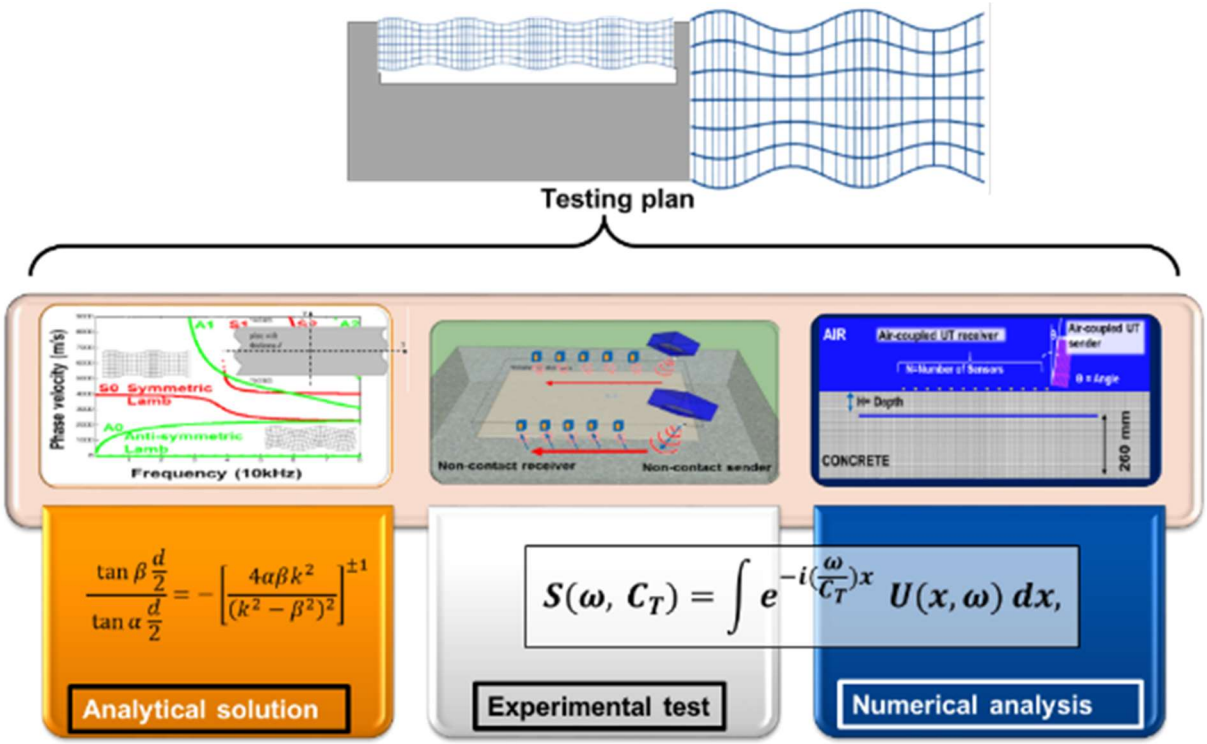

Figure 5.1 Illustration of research objective of the chapter: A verification and comparison among three different analysis.

5.1.1 Fundamental Theory

Our fully contactless UT system is used to detect delamination using a guided wave approach with energy shifts. Based on Lamb theory, analytical dispersion curves were created as shown in Figure 5.2. The analytical dispersion curves are compared to those obtained from a MASW analysis of signals. The

MASW results were obtained by numerical simulation, assuming 250 mm plate thickness and seven sensors with a spacing dx of 20 mm. These signals were collected from multiple data sites along a sensing array, which was detected by our robotic scanning system, as shown in Figure 5.3.

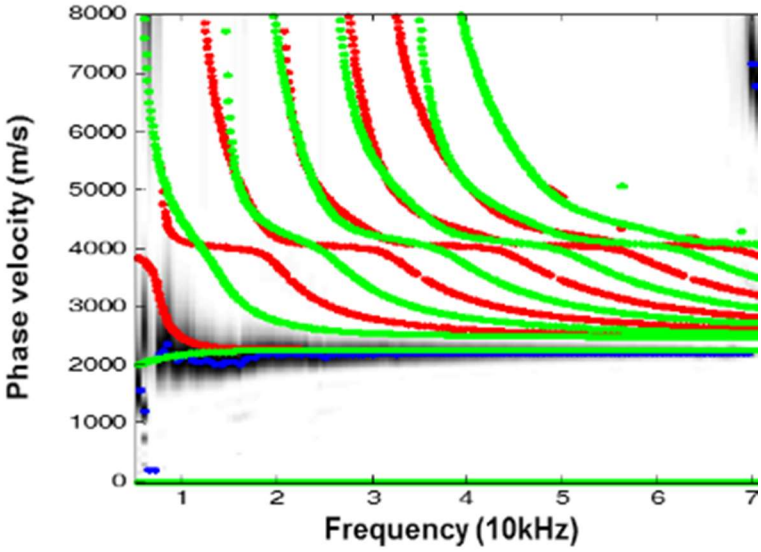

Figure 5.2 Phase velocity dispersion curve data produced by MASW processing shown with black points. Theoretically computed dispersion curves shown in green colored (anti-symmetric modes) and red colored (symmetric modes) lines (Ham & Popovics 2014).

The measured phase-velocity spectrum is obtained automatically from multichannel surface wave data using the plane-wave transformation technique (Park et al. 1998; Rydèn & Park 2004). In this chapter, the author use multiple MEMS array as illustrated in Figure 5.3 and MASW to create the dispersion curve. MEMS sensor array data collected from measurements at different offsets u(x, t) is transformed to the frequency–phase-velocity domain (Park et al. 1998), using

$$\boldsymbol{S(\omega, C_T) = \int e^{-i(\frac{\omega}{C_T})x}\, U(x, \omega)\, dx,} \qquad (5.1)$$

where U(x, ω) is the normalized complex spectrum obtained from the Fourier transformation of u(x, t), ω is the angular frequency, C_T is the testing-phase velocity, and S (ω, C_T) is the slant-stack amplitude for each ω and C_T. Calculating S (ω, C_T) over the frequency and phase-velocity range of interest generates a phase-velocity spectrum

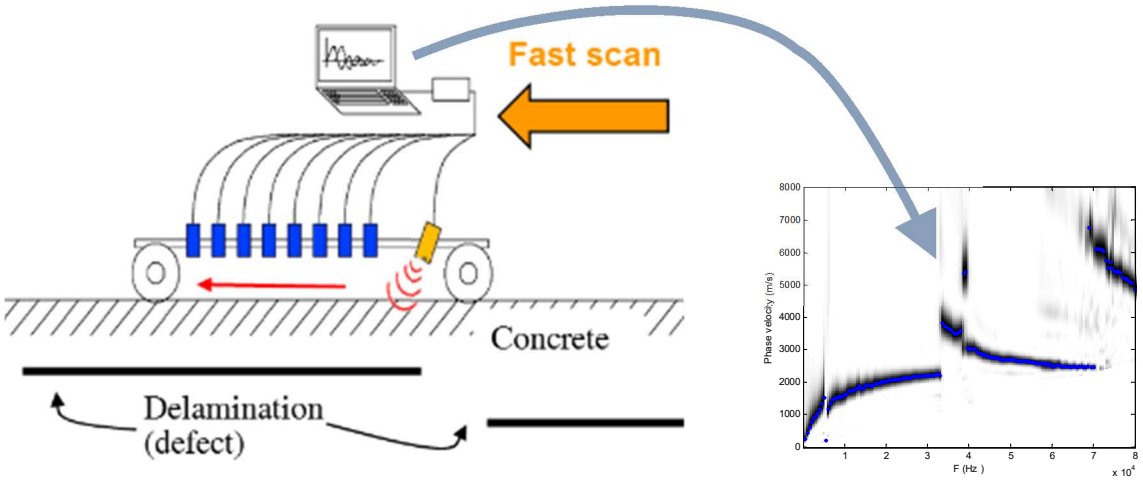

Figure 5.3 Illustration of the concept of MASW technique for deployment with air-coupled transducers for delamination detection in concrete *(Ham & Popovics 2014).*

5.1.2 Fast MASW 3-D Image Reconstruction

Also, the author reconstructed 3-D images using the following algorithm. Using our high performance, yet inexpensive contactless receiving transducers (sensors), the author collected multiple dispersion curve data and used them to construct dispersion curves in the x-direction (Figure 5.4, top left):

$$\boldsymbol{S_{max}(\omega(f_i))|_{x\_j} = max \quad S(\omega(f_i), C_T)\ )|_{x\_j}} \qquad (5.2)$$

where f_i is the i-th frequency, i is the index of the spectrum data within the range of a dispersion curve, and x_j is the jth scanned piece of data in the x-direction. The author also proposed a 3-D dispersion curve image. The maximum energy values were converted for both directions, $S_{max}(\omega(f_i))|_x$ and $S_{max}(\omega(f)_i)|_y$ at each frequency to an intensity of orange for a color map (see Figure 5.4, top right).

$$\boldsymbol{S_{3D}(x_j, y_k) = [S_{max}(\omega(f_i))|_{x_j}, S_{max}(\omega(f_i))|_{y_k}} \qquad (5.3)$$

where, y_k is the k-th data the in y-direction. Stacking color maps (bottom) can create 3-D images. The maximum values of the dispersion curves over the defect area are shown in Figure 5.4 (bottom). A 3-D image is constructed by stacking 2-D images to show the defect in the area and depth. In the future, 3-D imaging for large-scale slab or deck areas will be achieved by stacking these image data. The resulting image information allows for more insightful interpretations of damage areas related to

depth and area. The 3-D image reconstruction are used in the 5.3.2 section.

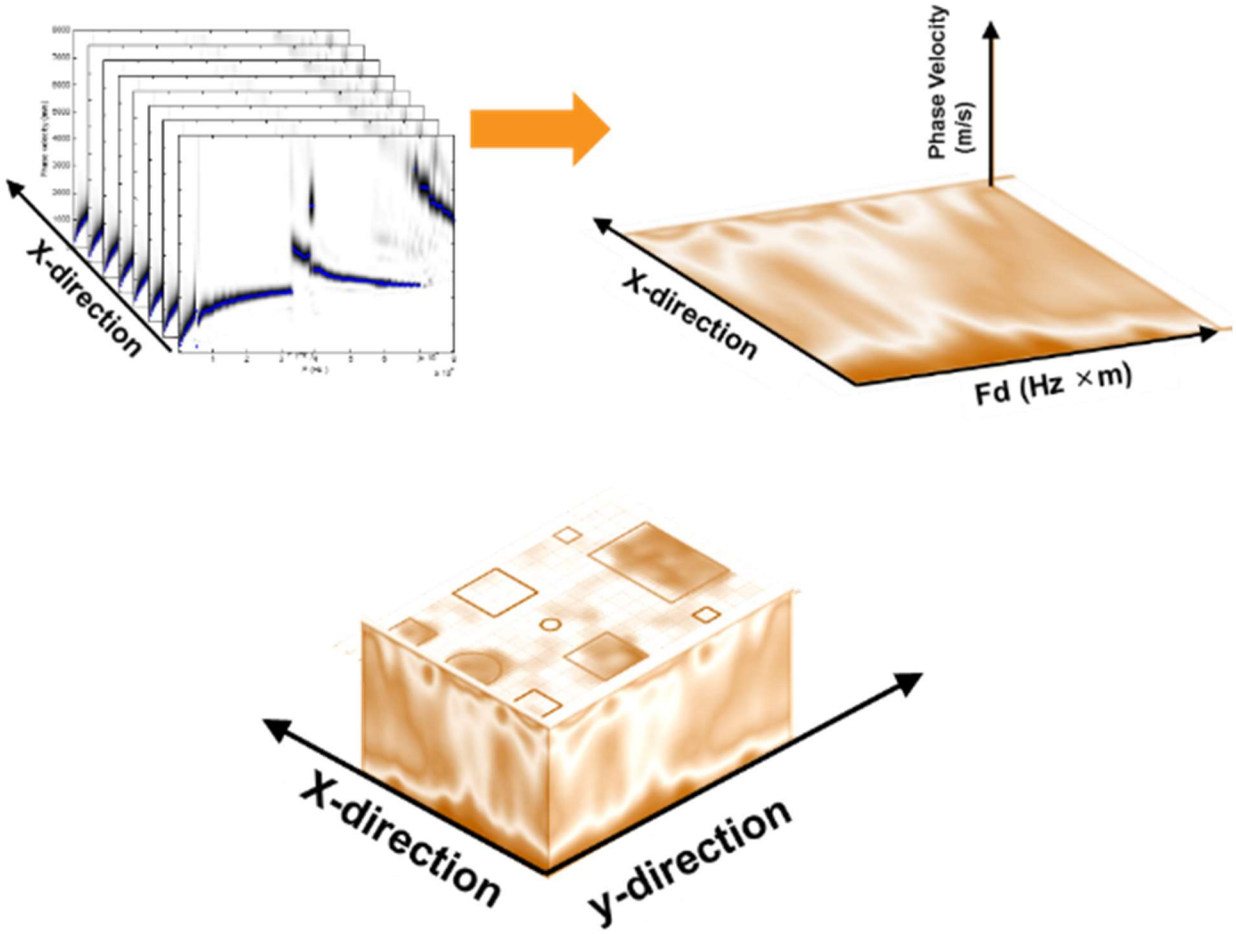

Figure 5.4 Concept of MASW imaging data: (top left) stacked dispersion curve data, (top right) 2-D image built up from $S_{max}(\omega(f_i))|_{x\_j}$ data, and (bottom) 3-D image built up by $S_{3D}(x_j, y_k)$ data.

The author intends to continue the research efforts as reported above, that pertain to the refinement and application of MASW analysis, including the application of surface waves. The purpose for the latter involves interfacial damage characterization. Finally, a vision for the implementation of automated large-scale scanning will be proposed. Details of the individual tasks are provided below.

5.1.3 Preliminary Test Results of MASW Application

This section serves the purpose of a preliminary study. Seismic time signal data collected from a 15-sensor set are shown in Figure 5.5. Contact accelerometers and contactless MEMS are included. Both the contact (left) and contactless (right) sensor data indicate the clear arrival of a surface guided wave, as indicated by the solid line. The approximate group velocity of that pulse is 2300 m/s for both data sets. The MEMS data set, seen in Figure 5.5 (right), also shows the arrival of a direct acoustic wave, indicated with a dashed line and a group velocity of 343 m/s. Although the arrival of the acoustic wave disrupts the surface wave signal of interest, meaningful information about the surface wave is provided by the signal before the acoustic wave arrival.

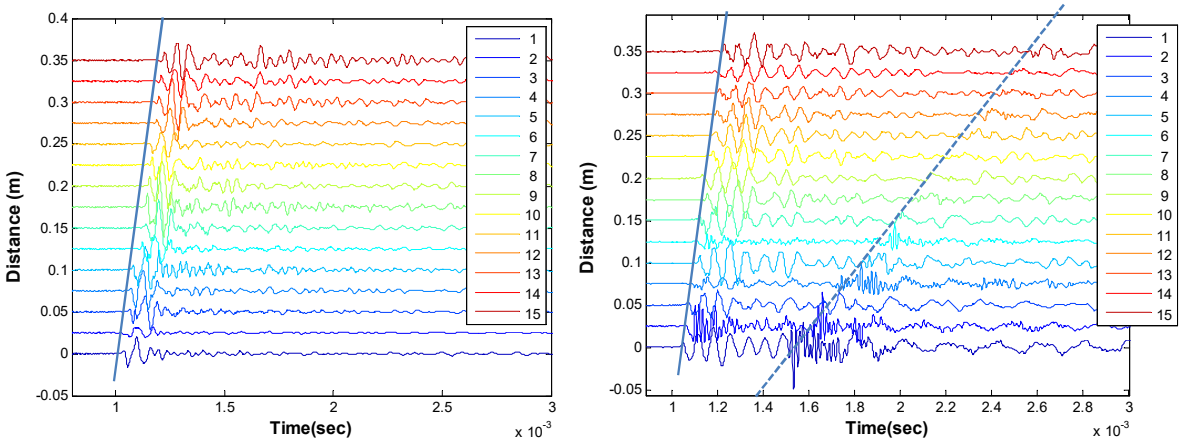

Figure 5.5 Time signals from sensor array collected from 200mm thick concrete slab; data from contact accelerometers (left) and contactless MEMS sensor (right). Blue solid lines indicate expected surface wave arrival, and a dashed line indicates expected acoustic wave arrival.

Figure 5.6 shows the MASW dispersion curve data field. It was calculated from the time dataset shown in Figure 5.5. The analytically-computed Lamb wave curves are overlaid on the MASW dispersion curve field. The green lines indicate anti-systematic Lamb modes, and the red lines indicate symmetric Lamb modes in the figure. The Lamb wave curves are computed assuming a plate thickness of 200 mm and bulk wave velocities of the material of 4058 m/s (P-wave) and 2485 m/s (S-wave). The MASW dispersion curve fields for the contact (left) and contactless (right) sensors show reasonable agreement with each other at lower values of frequency and phase velocity. In particular, results from the MEMS show excellent agreement with the fundamental anti-symmetric (A0) mode at all displayed frequencies. Data from the accelerometer show agreement only up to 15 kHz. The A0 mode converges to the Rayleigh surface wave, as frequency increases. Data collected from the MEMS sensors show a strong vertical

response at approximately 9 kHz, while those from the accelerometer show a weak response. This strong vertical response is referred to as an energy shift. Although explanations for this behavior merit deeper future study, ostensibly, the distinct behaviors between contact and noncontact sensors result from different coupling conditions. The coupling material of the contact sensor (accelerometer) is wax. The wax may affect the dynamic behavior and thus give rise to different responses from the air-coupled receiver, which has no coupling material. These energy shift responses from the noncontact sensors (see in Figure 5.6, right) are contained within a frequency range between 0.8 to 1 kHz. The energy response can be explained by dominant excitation energy of the first symmetric (S1) mode, which is known to be associated with the impact-echo mode of the entire plate (Bjurstrom & Rydèn 2013). Another possibility is differing mode excitability between A0 and S0 modes at a certain frequency with different plate thickness (Wilcox 2004). More descriptive discussion of the excitability is contained in section 5.2.3. The results indicate that the contactless sensor can be used to obtain meaningful MASW data, and in fact may provide more information, such as a clear energy shift, than contact sensors.

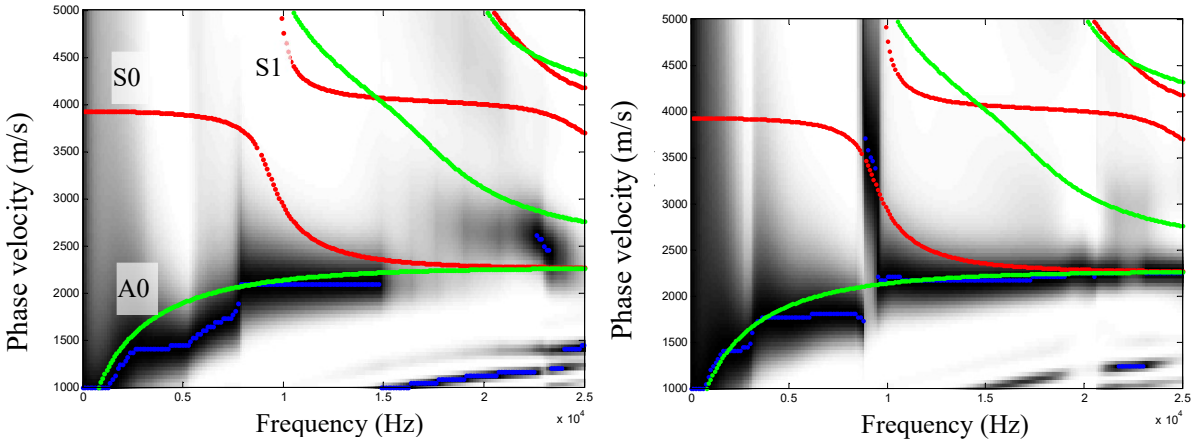

Figure 5.6 Dispersion curve data from MASW processing is shown as black points computed from seismic time signals from 200mm thick concrete slab; data from contact accelerometer (left) and MEMS sensors (right). Red and green lines indicate expected asymmetric and symmetric Lamb wave modes, respectively.

5.2 Numerical Analysis

Numerical simulation (dynamic FE) results are discussed in this section. Analogous experimental results will be explored subsequently. FE simulations are helpful for understanding the physical meaning of Lamb wave behaviors. There are two components in this study. First, a parametric study of testing configuration issues, such as incident angle of sending transducer, number detecting sensors, etc., is

reported. Second, a study of test configuration position with respect to damage areas is demonstrated. All FE detail models are described in Chapter 4.

5.2.1 Parametric Study of Testing Configuration

Here a parametric study explores the influence of variable depth of the delamination. Figure 5.7 shows dispersion curves obtained from MASW processing of FE simulation data, where both raw and normalized representations are shown. The figure on the left shows raw dispersion curve data without a normalization process applied, and the figure on the right show a dispersion curve with a normalization process applied. In the normalization process, all amplitudes divided by their maximum value of each respective frequency line. The dispersion curve without normalization exhibits multiple modes at each frequency and frequency to frequency fluctuations. The dispersion curve with normalization exhibits the dominant mode only at each frequency, selecting energy at the highest unit amplitude, and suppresses the data fluctuations. The positive energy shifts at the jump condition, from A0 to S0 modes are seen more clearly in the normalized data plot, as shown in Figure 5.7. However, the meaning of the absolute value of energy in the MASW is lost with the normalization process. Despite this loss of meaning with the energy vlaues, the normalized data interpretation of the MASW plots will be used in all subsequent work presented in the thesis, because it enables clearer identification and interpretation of the energy shift phenonmenon than the raw data do. .

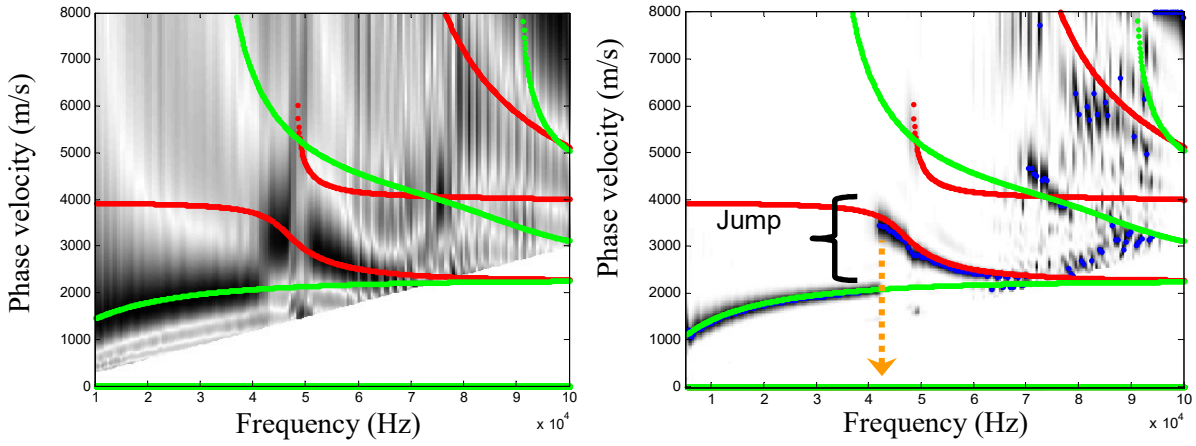

Figure 5.7 A dispersion curve obtained from MASW processing of FE data is shown as black points; red and green lines indicate expected asymmetric and symmetric Lamb wave modes, respectively. A thickness (h) of 40 mm, an incident angle (θ) of 85° and number of sensors (N) of 13 are assumed in the simulation: (left) without normalization, and (right) normalization process of each frequency line.

The effects of the incident angle were also studied. The angle of ultrasound incidence is measured with respect to the normal of the concrete surface. When the angle is close to perpendicular to the surface (90°), most of the energy shifts to the S1 mode from the S0 mode. An 85° incident angle excitation provides the clearest energy shift from A0 to S0. All subsequent experimental results utilize an 85° incident angle excitation.

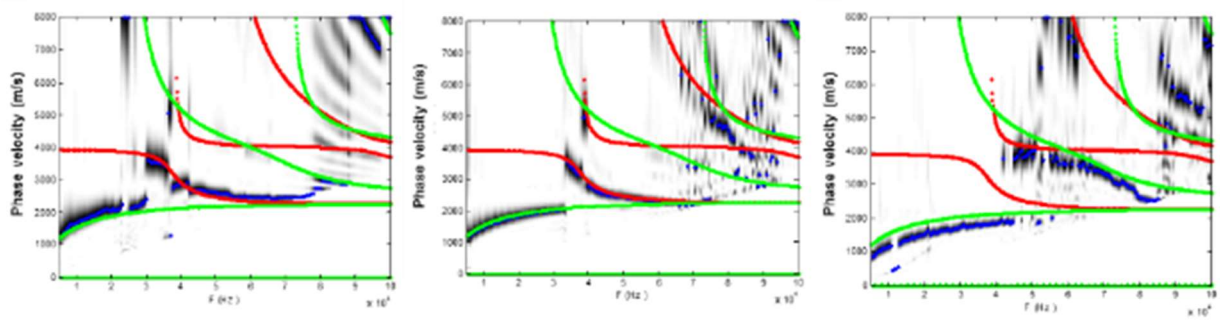

Figure 5.8 MASW results interpreted by energy shift analysis. Effect of incident angle (θ), for H=50mm and N=13: (left) θ = 60°, (middle) θ = 85°, and (right) θ = 90°. Angle measured with respect to plate surface. FE simulated data.

Another parametric simulation studies the effect of the number of sensors. In all simulations, the sensor spacing, dx, is 20 mm. Figure 5.9 shows the results for the effect of the number of sensors. As expected, clearer MASW dispersion curves results are obtained as the number of sensors (receivers) increases. However the use of the fewest number of sensors as practicable is desired when the method is applied in the field. The results with 13 sensors show the closest agreement to the analytical data (see Figure 5.9, left), but that agreement reduces and the number of sensors decreases. MASW dispersion curve data with less than four sensors do not show clear energy shift response because the data become increasingly blurry. However, results using four sensors does provide interpretable data and identifiable energy shift. Thus the minimum requirement of the number of sensors is four for this type of analysis.

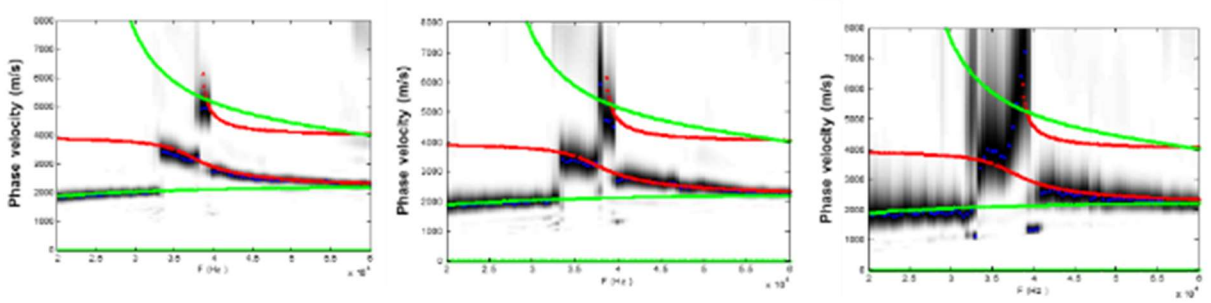

Figure 5.9 MASW results interpreted by energy shift analysis. Effect of number of sensors (N), for θ = 85° and H = 60mm: (left) N= 13, (middle) N= 8, and (right) N= 4 sensors. FE simulated data.

The final parametric study investigates the influence of plate (delamination) depth. As seen in Figure 5.10, the frequency at which the energy shift occurs changes as a function of plate depth, where the shift frequency decreases as the plate depth increases. The energy shift is indicated by the first positive Vp shift in the MASW plot data. Figure 5.11 (left) shows the computed energy shift frequency for plate depth H ranging between 20 – 70 mm, which is a typical expected delamination depth range for concrete bridge decks. A clear relation between the two parameters is seen, suggesting a possible approach to estimate delamination depth from MASW data.

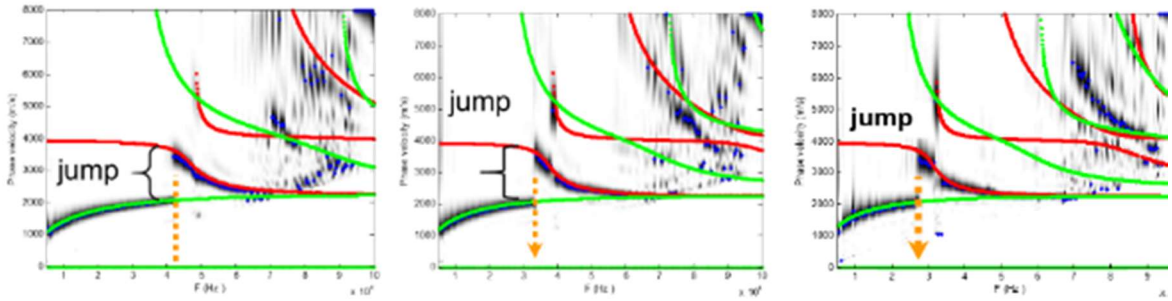

Figure 5.10 MASW results interpreted by energy shift analysis. Effect of plate depth (H) for θ = 85° and N = 13: (left) H= 40 mm, (middle) H=50 mm, and (right) H=60 mm. FE simulated data.

An alternative interpretation of MASW plot data is to monitor the phase velocity of a given mode at a given frequency as test parameters change. This analysis approach is considered for the case of changing plate depth, where the phase velocity of the A0 mode is monitored at 20 kHz. The results are shown in Figure 5.11 (right). The A0 phase velocity increases regularly and consistently as plate depth increases. However the relative change in A0 phase velocities is significantly smaller than that of energy jump frequency across the same plate depth range. Therefore, the energy shift frequency approach appears to

be a stronger predictor of plate depth using MASW plot data than the change of the A0 phase velocity.

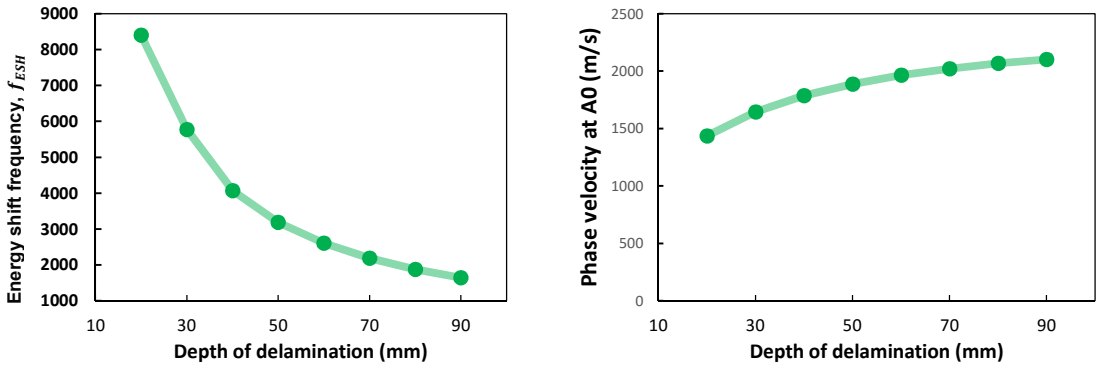

Figure 5.11 Numerically predicted data: (left) A0 to S0 energy shift frequency as a function of plate depth. For a 55mm delamination depth, a shift at 32 kHz is expected, and (right) A0 phase velocity at 20 kHz

The parametric study using FE simulated data suggest a best set of test parameters and analyses for the application of MAW plot data. Although experimental data, especially those obtained from fully air-coupled UT results do not exhibit the same quality dispersion curve, experimental air-coupled UT results do show the predicted energy shift from A0 to S0 in the case of thin plate depths over a delaminated area. The proposed Lamb wave approach is thus feasible for rapid near-surface delamination detection in concrete bridge decks when an optimal test configuration is used.

5.2.2 Parametric Study: Changed Material Properties

Further study is needed to understand the effects of changing material properties on the proposed MASW plot analysis parameters. A parametric study, using FEM data, is carried out to examine such effects. ABAQUS/EXPLICT is used for the FEM simulations of the concrete elements. The simulated model is based on actual laboratory concrete samples, as shown in Figure 5.7. The effects of variation of the following material parameters on the MASW plot parameters (f_{ESH} is and phase velocity of the A0 mode at 20 kHz) are considered:

$$f_{ESH} = f_{ESH}(E, \nu, \rho) \qquad (5.4)$$

Where E is elastic modulus ν is poison ratio, and , ρ is density. An isotropic, elastic plate with Young's modulus, E, Poisson's ratio, ν, thickness, h, and lateral extent, r, is modeled, which simulates 2-D and 3-D solid elements and assumes an infinite length for the model. Only a plain solid slab was simulated

in some cases; that is, a vacuum bound the free surface of the slab. Various materials are evaluated for parameters, such as density ρ, elastic modulus E and Poisson's ratio υ. Different defect locations and sizes then are simulated. Each of the material properties were changed by ± 5% from initial base values: E= 35000 MPa., ρ = 2400 kg/m^3, and ν=0.2, which represent typical values for concrete.

The results of the parametric study are presented in Figure 5.13 toFigure 5.14. Both energy shift frequency and A0 phase velocity show clear dependence on changes in the various material properties. For example, as the elastic modulus increases by 1%, the energy shift frequency increases by

These energy shift frequency $\boldsymbol{f}_{\boldsymbol{ESH}}$ with 1% increase of each material properties by linear regression are corresponding to,

$$\boldsymbol{f}_{\boldsymbol{ESH}}\big|_{\boldsymbol{E*1.01}} \approx \boldsymbol{f}_{\boldsymbol{ESH}}\big|_{\boldsymbol{E}} + \mathbf{9.5}\ \boldsymbol{Hz} \qquad \textit{(5. 5)}$$

$$\boldsymbol{f}_{\boldsymbol{ESH}}\big|_{\boldsymbol{\nu*1.01}} \approx \boldsymbol{f}_{\boldsymbol{ESH}}\big|_{\boldsymbol{\nu}} - \mathbf{3.3}\ \boldsymbol{Hz}$$

$$\boldsymbol{f}_{\boldsymbol{ESH}}\big|_{\boldsymbol{\rho*1.01}} \approx \boldsymbol{f}_{\boldsymbol{ESH}}\big|_{\boldsymbol{\rho}} - \mathbf{4.3}\ \boldsymbol{Hz}$$

as obtained from Figure 5.12. Both MASW parameters show this level of dependence on all three materials properties. However, these changes are relatively small (less than 5 % total change across studied material parameter range) as compared with the change of those MASW plot characteristics with regard to plate thickness change, which is on the order of a 70 % value change; see Figure 5.11, left. Therefore, the effects of varying material property likely have a negligible effect on the energy shift and A0 phase velocity parameters as compared with varying plate depth.

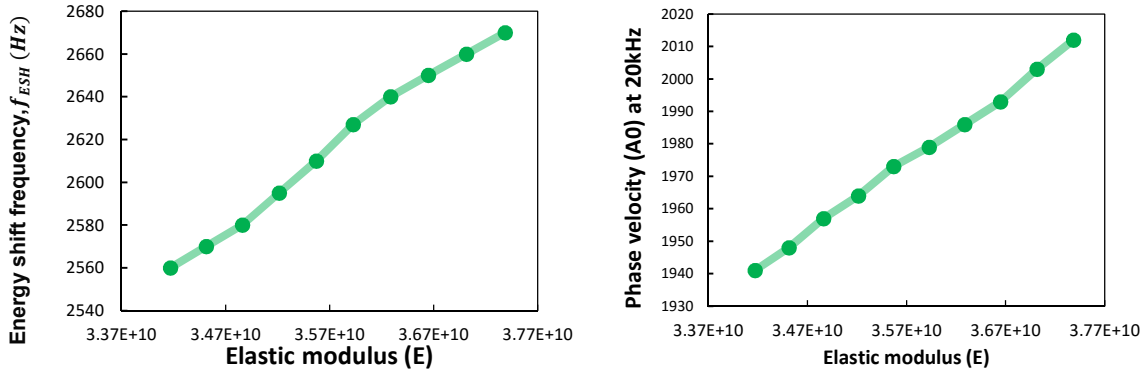

Figure 5.12 FE results with various elastic moduli. A thickness (h) of 60 mm, an incident angle (θ) of 85° and number of sensors (N) of 13 are assumed in the simulation: (left) Energy shift frequency and (right) A0 phase velocity at 20 kHz.

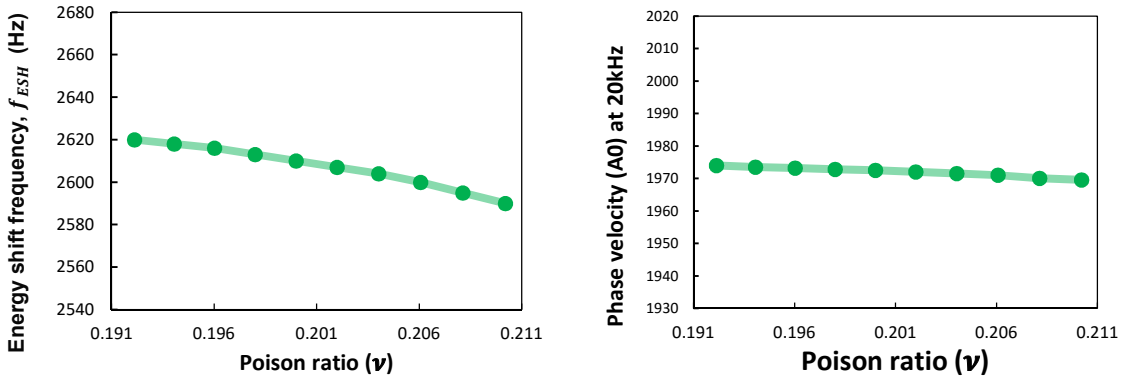

Figure 5.13 FE results with various Poisson's ratio (ν). A thickness (h) of 60 mm, an incident angle (θ) of 85°, and number of sensors (N) of 13 are assumed in the simulation: (left) Energy shift frequency, and (right) A0 phase velocity at 20 kHz.

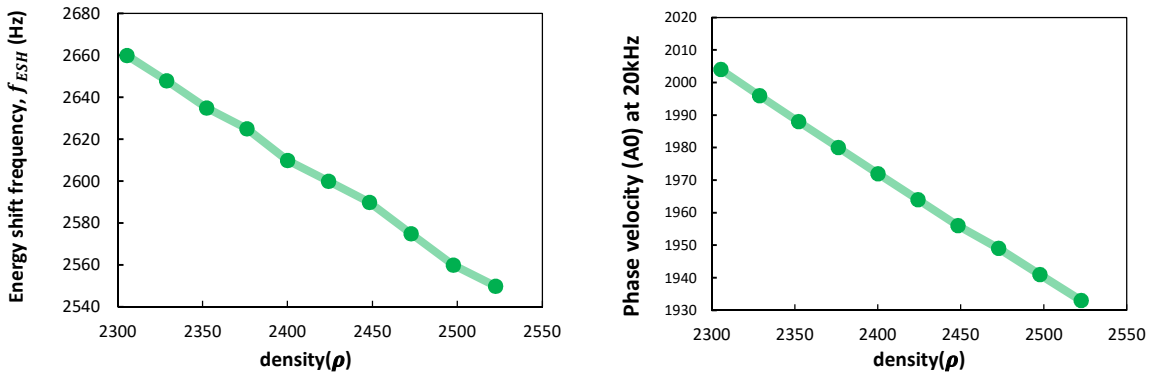

Figure 5.14 FE results with various density (ρ). A thickness (h) of 60 mm, an incident angle (θ) of 85° and number of sensors (N) of 13 are assumed in the simulation: (left) Energy shift frequency and (right) A0 phase velocity at 20 kHz.

5.2.3 FEA of Different Excitability

This section considers MASW dispersion curves obtained from different types of receiving and sending sensors. Several cases were tested with the FE model: case 1 involves a contact sender and contact receivers, case 2 involves a contact sender and contactless receivers, case 3 involves the contactless sender and the contact receivers, and case 4 involves a contactless sender and contactless receivers. Acceleration response in y direction was measured for the contact sensor signal, while pressures were collected for the contactless receiver. All cases show an energy shift, and results with fully contactless systems show the strongest jump condition. In 2004, Wilcox studied different directions of excitation. As shown in Figure 5.16, S0 are dominant from A0 at a certain frequency (Wilcox 2004) for the contact sender and receiver (in y direction). Further analysis for our energy shift on concrete structure will be

addressed in future work.

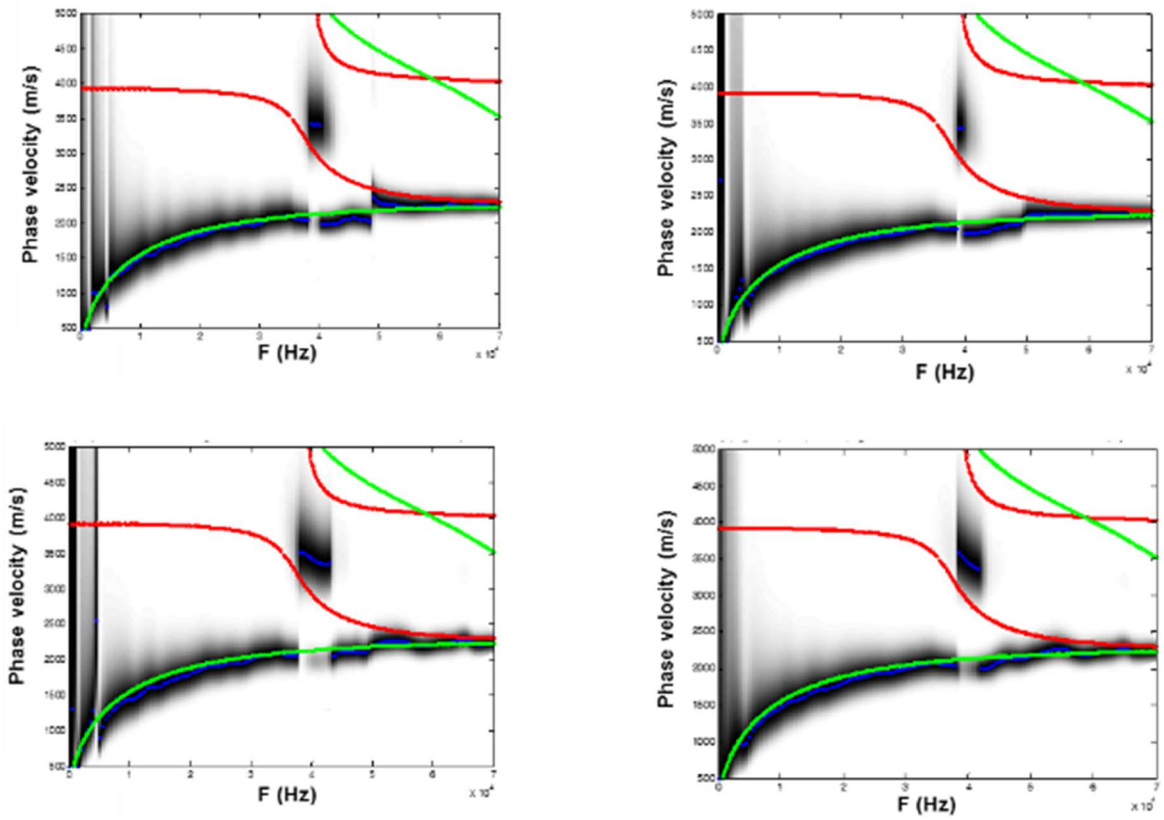

Figure 5.15 various excitability study for energy shift: (top left) case 1 for contact sender and receiver, (top right) case 2 contact sender and contactless receiver, (bottom left) case 3 contactless sender and contact receiver, and (bottom right) case 4 contactless sender and receiver.

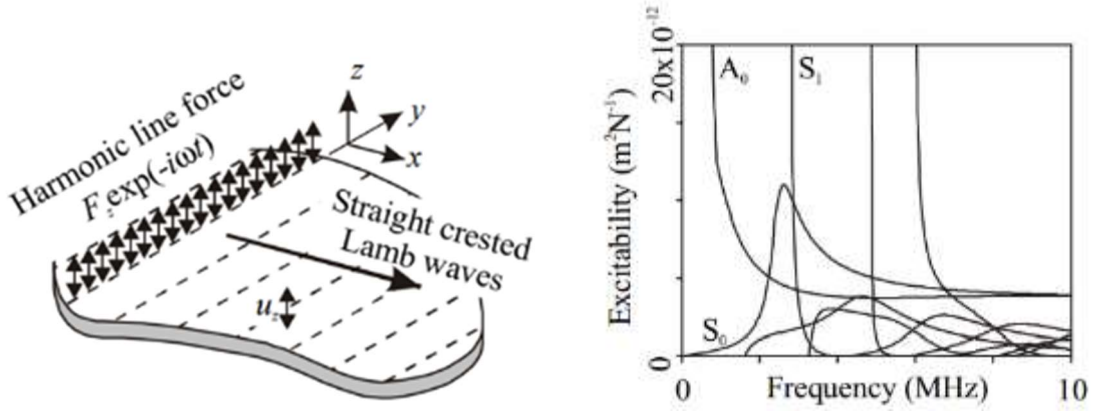

Figure 5.16 Excitability study : (left) schematic diagram showing force and the particle displacement component with direction of excitation(Wilcox 2004)***, and (right) excitability for 1mm steel plate***(Wilcox 2004)**.**

5.3 Experimental Results and Discussion

5.3.1 Specimen Description and Testing Set-Up

Fully air-coupled fast MASW tests were conducted on a reinforced concrete slab with two layers of steel bars at 60 and 200 mm depths, respectively. The size of the slab was 1.5 by 2.0 m with a 0.25 m thickness. The concrete has a 28-day compressive strength of 42.3 MPa. Ultrasonic pulse velocity measurements (ASTM, 1997) showed that the P-wave velocity of the mature concrete is 4,100 - 4,200 m/s. A maximum aggregate size of 2 cm were used for all experimental concrete specimens. This slab contains a variety of embedded artificial delaminations and voids. Double-layered plastic sheets and soft foam blocks simulate artificial delaminations. The locations of the delaminations and a grid area are based on test points, as shown in Figure 5.17. Near-surface rectangular areas (0.4×0.6 m^2) at a depth of 60 mm from the surface were selected for the fully air-coupled ultrasonic MASW tests, as reported here.

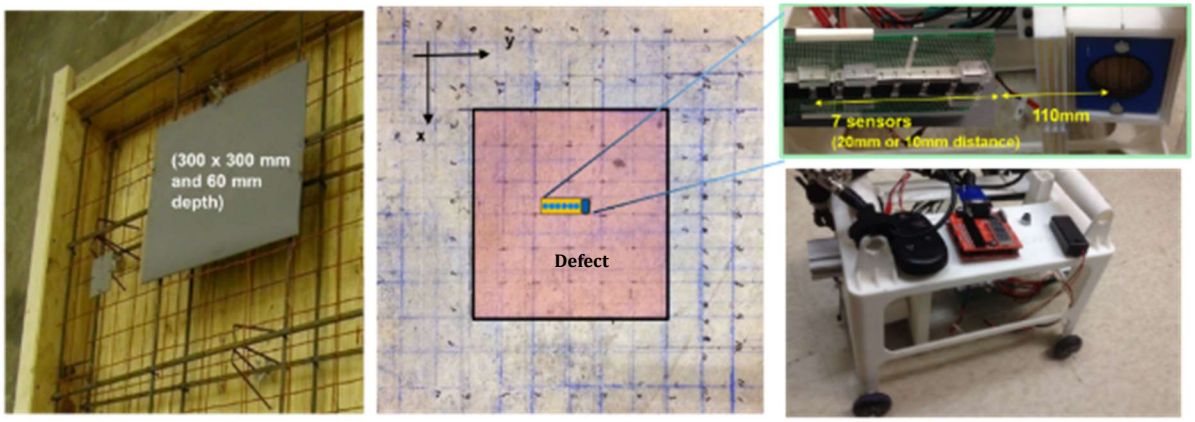

Figure 5.17 Reinforced concrete slab with artificial delamination: (left) embedded 30 x 30 cm and 55mm depth simulated delamination before casting (from Zhu & Popovics 2007), (middle) a grid for scanning, where red area indicates delamination, (right) testing hardware and robot scanning system.

5.3.2 Test Results and Discussion

Air coupled broadband (10 to 100 kHz) excitation is used for all cases. Figure 5.18 (experimental results over the delamination) show that the A0 mode dominates at low frequency, while the S0 mode dominates at higher frequencies, starting at a certain frequencies referred to as “jump condition” or “Energy shift", as shown in Figure 5.18. The author define this phenomenon as a positive energy shift. Based on the numerical simulation responses, not shown here, the presence of an underlying delamination defect

causes a positive phase velocity (Vp) shift at a given jump frequency. The nature of the dispersion curve indicates not only the presence of delamination, but also its depth. Figure 5.19 shows the test results on the defect (delamination) surface The Figure 5.20 shows testing results on the solid (no defects) region. The individual dispersion curves show predicted energy jumps. Figure 5.19 show the consistent of energy shift at 25 kHz which is 60 mm thickness

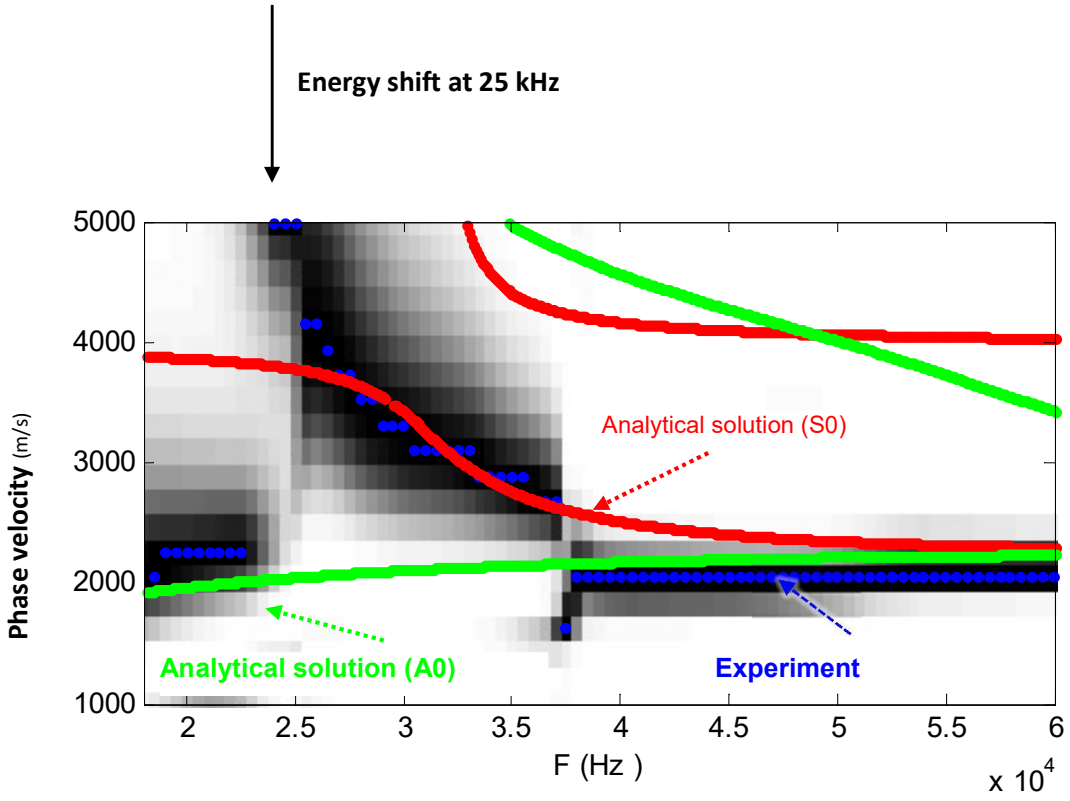

Figure 5.18 An excample of of ddispersion curve obtained from MASW result on delamination indicating that the curvev (blue dots) are well matched with analytical solutions, (indicating red and gree solid line) and showing an energy shift at 25 kHz, corresponding to 60 mm thickness.

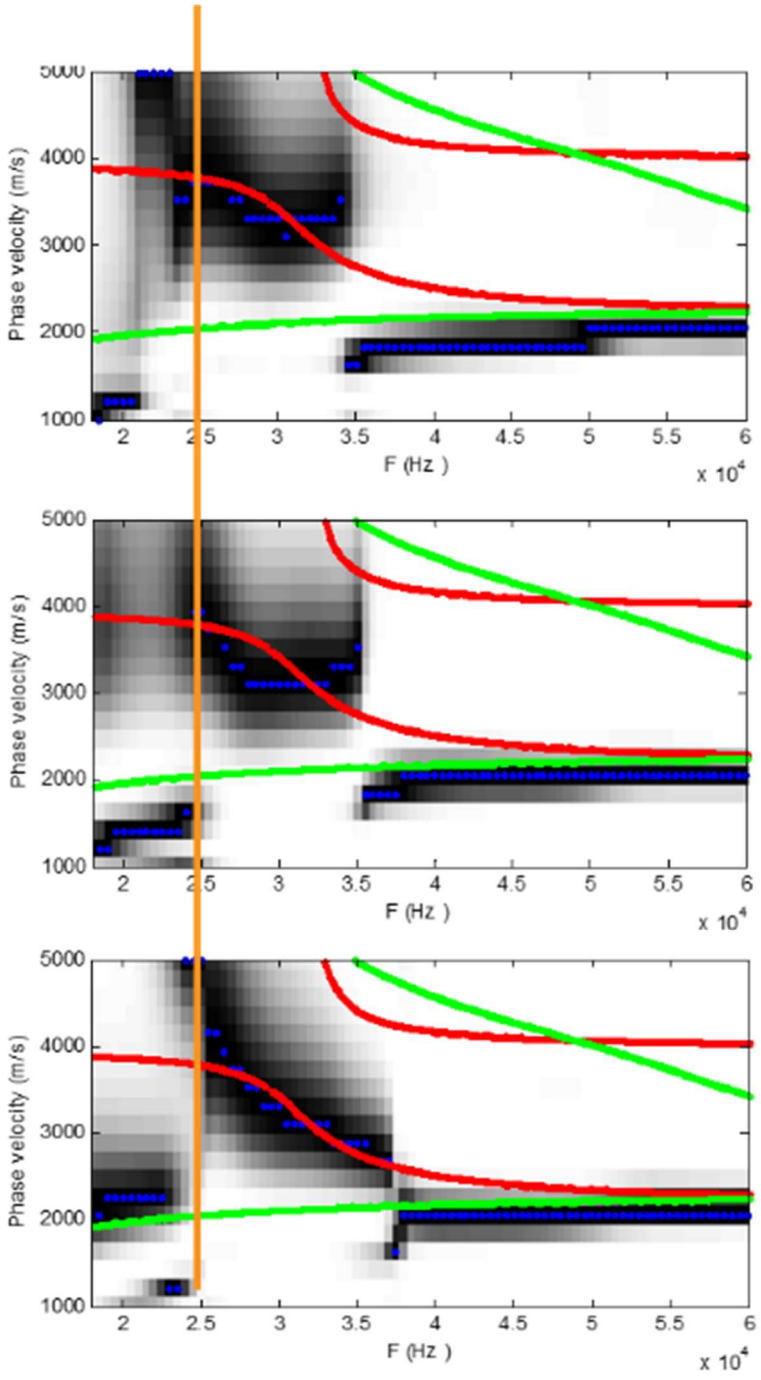

Figure 5.19 Dispersion curve with the MASW data on three different regions over the delamination, orange line is the expected energy shift at 25 kHz frequencies, which is similar to the case for 60 mm.

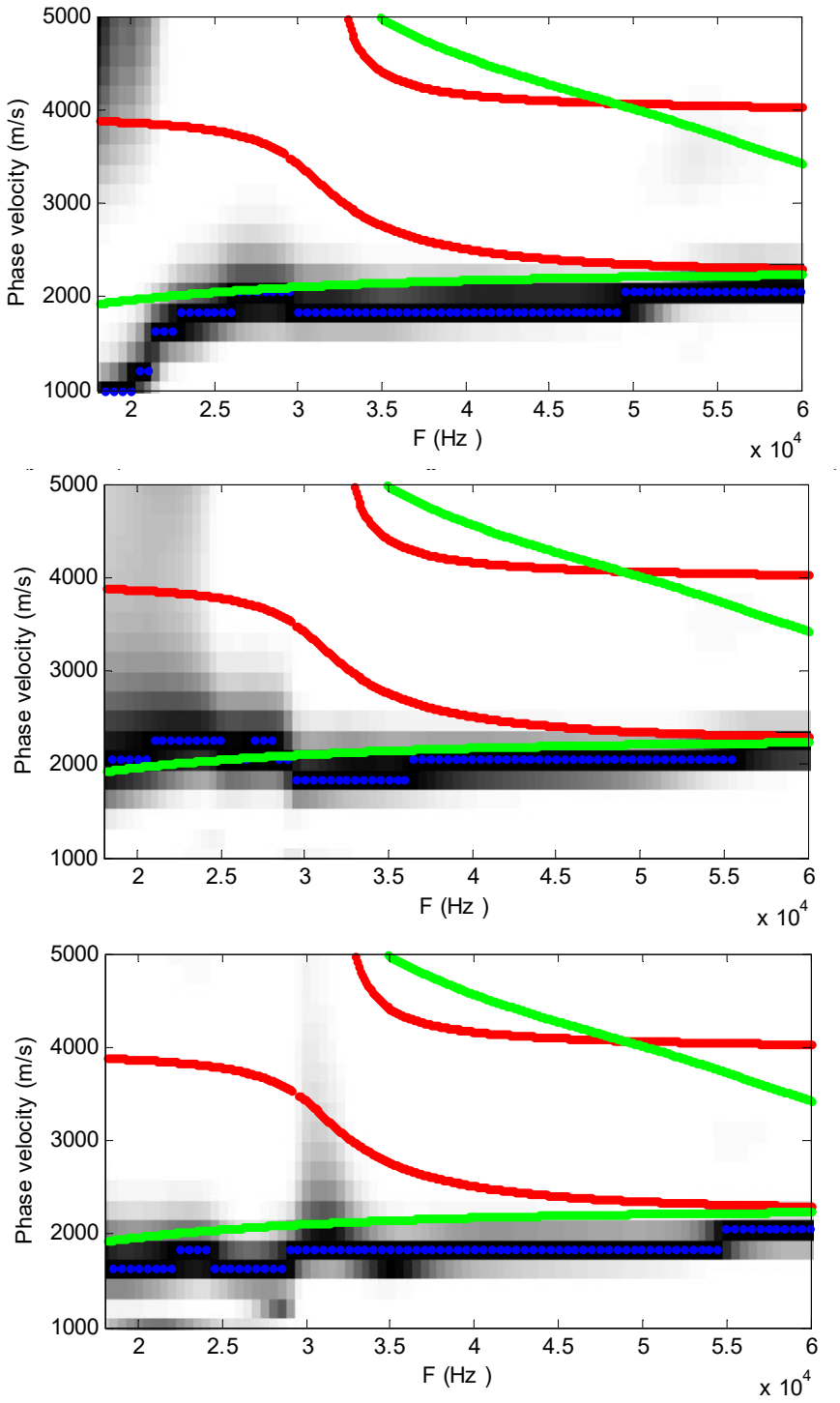

Figure 5.20 Dispersion curve with the MASW data on three different regions over a solid area, indicating that there is no energy shift.

The fully contactless UT results in Figure 5.19 show the predicted energy shift from A0 to S0 (showed as red color) in most delamination areas. The shift frequency (25 kHz) is reasonable for the region between 55 to 60 mm delamination depths. The large amounts of high quality data allow the MASW method to be employed. Multiple Lamb wave datasets can be used to accurately image delamination in concrete by monitoring shifts in energy between Lamb wave modes stacked curves. Figure 5.21, left botom and right bottom show the extent (length) of delamination along the stack direction. It also illustrates the 2-D image on two different regions. The 3-D experimental stacked image in Figure 5.22 also shows that Lamb wave interpretation of the MASW data can distinguish several 2-D images stacked on the region.

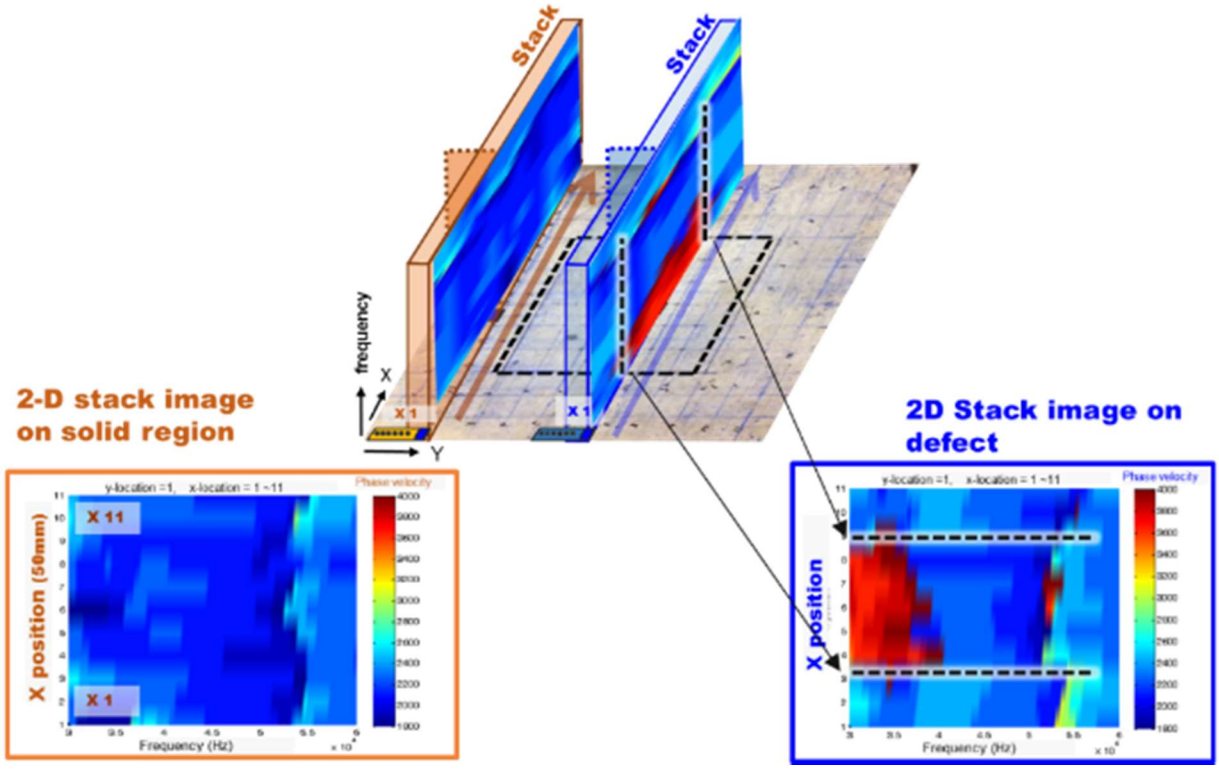

Figure 5.21 Illustration of dispersion curve data processing: (left) solid region, and (right) delamination region. Individual curves show predicted energy jump. Stacked curves show extent (length) of delamination along stack direction.

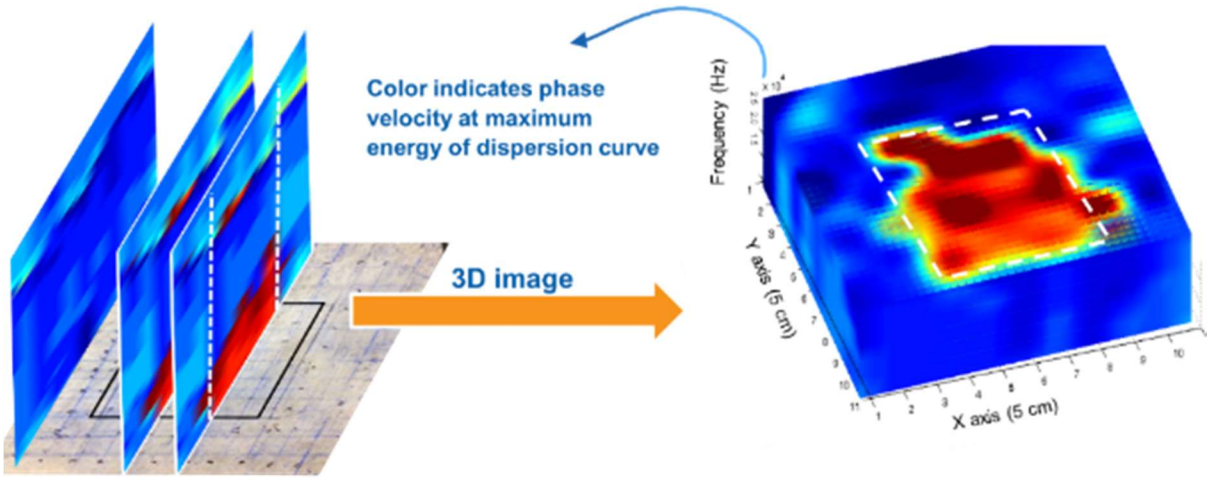

Figure 5.22 Illustration of MASW 3-D image reconstruction : (left) process of stacking 2-D MASW sliced images, and (right) 3-D MASW image shows energy shift with high phase velocity corresponding to S0 mode.

5.3.3 Comparison with Other Imaging Methods

Impact-echo is a reliable technique for monitoring delamination on a large-scale concrete bridge deck. Conventional semi-air-coupled Impact-echo (vibration resonance) data were compared with our MASW image. The author published Impact-echo (IE) testing results using vibration resonance data (Oh, Popovics, et al. 2013). The paper studies vibration resonance data from the square near-surface delamination defects in concrete using both the Impact echo test and the conventional modal analysis test (Oh, Popovics, et al. 2013). By overlapping the first three natural mode shapes, the researcher is able to form a modal image that accurately predicts the areal size of underlying delamination defects. A 2-D Impact-echo scanning test was carried out over the same delamination area (300 x 300 mm) (Oh, Popovics, et al. 2013). The measurement grid spacing is x = y = 2.5 mm in both directions. The measuring space (grid) is the same as the space of the MASW test. As shown in Figure 5.23, the results of our fully air-coupled ultrasound with a Lamb wave energy shift approach shows similar image quality to the semi-contact impact echo results. Non-contact excitation can increase signal consistency on different surface roughness. The employment of multi-sensors allows for fast scans of the entire area Multiple Lamb wave data can be used to accurately image delamination in concrete. This is significant because it indicates area and the depth of delamination clearly.

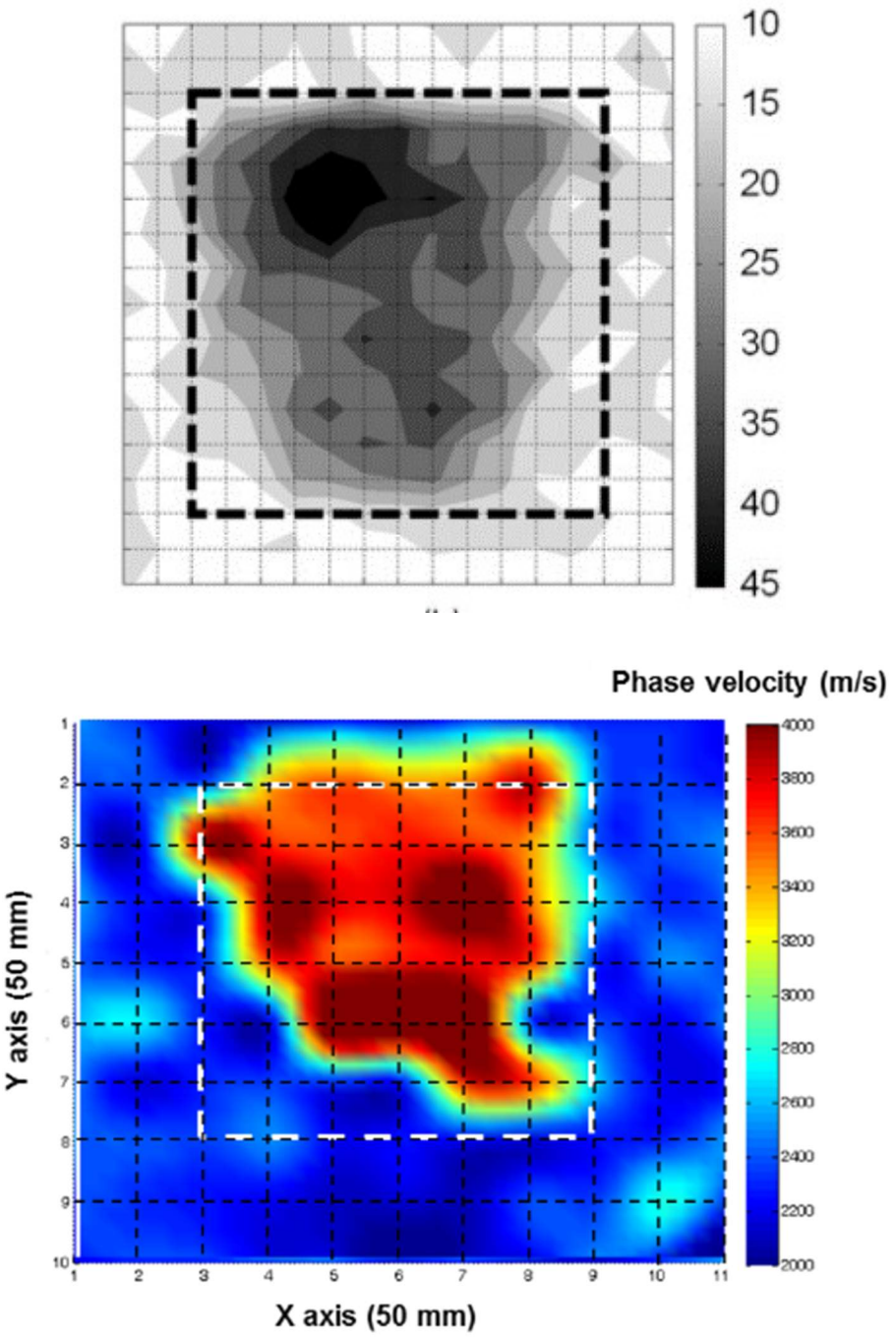

Figure 5.23 Comparison of delamination imaging data. Dashed line indicates actual boundary position of the delamination: (top) Contour plot representation of the spectral amplitude data using overlapped mode shapes for the square delamination. Data were obtained using the IE testing configuration(Oh, Popovics, et al. 2013), and (bottom) slice image of 3-D MASW at jump condition at 26 kHz using fully contactless ultrasound. The Contour plot representation of phase velocity (m/s).

CHAPTER 6 CONCRETE MICROCRACK CHARACTERIZATION USING WAVE SCATTER: PART 1 THEORY AND NUMERICAL ANALYSIS

Chapter 6 and Chapter 7 demonstrate a practical contactless ultrasonic testing approach that uses backscatter measurements to characterize distributed cracking damage in concrete structures. Many important damage mechanisms in concrete manifest through distributed cracking. Although previous research identified that ultrasonic and other nondestructive approaches are related to distributed damage content in concrete, the methods are either insensitive to early stages (low crack volumes) of damage, not repeatable, or inconsistent. These conventional NDE systems have potentially slow speed measurements. Efforts to overcome both issues by employing rapid ultrasonic surface wave backscatter phenomena are reported here. This chapter demonstrates that ultrasonic surface wave backscatter parameters have the potential for increased sensitivity to small (relative to ultrasonic wavelength) crack defects in concrete. These results were compared with other conventional data. Chapter 7 reports on the deployment of surface wave tests using a fully contactless (air-coupled) configuration. It provides the potential for a practical and efficient method for in-service infrastructure elements. Finally, the chapter proposes a physical meaning/basis for observed backscatter parameters, and it shows local images of backscatter. These contributions represent advances for ultrasonic nondestructive testing and the infrastructure of health monitoring communities.

6.1 Backscatter Analysis Approach

This section investigates several approaches for characterizing distributed microcracking damage in concrete. New extracted backscatter energy approaches are introduced that are based on time domain subtraction and power spectrum variance. Important concepts and detailed information are provided.

6.1.1 Existing Methods to Characterize Distributed Microcracking Damage

Most concrete infrastructures comprise large critical systems, such as bridges, pavements, and buildings. Significant progress has been made in recent years toward health monitoring and NDT of large critical concrete infrastructure systems *in situ* (American Concrete Institute (ACI) Committee 228 1998). However, most conventional concrete NDT methods, such as visual inspection, sounding (e.g., chain drag), pulsed microwave/radar techniques (GPR), and infrared thermography, cannot detect and characterize the extent of distributed microcrack damage in concrete (American Concrete Institute (ACI) Committee 228 1998). Conventional mechanical wave (ultrasound) methods, which utilize coherent

pulse propagation characteristics, such as wave velocity or attenuation, show sensitivity to large discrete cracks and defects. They are much less able to characterize the extent of microcrack damage, however, because of the relatively large wavelengths (with respect to crack size) needed to propagate in a highly inhomogeneous scatter medium, like concrete. To maintain a coherent ultrasonic pulse character through the highly inhomogeneous material structure, relatively low frequencies (less than 100 kHz, which corresponds to approximately 4 cm wavelength for p-waves) are employed. Despite large wavelengths, the use of coherent pulse p-wave velocity (Selleck et al. 1998; Ould Naffa et al. 2002), p-wave attenuation (Landis & Shah 1995; Selleck et al. 1998; Ould Naffa et al. 2002; Punurai et al. 2007; Saint-Pierre et al. 2007; Gaydecki et al. 1992; Suaris & Fernando 1988), and surface wave characteristics (Aggelis et al. 2011) to monitor microcracking in concrete have been reported. In such instances, some ability to detect and distinguish between different levels of damage has been reported (Selleck et al. 1998; Ould Naffa et al. 2002; Saint-Pierre et al. 2007; Suaris & Fernando 1988). However, sensitivity to low levels of cracking damage remains poor with coherent ultrasonic methods, and the results have not yet been directly related to a quantifiable measure of the damage, such as crack density.

Recent efforts to improve the sensitivity of UT measurements to microcracking damage and other microstructural modifications in concrete have focused on nonlinear (Gross et al. 2013; Chen et al. 2008; Chen et al. 2010; Shah & Ribakov 2009; Kim, In, et al. 2014), and diffuse field measurements (Shokouhi 2012; Larose & Hall 2009; Schurr 2010; Anugonda et al. 2001; Deroo et al. 2010; Quiviger et al. 2012; Deroo 2009). Chapter 2 also introduces several technologies in detail. The nonlinear measurements use amplitude-dependent softening (Gross et al. 2013; Chen et al. 2008; Chen et al. 2010) through nonlinear resonance spectroscopy, or higher harmonic generation (Shah & Ribakov 2009; Kim, Kim, et al. 2014) phenomena to extract nonlinear signal parameters. The extracted nonlinear parameters demonstrate superior sensitivity to the presence of damage, including the early stages of microcracking damage, as compared with conventional coherent ultrasonic wave velocity and attenuation measurements. None of the research reports on the ability of these advanced UT methods for concrete to quantify and distinguish the different damage extents uniquely and reliably. An example would be using statistical significance with a different null hypothesis in confidence analysis to interpret the data. This suggests that ultrasonic nonlinear measurements may be adversely affected by high-test variability or other experimental disruptions. Further, the nonlinear resonant spectroscopy test configuration requires test samples of specific size and geometry, and as such, are laboratory-based methods that cannot be applied to large concrete structures *in situ*. Ultrasonic diffuse field measurements have been applied to concrete to detect

microcracking damage (Shokouhi 2012; Schurr 2010; Anugonda et al. 2001; Deroo et al. 2010; Deroo 2009), discrete cracking (Quiviger et al. 2012), and applied stress (Larose & Hall 2009) in concrete. The diffuse field data are interpreted through scattered field analysis, via a classical diffuse wave interpretation (Anugonda et al. 2001), or coda wave interferometry (Shokouhi 2012; Schurr 2010). However, the practical application of diffuse field methods to characterize damage in concrete remains rare. As far as the authors are aware, the application of ultrasonic diffuse wave measurements to concrete structures *in situ* has not been reported. This situation likely occurs because of limitations associated with sample size, a need for specialized high-end testing equipment, experimental limitations related to test data variability, or the ability to uniquely and reliably quantify and distinguish different extents of microcracking damage. Concerning this last point, none of the research reports the ability of diffuse wave methods for concrete to quantify and distinguish the different damage extents uniquely and reliably. One such example would involve using statistical significance with different null hypothesis in confidence analysis to interpret the data.

6.1.2 Approach to Extract Backscatter Characteristics

Mechanical wave scattering falls under two categories: weak scattering and strong scattering. Weak scattering occurs when either the constitutive properties of the scatterers are close to the properties of the background material, or when the scatterers are very small compared to the wavelength of the propagating wave. Under weak scattering conditions, simplifying approximations can be made, for example, by assuming a plane wave incidence. This leads to important conclusions that relate the scattered field to geometry, property, and size of the underlying scatterers.

To understand the relationship between scattering direction and dependence on the type of backscatter, a Born approximation of scatter in a fluid can be examined. Assuming harmonic wave propagation, $p(\vec{x},t) = p(\vec{x})e^{j\omega t}$ the classical wave equation reduces to the Helmholtz equation (Morse & Ingard 1939),

$$\nabla^2 p(\vec{x}) + k^2 p(\vec{x}) = S(\vec{x}) \qquad (6.1)$$

where p is the acoustic pressure, k is the acoustic wavenumber, $S(\vec{x})$ is Fourier transform of the object function and ∇^2 is the Laplacian operator. Assuming plane wave incidence in a fluid and invoking the Born approximation yields a scattered pressure field from the scattering sources (Morse & Ingard 1939)

$$\boldsymbol{P_{sc}(\vec{x}) \approx \frac{P_0 k^2 e^{jkr}}{4\pi r^2} \int_V S(\vec{x}) e^{-j\vec{K}\cdot\vec{x_0}} d^3 x_0} \qquad (6.2)$$

where P_0 is the magnitude of the incident pressure field and $\vec{K}$,the scattering vector, is defined as the difference between the incident field direction and the scattered field direction, i.e., the direction of observation of the scattered field relative to the incident field,

$$\vec{K} = \vec{k}_{sc} - \vec{k}_{inc}. \qquad (6.3)$$

Equation (6.2) can be thought of as the Fourier transform of the object function, $S(\vec{x})$. By observing the scattered field across many different angles, different parts of the object function can be mapped in terms of the object k-space. For example, forward scatter occurs when the observed scatter field indicates the same direction as the incident field yielding.

$$\vec{K} \approx 0. \qquad (6.4)$$

Hence, forward scatter would provide information about the object function related to a low wavenumber or object features that are larger than a wavelength. In the backscatter direction, the scatter vector is

$$\vec{K} = -2k\hat{k}, \qquad (6.5)$$

which suggests that the backscatter is smaller and sensitive to smaller scale structures on the order of a wavelength.

This analysis is not intended to suggest that scatter from a solid like concrete with microcrack is best formulated by the Born approximation. This analysis is intended to suggest that the choice of backscatter for analysis would be more sensitive to small cracks than the forward scattered field. At ultrasonic frequencies of 50 kHz, the wavelength of surface waves in concrete is on the order of 5 cm, with cracks typically 1 mm or smaller in diameter. Therefore, our interrogations of concrete using 50 kHz ultrasound suggest that the scatterers would be very small relative to a wavelength ($ka < 0.5$). Furthermore, using a weak scattering formulation suggests that the backscatter power would be proportional to the number density of cracks in the field. The analysis of scatter by very thin cylinders indicates that the dependence of backscatter is largely insensitive to the orientation of the cracks to the incident field. Hence, backscatter power can be directly related to the presence and concentration of cracks and, therefore, to the aging of concrete.

The conventional approaches implemented in this dissertation – wave velocity, amplitude, and energy attenuation – show the results for the characterization of different levels of damage samples. Typically, low frequency waves are used with these methods in concrete to minimize the effects of aggregate scatter and other inhomogeneity. However, they do not distinguish among different levels of microcrack damage due to their large wavelength. "Scattering" is defined as the movement of ultrasonic energy away from the original direction of propagation caused by reflection, refraction, and mode conversion from reflectors. Scattering causes signal loss, signal dispersion, and scatter "noise," as illustrated in Figure 6.1. Further, backward propagating time signals have both coherent and incoherent wave content. The coherent part is the backward propagating pulse generated due to the beam spread of the contactless sender. The incoherent content results from the random backscatter of distributed reflectors, including microcracks.

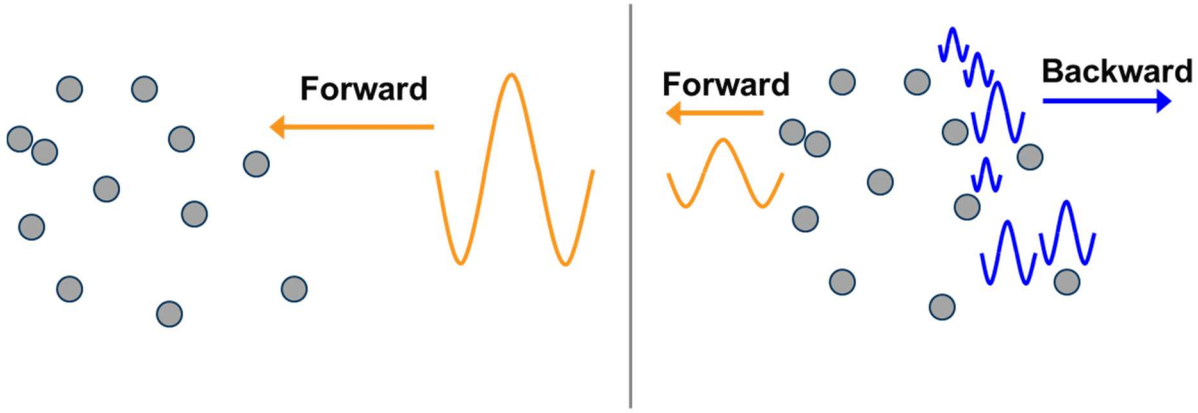

Figure 6.1 Concept of Rayleigh regime (large wavelength) wave scattering from multiple discrete reflectors: (left) shows coherent forward propagating wave in orange color, (right) illustrates scatter interaction where most energy propagates forward (orange color), with some portion of energy scattered backward (blue color). (Illustration courtesy of Michael L. Oelze).

To see the backscatter waves, all receivers are placed in the opposite direction of the incident angle, as shown in Figure 6.2. The baffle wall is intended to block or delay direct acoustic waves. Seven MEMS sensors are located at different positions about 120 mm behind the contactless sender. The seven sensors are positioned in a 2D array. A MEMS sensor was used to measure the forward waves. All senders and receivers are 10 mm above the concrete surface. Only sensors 1, 2 and 3 within the 2D array, illustrated Figure 6.2, were used for backscatter energy study described here. Averaged data from sensor 1, 2, and 3 were used for experimental results. The lateral sensor spacing (between sensors 1 and 2 and 2 and 3) was 10 mm.

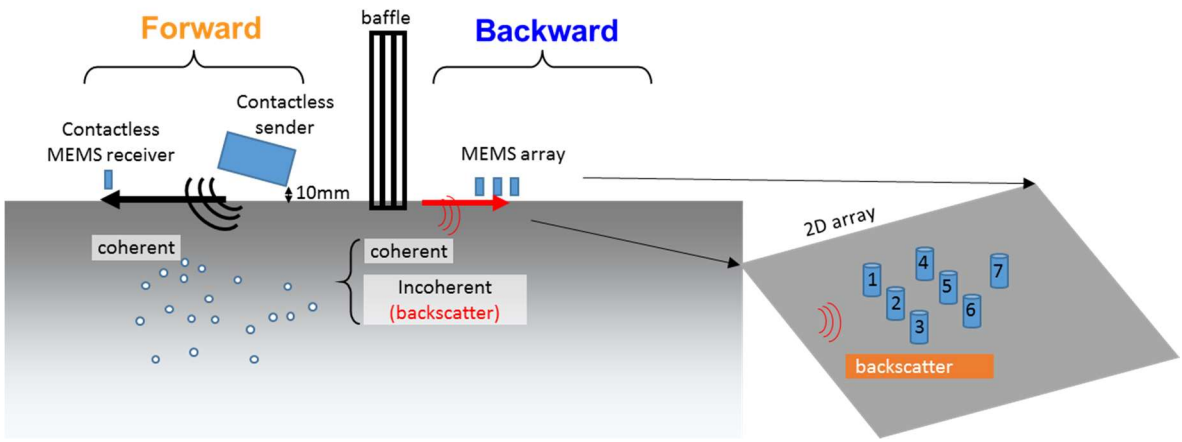

Figure 6.2 Illustration of contactless ultrasonic testing configuration for backscatter analysis.

Two methods were used to analyze backscatter data for numerical and experimental results. The first method is a scattered energy subtraction analysis (ESA). For ESA, several time signals, $\boldsymbol{Bv(t)_i}$ are collected from backward sensors along ten separate parallel paths that form a data set. The paths are separated by 20 mm because it needs to be wider than the ultrasonic beam width, around 12 mm. In addition, considering the maximum 1 inch aggregate size, a total scanned width of 200 mm (20 mm x ten scanned lines) is wide enough to characterize such heterogeneous material.

The ten signals are averaged into one signal that represents the coherent pulse, propagating along the test zone. The scattered energy is computed for wave propagation in the forward and backward directions, illustrated in Figure 6.1 and Figure 6.2. Some small coherent pulse energy is measured in the backward direction because of the beam spread in the air from the transmitting transducer that sends some energy backward. Backward signals were collected along 10 distinct parallel wave path, where for each path the averaged signals from sensors 1, 2 and 3 was collected. Each of the individual signals $Bv(t_{\ i}$ is subtracted from the spatial averaged signal $< Bv >$ from these scanlines in order to extract the incoherent scatter field from the coherent pulse content for each signal,. The extracted signal is,

$$\boldsymbol{B_i = Bv(t)_i - < Bv >} \qquad (6.6)$$

where B_i is the extracted scattered signal, $Bv(t)_i$ is i^{th} time signal, and $< Bv >$ is spatial average over all $Bv(t)_i$. The scattered energy, EB_i, is obtained by integrating the individual scattered signals over a

given period of time in the signal

$$\boldsymbol{EB_i = \frac{1}{t2-}\int_{t1}^{t2}|B_i(t)|^2 dt.} \qquad (6.7)$$

With our FE and experimental data, t1 is 0, and t2 is 3.5x 10^{-4} seconds. The t2 between 2 x 10^{-4} and 3.5 x 10^{-4} seconds generate similar trends of damage characterization. Direct acoustic waves through air were propagated in this setup after 3.5 x 10^{-4} seconds. Therefore, signals were measured up to time. The researcher also calculated normalized EB_i,

$$\boldsymbol{EB_{Nor\_i} = \frac{EB_i}{VI_i}} \qquad (6.8)$$

where VI_i is the integration of the i[th] forward propagated signal. Using the FE model or testing data, the forward propagated energy was calculated by integrating, over time, signals from 0 to the third peak arrival point. After the third positive peak, the direct acoustic waves arrived without the acoustic baffle wall set up. The forward propagated energy is

$$\boldsymbol{VI_j = \frac{1}{t4-}\int_{t3}^{t4}\left|Fv_j(t)\right|^2 \, dt} \qquad (6.9)$$

where, $Fv_j(t)$ is a forward propagating time signal. With the FE and experimental data, the t4-t3 is defined as dt which is from signal initiation to the third peak arrival time which occurs at approximately 2.5 x 10^{-4} second.

The forward propagating surface wave velocity V_s was computed by slopes through the arrival of the positive peak of forward propagated signal sets. The phase velocity is computed by

$$\boldsymbol{V_s = \frac{d2-d}{t2-t1}} \qquad (6.10)$$

where d1 = distance of first sensor, d2 = distance of 2[nd] sensor, t1 = first peak arrival time from the first sensor, and t2 = the first peak arrival time from the 2[nd] sensor.

The second method is Spectral Variance Analysis (SVA). For SVA, the first step involves converting the time domain to the spectral domain and dividing each power spectrum P_i by the averaged power (P_{avr}). The ratio of the power spectrum values ("power spectrum dissimilarity"), $PD_i(f)$ in the dissertation is

$$\boldsymbol{PD_i(f)|_{f_i} = \frac{P_i(f_i)}{P_{avr}(f)}} \qquad (6.11)$$

where $P_i\_peak\ (f)$ is the peak power of each spectrum, and P_{avr} is the average of ten power spectra. Figure 6.3 illustrates the position of $P_i(f)$ and $P_{avr}\ (f)$. In our case, central frequency, f is 50 kHz. When f is at maximum power of $\boldsymbol{P_{avr}}$, the power spectrum dissimilarity is

$$\boldsymbol{PD_i(f_{avr})|_{f_{peak}} = \frac{P_i|_{f_{peak\_i}}}{P_{avr}|_{f_{avr}}} = PD_i} \qquad (6.12)$$

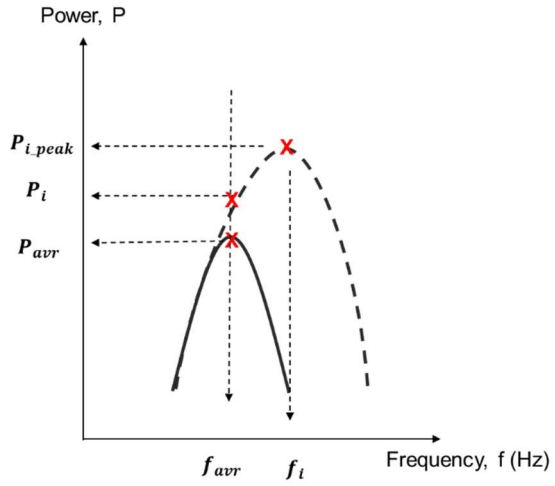

Figure 6.3 Illustration of analysis in power spectrum.

In our FE and experimental data, ten of $PD_i(f)$ values are used to calculate a variance. The variance is obtained by

$$\boldsymbol{P_{va} = \sqrt{\frac{1}{N}\sum_{i=1}^{N}(PD_i - < PD >)^2}} \qquad (6.13)$$

where PD_{avr} is an average of power spectrum dissimilarity, N is number of samples, and P_{va} is the variance of power spectrum dissimilarity values.

6.1.3 Statistical Analysis

Statistical analysis is important to establish the effective sensitivities of test data to different material parameters, such as the level of damage. A statistical analysis is based on reliable criteria that provide some level of confidence about relative test sensitivities. One such statistical analysis method, appropriate for several population groups, is Single-factor Analysis of Variance (ANOVA). This method

is used to compare more than two population sets. There are several methods to apply ANOVA. The work in this study uses a computed "P-value" to establish an acceptance decision concerning the null proposed hypothesis, based on some prescribed level of confidence (Elderton 1902).The null hypothesis tested by ANOVA is two group's population means for all conditions are the same. If the P-values are less than the pre-defined α (confidence level), then the null hypothesis is rejected, indicating a significant difference statistically among means by analyzing variance in certain confidence level. ANOVA P-value analyses were conducted to quantify the ability of data extracted from tests to distinguish among different levels of damage in concrete. Specifically, single-factor ANOVA was used to test for statistically significant differences between the mean values of specific data parameters, such as $\mathrm{EB}_i, \mathrm{EB}_{nor\_i}, VI_i, and\ V_{s\_i},$ associated with each damage level (10 estimates for each damage level). The ANOVA process is calculated with single-factor analysis tools in Excel that were compared and verified with the P-value from Minitab (Minitab Inc., State College, PA). A P-value < 0.05 for the $EB_i,$ estimate, when comparing between two damage levels, was considered to indicate a statistically significant difference with a 95% confidence level.

6.2 Numerical Analysis

Numerical simulation results are discussed in this section. A later section will explore the experimental results of synthetic and real cracking damage samples. Numerical analysis, or finite elements analysis (FEA or FE), results are discussed in this section. Such analysis is helpful for understanding the physical meaning of backscatter behaviors with clearly qualitative damage. There are two subsections in this part. First, a study of characterization among different levels of damage is presented. Then, effects of different testing setups are discussed. Second, a study of the moving scan position over damaged areas is demonstrated. All detail models are described in Chapter 4.

6.2.1 Distinguishing Levels of Damage

The exact amount of damage in the actual structure will be unknown, and damage levels will vary. Numerical analyses are needed to better understand the responses of backscatter data, which indicated different levels of damage. A parametric simulation enables us to control for the exact percentage of damage level. This elastic model also allows the project to focus on the problem of random backscatter behaviors without concern for other factors, such as inelastic behavior, or material inhomogeneity. The simulation results of the FE models revealed increased backscatter energy values with higher levels of

damage by volume. The FEA results prompt an interpretation of scatter responses of microcrack damage with large wavelength excitation. Microcrack damage levels in the FE model present a pattern of 0, 1, 2, 4, and 8 % damage by volume of the area (see the red box in Figure 4.5 from chapter 4). Ten different random damage patterns correlate to a 1% damage group. Other damage groups, 2, 4, and 8%, also correlate individually to ten random damage patterns that are different.

Figure 6.4 shows the results of a coherent forward propagating wave velocity. The wave velocity is computed from the first positive peak of the forward propagated signal. The wave speed was observed to decrease with increasing damage. However, the speed does not monotonically decrease. The wave speeds at 0% and 1% were not significantly different statistically. Two groups, between 1% and 2%, and between 4% and 8%, were significantly different statistically ($P < 0.05$), as indicated in Figure 6.4 (top right).

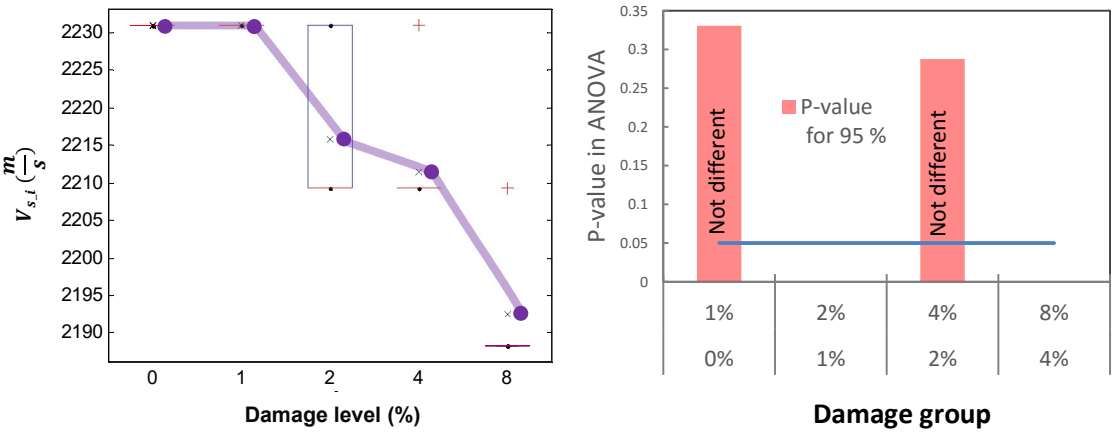

Figure 6.4 Forward-propagating surface waves with different levels of simulated damage: (left) surface wave phase velocity V_{s_i}, and (right) integrated forward-propagating surface wave velocities, V_{s_i} ; box plot illustrates data variation for ten signal sets. (FE simulated data).

Eqn. (6.9) was used to compute the integrated signal energy VI_i of the forward propagating time signals from the forward sensor. Values fluctuated relative to damage level. The VI_i decreased with damage up to 4% and then increased with further damage, as shown in Figure 6.5 (top left). Statistically significant differences were observed from only 0%- 1%, 1%-2%, and 2%-4%. These groups between 4%-8%, 2%-8%, and 1%-8%, were not statistically different (see Figure 6.5, right). The results of the first peak and the second peak demonstrate almost opposite trends (see Figure 6.5, bottom). The peak amplitude does not show consistent trends between the first peak and second peak values (not shown here). Direct peak points, or a coherent energy approach, cannot be a standard damage index due to an uncertainty related

to random scatter. Some groups of wave velocity and integrated values do not show significant differences. Table 6.1 summarizes the statistical results.

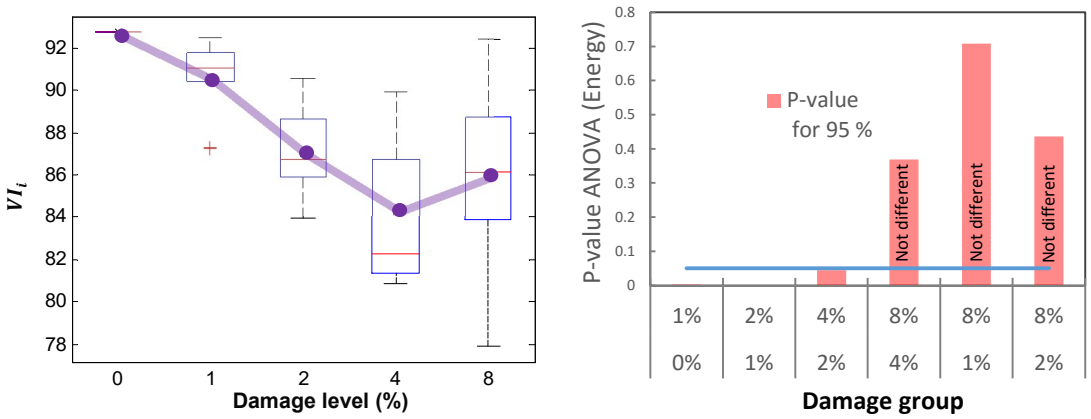

Figure 6.5 Forward-propagating surface wave energy content with different levels of simulated damage: (left) integrated signal energy, VI_i, (right) ANOVA results of data.

Table 6.1 ANOVA results for forward propagating wave properties at different levels of damage.

Damage volume	P-value			
	Wave speed		Energy	
0% - 1%	0.3306	not different	0.0020	
1% - 2%	0.0002		0.0006	
2% - 4%	0.2878	not different	0.0448	
4% - 8%	0.0000		0.3690	not different

A backscatter energy approach is studied first using simulated numerical results. Figure 6.6 shows the ten overlaid time signals each for two different damage levels assuming noncontact sensors are employed. The output and input of contactless receivers represent the pressure of the leaky acoustic wave in air. Signals were also simulated assuming contact receivers (results not shown here), where both contact and contactless data show similar waveforms, except for scale. The 0% damage case (solid, no damage) shows 10 identical waveforms stacked on top of each other at all times, indicated by red lines in Figure 6.6. However damage material (8% damage case) show more varied waveforms, especially at later times in the signal, which is presumably caused by random backscatter from the damage points.

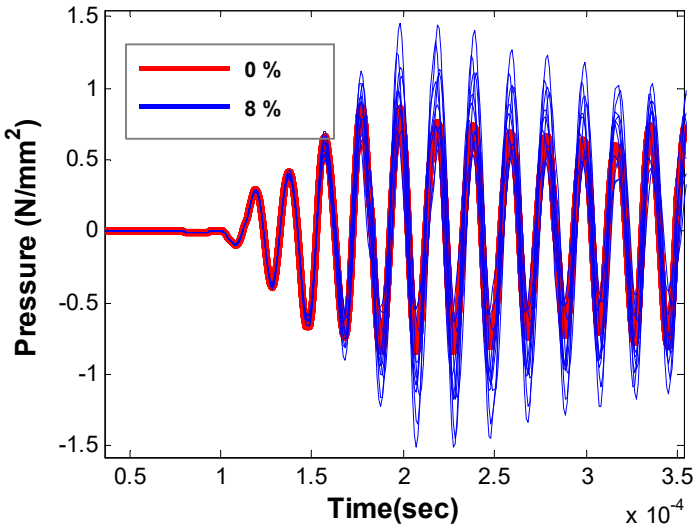

Figure 6.6 Simulated contactless surface wave time signals with different levels of simulated damaged. (FE simulated data).

Figure 6.7 shows the FE simulation results carried out by Energy Subtraction Analysis (ESA). The figure (left) represents 10 different extracted backscatter signals, B_i of five different damage levels processed from Eqn. (6.6) in the Methods section. The signals were collected from the 90 mm listing position to measure acoustic pressure, referred to as MEMS 1 in Figure 4.5. Figure 6.7 (right) shows box plots of backscatter energy, EB_i computed by Eqn. (6.7). Each data point represents the averages (in the orange color) from ten random signals from different damage levels. The highest damage level (high void volume fraction) resulted in the largest EB_i, while the 0% model had close to zero energy due to the absence of backscatter in the model. Statistically significant differences were observed among all groups when comparing the average of EB_i. The EB_i values estimated from the backscatter were quantified through FEA simulations. The simulation results indicate increased EB_i values with higher levels of damage by volume clearly and monotonically.

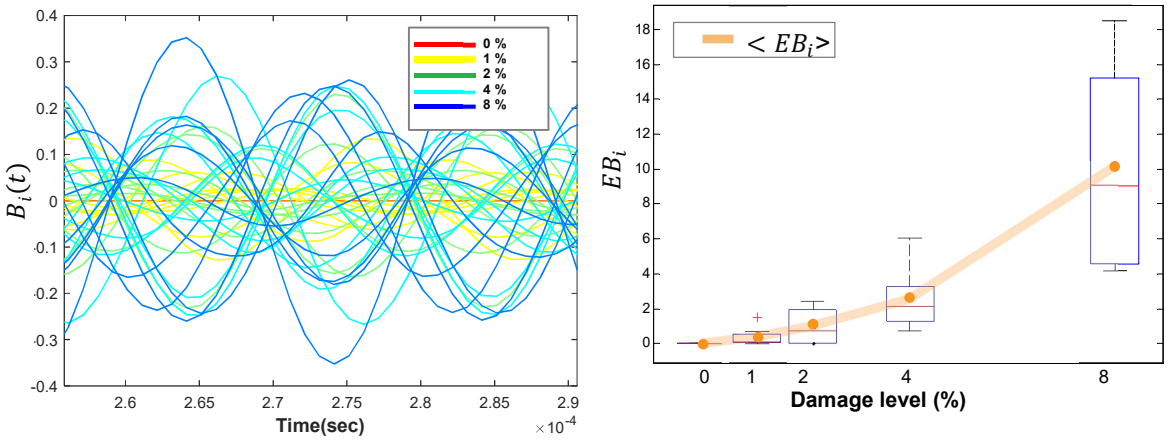

Figure 6.7 Properties of backscatter energy with different levels of simulated damage: (left) extracted backscatter time signals $B_i(t)$, and (right) box plots of the backscatter energy EB with averaged value shown in orange (FE simulated data).

Table 6.2 shows P-values of a Single-factor ANOVA. When the P-value is less than 0.05, these groups are significantly different at the 95% confidence level. All cases present P-values less than 0.05, although the differences in damage are minor. These results indicate that the backscatter approach distinguishes small changes in reflector content.

Table 6.2 Single-factor ANONA results of FEA models simulating different damage extents.

Groups		P-value for 95 %
0%	1%	0.0198
1%	2%	0.0367
2%	4%	0.0478
4%	8%	0.0014

Figure 6.8 shows FE results, proceeded by Spectral Variance Analysis (SVA), as described in a previous section: (left) exhibits the spectrum plots of the backscatter signal with different damage levels, and (right) shows power dissimilarity $PD_i(f)$ with power spectrum variance P_{av}. Other results of EVA are shown in the figure (bottom left and bottom right). These ten blue lines (8%, the highest void fraction as a highest damage level) in the figure (left) indicate more variation at 50 kHz compared to other lower damage levels. Figure 6.8 (right) shows the boxplots of the distributed $PD_i(f)$ values. Increased variation means that all boxplot results becomes varied with increased damage levels due to wave backscatter.

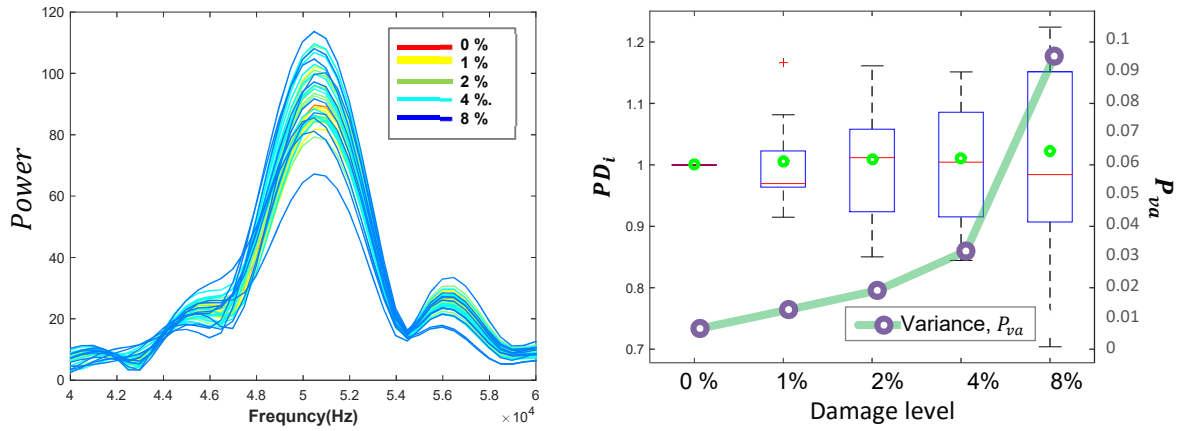

Figure 6.8 Properties of spectral variances with different levels of simulated damage: (left) power spectrum, and (right) power spectrum dissimilarity $PD_i(f)$ with power spectrum variance P_{vai} (FE simulated data).

The overall results from ESA and SVA indicate that the backscatter dataset increased according to the level of damage. Backscatter energy by ESA and variance by SVA increased approximately 4 times with an increase of a doubled amount of damage level. The results of ESA and SVA show an exponential increase by linear damage due to the energy calculation. The reason for these trends is because the ESA used a voltage square unit, and SVA has a power spectrum.

The results from the process of EB_i related to forward instead of backward signals, which demonstrates the importance of the backscatter setup. As shown in Figure 6.9 (left), the trend does not remain consistent. The averages of backscatter energy $<EB_i>$ (from Figure 6.8, top right results) are compared with the forward backscatter energy in Figure 6.9 (right). The figure shows forward energy processed by the energy extraction method Eqn. (6.7). The energy does not monotonically increase, and 8% values are smaller than 4%. Comparatively, changes in energy with different levels of damage are small and less sensitive than backward energy processed by the same equation. Clearly, most energy comprises coherent energy, and the waves will be insensitive to damage from small voids. Forward input signals are relatively higher than backward input signals. So, although backscatter wave energy from both backward and forward directions produce similar energy, the forward backscatter energy is relatively small, and these waves merged into a large forward input signal. Given this result, both the algorithm and testing configuration is very important when characterizing microcrack damage.

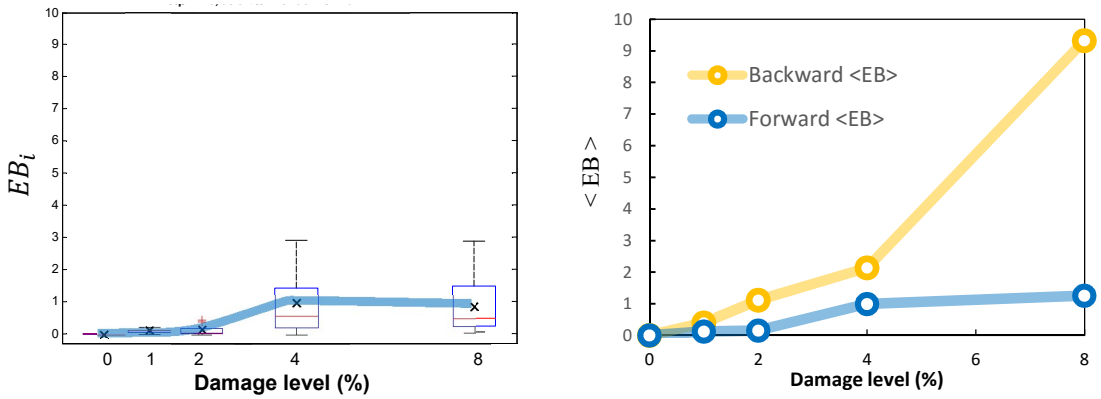

Figure 6.9 (left) Forward scatter energy EB_i computed from signals detected by the front sensor (sensor #8), and (right) comparison of $< EB_i >$ forward scattered and backscattered energies (FE simulated data).

FEA results of contact and contactless receivers were compared (results not shown here) to understand how the sensor array setup influences backscatter results. The results from three different sensor positions (10 mm gap) show similar trends. Therefore, it may be concluded that a 10 mm distance among sensor positions would not affect backscatter results. Further, this indicates that both methods are repeatable. The FEA results of contact and contactless receivers were compared. Both results also indicate an increase in backscatter energy or variance as well as an increase in damage. Therefore, the results hold for both contact and contactless receivers.

6.2.2 Effect of Test Configuration

In addition to exploring the extracted backscatter energy for different levels of damage, the author also explored the importance of the output pressure of the transducer and the sensitivities of receivers on the estimates of EB_i. The author investigated four different damage level models (0, 1, 2, 4, and 8%) and two cases with different pressures of ultrasonic excitation signals. The excitation pressure of these models (see Figure 6.10) is doubled, but they have the same 2% damage level and an 80° incident angle.

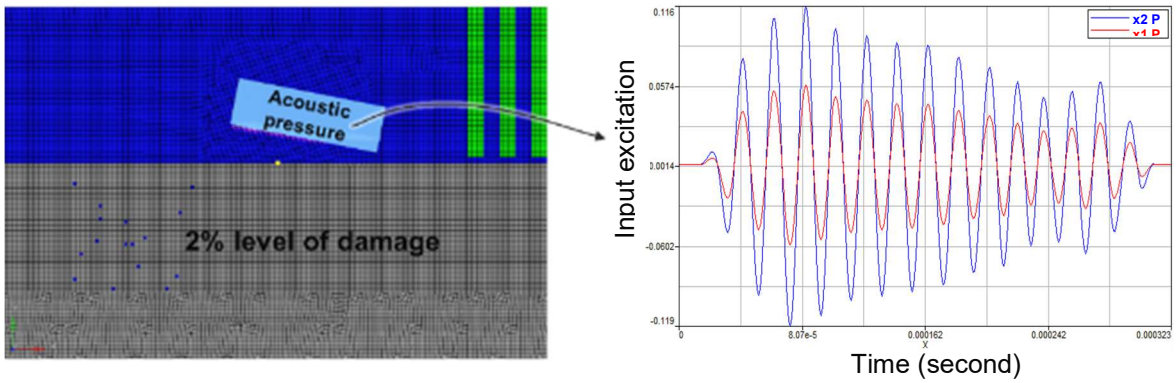

Figure 6.10 Description of FE model; (left) shows excitation configuration, and (right) shows a comparison of two different input pressures (FE simulated data).

The FE simulation results demonstrated that by increasing the pressure of the transmitter, the estimate of EB_i increased independently of the level of damage in the sample. Therefore, this observation prompted a revised approach for estimating EB_i from the scatter signals. Specifically, to make the estimate of the EB_i system and operator independent, the backscatter energy was first divided or normalized by the energy in the forward propagating wave. MEMS sensors with matched properties received both the forward and backscatter signals. In addition, the experimental test revealed that whole signal energy is affected by the location or target of excitation. The forward signals serve as a reference for indicating an initial energy level. Figure 6.11 demonstrates the plots of the EB_i estimate without the normalization step for two output pressures (left) and the normalized results (right). The results of the normalized EB_i represent two estimates that are almost equal. These results (Figure 6.11, right) indicate a normalized dataset computed by processed backscatter energies (shown in Figure 6.11, left) divided by the forward signal area. The forward energy is integrated from 0 to 200 μs. The time range of the backscatter energy computation is from 0 to 400 μs. The results of the normalized EB_i represent two estimates that are almost equal.

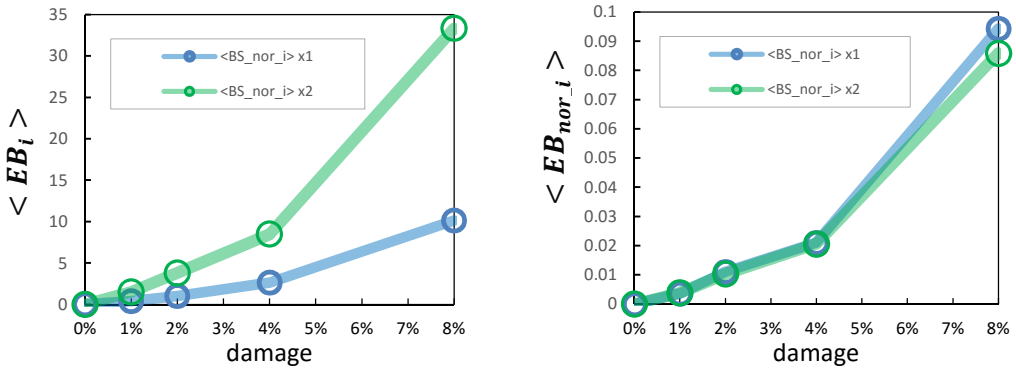

Figure 6.11 FE results owing to different pressure excitations: (left) average of backscatter energy from two different excitation pressures and (right) normalized backscatter energy $< EB_i >$ (FE simulated data).

In the next parametric study, different incident angles of transducers were considered from 78 to 82° in 1° increments. This study evaluates the effect of slight angle variations in scanning. The models have a 2% damage level, and the model details are described in section 4.2.2. The first peak amplitudes of the time signal for each different angle are shown in Figure 6.12. The results indicate the angle between 80° and 81° and demonstrate maximum excitation amplitude.

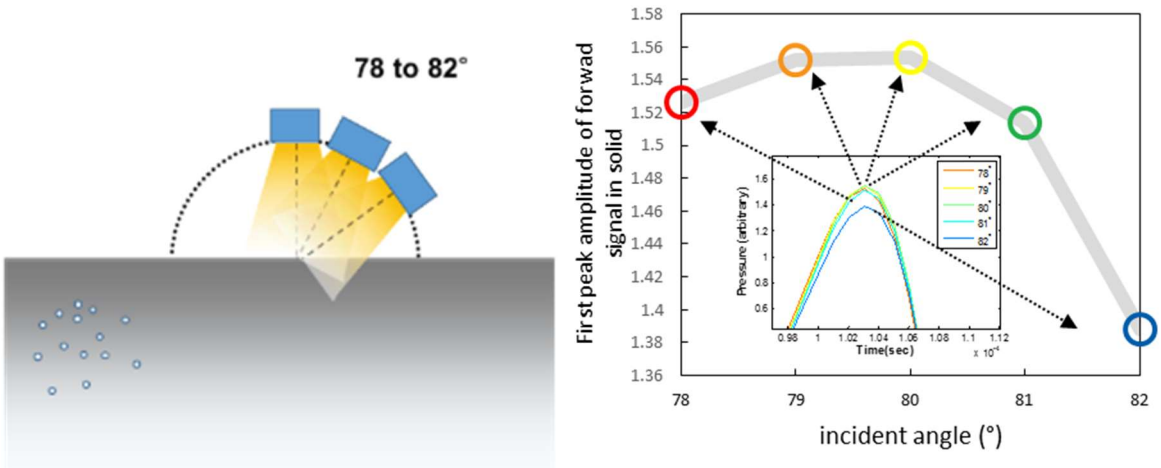

Figure 6.12 Effect of incident angle on wave generation: (left) model for varying angle configuration and (right) first positive peak amplitude of the raw time signals at each angle (FE simulated data).

Figure 6.13 shows the FE results of backscatter energy with varying angle. The steepest slope of damage versus backscatter energy is 80°, which is the critical angle. The forward wave at the critical angle

generates the most backscatter energy. A change of 78 to 82 degree shows a 4% difference in results. Considering a 10% change of backscatter energy with a 1% increase of level of damage, this 4% difference is not significant.

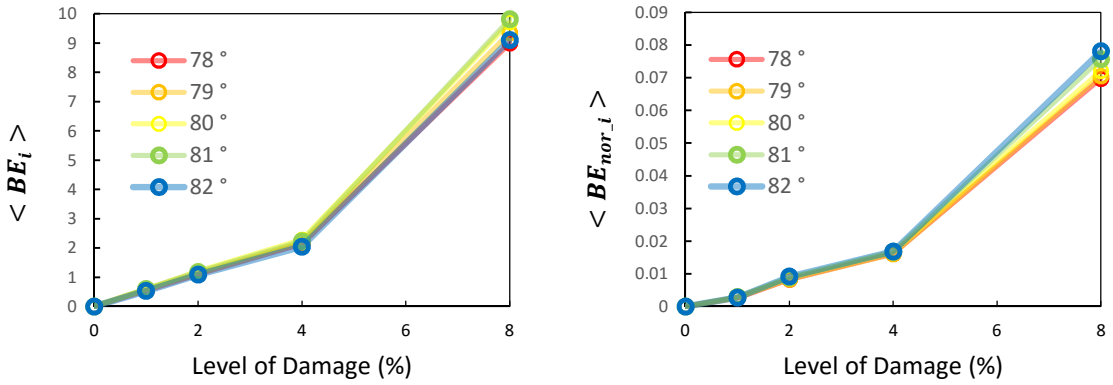

Figure 6.13 Backscatter results with varying angle: (right) backscatter energy, and (right) normalized backscatter results (FE simulated data).

6.2.3 Effect of Position of Damage

In the next set of simulations, the location of the scatter region was investigated using the FE model described in the previous section. The study described in this section examines the effects of the locations of distributed damage on backscatter responses in the concrete model. Figure 4.33 (in Chapter 4) shows the damaged regions from L1 to L9. L1 is the closest to the UT sender, and L9 is the furthest in the results. Figure 6.14 (left) shows the ten extracted backscatter time signals$B_i(t)$. Each region contains ten different damage patterns, thus creating ten different damage profiles for different regions. Clearly, the extracted signals $B_i(t)$ demonstrate almost zero amplitude at the L1 region. A 4% void volume in the 40 x 40 mm volume area represents the simulated damage. Figure 6.14 represents backscatter energy EB_i and averaged value $< \mathrm{EB}_i >$ in regions from L1 to L9. EB_i from L1 and L4 regions are close to zero. Damage at the L5 position shows the highest backscatter energy, which indicates that it is the most sensitive area with respect to the testing configuration. As the damage position moves from L5 to L9, received backscatter energy reduces rapidly. Because the forward propagating wave does not interact with regions L1 to L4, these regions contribute negligible backscatter energy. These results suggest that regions directly underneath and behind the sender (regions L1 to L4 with respect to the testing

configuration) do not contribute to the detected backscatter field. Further, damage positions beyond L7 decreased energy significantly. These overal results provide information of the effectivbe backscatter energy area in image of the localize dmage.

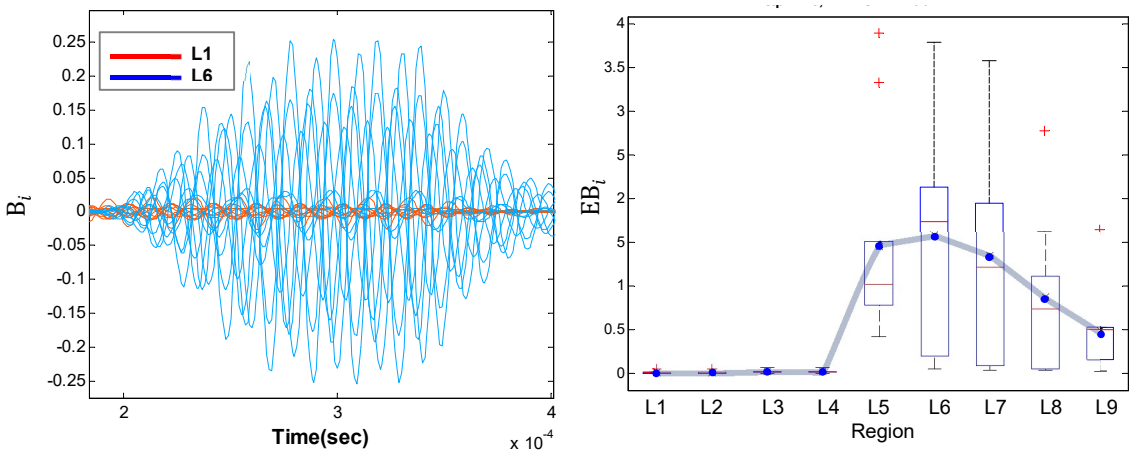

Figure 6.14 Effect of damage position on backscatter results: (left) extracted backscatter time data $B_i(t)$ at two damage positions and (right) average back scatter energy (FE simulated data).

Combinations of damage regions are studied next. Examining combinations of distributed crack models allows for the investigation of the extent to which damage areas affect backscatter energy. Figure 6.15 shows the combinations of four different combined regions, identified as regions A, B, C, and D. The damage regions are illustrated in Figure 4.7 in chapter 4. Region A is only the L5 region. Region B represents L5 and L6 together. Region C represents L5, L6, and L7 together. Region D represents L5, L6, L7, and L8 together. Figure 6.15 shows the FEA results of the combined damage. Region B, Region C, and Region D produce similar averages of backscatter energy $< EB_i >$ as seen in Figure 6.15 (left). Additional regions after L4 on the scan area alter results only slightly. Also, Figure 6.15 (right) shows that the variance values of Region C to Region D are very similar. L5 and L6 regions affect backscatter energy significantly.

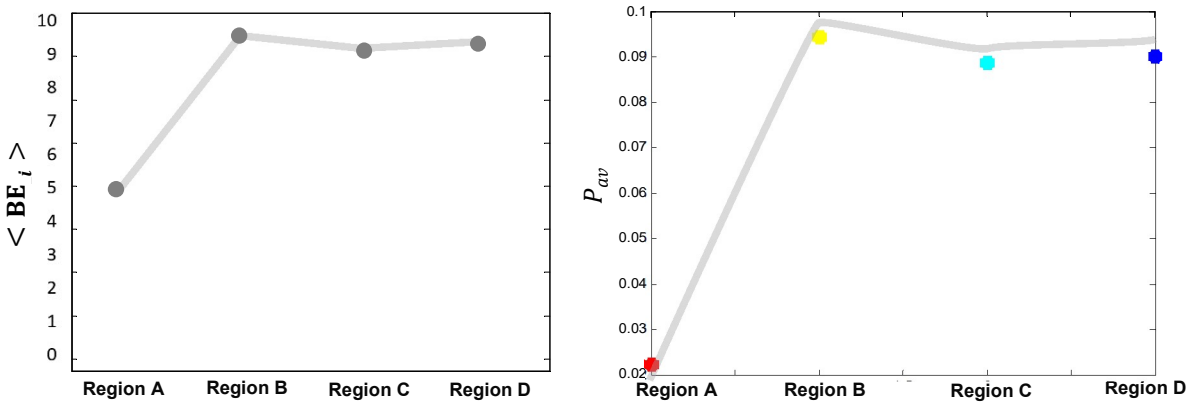

Figure 6.15 Effect of different combined damage areas on backscatter results: (left) backscatter energy EB_i, corresponding to four different combinations of damage regions and (right) P_{va}variance data for the same data set (FE simulated data).

Another purpose of the FE simulation is to recognize localized damage containing different damage level within scanning area. This is accomplished by comparing two cases of FEA models with different damage level combination. FE sending and receiving positions are the same (see section 4.2.1). Each case has ten different random damage patterns with damage level combinations. Figure 6.16 all patters at the 1% damage level. The "P1mix"represents nine patterns of 1% damage level and one 4% damage level at the 9th path. An outlier in the P1mix in the figure (left) indicates the 4% damage position. Further, EB_{nor_i} value also exhibits at each position in x axis. The 1% mix case indicates a higher EB_{nor_i} at 9th path, as shown in Figure 6.16 (right).

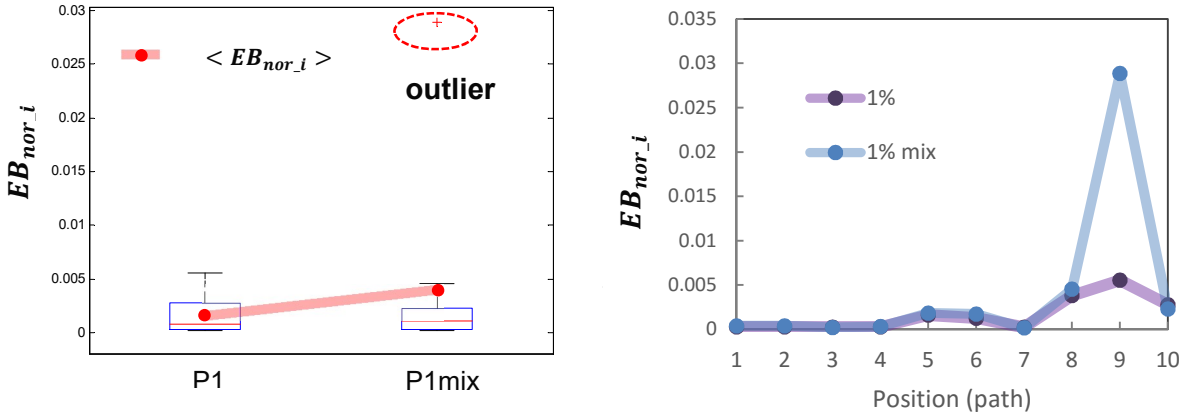

Figure 6.16 Comparison of normalized backscatter energy, EB_{nor_i} of two different groups: (left) boxplots of EB_{nor_i} comparisons of two different cases. Each box plot has 10 different random damage patterns (position). P1 has all position has 1% damage pattern. P1mix has 9 positions have 1% damage patterns and one position for 4 % damage pattern (Right) EB_{nor_i} represents for each positions. In the P1mix case, a 4 % damage pattern was placed in the 9th position.

In this section, the study explores more localized damage. Practically, one path can have more damage than others paths. There are three cases with combinations of different damage levels. Each case has ten different random damage patterns, regardless of level of damage (percentage). T4 has ten 1% damage regions. T5 has eight 1% damage regions, and two 4% damage regions representing the 9th and 10th paths. T6 has nine of 1% damage, and a 8 % damage at the 10th path (position). Figure 6.17 (left), indicating T4, shows the lowest average of EB_{nor} values, and T6 shows the highest values. T3 outliers indicate a 10% damage path (see the figure left). The average of the backscatter of T6 (one 8% local damage) provides more backscatter energy than T5 (two 4 % damage areas). Local EB_{nor_i} values for each path are shown in Figure 6.17 (right). The results indicate that the EB_{nor_i} values increase when the damage levels increase, corresponding to a specific path or position. Both cases, T5 and T6, show increases in EB_{nor_i} and P_{av} (not shown here).

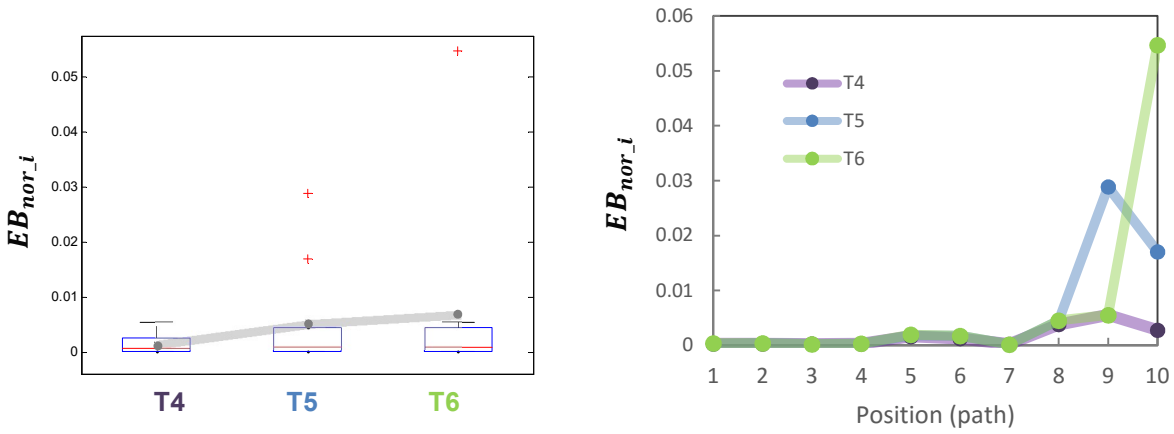

Figure 6.17 Comparison of the normalized backscatter energy EB_{nor_i} with various combination of different damage level: (left) box plots for three different cases: T4 has ten 1% damage zones, T5 has eight 1% damage and two 4 % damage zones, T6 has the nine of 1% damage and 8% damage zones; and (right) average of normalized backscatter energy for each path.

CHAPTER 7 STUDY OF SCATTER AND MICROCRACK CHARACTERIZATION: PART 2 EXPERIMENTAL RESULTS

This chapter continues to study the characterization of microcracking damage. It reports on the deployment of surface wave tests in the experimental phase using a fully contactless air-coupled configuration. It provides the potential for a practical and efficient method for in-service infrastructure elements. Finally, the chapter shows the physical basis for backscatter results, and it provides local images of backscatter. Such contributions represent advancements in the ultrasonic nondestructive testing and infrastructure health monitoring communities. Specific concrete mixture design information are discussed in the each section. All concrete has 2 cm maximum aggregate size.

7.1 Experimental Study: Application of Backscatter to Characterizing Well-Controlled Synthetic Distributed Cracking

This section studied the exact quantified scattered samples using polymer fiber fillers in an experimental phase. The distributed fibers are representative of a synthetic well-distributed cracking sample. Using the exact values of synthetic damage levels of the samples, several approaches are compared, including forward and backward analysis.

7.1.1 Specimen Description and Testing Set-Up

There are four different specimens: a PMMA (poly-methyl-methacrylate) plate (1500 x 1000 x 100 mm), and three different fiber (or filler) components (0, 0.3, and 0.6%) in concrete blocks (300 x 300 x 600 mm), as Figure 7.1 demonstrates. The PMMA specimen represents close to zero backscatter energy, while the 0% fiber concrete has a natural void and inhomogeneous material. This may reveal itself as a randomly distributed scatter even in non-damaged samples of a small amount. The plastic polymer represents synthetic micro cracks. All concrete samples had identical ages and curing conditions (older than 24 months). The mature concrete sample contained a water-to-cement ratio of 0.42 and a maximum aggregate size of 2 cm. The samples had identical constituents, except for the randomly distributed polymer fiber content (soft scatter): 0, 0.3 and 0.6% by volume. Here, compliant polymer fibers were used to simulate uniformly distributed cracking damage (air-filled micro-cracks and voids) in concrete in a controlled manner.

Other researchers mimic cracking damage in concrete using distributed internal polymer fibers (Aggelis & Shiotani 2009). The fibers simulate internal reflectors with strong scattering characteristics for ultrasonic multiple-scattering studies and can be apportioned in a controlled manner (Aggelis & Shiotani 2009). Both PMMA and undamaged or no filler concrete samples exhibited low scattering. The PMMA specimen represents a material that should provide essentially zero backscatter energy, resulting from a forward propagated wave pulse. The 0% fiber concrete naturally contains voids and mineral aggregate inhomogeneity across a range of length scales that serve as randomly distributed scatters even in non-damaged samples.

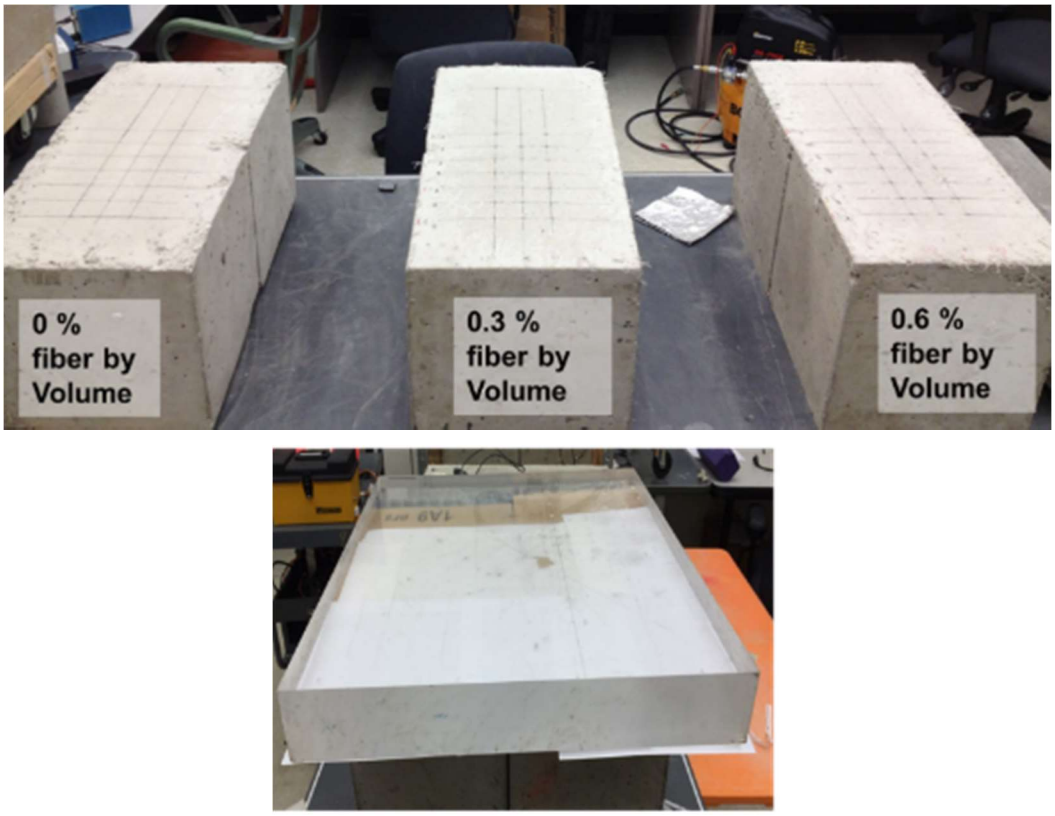

Figure 7.1 Test samples for well-controlled levels of synthetic damage: (top) large concrete beams with three different polymer fiber contents: 0, 0.3 and 0.6% by volume, and (bottom) PMMA specimen.

Fully contactless (with a MEMS) systems were used. Tests were carried out on these four different samples. 50 kHz, fully contactless ultrasonic surface waves were sent and detected along the top surface of each beam for ten different path lengths, up to a maximum length of 400 mm. Conventional UT approach and backscatter approach are compared.

7.1.2 Forward Coherent Wave: Velocity and Amplitude

All three specimens were scanned with the fully contactless UT system. Coherent surface wave velocities were measured at a 320 mm fixed distance along the transverse direction. By stacking multiple paths, a B-scan image was created, as shown in Figure 7.2. For each received surface wave, the arrival time and the signal amplitude of the surface wave pulses were measured. Arrival time was indicated by the first leading edge arrival of the pulse. Further, the pulse arrival time was automatically determined for each signal using a statistics-based criterion, which calculates reasonable threshold value based on the character of the noise region before the wave arrival within each time signal (King 2012). This computation was carried out using a Matlab routine designed by the investigators. The amplitude in this case was defined as the amplitude of the first positive peak in the pulse after the defined pulse arrival time, and this value was also determined automatically for each signal. The automatic signal arrival time and amplitude estimations were carried out using a Matlab software routine. Ultrasonic stacked time signals were collected from each concrete sample at different offset distances with the optimal sending configuration. A contactless MEMS sensor detected the signals.

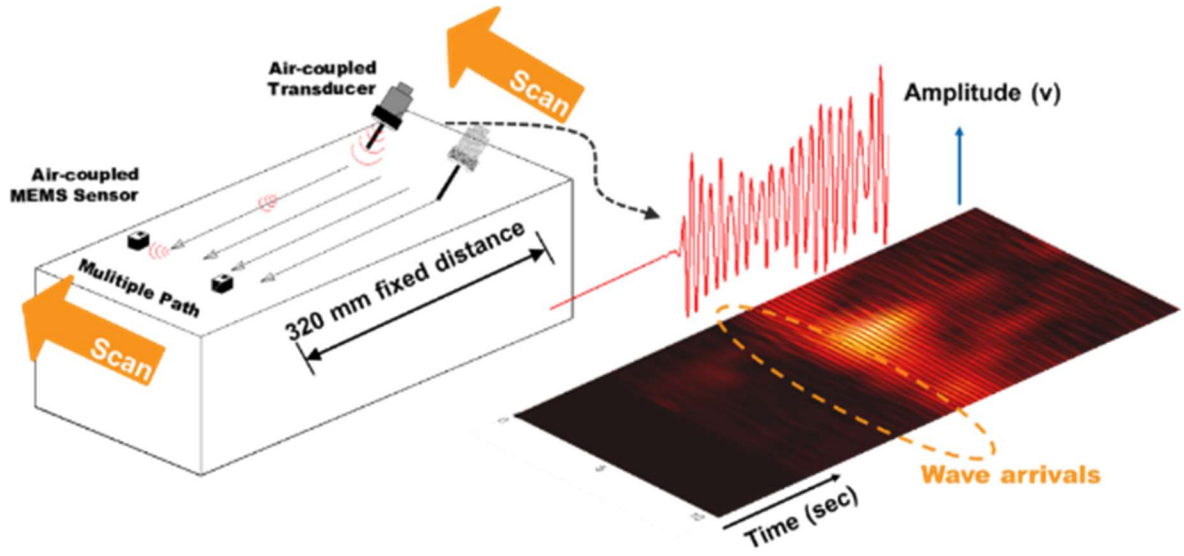

Figure 7.2 Ultrasonic scanning configuration: (left) direction and testing setup for transverse scanning and (right) stacked time signal image for 0 % concrete sample. Brighter colors indicate higher amplitude.

The tests revealed that the three beams exhibited similar averaged surface wave velocities of 2161 m/s as measured by the contactless sensors. Microcracks require more sensitive measurements and more precise analysis than do wide, individual cracks. An interpretation of B-scan images of the stacked signal

and statistical criterion of three different beams (0, 0.3 and 0.6% fiber content) for the fully contactless UT results are shown in Figure 7.3. Although reliable and high-quality surface wave velocities were obtained, it was still difficult to distinguish the three different synthetic cracking contents based solely on arrival time.

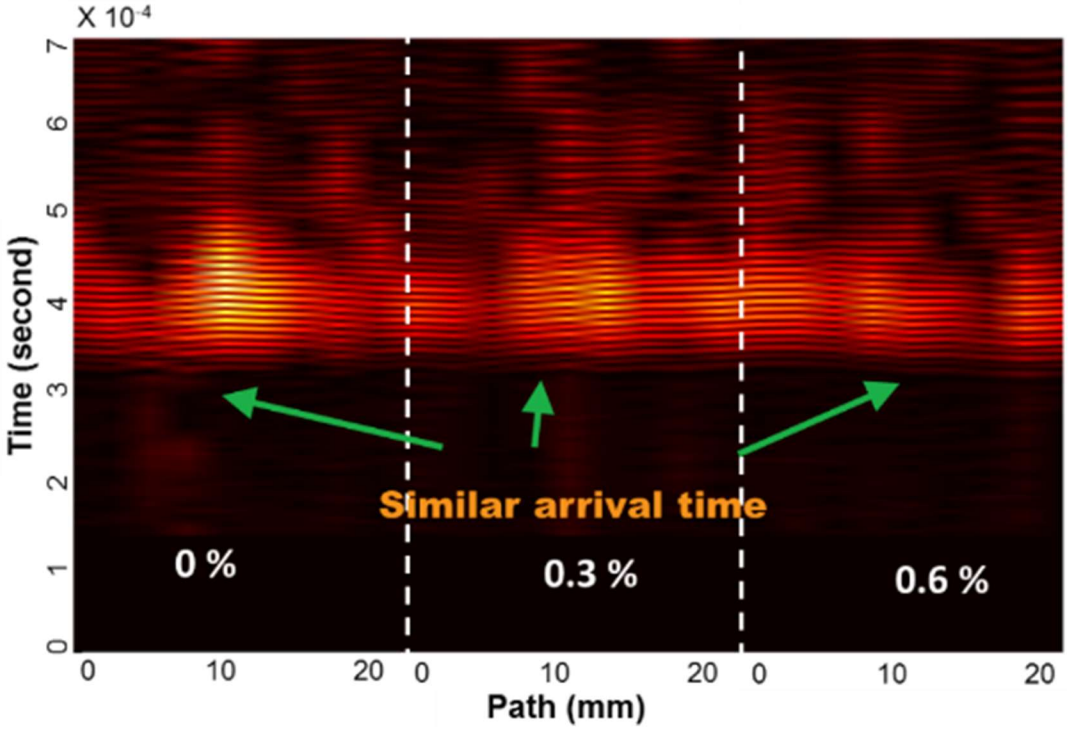

Figure 7.3 Stacked time signals across three fiber samples, where the wave font indicates arrival time of the surface waves.

Figure 7.4 shows the plots of scanned wave velocities: (top left) 0% filler, (top right) 0.3% filer, and (bottom) 0.6% filler. Each plot has ten different scanned lines. The scanned lines are composed of 13 different distances between sender and receiver starting from 0.08 to 0.2 m every 10 mm. These numerous data points generate solid fit curves for estimating surface waves. Each plot indicates a slope from the averages of ten different signals by linear regression.

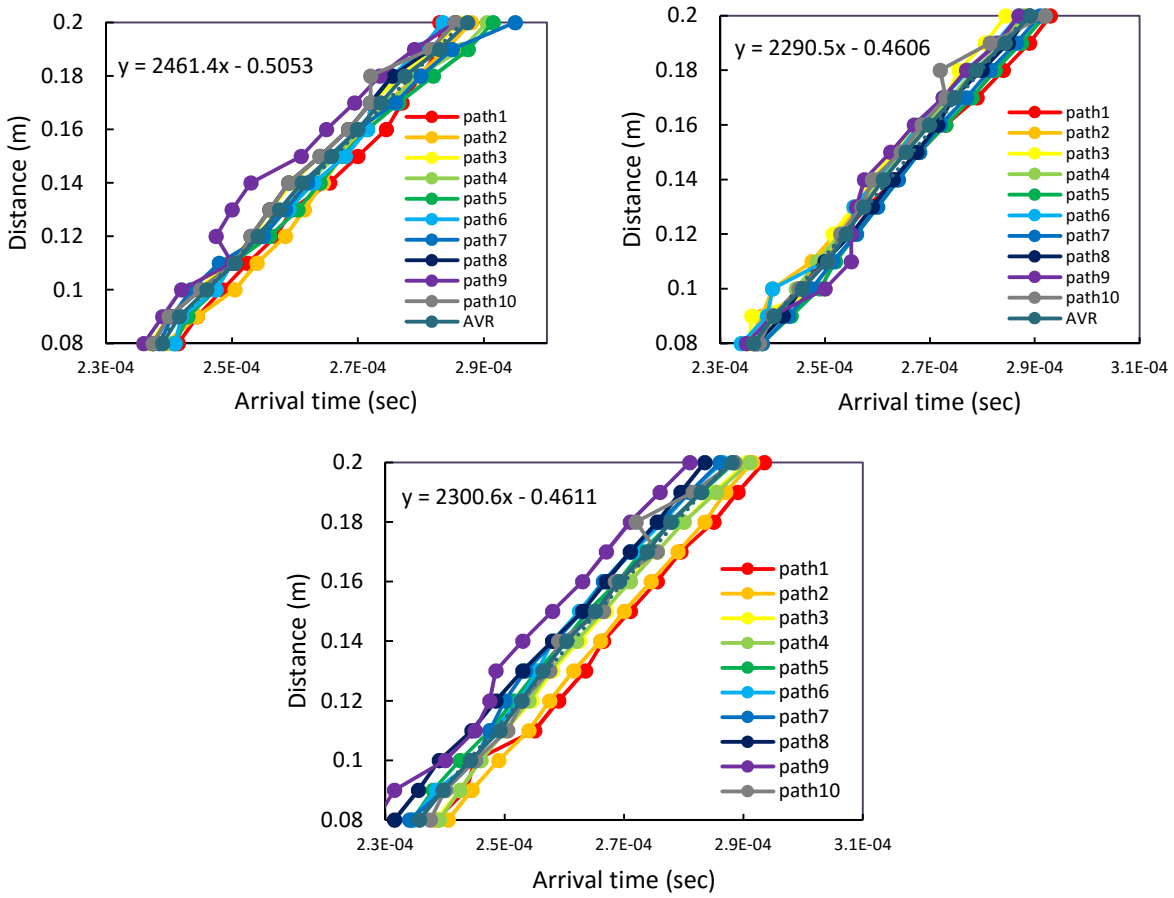

Figure 7.4 Experimental forward propagating arrival time results from samples with different fiber contents by volume: (top left) 0%, (top right) 0.3%, and (bottom) 0.6%.

Average wave velocities for the different fillers' volumes are shown in Figure 7.5. The bar indicates the maximum and minimum velocities for each group. Typically, the wave velocity decreases with more synthetic damage (fiber filler) owing to scatter. Damaged statues showed no clear distinction among these three samples. The trend does not correspond to a gradual or staggered decrease, as shown in Figure 7.5 (left). The average of 0.6% wave velocity is faster than velocity on the 0.3% sample due to large variations of the data. The surface wave velocity groups between 0.3 and 0.6% are also not statistically different as the P-value is 0.74. The other groups are significantly different statistically ($P < 0.05$).

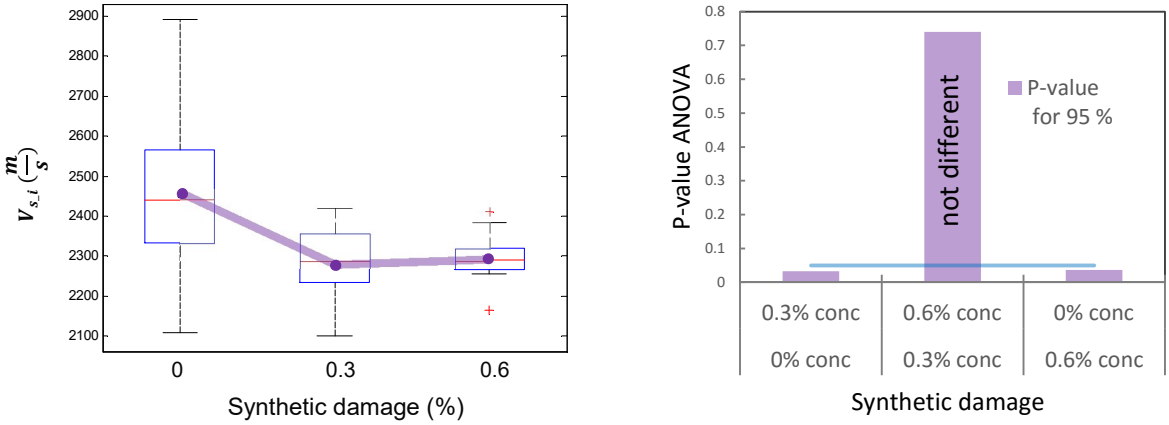

Figure 7.5 Analysis of experimental forward wave velocity data: (left) surface wave velocity along ten different paths, where average values indicated by the purple solid line, (right) ANOVA results with P- value.

Interference of the direct wave with multiple scattered waves results in a complex interference pattern that is apparent in the recorded time signals revealed over the whole time duration. It is noted that there is little distinction among the signals from the different samples at the first coherent portion of the signal pulse; thus, conventional group velocity or initial amplitude would not accurately distinguish among these different materials. Yet, the differences between the signals, as well as the effects of multiple scattering compounds themselves, become much more pronounced as the signal duration increases. Additionally, although contact sensor results were not reported in this chapter, tests showed that it was difficult to characterize between 0.3 and 0.6% polymer concrete due to the nature of the coupling problem with the use of a contact sensor. This air-coupled method has the potential to characterize microcracking in concrete distributed damage information. This is what makes this method unique and worth researching and implementing in the field.

Scanning was performed along the transverse direction and with variable distance (longitudinal direction) between sender and receiver. The shortest distance was 80 mm, and the longest was 350 mm (see Figure 7.6). Therefore, each path has a range of distances across which one can measure attenuation. To calculate coherent signal energy, the area of the square of a signal up to the third positive peak was used with a statistics-based criterion.

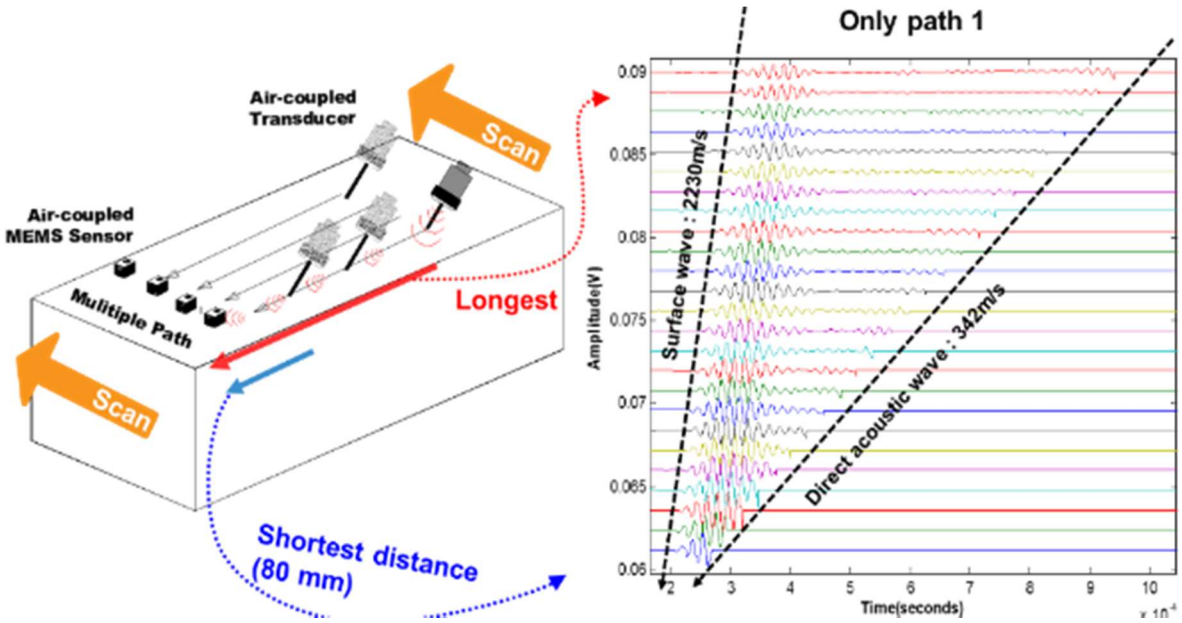

Figure 7.6 Variable distance scan: (left) testing configuration for the energy attenuation, and (right) waterfall plots along the first path, where multiple surface wave signals were collected with different distances between the sender and the receiver.

The signal energy results of a single path were used. Considering a specific distance, VI_i values do not show the expected trend with increasing fiber content (see three energy values indicated by the red "x" mark in Figure 7.7 left.). Testing at greater distances resulted in greater attenuation with normalized data. The VI_i by Eqn. (6.9) shows an increasing trend of attenuated signal with increasing fiber content (simulated cracking). These results show that amplitude attenuation (see Figure 7.7, top right) is much more sensitive to damage than velocity (see Figure 7.5, top left). It suggests that the ultrasonic wave energy attenuation is a superior approach for distinguishing microcracking levels in concrete. The primary source of ultrasonic attenuation in the damaged specimens was the large number of microcracks, whose interfaces scattered and attenuated the ultrasonic waves. The more concentrated damage zones affected the ultrasonic wave amplitude to a greater degree. Compared to individual aggregates in concrete; fibers, which simulate internal air-filled microcracks, act as relatively strong scatters and set up a "multiple scattering" situation. The different path lengths traveled by the multiple scattered waves (interacting with several reflectors between the path from sender to receiver) will result in arrival times from different scattered components of the original wave pulse that are different from the direct wave

arrival time or amplitude. However, the energy attenuation shows a limitation: the absolute energy or amplitude values are varied and do not correlate to different synthetic damage levels. In addition, the attenuation values are close to each other.

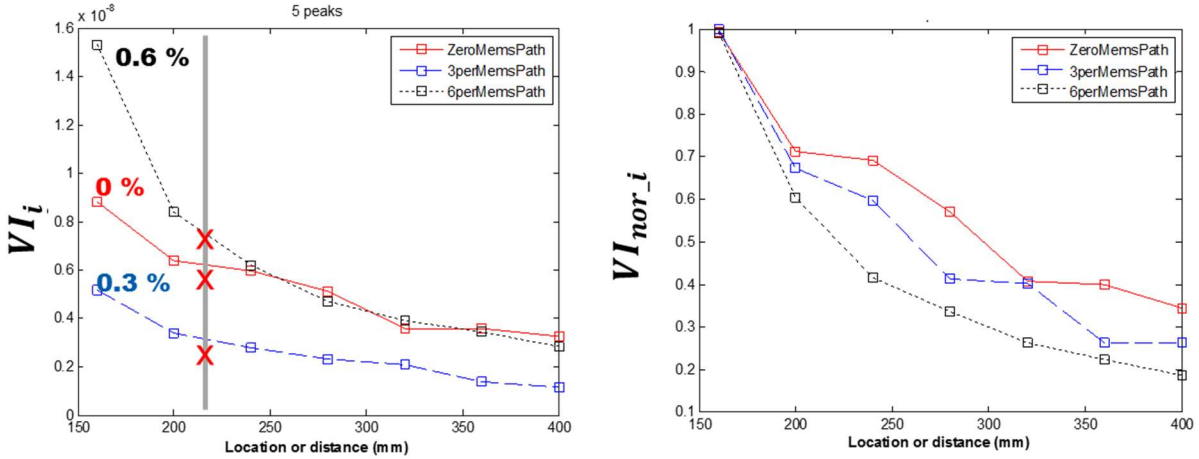

Figure 7.7 Experimental results of integrated signal energy VI_i for three different levels of synthetic cracking: (left) integrated signal energy value as a function of distance, (right) normalized VI_i computed with respect to maximum of VI_i at each damage state.

To determine more accurate calculations of energy attenuation, finer spacing between scanning points were used to collect the surface waves. The fine scanning protocol incorporates 22 different distances between the sender and the receiver that possibly help to observe clear attenuation behaviors. Figure 7.8 shows stacked coherent energy along multiple paths of normalized integrated signal value. VI_{mnor_i} were computed by dividing the VI_i by the maximum of the VI_i along each line or single path. VI_{mnor_i} uses a different algorithm from our new backscatter approach. The normalized integrated signal value, VI_{mnor_i} decreases by increase distances. This image shows the distinction among the three different levels of damage.

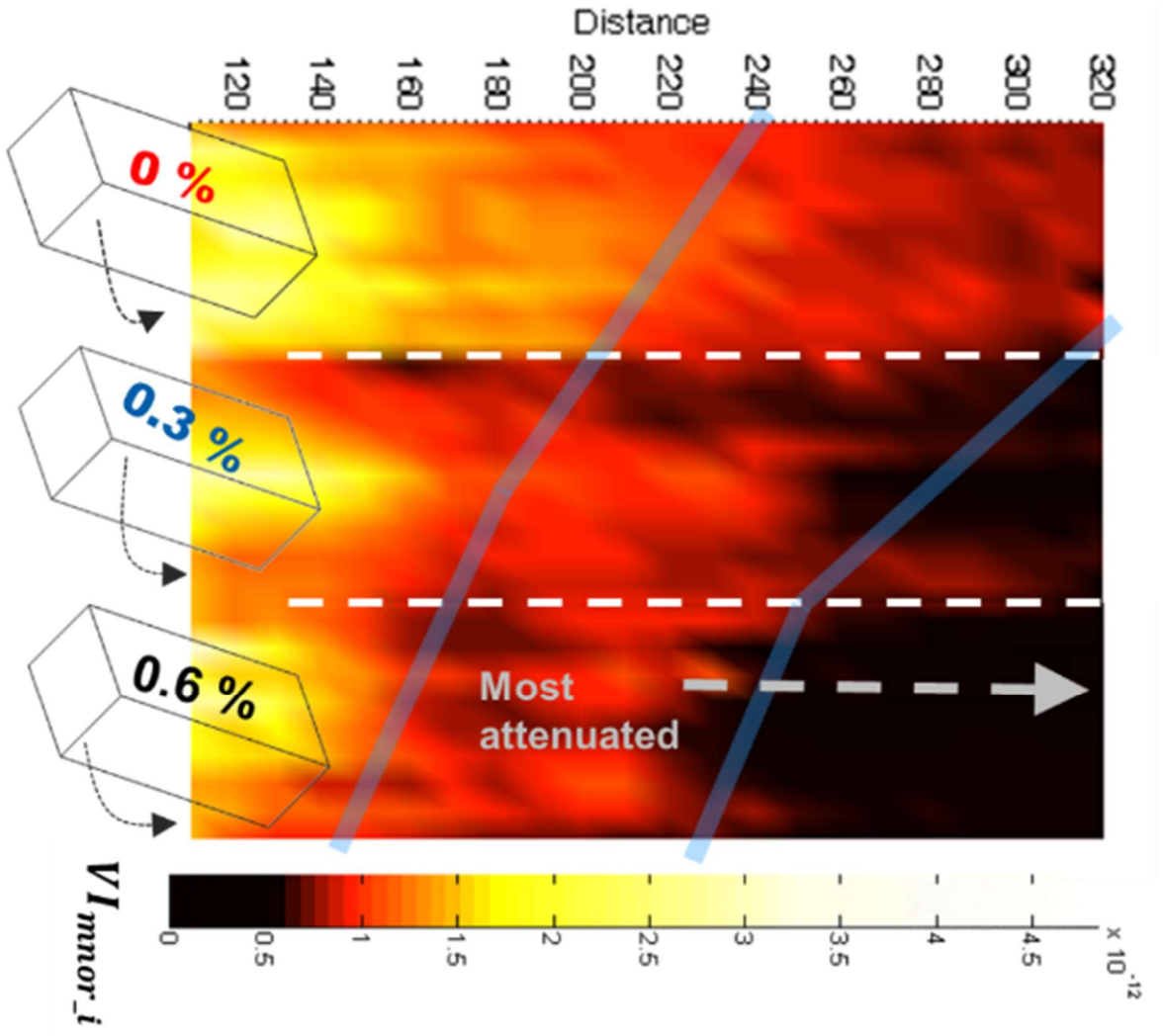

Figure 7.8 VI_{mnor_i} results stacked across multiple paths along surface of all three synthetic damage samples. The color map indicates normalized, integrated signal VI_{mnor_i} indicating black with minimum and bright color with maximum values.

To attain reliable values of the attenuation coefficient, the same ten individual scanned lines were used. Ten different lines are collected for these results. 50 kHz 16 cycles of ultrasonic input signals are excited from a contactless sender and contactless MEMS receivers are used to collect leaky surface waves. The slopes with a first positive peak of forward propagated signals compute wave energy. VI_i was calculated by the Eqn. (6.9) by integrating a forward time signal over time to a time at the third positive peak. Figure 7.9 (top row) shows the logarithm of the average integrated forward signals VI_i from three

samples. Typically, the integrated signal values decrease with more damage, and the decrease is due to large variations of the data. The VI_i from the forward sensor follows the trend relative to the damage level, as shown in Figure 7.9 (top right). Forward VI_i with statistically significant differences were observed from the forward scatter in only one group between 0 to 0.6 % (P-values are much smaller than 0.05). These large variations indicate low sensitivity and statistical similarity.

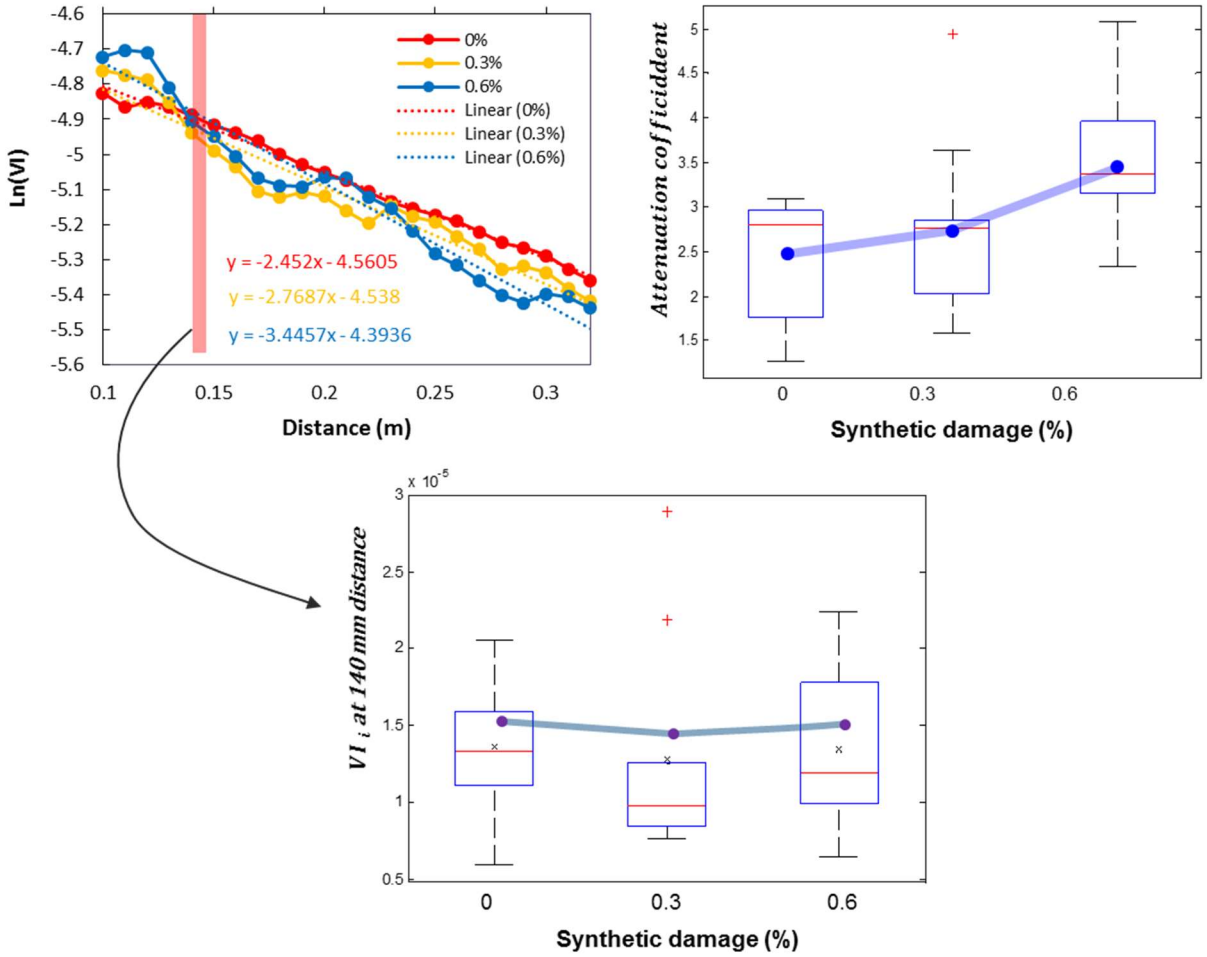

Figure 7.9 Analysis of experimental coherent wave energy data: (top left) typical signal decay curves showing best fit linear regression, (top right) boxplots for ten attenuation coefficients computed from the best fit line, and (bottom) boxplots for ten VI of with 140mm distance between sender and receiver.

7.1.3 Extracted Backscatter Results

Figure 7.10 (top left) shows sets of ten backward propagating time signals obtained from three different samples. Each sample is indicated by color, and each sample has 10 signals overlaid on the figure. These results indicate that the first peak of the raw time signal of 0.6% fiber concrete has higher amplitude than 0%. However, it is not easy to distinguish the microcracking damage levels from the raw signals alone. In addition, signals from Polymethyl methacrylate (PMMA) plate had the highest amplitude, although PMMA had almost zero scatter due to the close homogeneity of the material. The result is due to detected signals from the rear sensors composed of initial surface waves by beam spread and backscattered waves. Given these reasons, the backward signals from PMMA material had higher amplitude/energy than those of the 0% concrete sample, due to less energy absorption and/or attenuation of the coherent forward wave (see comparison of red with black solid line in Figure 7.10, top left).

The energy/amplitude of signals commonly increase, regardless of the amount of scatter, due to different material properties, such as different elastic modulus of concrete structure. Therefore, an extracted backscatter energy process is necessary. The refined signals, $B_i(t)$ from the ESA procedure were performed to refine the pure backscatter energy, EB_i. Therefore, Figure 7.10 (top right) shows how the process improved and extracted backscatter energies, EB_i. The values indicate different amplitudes of scatter behavior, regardless of different material properties. Given these results, the ESA is needed to establish EB_i. Figure 7.10 (bottom) shows normalized backscatter energies, EB_{nor_i} values. As expected, the trend line for the averaged EB_{nor_i} (see the orange solid line in the figure, bottom) is monotonically raised due to an increase of backscatter energy with a higher volume of scatter samples.

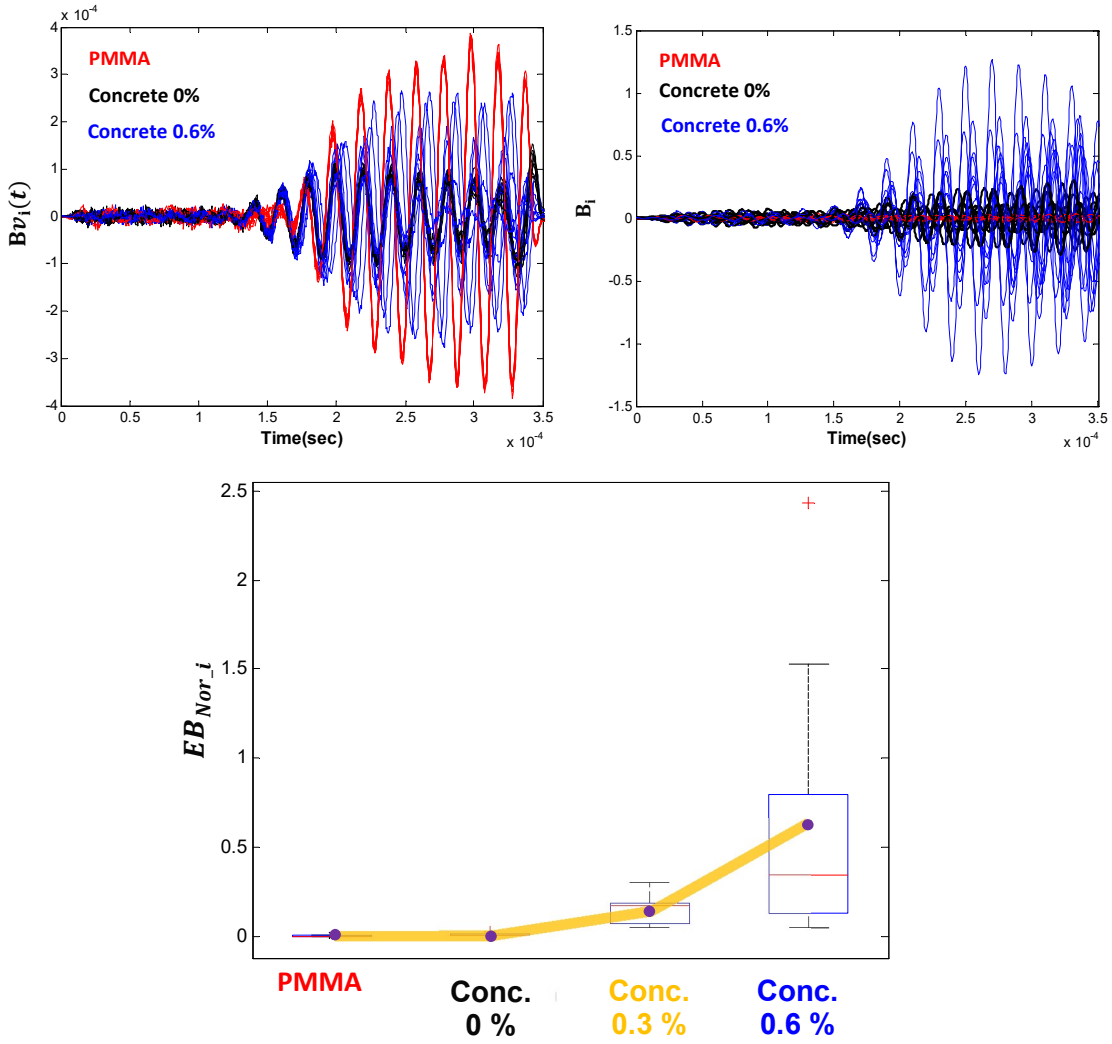

Figure 7.10 Effect of internal scatter content on backscatter: (top left) example backward propagating time signals from several materials, (top right) extracted backscatter signals $B_i(t)$, and (bottom) normalized backscatter energy for all materials.

A spectral variance analysis (SVA) approach was performed with the same experimental samples. Figure 7.11 (top left) shows 30 different power spectrum plots, presenting the central frequency around 50 kHz. Power spectrums indicate the largest variations in 0.6 % filler concrete sample. The power spectrum with the PMMA results show high power spectrums obtained from the sensors; the ten spectrums of PMMA are identical. Figure 7.11 (top left) shows extracted power spectrum dataset, PD_i computed by Eqn. (6.10). The results show clearly characterized scatter behaviors, indicating that PMMA power

spectrum values, $\mathrm{PD_i}(f_{avr})|_{f_{peak}}$, are close to zero. The variance P_{av} increases monotonically as damage increases. The trends are close to normalized backscatter energy. Regardless of the material properties of the different types, these two methods indicate more clearly defined scattering estimates.

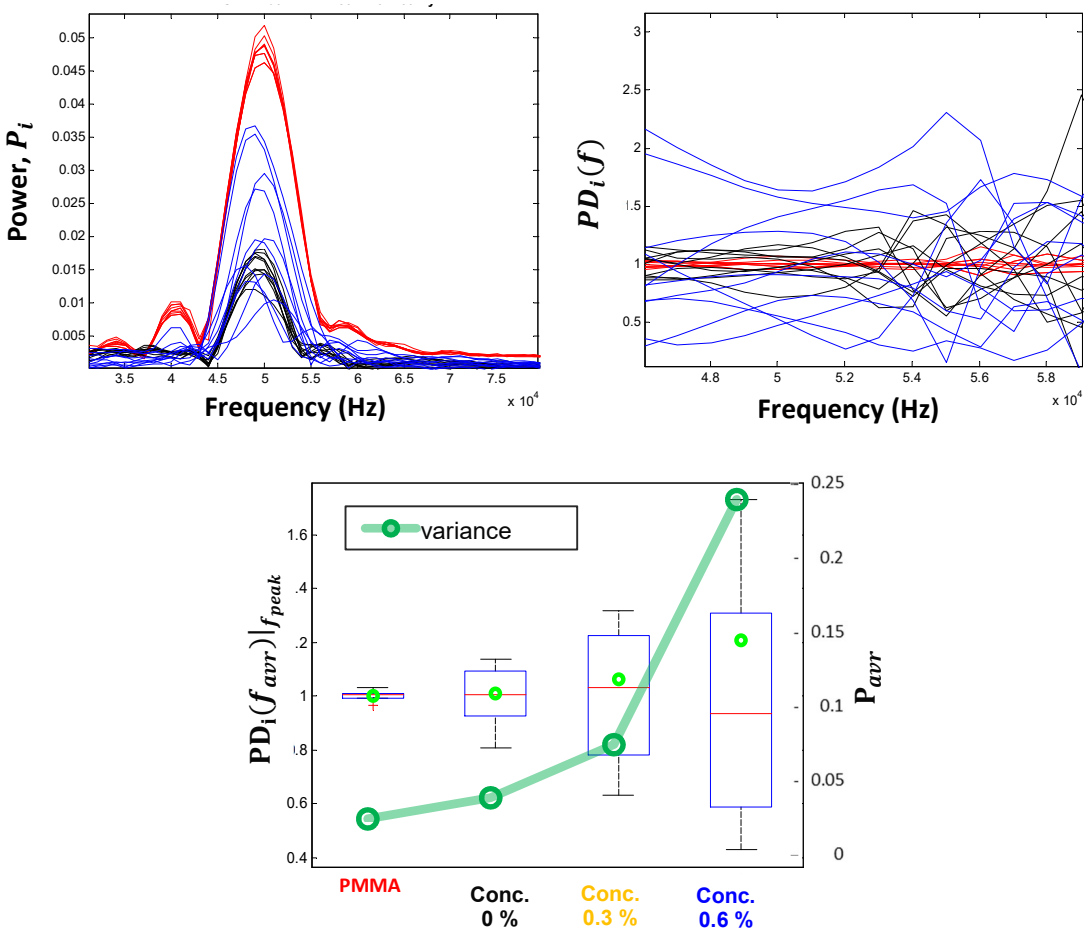

Figure 7.11 Effect of internal scatters content on backscatter in power spectrum: (top left) example backward propagating power spectra, (top right) extracted power dissimilarity $PD_i(f)$, and (bottom) power dissimilarity with peak frequency $PD_i(f_{avr})|_{f_{peak}}$. The green line indicates the variance of PD_i.

`

The normalized backscatter energy, EB_{Nor_i} was calculated using Eqn. (6.8) (see Figure 7.12, top left). The length of the boxes represents ten different backscattering energies distributed. In general, the length of the boxes of the EB_{Nor_i} data represent shorter than the box length of normalized backscatter energy, $\mathrm{EB_i}$. The reason for this is because it reduces unexpected inconsistent signal energy, such as electronic noise and the uncertainty of signals due to variable target location of ultrasonic. Figure 7.12 (middle

rows) show P-values with ANOVA analysis of EB_i (middle left) and EB_{Nor_i} (middle right). All groups are significantly different, as shown P-values are smaller 0.05. P-values of EB_{Nor_i} are generally lower than EB_i due to reasons similar to those described earlier. The averages of EB_{Nor_i} show a similar trend to the variance data, as shown in Figure 7.12 (bottom), while 0.6 % normalized backscatter energy are slightly different from spectrum variances. Since it is calculated by dividing the backscatter energy EB_i by the forward coherent energy VI_i (from Eqn. 6.8), EB_i is unitless. Therefore, these two methods can characterize scattering components regardless of material properties, and this normalized approach gives a general damage index.

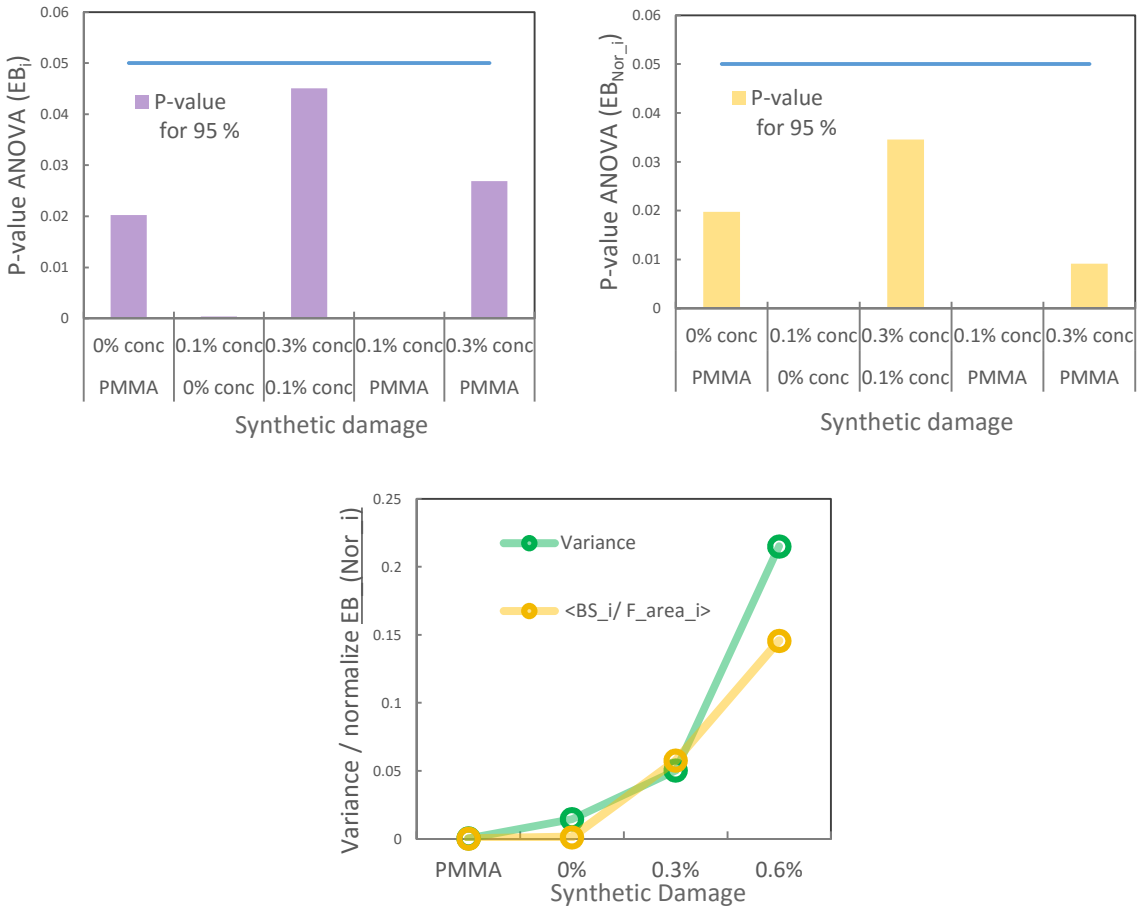

Figure 7.12 Backscatter results from experiments: (top left) average of backscatter data, (top right) average of normalized backscatter data, and (bottom) comparison of normalized backscatter and variance datasets.

7.2 Experimental Study: Application of Backscatter to Characterize Actual Distributed Cracking

This section is a study of the characterization of a global area. A single numeric figure was determined based on scanning the entire area. Ultrasonic datasets indicate the damage level by thermal shock cycles. Repeatability tests were conducted. Backscatter energy by ESA and variance datasets by SVA are presented with regard to different levels of damage and different thermal shock cycles. These results are then compared with standard resonance vibration and other conventional ultrasonic test results.

7.2.1 Specimen Description and Testing Configuration

Three different sized concrete blocks of the same age were used with a fully contactless ultrasonic system: contactless MEMS receivers and contactless capacitance senders. Tests were carried out on three concrete beam samples, as shown in Figure 7.13: small block (100 x 355 x 100 mm), referred to as B, large block (160 x 160 x 510 mm) referred to as C, and slab (360 x 480 x 140 mm), referred to as D. All concrete samples were of identical age and curing conditions older than 60 days with a water to cement ratio of 0.38 and a maximum aggregate size of 2 cm. 50 kHz and 60 kHz, fully contactless ultrasonic surface waves were sent and detected along the top surface of each beam for ten different path lengths.

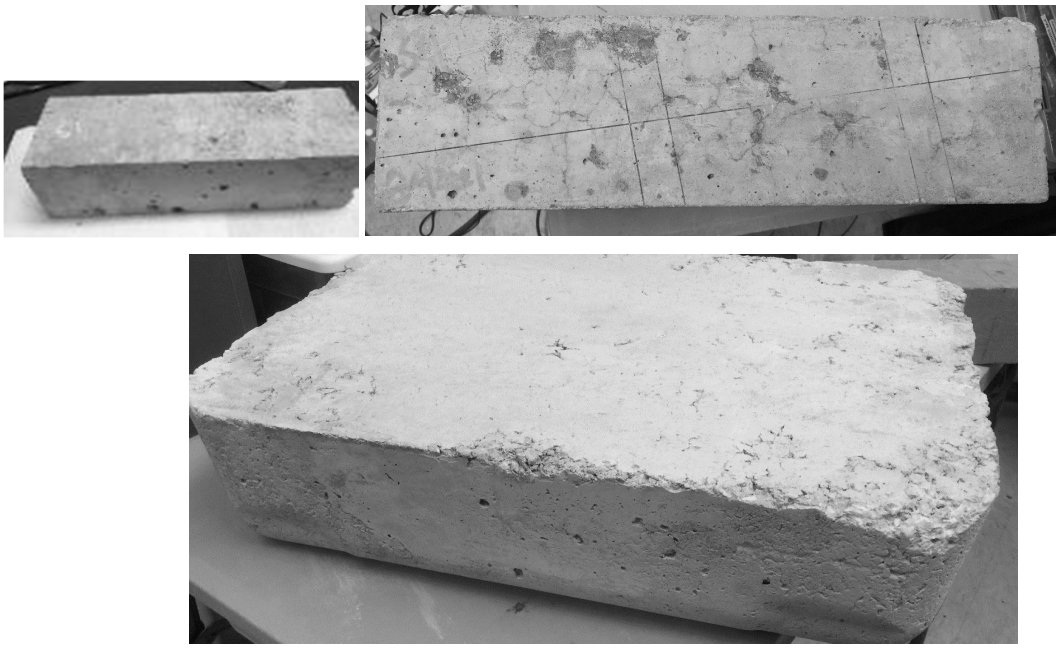

Figure 7.13 Thermally cycled concrete test specimens: (top left) small prism for resonance test, (top right) medium sized concrete prism, and (bottom) slab sample.

Thermal cycling shock tests were performed to generate real distributed internal cracking damage in the concrete. There are three different test steps to thermal shock tests. In Task 1, concrete samples were kept curing in 68 °C water temperature for 12 hours then instantaneously submerged into ice water for a duration of 1 hour. Task 2 is a similar procedure, but the sample was cured in 80 °C water and submerged into ice water for a duration of 1 hour. In Task 3, these concrete samples were oven-dried at 130 ºC for 4 hours and then submerged into water at 23 ºC (see Figure 7.14 (bottom row)). Tasks 1, 2, and 3 were performed sequentially. For each cycle, the author carried out ultrasonic tests after 1 hour of taking samples. Figure 7.14 (top row) represents photos of Tasks 1 and 2.

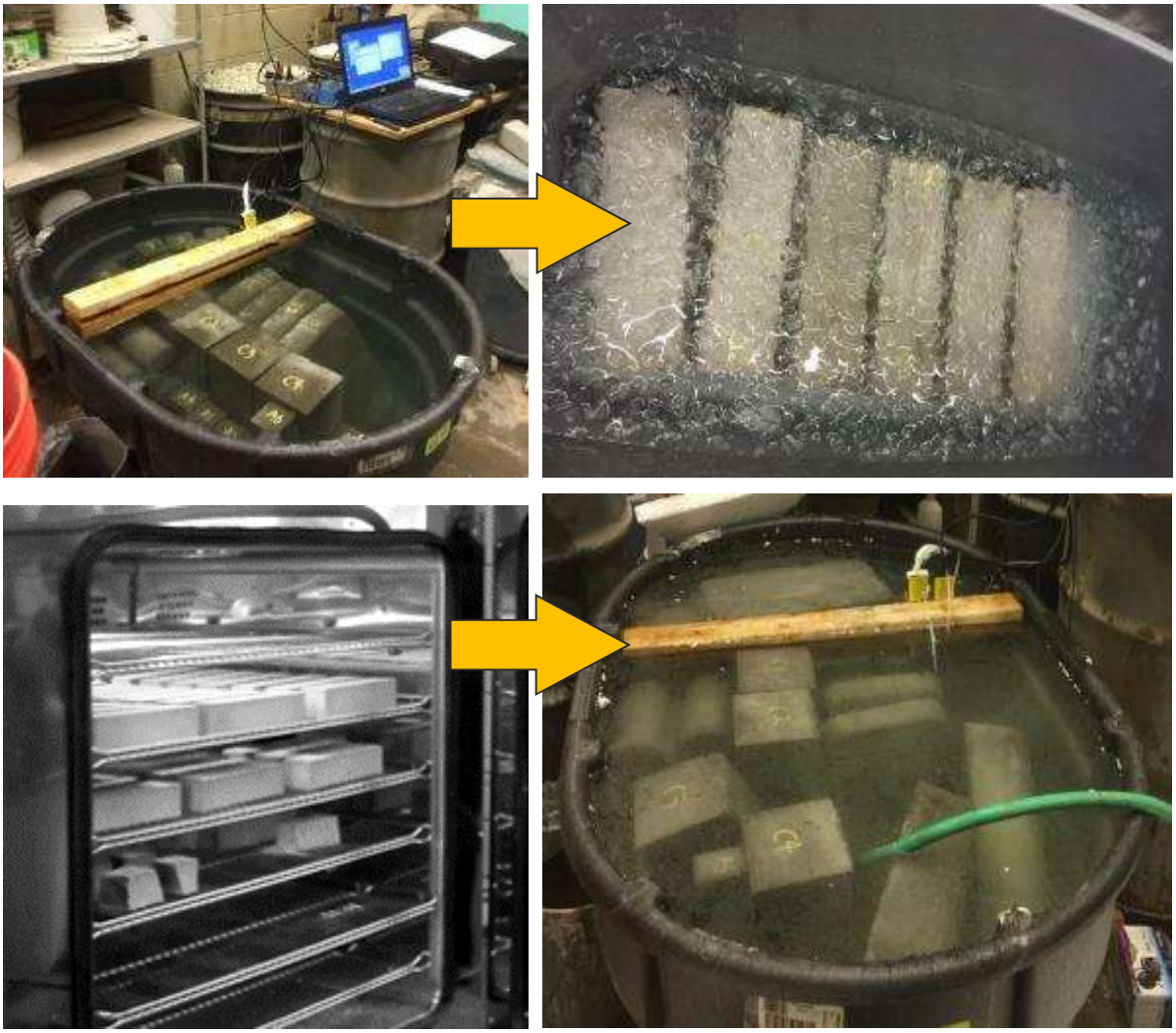

Figure 7.14 Illustration of thermal cycling shock tests: (top row) hot-cold wet exposures for Tasks 1 and 2, and (bottom row) wet-dry exposures for Task 3.

7.2.2 Visual Images of Test Samples

Photos were taken when the thermal shock test reached 20 cycles. During thermal shock cycling, the author found a concentrated water-zone pattern on the specimen 30 minutes after taking them out of the water (see Figure 7.15, top left). However, after 5 minutes the pattern disappeared. Water was being contained in the pattern area, but after 5 minutes the cracks were not visible. Perhaps this could be explained by the fact that there are sub micro-cracks, large sub-cracks, and/or invisible micro-open surfaces–crack embedded in the concrete.

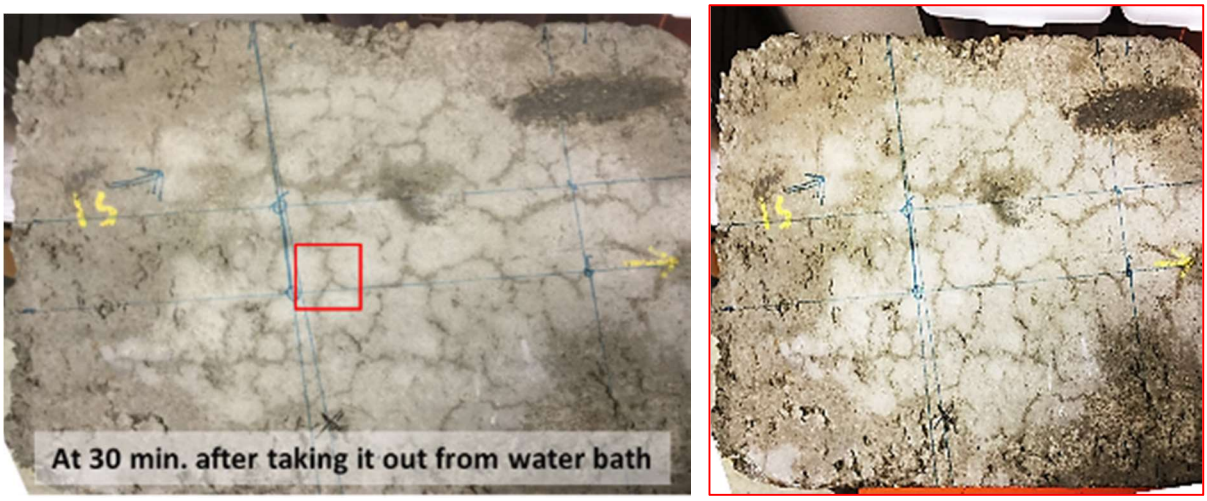

Figure 7.15 Visual observations of concrete test samples: (left) photo of top surface concrete slab 30 minutes after removing from saturation condition and (right) zoomed image within the red box area.

Figure 7.16 shows one of these internal samples, B. After 16 cycles in Task 3, the sample is split into two parts, showing that all microcracks are coincidently extended around the surface area. In addition, as shown in Figure 7.16 (bottom left and right), the microcracks are distributed in the concrete sample. Other samples show localized microcracks by cutting them (not shown). Since a high-resolution camera took these photos, millimeter scale-sized cracks can be detected.

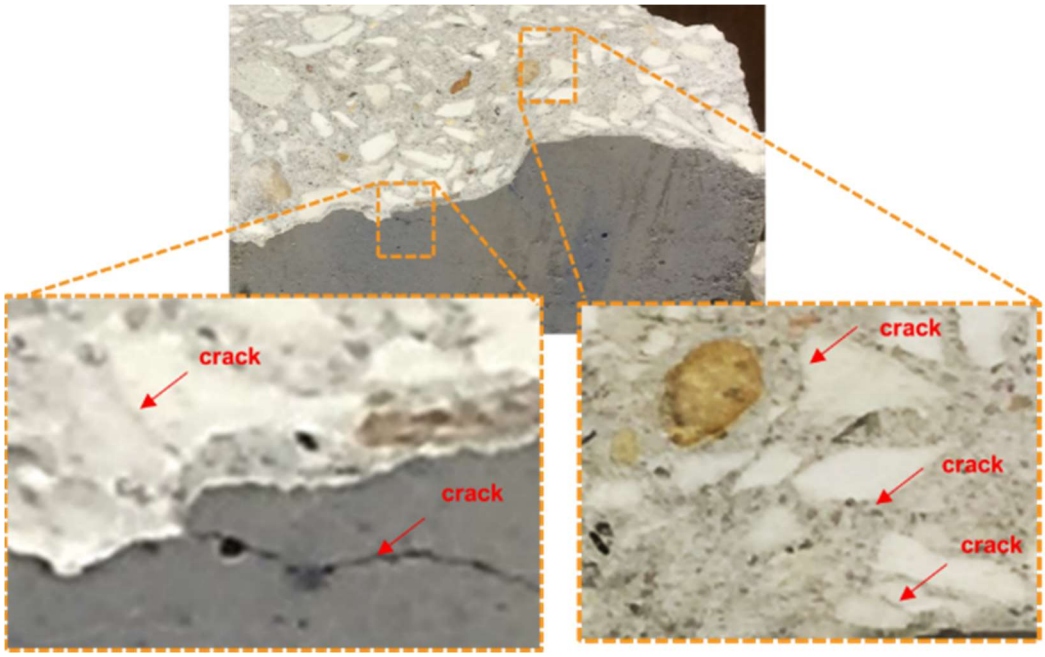

Figure 7.16 Illustration of internal and external cracks in thermally-cycled concrete samples after 16 cycles of Task 3 loading.

Other visual representations are shown in Figure 7.17 with four different steps. The author noticed that the patterns are denser and clearer than before, suggesting that damage progressed. However, these patterns mostly disappear after 5 to 10 minutes, even at a high damage level stage.

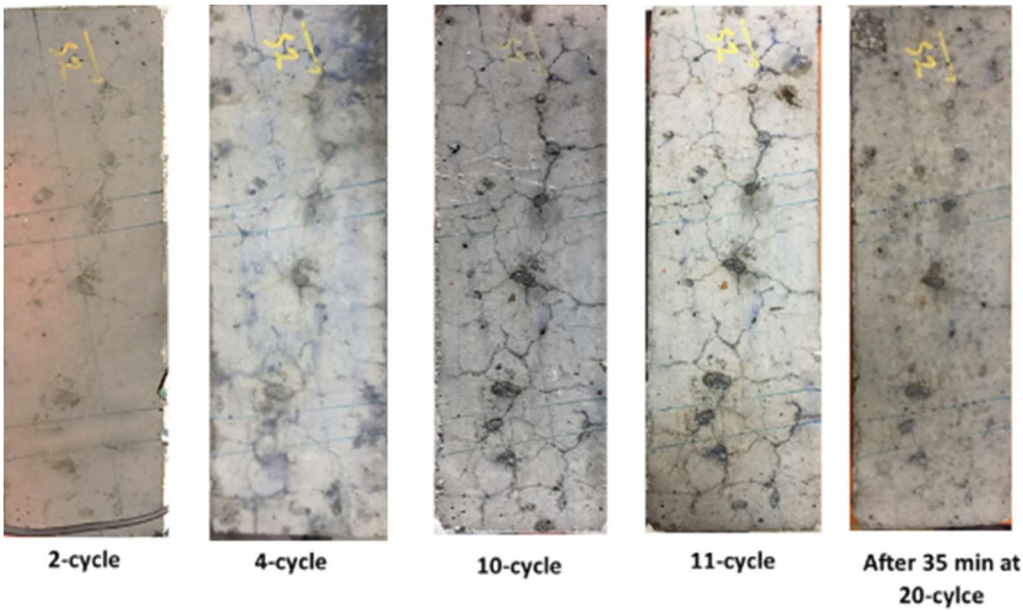

Figure 7.17 Photo images of top surface of specimen C at different levels of thermal cycling. Appearance of crack enhanced by surface moisture.

Figure 7.18 shows optical images of samples. The top rows show 2mm scale images of one zero cycle sample and two of the 10 cycled-damaged sample in Task 2. The zero cycled image shows less pores around the interfacial transition zone (ITZ) area between aggregate and cement paste, while 10 cycled samples show more pores. Figure 7.18 (bottom rows) show images with vacuum red dye impregnation, and it is polished. The pore filled with red dye then indicates a void or damage spot. So, these figures also indicate that the ITZ has more porous material in the 10-cycle image. It is possible that the coefficients of thermal expansion will be different for aggregate and cement paste when the samples are subjected to thermal shock testing.

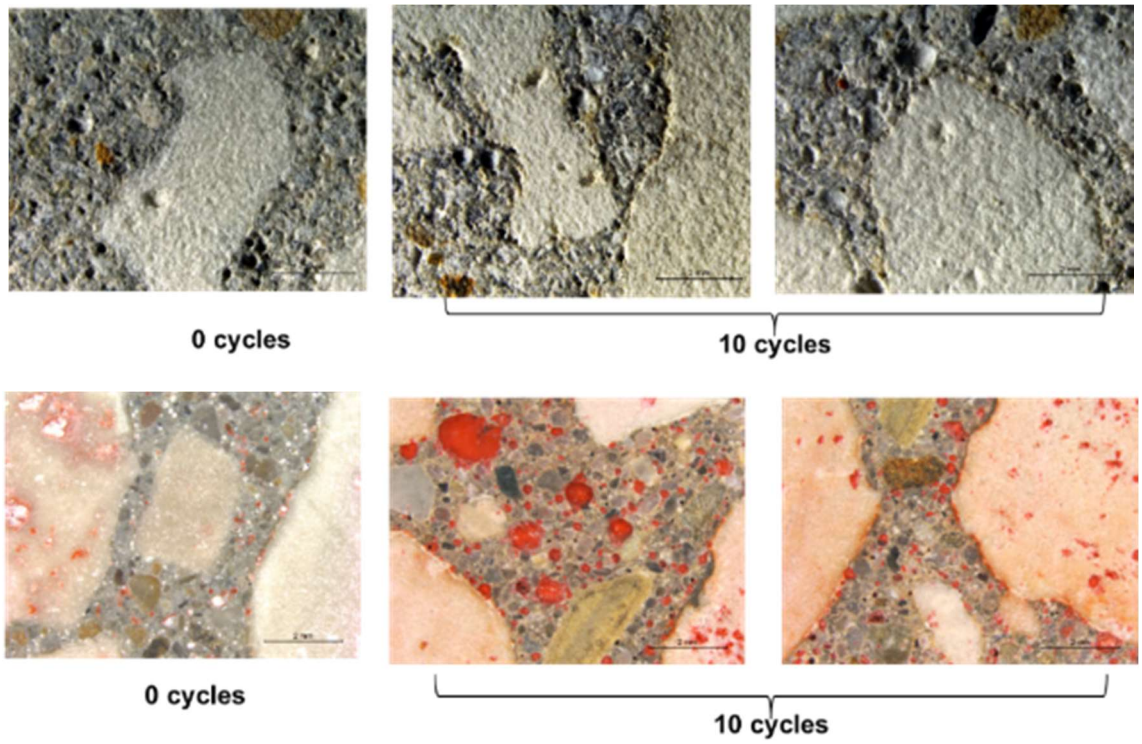

Figure 7.18 Optical images of thermally-cycled concrete samples: (top row) concrete sample with two different levels of cyclic damage under Task 2 loading, and (bottom row) same samples with red dye impregnation.

Figure 7.19 replicates scanning electron microscope (SEM) images. Top rows show backscatter electron microcopy modes with two different levels of damage. Left image shows 0 cycle, 400 um scale. It has few microcracks that occur naturally, while top middle and right images show a significantly larger number of cracks and larger depth and width, through aggregate and cement paste, and ITZ (interfacial transition zone). Figure 7.19 (bottom rows) shows images taken by a secondary electron microcopy mode with two different damaged samples. The bottom left image indicates a zero cycle mortar sample,

while middle and right images indicate 1 cycles damage (from it in 110 °C dry condition for 24 hours to 23 °C water) that result in wider and deeper cracks than the zero cycle's sample. The possible reasons are the same as indicated above. Figure 7.19 (left) shows a nominally undamaged sample where the mineral aggregate (dark gray), cement binder (light gray), and air pore (black) phases are visible. Although the sample is nominally pristine, some fine cracks are still seen in the image. The figures on the right show the same material after being exposed to several extreme hot-cold (70 °C – 0 °C) temperature cycles. The thermal cycles cause the creation of additional thin (on the order of 1 μm in width) microcracks that exist in the cement matrix, along the aggregate-matrix interface, and in the mineral aggregate. Although small in width, micro crack networks adversely affect material mechanical strength, stiffness, and permeability. Moreover, it increases the ingress of aggressive substances into the material that enhance future degradation mechanisms. It follows that microcracks adversely affected by the resilience and sustainability of the structural system are compromised. In order to apply effective monitoring and maintenance procedures, and to more accurately predict service life and monitor structural condition, a nondestructive testing (NDT) technology is required that provides accurate and sensitive characterization of distributed cracking damage in concrete, including fine microcracks.

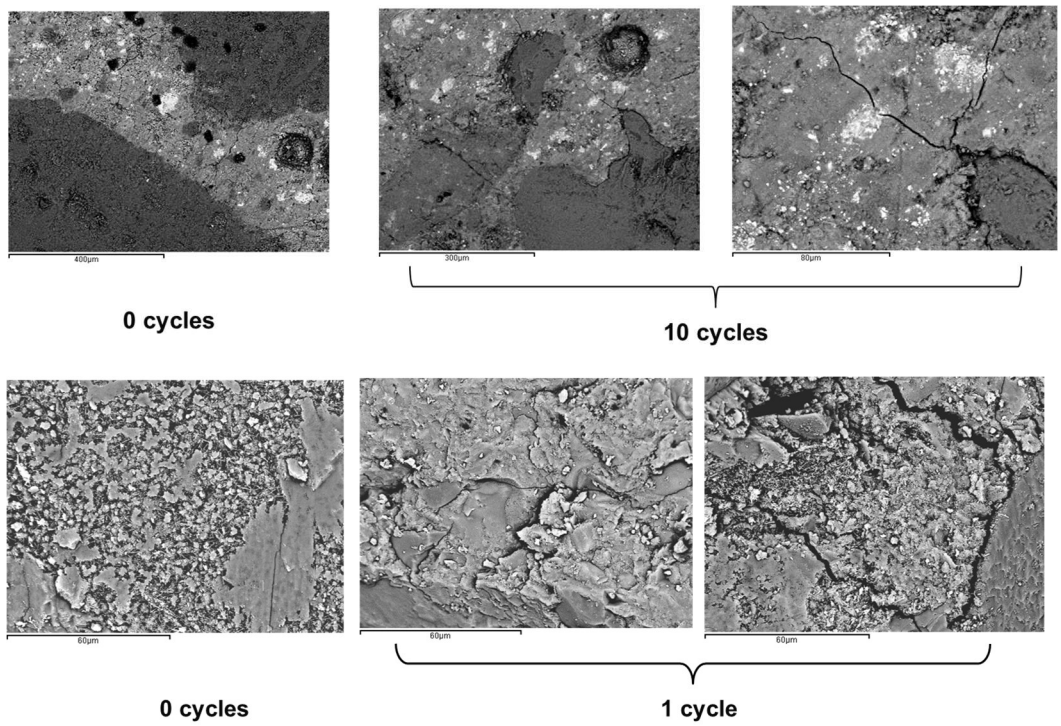

Figure 7.19 SEM images of thermally cycled concrete samples: (top row) backscatter electron microscopy under Task1 loading, (bottom row) secondary electron microscopy.

7.2.3 Standard Resonance Vibration Test Results

ASTM standard resonance tests were compared with our UT backscatter results. The testing methods are described in section 2.3.3. Standard resonance vibration tests were carried out on three different concrete samples that are described in the previous section. Figure 7.20 shows the resonance-testing configuration on the simply supported sample. The resonance vibrations were set up by an impact event of an 11-mm diameter steel-ball, and the resulting vibration motion was detected by a contact accelerometer. One contact accelerometer was attached near the end of the simply supported beam and used to collect vibration data to be compared with backscatter datasets that were collected by the nearby MEMS sensor. A second accelerometer was attached at the center of the beam to provide a timing trigger for the data collection process. The contact accelerometer was connected to a power source and preamplifier, and the signal was transferred to DAQ. The data were sampled using 16-bit resolution at a sampling frequency of 1 MHz. Each time signal had a duration of 2 ms, which provides a frequency domain resolution of 500 Hz. The signal acquisition process was carried out using the LabVIEW Signal Express program. Digitized time data were then processed using a Fast Fourier Transform algorithm to convert power/frequency response using Matlab.

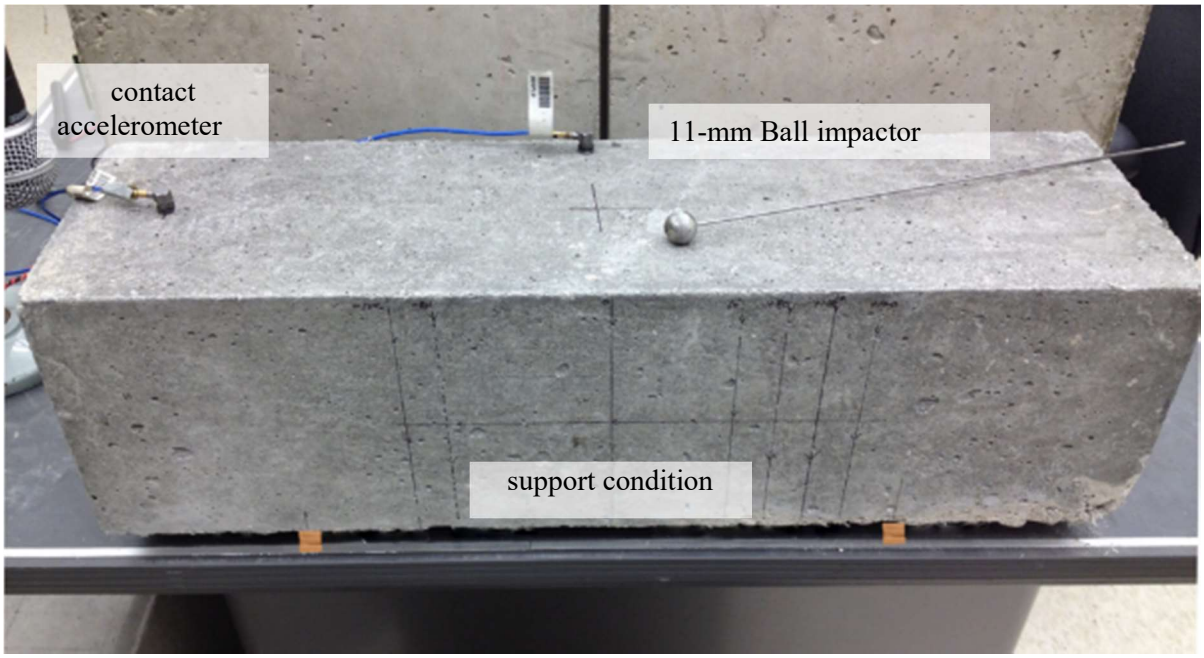

Figure 7.20 Testing configuration for vibration test.

Resonance test results are shown in Figure 7.21. Each test sample (3 total) has 24 cycles in three different thermal shock test steps. A decrease in peak frequency (resonance frequency) is known to be associated with an increase in the level of damage degradation in the sample. General trends show that smaller sized samples have greater levels of decrease in peak frequency. In lower cycles (0 to 8 cycles) in Task 1, the peak frequency does not change. These results will compare with new ultrasonic backscatter results.

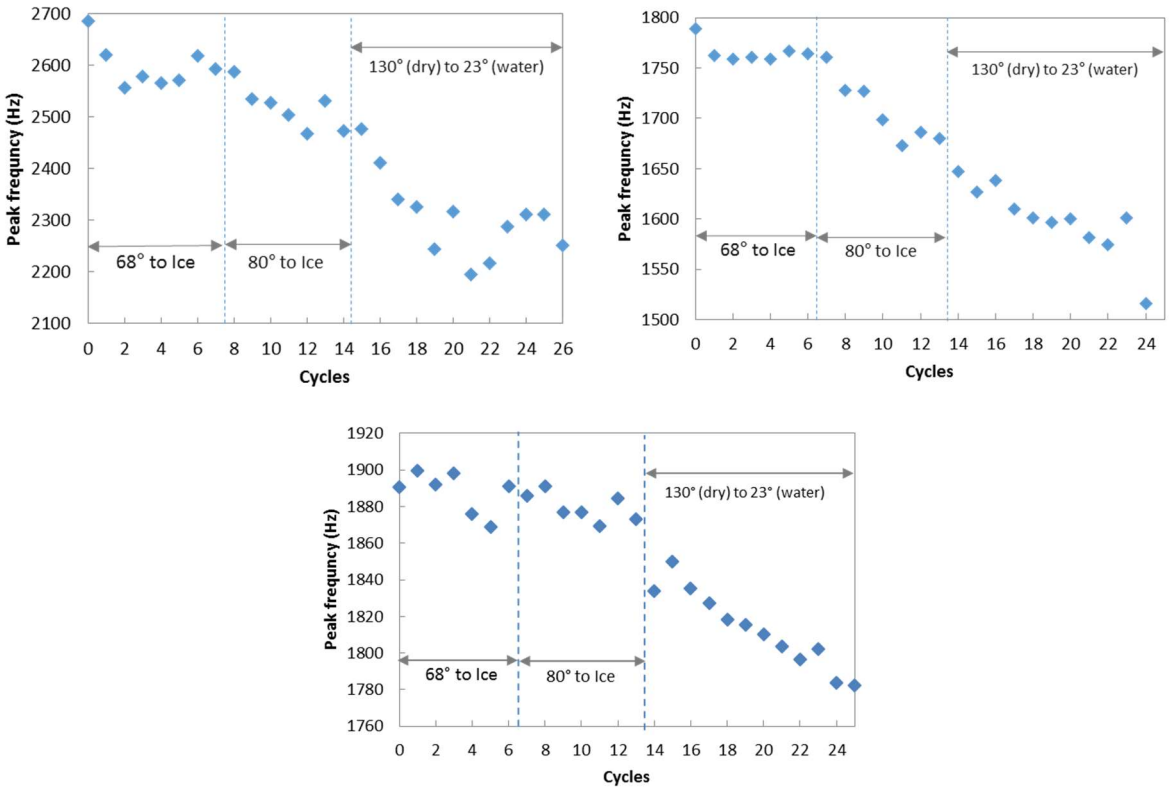

Figure 7.21 Resonance test results with thermally cycling shock tests: (top left) small block (100 x 355 x 100 mm) as referred to as sample B, (top right) large beam (160 x 160 x 510 mm) as referred to as sample C, and (bottom) slab (360 x 480 x 140 mm) as referred to as sample E. All concrete samples have same age, same mixture design, and same curing conditions.

7.2.4 Effect of Localized Damage on Resonance Test Results

This section studies resonance vibration data with local damage on specific sides of a prism-shaped sample. The FE models are described in section 4.2.3. Real damage can occur in distinct locations: one side can be more damaged than other sides or areas.

Model I in Figure 7.22 (top) shows 1.83 kHz as first peak frequency (dashed line) of resonance vibration from an undamaged sample. This peak frequency indicates a typical first bending mode of this size of the beam with material properties. Lower peak frequencies demonstrate that the sample is damaged. Figure 7.22 (middle-top and middle bottom) shows the results of model II. There are four different test results in model II. Each name identifies the sides of impact and listening position. S1 and S3 show the lowest frequency values. The results of model III show similar trends. Model II and model III show that all sides have lower peak frequency values. This finding indicates that local damage influences global peak frequency results. Importantly, UT local damage detection can detect specific sides or areas, although the vibration test cannot.

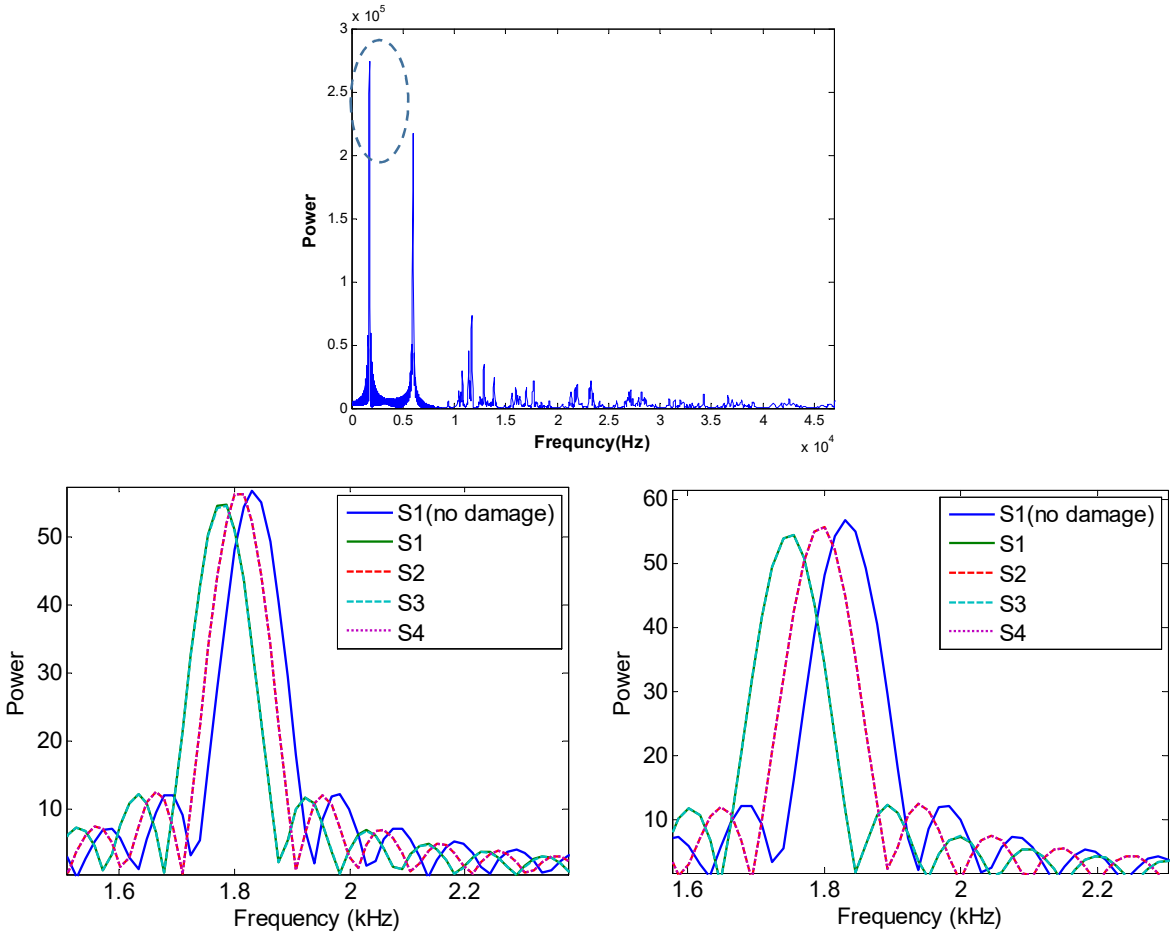

Figure 7.22 FEA result: (top) power spectrum response of intact model, (bottom left) simulated vibration spectra from model II, (bottom left), and (bottom right) simulated vibration spectra from model III.

7.2.5 UT Result: Forward Coherent Wave

The study shows how conventional UT scanning approaches work sensitively for distributed micro cracking damage. In this section, wave velocities, amplitudes and energies were used for monitoring different cycles of damage. These test results are measured by the same approach described in section 7.1.2. The first test is wave velocity as shown in Figure 7.23. The dataset show a slight decrease with more cycling damage. However, there was less than a 1% decrease between 0 and 24 cycles. These conventional analyses (the peak amplitude and energy) with forward propagating coherent waves show an unclear distinction among the different damage levels. These analyses are insensitive to small cracks because initial excitation pulses are more dominant than the forward scatter. These phenomena occur when the cracks are much smaller than the coherent wavelength.

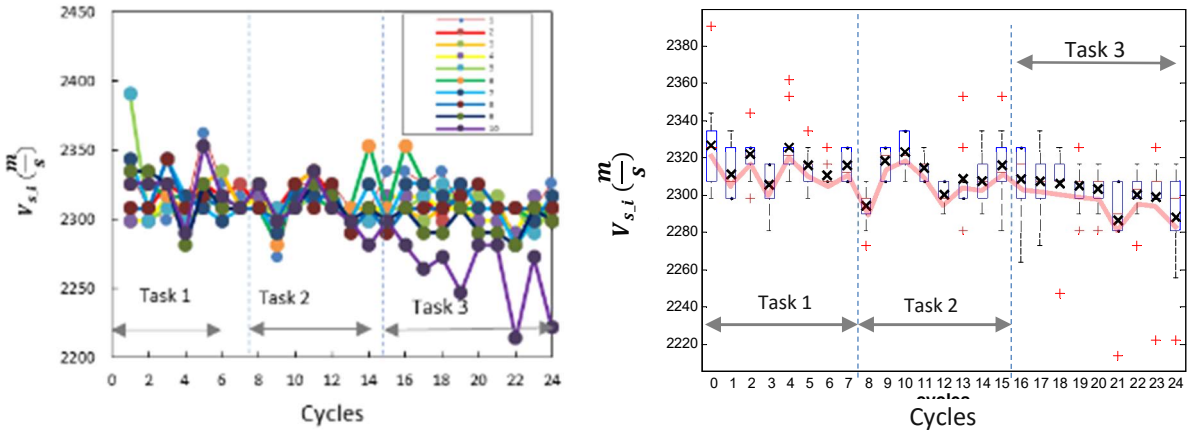

Figure 7.23 Experimental forward propagating surface wave ultrasonic data collected from concrete with thermal cycling damage: (left) surface wave velocities of ten different regions, (right) boxplot of these surface wave data with average value $< V_{s\_i} >$ shown as solid line.

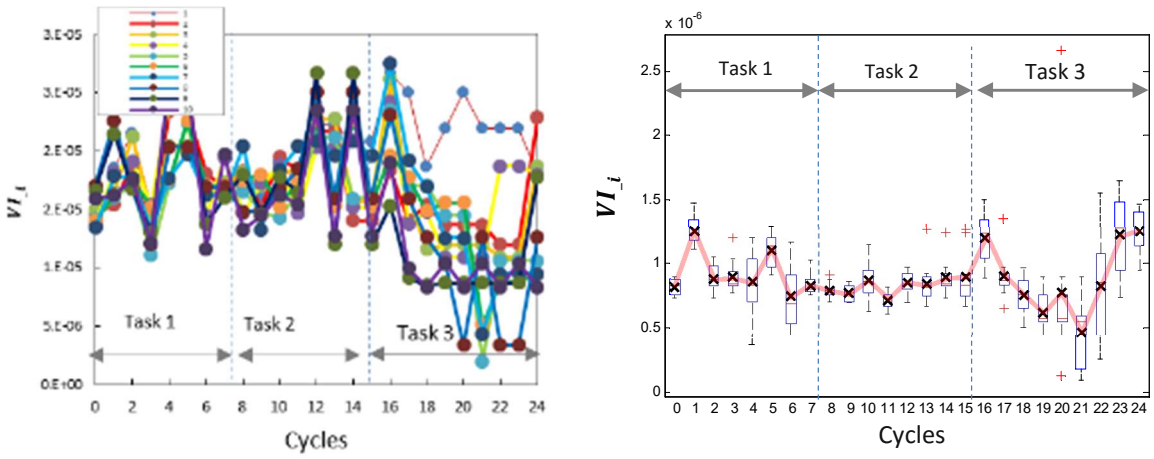

Figure 7.24 Experimental energy VI of forward propagating ultrasonic wave collected from concrete with thermal cycling damage: (left) overlaid VI_i of ten different regions, and (right) boxplots of these data VI_i shown as solid line

7.2.6 UT Result: Backscatter Analysis

In this section, the backscatter approach is applied to thermally cracked concrete samples, using global monitoring of a large spatial area. First backscatter data are compared with resonance testing results. The resonance frequency tests are standard and reliable methods. Figure 7.26 shows a comparison between ultrasonic backscatter data and resonance data. Figure 7.26 (left) shows the averages of backscatter energy results calculated by the ESA approach described in section 6.1.4. These values for different cycles show averages of normalized backscatter energy of all four sides, $< \mathrm{EB}_{\mathrm{nor\_i}} >_{all\ side}$ of sample C. Each side's $<\mathrm{EB}_{\mathrm{nor\_i}}>$ is an average of backscatter energy from ten different scanning positions. This global scanning dataset has values that are relatively close to the resonance test results, which considers the whole body structure. Both results show clear distinctions among the different cycles. The resonance and ultrasonic results demonstrated small increases between 0 and 6 cycles. However, the ultrasonic BE_{nor_i} values monotonically increase, while the peak frequencies in the resonance test increase again around 5 or 6 cycles. This result indicates that the resonance tests are less sensitive than the ultrasonic backscatter approach.

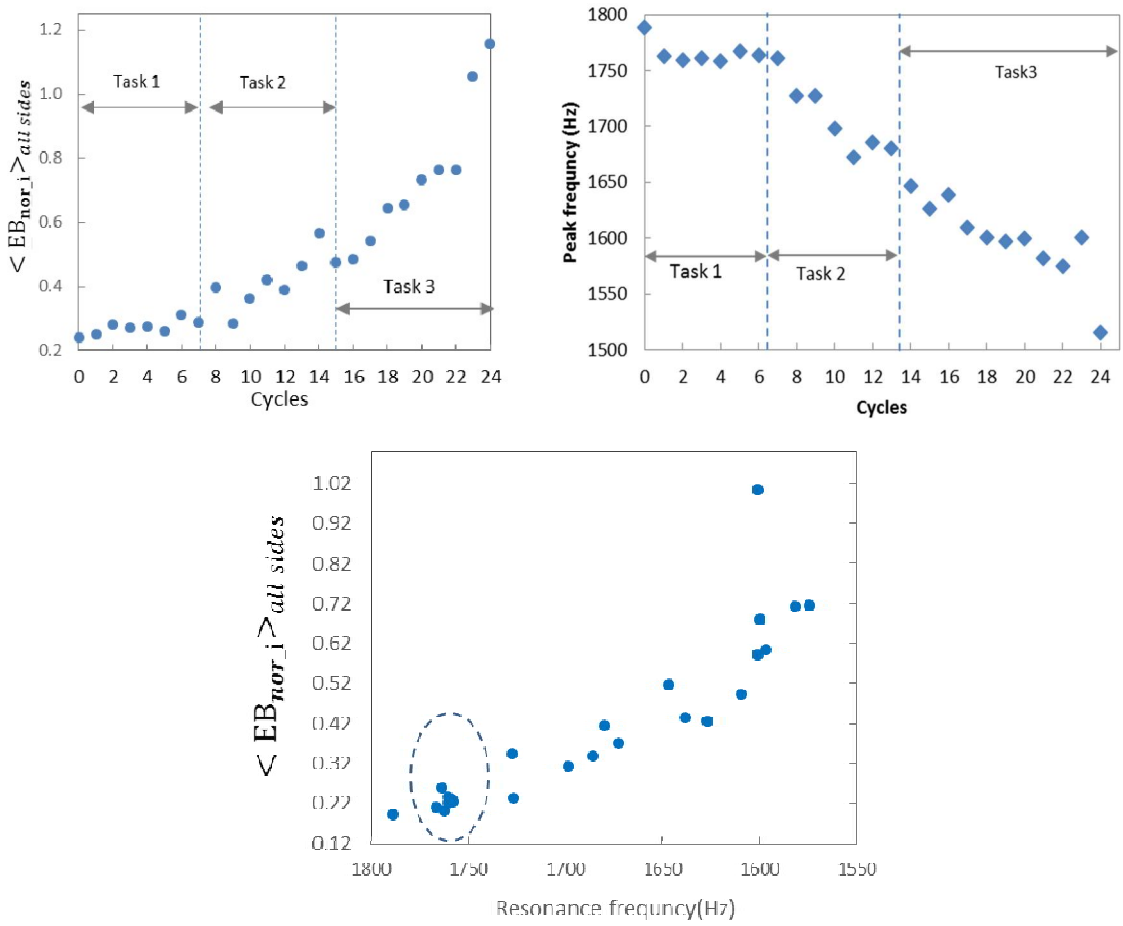

Figure 7.25 Experimental results of backscatter energy for sample C: (top left) average values of backscatter energy for all surfaces, (top right) resonance test data, and (bottom) comparisons of two approaches, where dashed line indicates data cluster due to insensitivity of resonance frequency in Task 1 thermal cycling.

Figure 7.26 shows a comparison of ultrasonic data with resonance data. Figure 7.26 (left) shows variance of backscatter results calculated by the SVA approach described in section 6.1.4. The variance values are $< P_{av} >_{all\ sides}$ of all four sides of the sample "C." Each side's variance is an average of variances from ten different scanning positions. This global scanning is relatively close to the resonance test result, which considers the whole body structure. The higher variance value indicates more backscatter from damage, while the resonance frequency decreases with damage. These results show similar trends. Between 0 and 8 cycles, however, resonance frequency is flat, while variance data show more sensitivity to the damage. Another benefit of the ultrasonic backscatter approach is that every spot and side can be viewed separately.

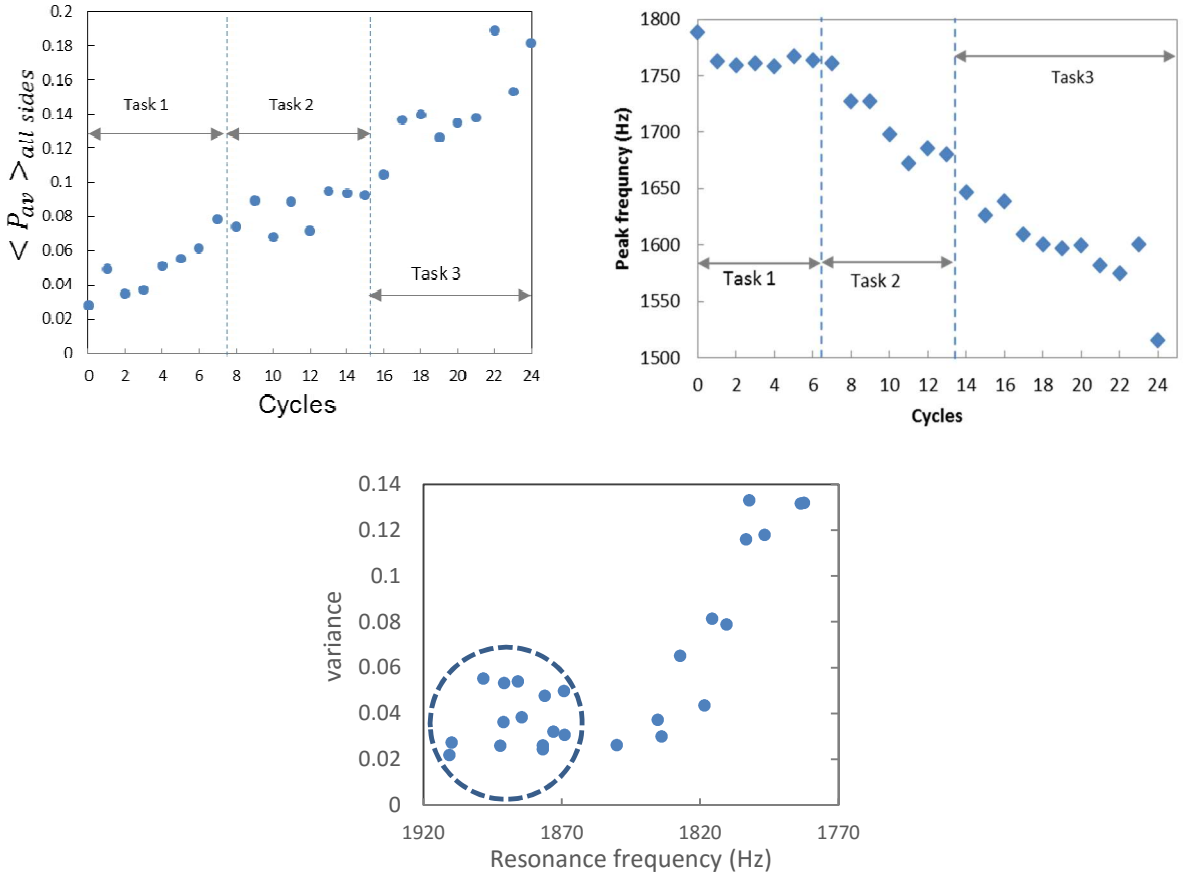

Figure 7.26 Experimental results of variance for sample C: (top left) backscatter variance $< P_{av} >_{all\ sides}$ test results, (top right) resonance test data, and (bottom) comparisons of two approaches. Dashed line indicates data cluster due to insensitivity of resonance frequency in Task 1 thermal cycling.

Figure 7.27 shows ESA results which indicate the graph of the normalized backscatter energies, BE_{nor_i} are smoother than the graph of the non-normalized backscatter energy BE_i. Typically, BE_i increases with higher levels of damage. The normalizing process adjusts for uncertainties in the testing configuration, signal noise, and excitation of inhomogeneous material. Important notices of the results include S1, top surface shows faster damage progress. In addition, BE_{nor_i} value at the initial cycle is higher than the values of the other sides. This is because the top surface was cast side, which possibly has dry shrinkage and rough surface even at initial stage. Since the cast side has more capillary pores, the damage progress is faster than other side.

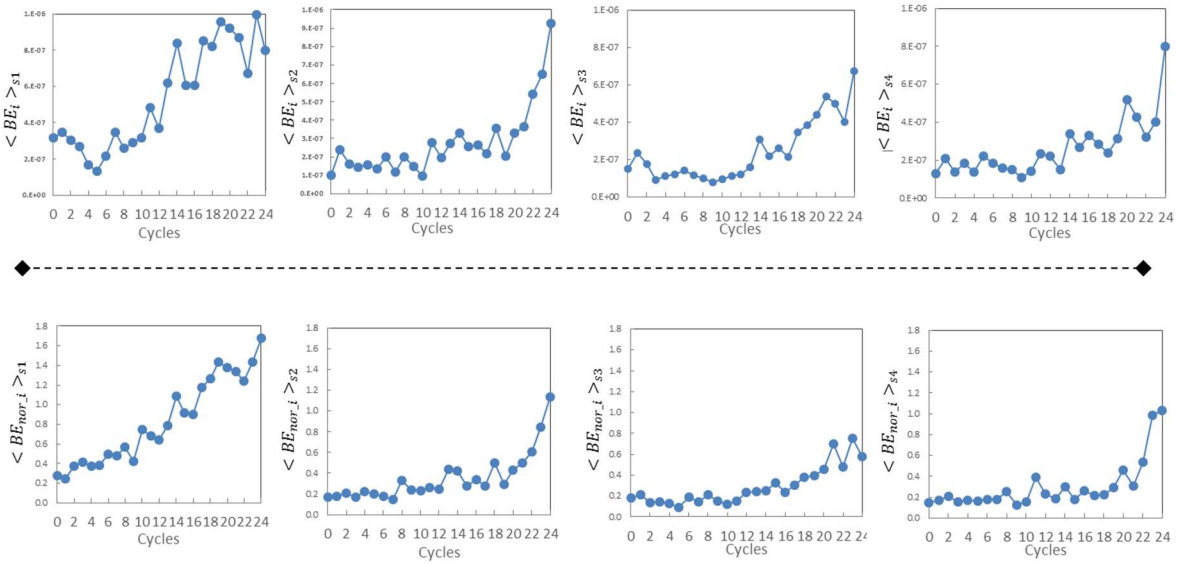

Figure 7.27 Normlized backscatter data for thermally damaged concrete: (top row) $< BE_i >$of four different sample surfaces from sample C, where S_i indicates the i^{th} surface. S1 indicates top surface (cast surface) and S3 indicates bottom surface; and (bottom row) $< BE_{nor\_i} >$ of same surfaces.

The trend is analogous to $< \mathrm{BE}_{\mathrm{nor\_i}} >$ to the ESA process, previously. Figure 7.27 (top) shows the variances $< P_{av} >_{Si}$ results of the four different sides (called S1, S2, S3 and S4) by SVA in the backscatter results of sample C. Figure 7.28 (top) shows variance data of each side and averaged data. Each side shows different amounts of increase by damage level. The results of each side show a different slope and amount of increase from the damage. The most critical increase and the highest initial value are on side 1, which is top surface and cast side.

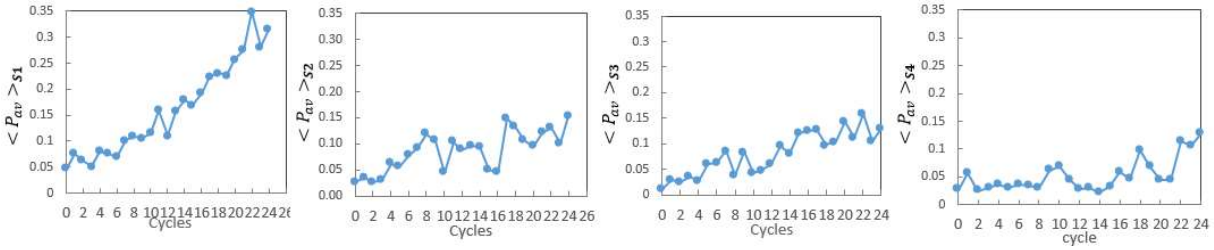

Figure 7.28 Average variance values for thermally damaged concrete $< P_{av} >_{Si}$ from four different surfaces of sample C. S_i indicates ith surface, wehere S1 indicates top surface (cast surface) and S3 indicates bottom surface.

A backscatter approach was carried on sample E, slab. First of all, the author compared backscatter data with resonance testing results. Figure 7.29 shows a comparison between ultrasonic backscatter data and

resonance data. Figure 7.29 (left) shows the averages of backscatter energy results calculated by the ESA approach described in section 6.1.4. The values for different cycles show the averages of the normalized backscatter energy of two sides (top and bottom surface), $< \mathrm{EB}_{\mathrm{nor\_i}} >_{all\ side}$ of sample E. Each side's $<\mathrm{EB}_{\mathrm{nor\_i}} >$ is an average of backscatter energy from ten different scanning positions. Both results show clear distinctions among the different cycles. The resonance and ultrasonic results demonstrated minor increases between 0 and 8 cycles. The size of the slab is larger than that of specimen C. The damage progress of the larger structure slowly developed due to inside temperatures that slowly changed.

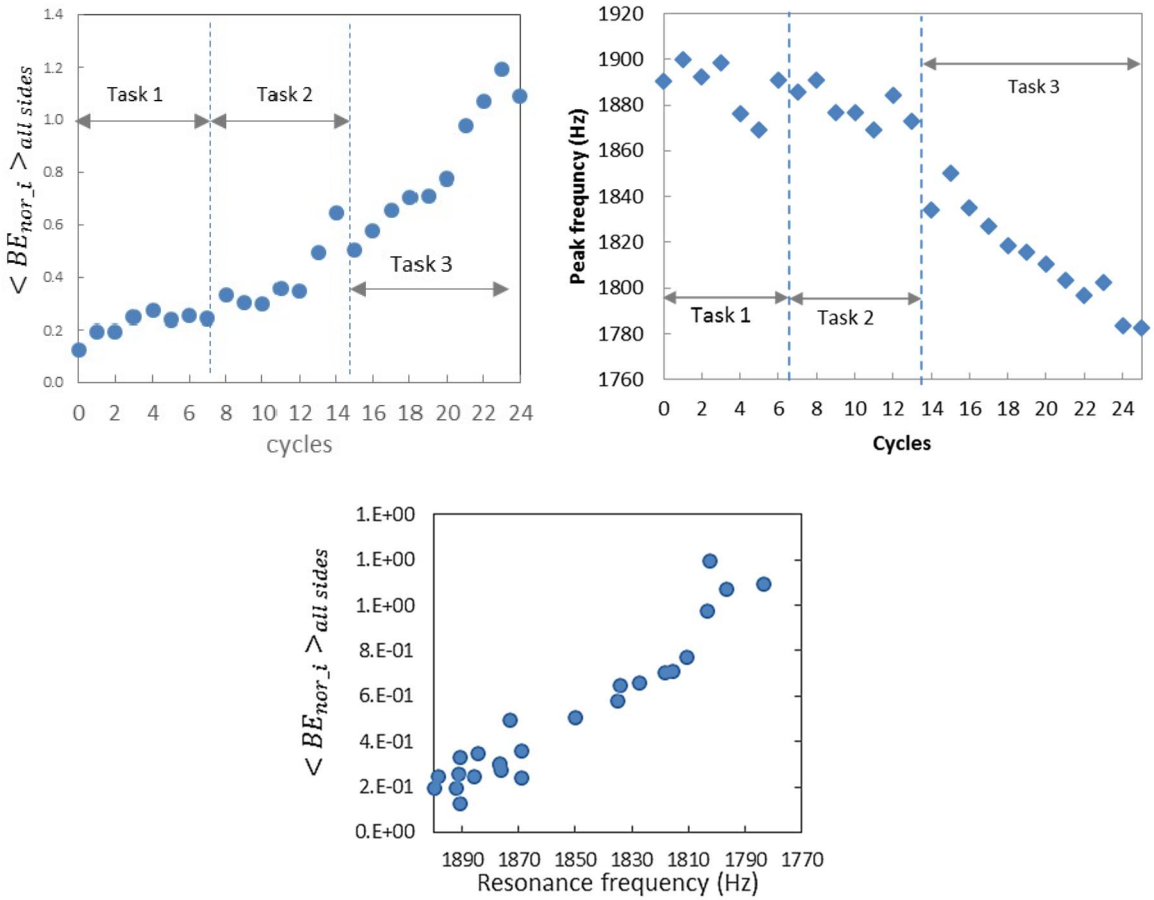

Figure 7.29 Experimental results of backscatter energy for sample E, slab: (top left) average of backscatter energy for all sides test results, (top right) resonance test data, and (bottom) comparisons of two approaches.

Figure 7.30 shows a comparison of ultrasonic data with resonance data. Figure 7.30 (left) shows the

variance of backscatter results calculated by the SVA approach described in section 6.1.4. The variance values are $< P_{av} >_{all\ sides}$ of all four sides of the sample "E", slab. Each side's variance represents an average of variances from ten different scanning positions. This global scanning is relatively close to the resonance test result, which considers the whole body structure. The higher variance value indicates more backscatter from damage, while the resonance frequency decreases with damage. These results show similar trends. Between 0 and 8 cycles, however, resonance frequencies are flat, while variance data show more sensitivity to the damage. P-values between 0 cycle and 6 cycles from $< P_{av} >_{all\ sides}$ has less than 0.05, indicating that the groups are significantly different statistically. The variance data are compared to resonance data. The variance data also show crust in initial damage. Another benefit of the ultrasonic backscatter approach is that every spot and side can be viewed separately.

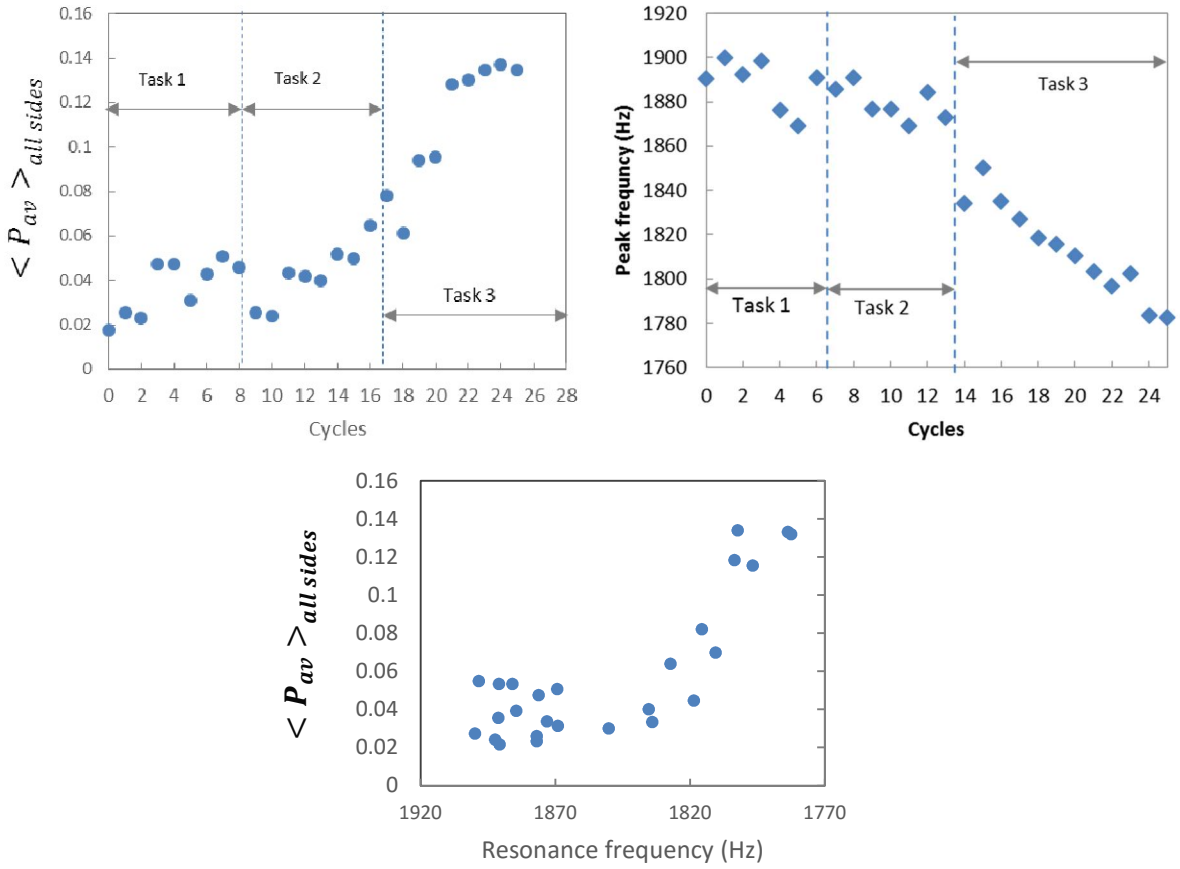

Figure 7.30 Experimental results of variance for sample E, slab: (top left) backscatter variance $< P_{av} >_{all\ sides}$ test results, (top right) resonance test data, and (bottom) comparisons of two approaches.

Figure 7.31 shows the effect of averaged normalized backscatter energy $< EB_{nor\_i} >$. The figure (top row) represents two different sides: s1 indicates the top surface, and s2 indicates the bottom of the slab. Both non-normalized backscatter energy $< EB_i >$ values of s1 and s2 demonstrate irregular and oscillating patterns at certain cycles. This is possibly due to the uncertainties of testing confirmation, electric noise, and excitation of homogenous material. After the normalized process, these backscatter results for both sides were improved.

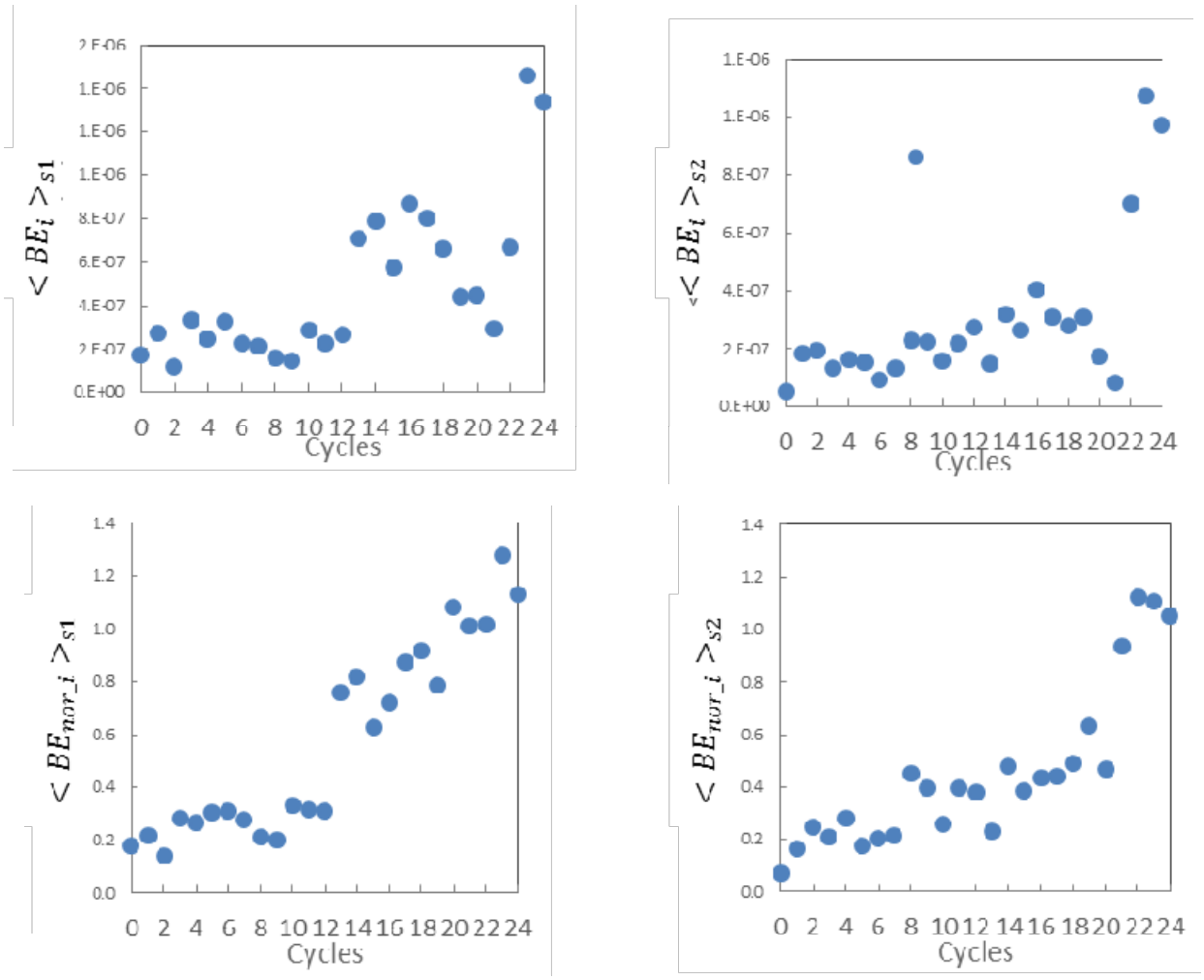

Figure 7.31 Averaged normalized backscatter data from thermally damaged concrete in sample E, slab: (top row) $< BE_i >$ of two different surfaces, where S1 indicates top surface (cast surface) and S2 indicates bottom surface, and (bottom row) $< BE_{nor\_i} >$ of same two surfaces.

7.3 Experimental Study: Application of Backscatter to Locate and Image Damage

This section studies a local monitor with the same dataset. The localized images show where the distributed micro crack damage is located. These images allow us to understand specific damage areas in the field. The defective area is not visible upon visual inspection. FEA data verified these testing results in the section.

7.3.1 Testing Setup

The samples and testing configurations are the same as the previous section, 7.4. Figure 7.32 shows the ultrasonic scanned area. It is shown as a white dot box area on the slab, Sample E1. The scanning system collected data every 20mm. The gaps between receivers' linear arrays were 5 mm.

Figure 7.32 Concrete sample D subjected to thermal cycles. Tested area indicated by white box.

7.3.2 Repeatability and Scan Line Position Study

Before exploring local monitoring results, repeatability was studied in this section. Repeatability increases reliability and quality of the NDE concrete monitoring system because it shows that the tool can be used regardless of external effects, e.g., system noise or uncertainty of field test. The UT system scans ten different regions at the 22-cycle stage in Task 3 thermal shock test. First region is named

"position-1", and last region "position-10" (see in Figure 7.33, top). UT scans were repeated three times, and Figure 7.33 (right) shows the testing results. Each box plot has ten different positions. The orange circles indicates the mean value with a trend line, and the red plus symbol shows the outliers. Mean values are similar to each other. The results show that global scanned data is consistent, and this method is repeatable. All readable data show P-values greater than 0.05, therefore the population means are not significantly different at 95% confidence level.

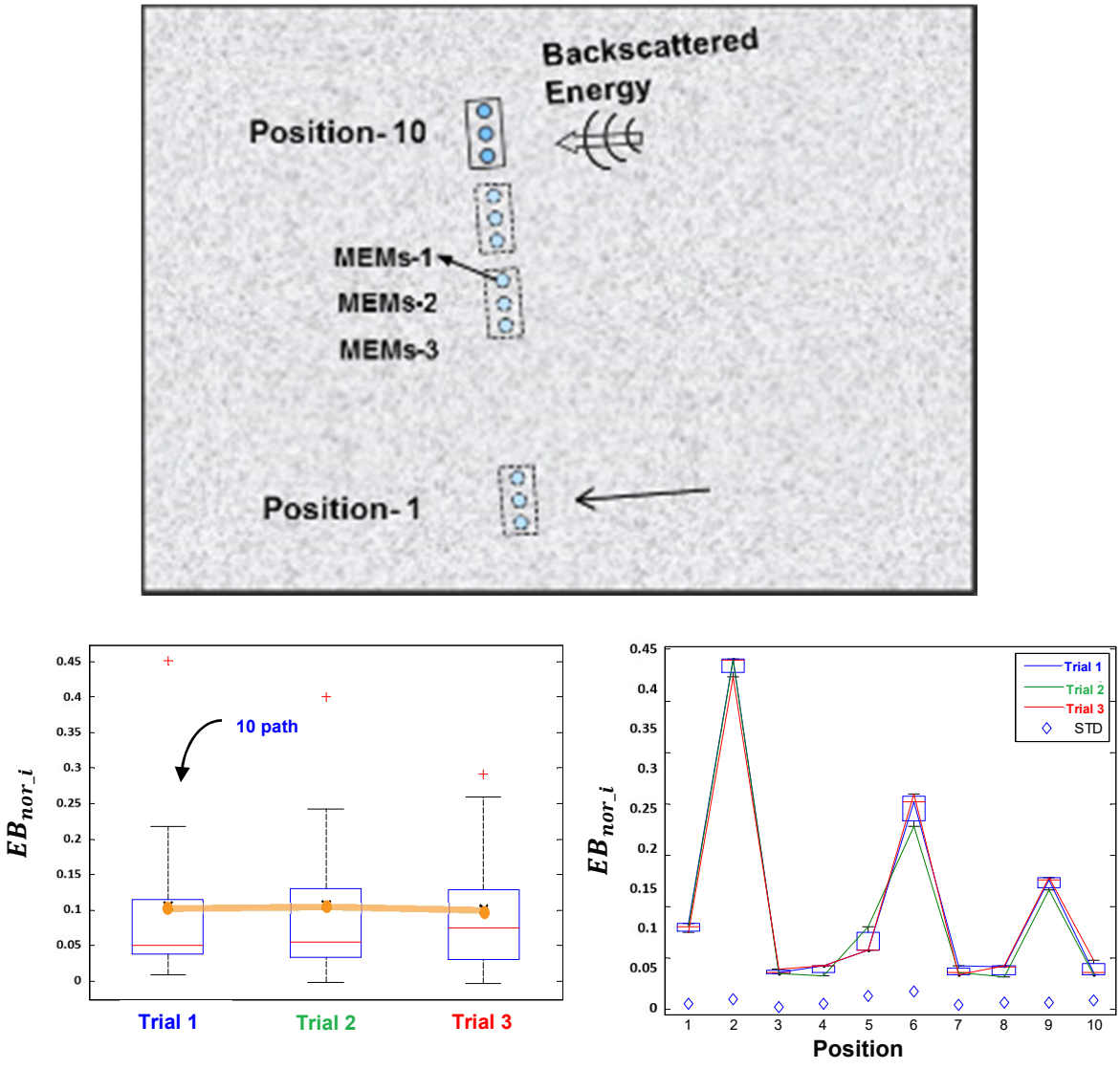

Figure 7.33 Repeatability study of ultrasonic system. Three repeated sets (trials) of multi-line scan data collected at the same location: (top) testing configuration, (bottom left) normalized backscatter energy across trials, and (bottom right) normalized backscatter with scan position for three trials.

Now, each position is investigated. Figure 7.34 (top right) shows the testing results. Although each position has different backscatter energy, the three repeated data for each position are very close to each other. The averaged standard deviation value is 3. Considering a strong level of repeatability from these results, the high energy in position-2 and 6 indicates high backscatter energy from the local damage area. Therefore, the next section will discuss how to locate specific damaged areas.

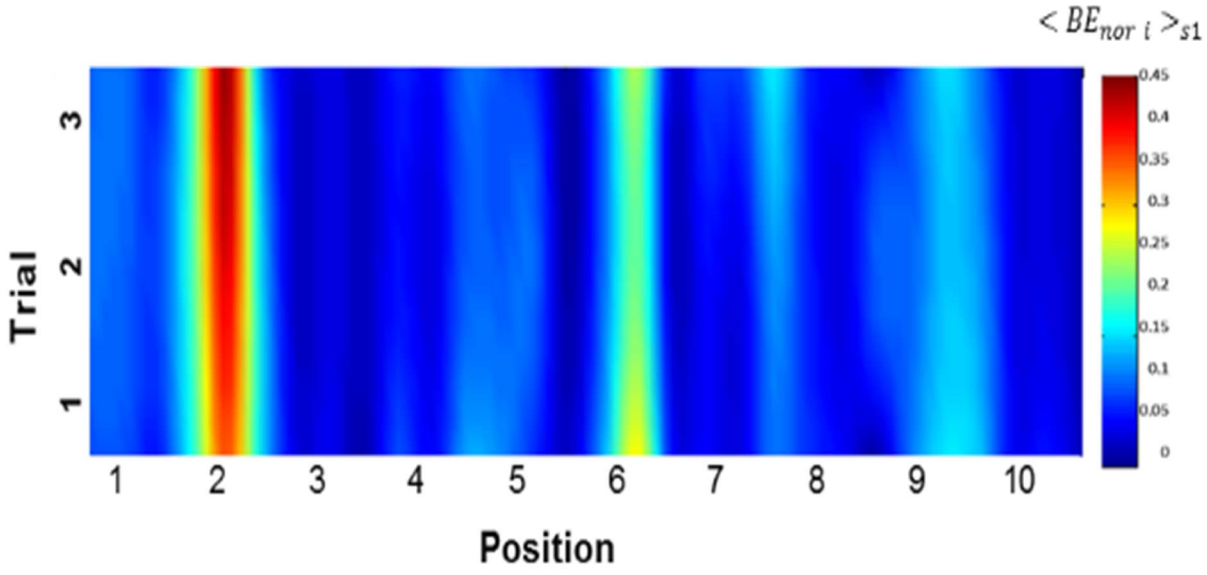

Figure 7.34 Stacked 2-D image of normalized backscatter parameter across all test trials and scan positions using data reported in Figure 7.33.

The next experiment is a parametric study of different spacing between the scanning lines. The study considers how EB_i vary with regard to scanning resolution (scan line spacing). Most scan line spacings in these tests are 20 mm. In this study, three different scan line spacing cases are considered, as shown Figure 7.35. Case 1 is scanning side by side with 30 mm spacing, while Cases 2 and 3 have 20 and 10 mm spacing, respectively. All cases show similar averages, and the data distributions are statistically similar. The global scan, with different scanning gaps, indicates P-values with a wider gap case (30mm and 10mm gap) closer to 0.05. A group between 10 mm to wider than 30 mm possibly show significantly different statistical (P-values <0.05).

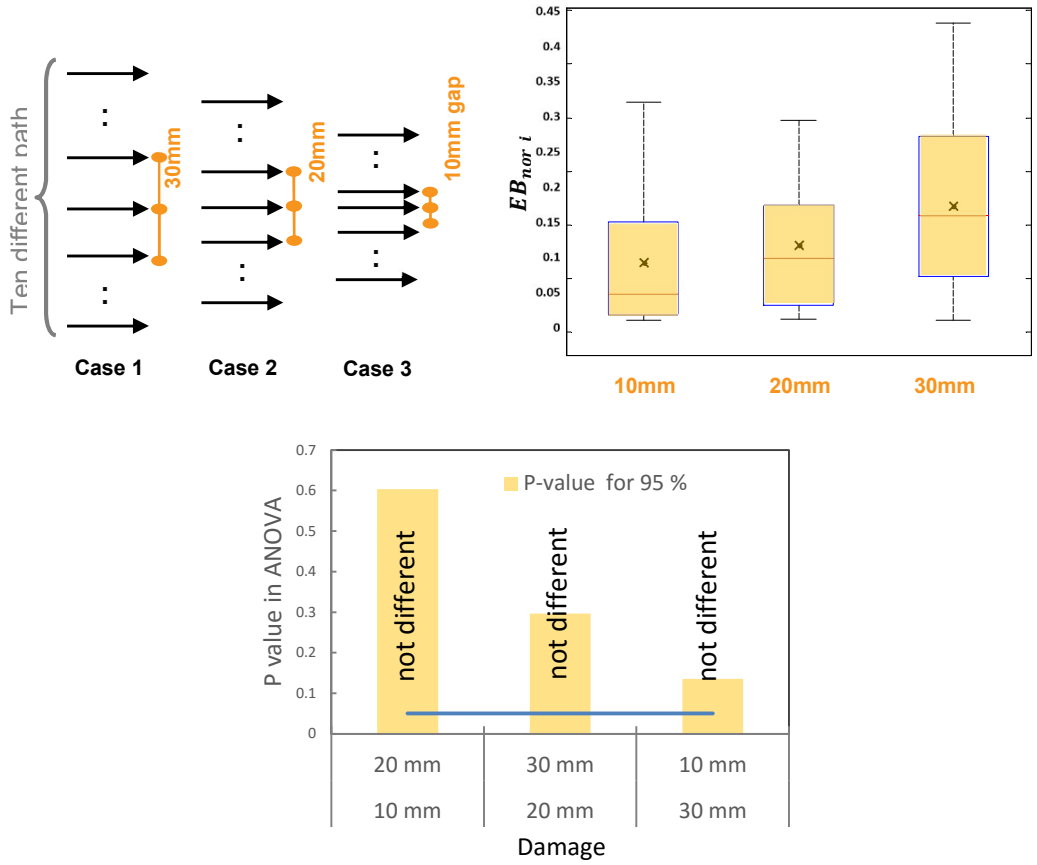

Figure 7.35 Effect of scan line spacing on normalized backscatter parameter: (top left) illustration of testing configuration with different scan line spacings, (top right) EB_{nor_i} values and average of each line spacing case, and (bottom) P-values for each scan line spacing.

7.3.3 Localized Damage Identification

Here, I present the testing results from the thermal shock experiments. Backscatter energy was collected from ten different positions as shown in Figure 7.36 (top left). Each position has three sensors to construct a more accurate image (high resolution). Figure 7.36 (bottom) shows the line scan image built up of EB_{nor_i} data from a sample across 25 different damage cycles. The color map shows backscatter energy: the red color indicates high energy (more damage), and the blue color indicates lower energy (less damage). In the lower cycles (zero to ten cycles), lower energy is dominant (little damage), while in the higher cycles, there is higher energy (increasing localized damage). Around 12-cycle stage show quick damage progress indicating that some of regions have high EB_{nor_i} values.

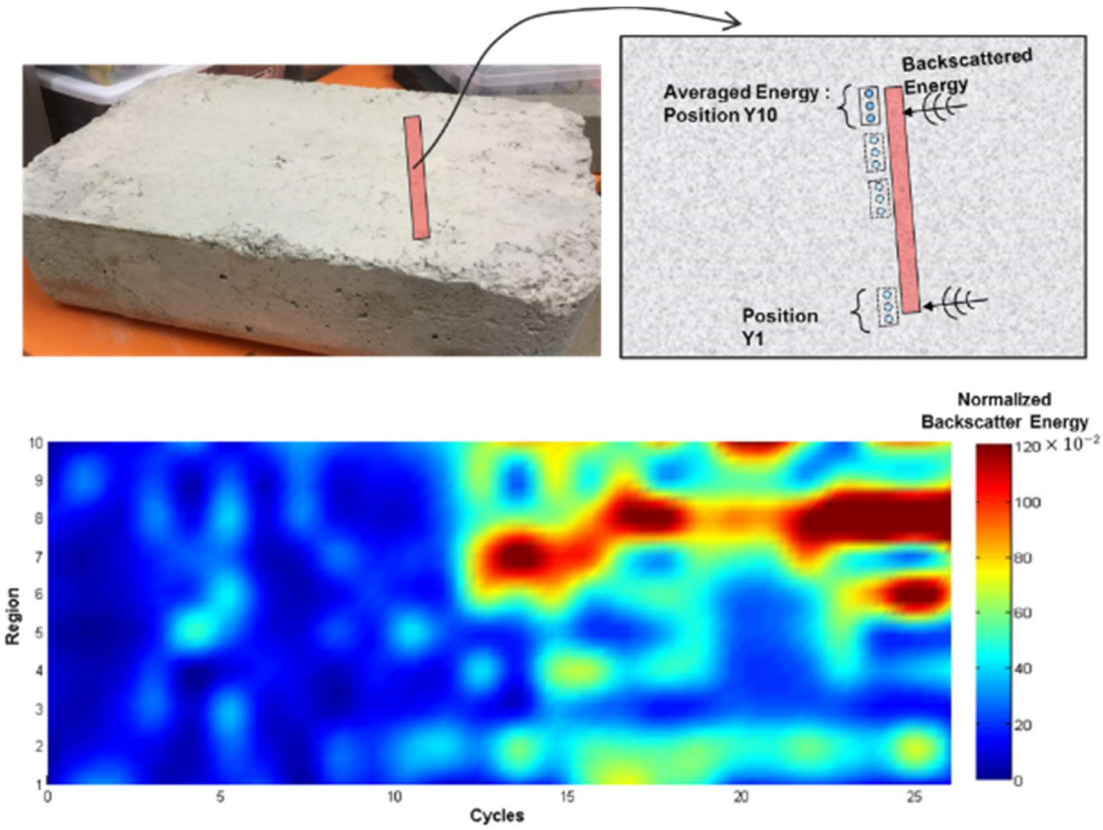

Figure 7.36 Normalized backscatter presented at a single scan location for increasing damage levels: (top left) testing location on sample, (top right) testing configuration, and (bottom) EB_{nor_i} values as a function of increasing thermal cyclic damage.

Next backscatter test datasets are used to reconstruct a 2-D map of local damage. Figure 7.37 shows the testing configuration for the scanning process. Figure 7.37 (left) illustrates the scanning area indicated by a red box. The right image shows each local scanning position, indicating the number of data points. The each scanning position has 2-D sensor array (2 x 3), which allow 6 data at the same time.

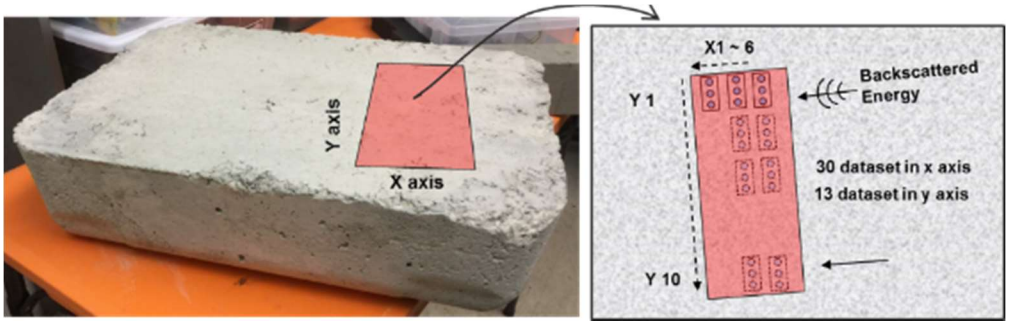

Figure 7.37 Testing configuration for consistent area scan tests: (left) scanned area from top surface of slab E, and (right) 2-D receiver array configuration needed to collect data for area scan.

Figure 7.38 shows 2-D local damage image with normalized backscatter EB_{nor} and four different damage steps of: 0, 23, 24, and 25 cycles. The EB_{nor} results indicate strong repeatability where the damaged area is higher. The image indicates local damage area.

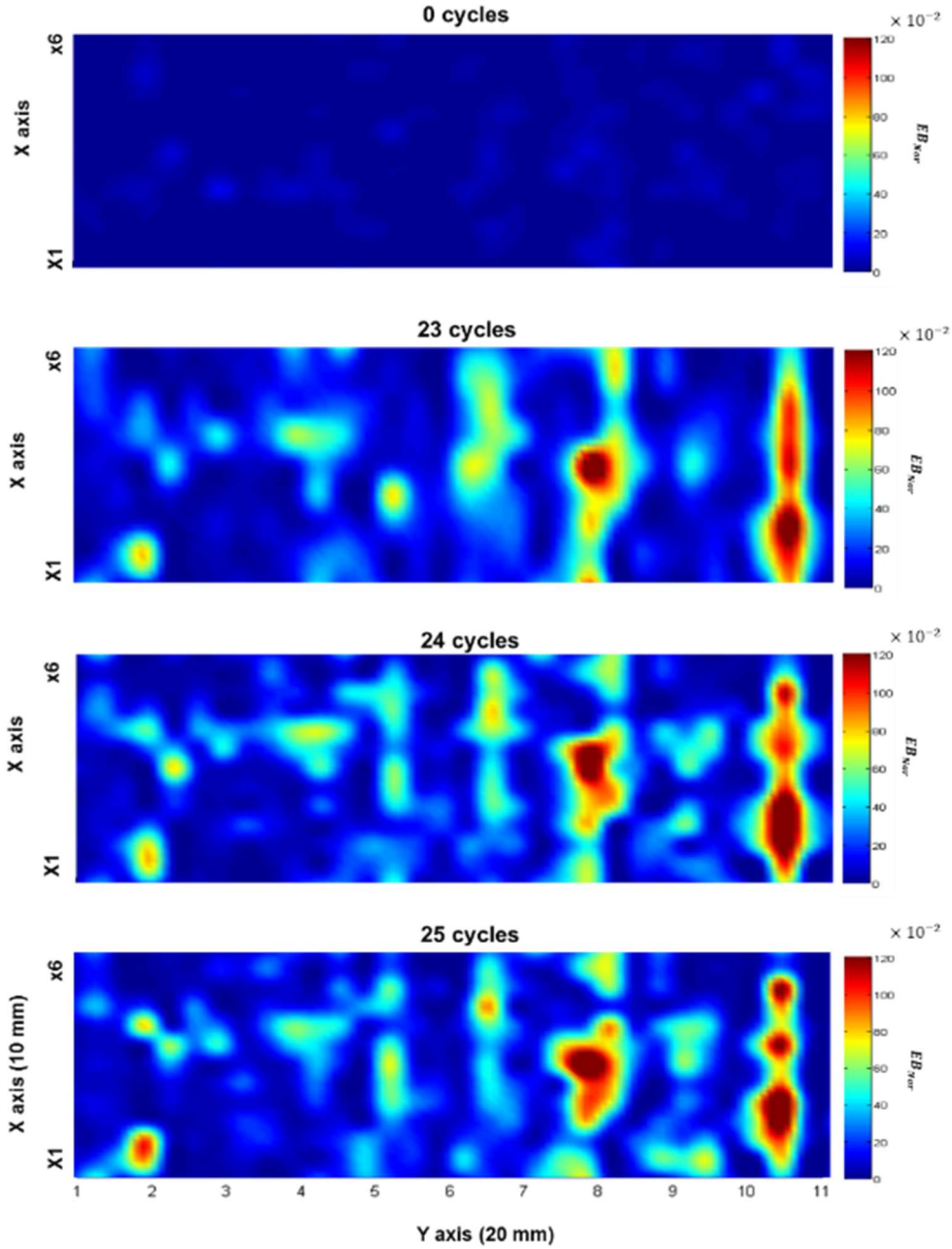

Figure 7.38 Normalized backscatter presented at a consistent scan area on sample E for increasing thermal cyclic damage levels from undamaged (top) to 25 thermal cycles (bottom).

The slab, sample "E" was cut after final cycle as shown in Figure 7.39. The cutting area includes the total scanning area to verify internal cracking. Figure 7.40 shows a comparison with an actual internal cracking condition. The author inspected and compared the SEM image among low cycles damage. Multiple microcracks (more than 6 um) appeared at the 6-cycle stage. The higher energy EB_{nor} region shows multiple microcracks that are bigger and denser than the other area.

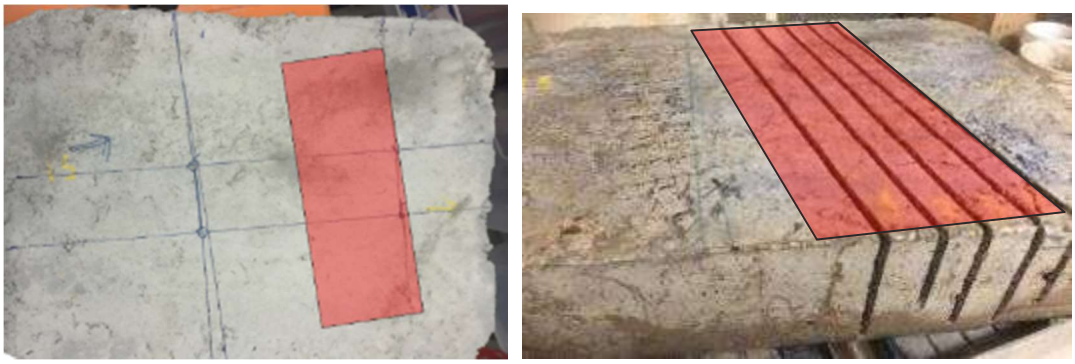

Figure 7.39 Slab sample E: (left) the top surface of sample where scanned area is indicated by red box, and (right) top surface after cutting.

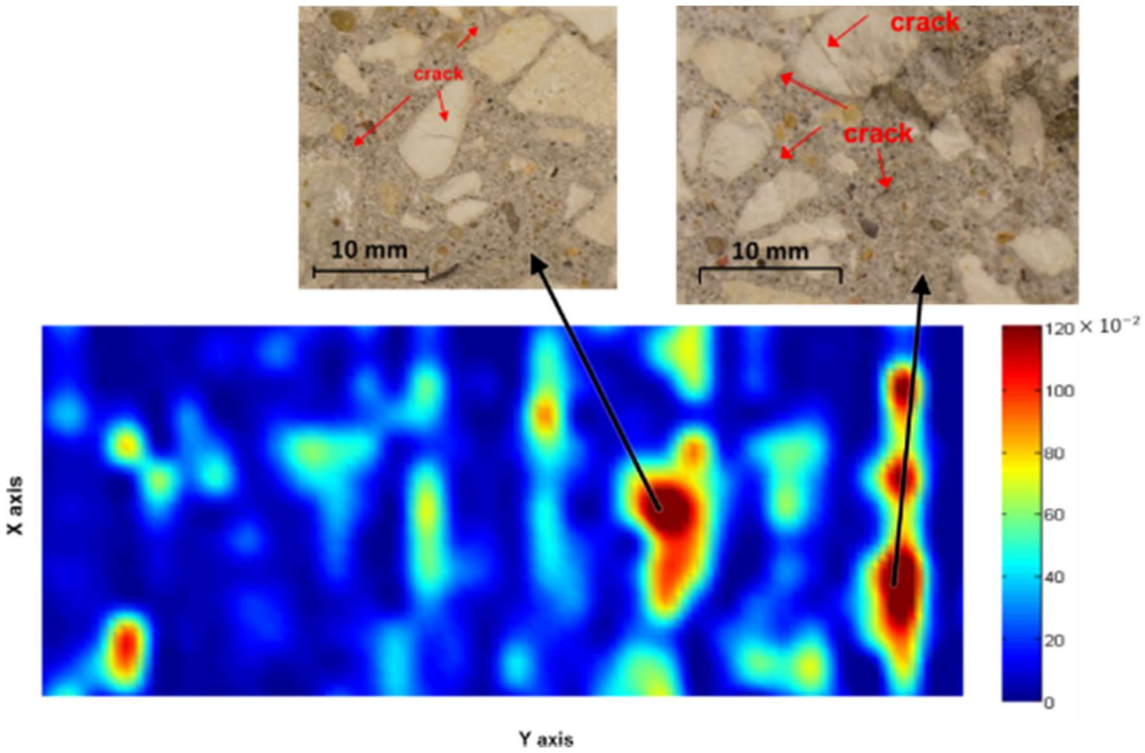

Figure 7.40 Normalized backscatter parameter across scan area for the case of 25 thermal cycles (represented from Fig. 7.38) with high-resolution optical image insets showing damage at regions of high backscatter. Color bar represents EB_{nor} Values.

CHAPTER 8 APPLICATION OF SURFACE-GUIDED WAVES FOR INTERFACIAL DAMAGE (RSD) CHARACTERIZATION IN RAIL TIES

Contactless UT surface waves are deployed to characterize the interfacial condition between a concrete and rail pad system affected by rail seat deterioration (RSD). More detailed explanations of RSD may be found in section 2.1.3. An objective of this section is to develop a sensitive and nondestructive testing approach for the cost-effective inspection of a large number of concrete crossties. The surface wave will be generated between the top of the concrete rail tie and the bottom of the polymer-bearing pad. This task will be completed in an effort to understand the relationship between damage and surface wave behavior. It will then develop robust signal generation techniques and effectively deploy these concepts and methodologies for testing concrete. Experimental results can quickly provide clear distinctions among the different damage levels with statistical analysis not only by close proximity scanning but also by the practical, new large offset. Fully contactless (with a MEMS) systems were used. 60 kHz fully contactless ultrasonic surface waves were sent and detected along the top surface of the concrete rail tie sample in all RSD test. Specific mixture design information of the specimens are addressed in the each section. All concrete rail tie samples have a maximum aggregate size of 2 cm.

8.1 Close Proximity Scanning

In this section, close proximity (CP) scanning techniques are applied. The scan distances are typical contactless testing configurations, providing an outstanding signal to noise ratio (SNR) of these signals that allows for a preliminary study and multiple analyses without interfering noise. This study investigate the inter-relations between damage and surface wave behavior. Signal analysis procedures are described in each subsection.

8.1.1 Specimens

Three rail tie samples, each with different RSD conditions, are studied: an undamaged sample (referred to as R1), a sample with moderate damage (referred to as R2), and a sample with severe (referred to as R3), as shown in Figure 8.1 (bottom). The average vertical roughness for each case are detailed in the caption of the figure. The wavelength to severe roughness (R3 case) ratio is approximately 9. These samples were extracted from actual field rail structures, obtained through an agreement with the American Association of Railroads (AAR). The RSD damage severity was defined by the AAR, and is

based on visual observation of surface condition underneath the pad. Aside from the RSD damage level, these samples are similar to each other in terms of constituent materials and age.

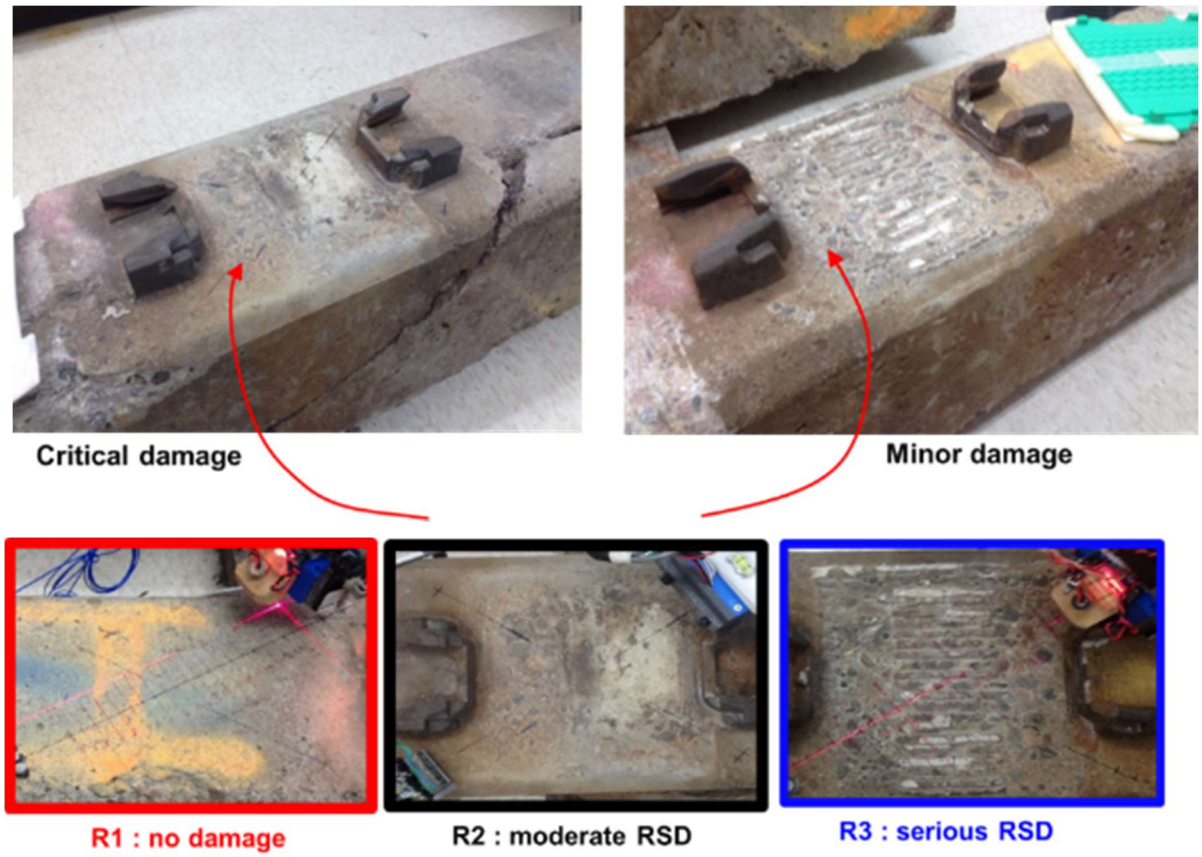

Figure 8.1 Photos of different levels of damaged RSD samples in concrete rail ties; (top) full perspective and (bottom) detail of three different levels of RSD damage. : R1 has less 1 mm average vertical roughness, R2 has 2 mm average vertical roughness, and R3 has 5 mm average vertical roughness.

8.1.2 Diagonal Scanning: Tests With and Without Rail Pad

The ultrasonic system with an auto-scanning frame collected surface wave datasets of RSD regions, as shown in Figure 8.2 (top right). This sample of conditions revealed very limited access to generate either contact or noncontact mechanical signals on the concrete. Possible positions for senders and receivers are at the corner of the rail pad in order to generate maximum energy (see Figure 8.2 top left and top middle). The contactless sender generates surface waves, which propagate onto the RSD region. A

seven-sensor contactless receiving array system was designed: the MEMS sensors were positioned next to each other in order to receive seven concurrent surface wave signals, as shown in Figure 8.2 (bottom). This system allows for fast scanning and collection of multiple datasets.

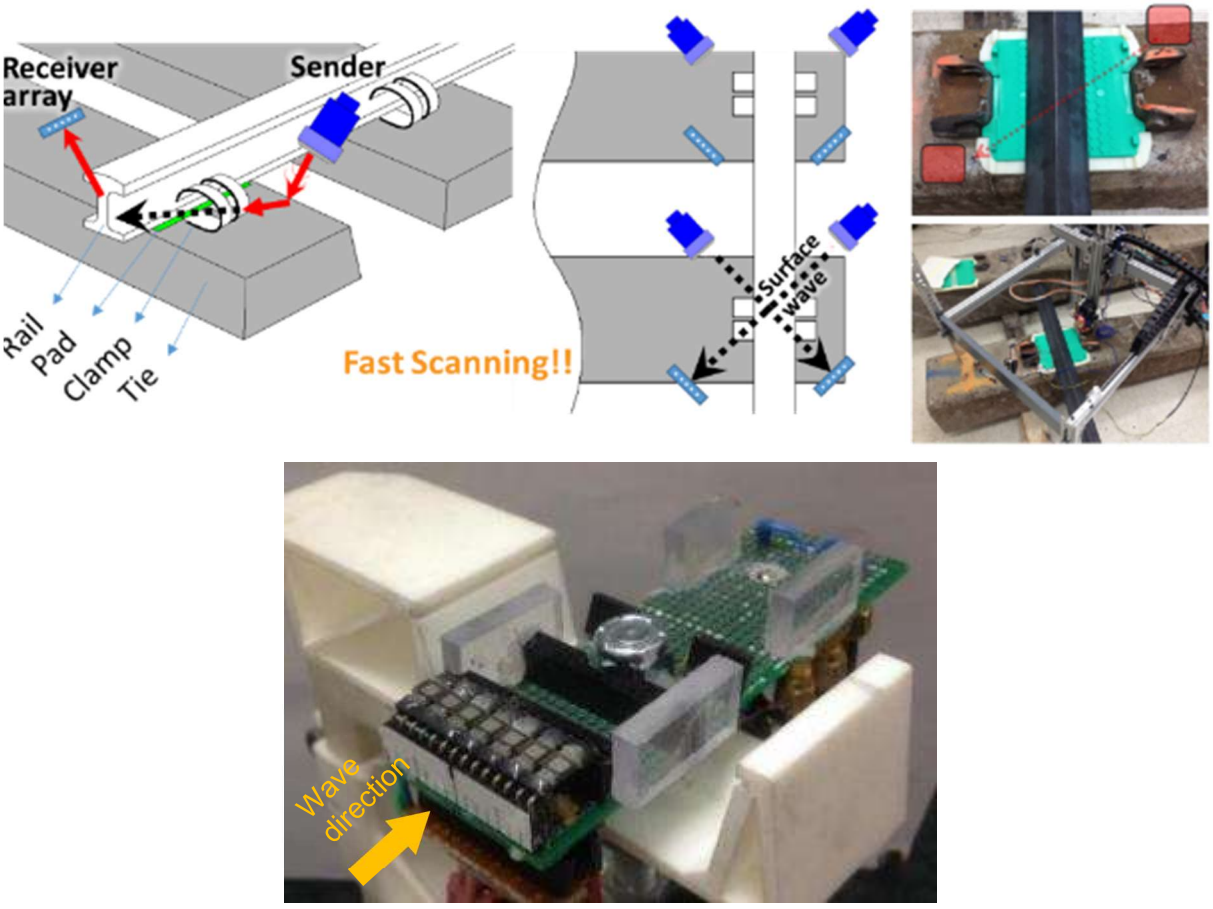

Figure 8.2 Illustration of close proximity (CP) testing configuration: (top row) wave direction and position of sensors, and (bottom row) contactless receiving-sensor array, with sensors spaced laterally 2 mm.

In practical conditions, the rail pad and the rail are supposed to be placed on a RSD region. The primary test examines the effect of padding. As described in section 8.1.2, a fully contactless ultrasonic system was used. Figure 8.3 shows the testing conditions for the effect of rail padding. In one case, the surface wave propagated without a rail and a pad on the concrete rail tie, as shown in Figure 8.3 (left). Another case involves a pad and steel material that had practically the same pressure as that of a rail seat on the area. Results from the two different tests are compared.

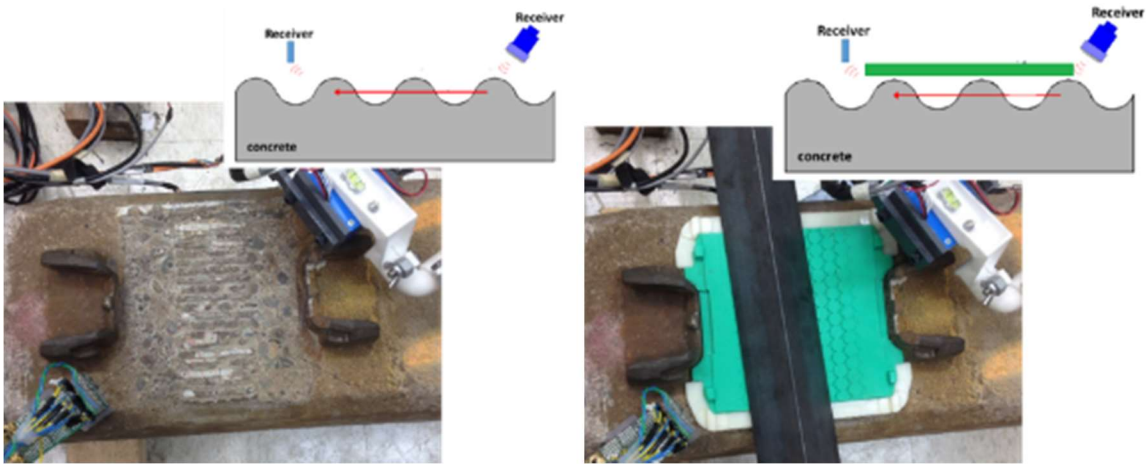

Figure 8.3 Illustration of close proximity tests of RSD samples: (left) tie surface without pad, and (right) tie with pad and rail load on top.

Figure 8.4 shows two overlaid time signals for the effects of the rail pad. All solid lines in the figure indicate the results without a pad, while the dotted lines indicate signals with pads. The two cases show almost identical signals in raw time until 600 us. Subsequently, a large wave component is revealed. In contrast, direct acoustic waves arrive at a later time (900 us). This additional wave is from the plastic rail pad, which is identical to the expected surface wave speed in plastic sheets. The surface wave velocity of plastic is much slower than the surface waves of concrete. From this result, the rail pad does not affect signals. Therefore, a test without a pad would have a similar result. This information also shows that different kinds of rail pads would not affect the signal.

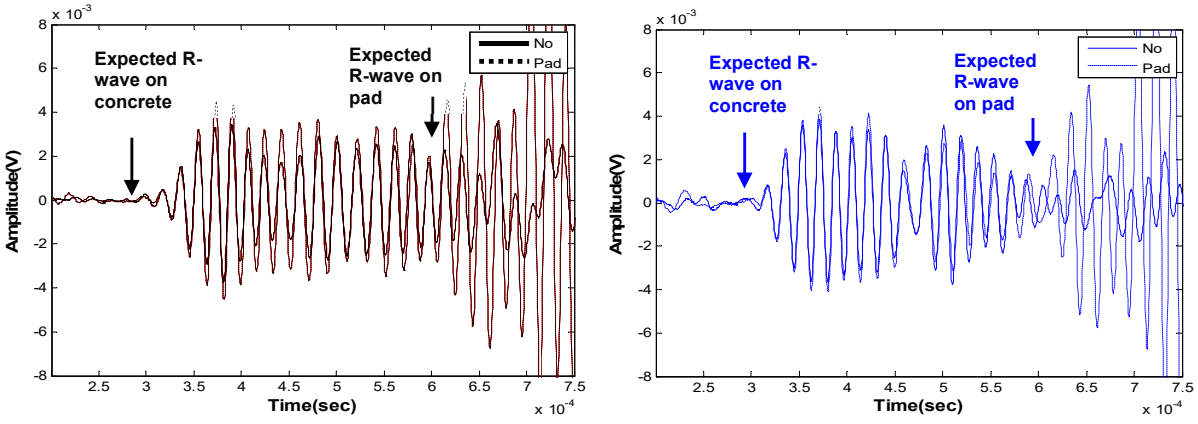

Figure 8.4 Overlapped time signals and effect of rail pad: (left) testing on R2 sample with and without pad, and (right) testing on R3 sample with and without pad.

8.1.3 Energy Attenuation Analysis by STIA

The low frequency (60 kHz) used with inhomogeneous materials presents a challenge for the use of diffuse wave analysis. There are also existing limitations for the use of the coherent wave technique, due to similar arrival times of surface waves and inconsistent trends of amplitude at coherent parts in the three different fibered samples analyzed. In this section, experimental results from concrete samples with randomly distributed synthetic cracks are presented. Figure 8.5 shows expected, reasonable trends of short-time-interval average signal (STIA) described in section 2.5.3. Each plot shows spatially-averaged data from four different path locations. STIA energy, E_{STIA} is computed by integrating by the logarithm STIA signal, ln (E) over some time range. E_{STIA} is an index to indicate the amount of energy loss owing to scattering in the concrete sample.

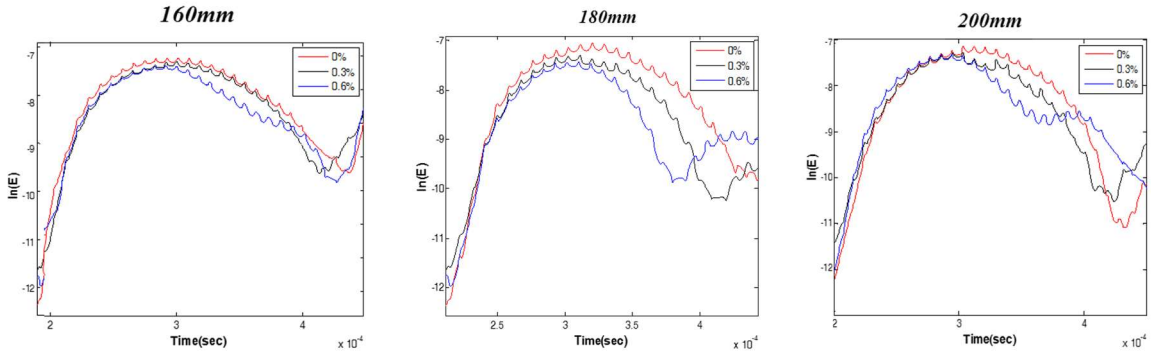

Figure 8.5 Illustration of signal data processed to exhibit diffuse wave characteristics for three different surface wave path lengths: 160mm (left), 180 mm (center), and 200 mm (right).

8.1.4 Characterization of RSD with STIA

The next test develops a system to distinguish three different levels of damage with the STIA approach: solid, undamaged sample (R1), mild damage (R2), and severe damage (R3). As previously described, the STIA approach was used for characterizing different damage levels of RSD samples. Figure 8.6 (left) shows time signals for the three types of samples. Figure 8.6 (right) shows the results of integrate signal energy analysis. From the figure, R1 indicates the largest amount of ln(E), most of which is dominant in the early stage due to the fact that it has less scattered energy compared to other damaged samples. R2 shows slightly higher ln(E) than R3. These results are expected and based on ordinary visual inspection. However, the integrated signal energy analysis is more effective than visual inspection or raw time signals, because it allows us to see more clearly how ln(E) changes over time and how much energy

dominates, depending on different levels of damage. Although individual signal data are reasonable, there are not enough data to be statistically reliable for inhomogeneous concrete.

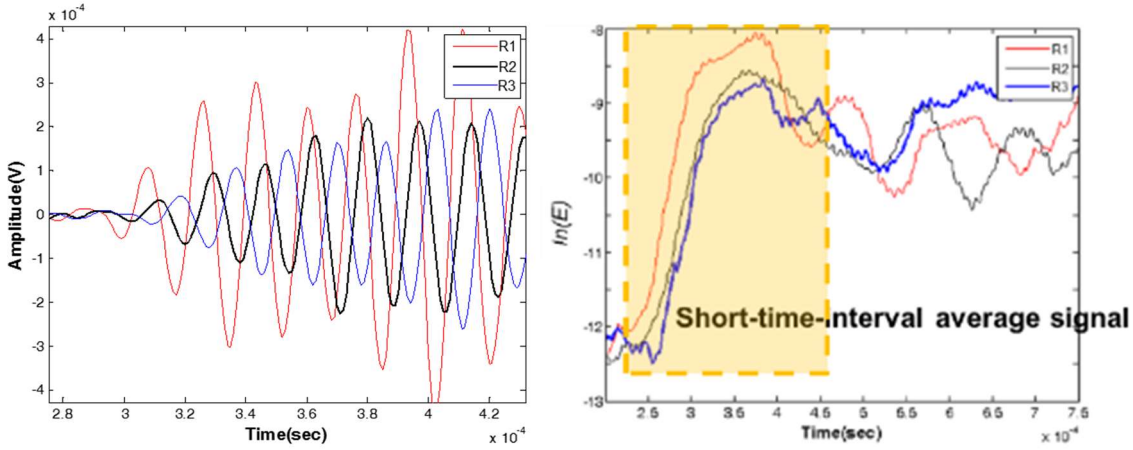

Figure 8.6 Experimental results for three cases of RSD damage: (left) time domain signal, and (right) integrated signal data. Data used for STIA analysis shown by dashed line.

Now, instead of receiving an individual signal, the author used an array of seven MEMS sensors to detect multiple signals at once. Instead of scanning diagonally, the author now scan perpendicularly to the rail tie direction as shown in Figure 8.7 (right and left). Ten different positions were scanned. Each group used seven MEMS sensors. Overall, 70 signals were collected for each level of damage, A spatially averaged signal is calculated by

$$\boldsymbol{ln(E)} = \frac{\mathbf{1}}{\boldsymbol{N_{path}}} \sum_{\boldsymbol{y=1}}^{\boldsymbol{N_{path}}} \boldsymbol{ln(E_i)_{avr\_y}(t)} \qquad (8.1)$$

where, $\ln(E_i)$ is the STIA signal of the i^{th} path and $\ln(E)$ is spatial average of $ln(E_i)_{avr\_y}(t)$. The averaged signal is obtained from seven MEMS sensors.

Figure 8.7 UT surface wave vertical testing configuration: (left and right) photos showing contactless UT system for multiple scan lines.

Testing results are shown in Figure 8.8. The integrated signals (STIS) show stronger distinctions among the three different damage levels of samples. Figure 8.8 (bottom left) shows the highest energy, while Figure 8.8 (bottom right) shows consistently low values of ln (E), due to scattering in the damage region. In general, surface waves show the maximum energy and the least delay when there is no damage. However, damage causes surface wave to delay and energy to fragment. At the middle damage level, a partial group shows no surface wave delay, and another group shows delay and energy fragmentation. In addition moderate level and severe damage show humps with STIL result (see bottom row in Figure

8.8). The author could clearly explain the behavior, but delamination underneath the RSD region is placed possibly.

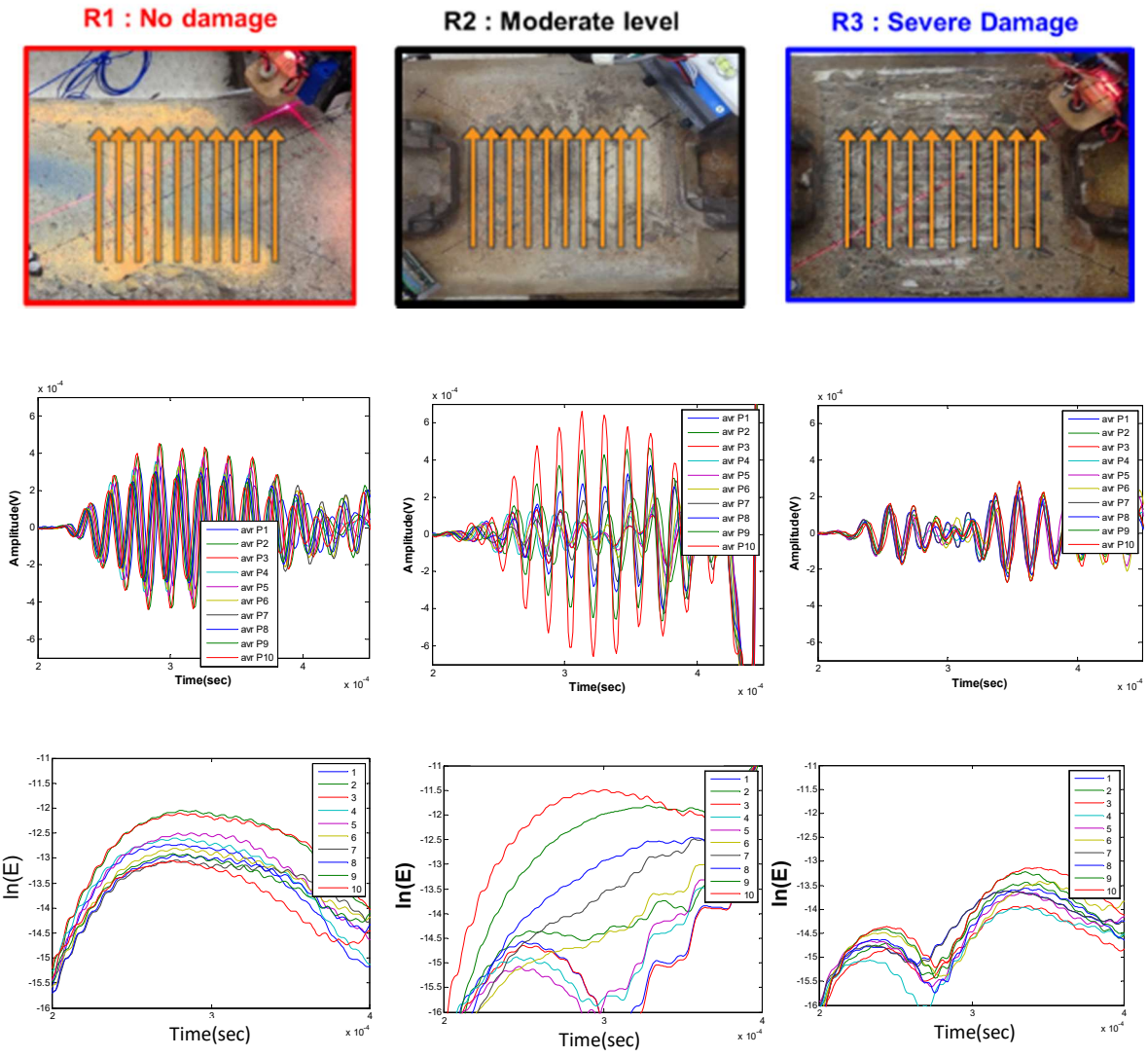

Figure 8.8 Close proximity test results from RSD samples; (top row) testing configuration with scanning direction for each specimen, (middle row) ten averaged time signals collected from 7 MEMS sensor, and (bottom row) STIA processed data obtained from raw time signals.

The energy of the STIA signal, defined as E_{STIA} , is calculated by

$$E_{STIA} = \int_{t1}^{t2} |ln(E)|^2 dt. \qquad (8.2)$$

where, t1 is 0 and t2 is 3.2^{-4} seconds. After the allotted time, the direct acoustic waves arrived. Figure

8.8 shows a procedure of statistical analysis for averaged E_{STIA}. A large amount of data is needed for reliable testing results because the material is concrete, which is inhomogeneous. Also, statistical analysis facilitates an understanding of distributed energy values in each position. Note how the figure (left) shows that an averaged integrated signal is calculated from seven contactless receivers. Therefore, a boxplot in the figure includes seven datasets. The red bar in the box indicates the median value, and the length of the box shows the range of the dataset (statistic distribution).

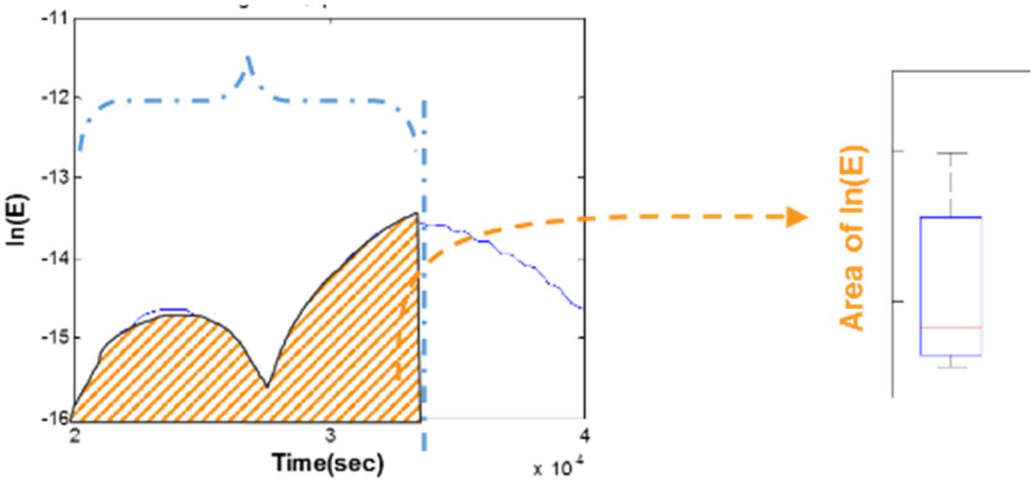

Figure 8.9 Illustration of the calculation process for E_{STIA}: (left) average of STIA(t) signals, (right) a box plot comprising seven E_{STIA} data which are calculated by area of each STIA(t) signals shown by the shaded area.

The sample is a seriously damaged sample (R3), which is shown in Figure 8.8 (bottom right). Figure 8.9 (right) shows the boxplots from ten different positions. These ten different boxplot values indicate local E_{STIA} distribution. Figure 8.10 shows a comparison of E_{STIA} among three different levels of damage. Each dashed line indicates the total average of ten box plot values. The total averaged $E_{STIA}$is the highest for R1, and it is lowest for R3. One significant point is that the total averaged value of R2 is between those of R1 and R3. Also, R2 has two different groups of E_{STIA} values. One side is high, while the other side is lower. This indicates that the sample has more damage on one side than the other. Therefore, these statistical analyses easily detect damage levels.

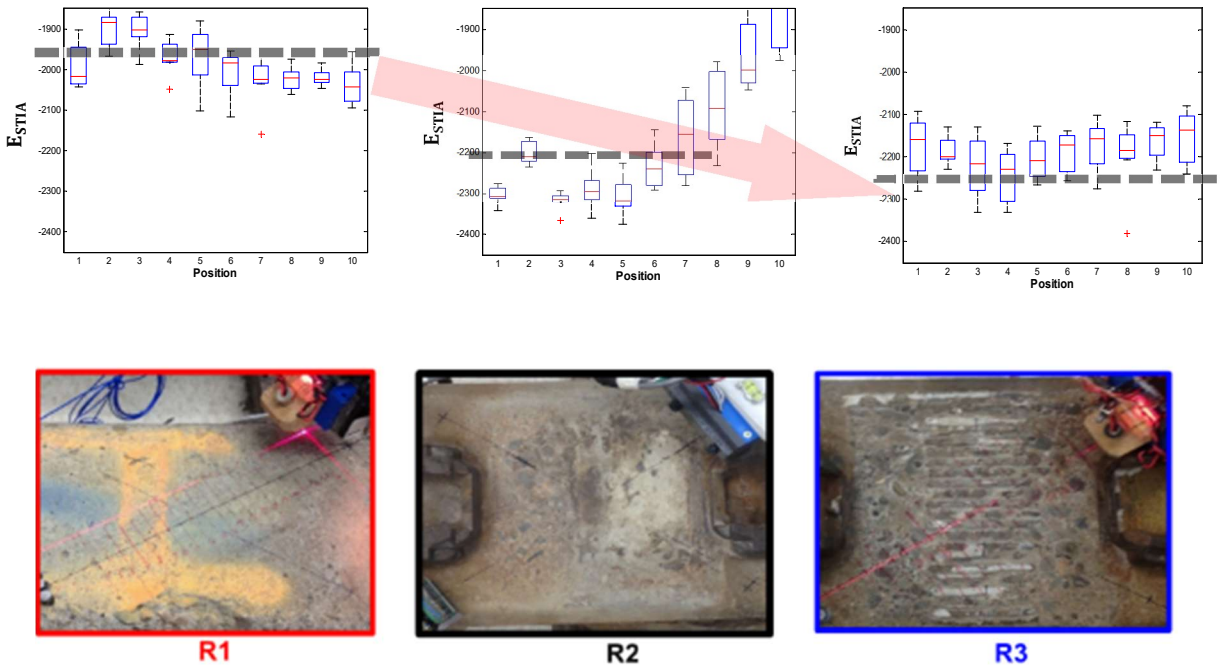

Figure 8.10 E_{STIA} data collected from rail tie samples: (top row) E_{STIA} values for each damage condition, where dashed lines indicate average value, and (bottom) photos showing three different RSD damage level images, which correspond to the top row results.

8.2 Large Offset Scanning

Large offset prototype and analysis procedure for field-testing were prepared and tested. Various parametric studies of sender height and reviver height were investigated to find the limitation of the offset configuration. All signal values and analysis are reposted in the section.

8.2.1 Preliminary Tests on Undamaged Rail Tie Sample

The preliminary test, comprised of two parts, includes a long scan distance between sender and receiver to prepare for practical field-testing without damage characterization. Notably, the energy loss can affect signal analysis. The main purpose of testing is to identify the extent to which a greater offset distance decreases the amplitude of leaky waves. In the first part, the sender retains a short offset distance of 35 mm, while the receiver offset distances are varied from 10mm to 200mm in 10 mm increments.

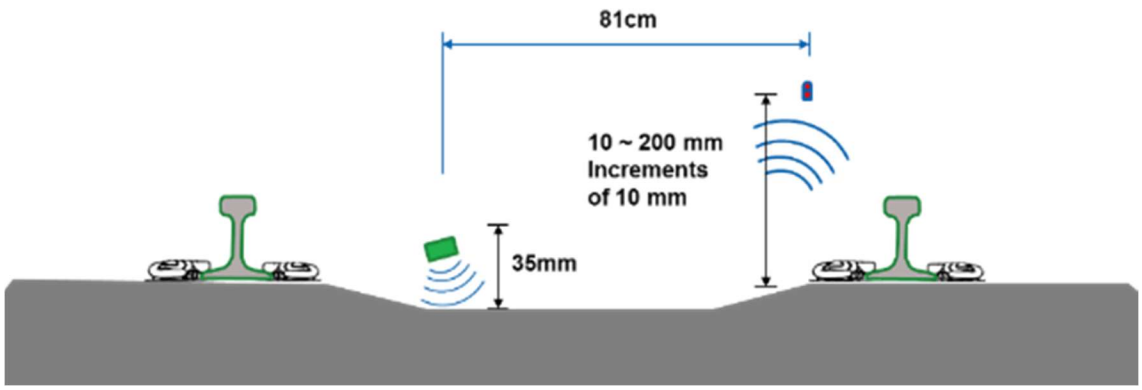

Figure 8.11 Testing configuration for the large offset system with varying receiver height from 10 to 200mm.

Figure 8.12 shows testing results. The figure (left) shows 20 time signals with varying receiver heights. Blue indicates the shortest offset, while red indicates the largest offset. The whole surface wave signal dataset shows clear results. The figure (right) shows the peak amplitude of each signal. There is a 20 % decrease from shortest to largest offset results.

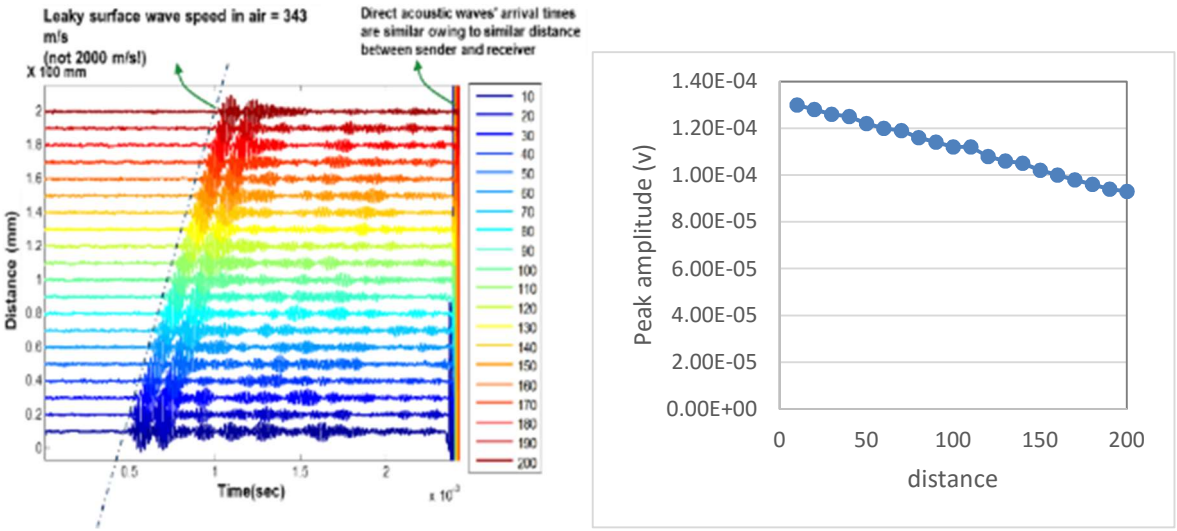

Figure 8.12 Large offset test results with varying receiver offset distance: (left) 20 time signals where the color scale indicates specific path distances and (right) peak amplitudes of each signal.

The construction of the second test is the same testing configuration as the first test except for the sender heights. In the second test, the sender heights are varied with a fixed receiver height of 200mm, as shown

in Figure 8.13. These testing results inform our understanding of attenuated energy of surface waves with a larger sender offset. Next test is study of various sending height with fixed 200 mm.

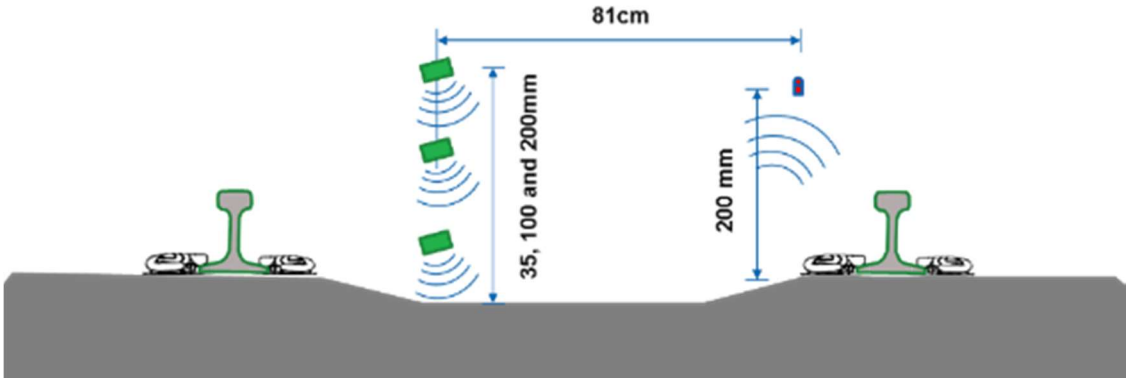

Figure 8.13 Large offset scanning configuration with varying sender height.

The testing results are shown in Figure 8.14. The figure (left) shows three time signals with varying sender heights. In this test, our goal is fast data collection. The signals were collected within 2ms without time-averaged processing. Considering there was not a time-averaged process, these results show higher SNR. The figure (right) shows the third peak amplitude of each sender height. Amplitude decreased by only 2.3 percent from 30 mm to 200 mm, which is a strong field testing condition. Compared to Figure 8.12 results, the amplitudes are additionally decrease by 20% due to sender height increase as well. However, overall signals have good SNR.

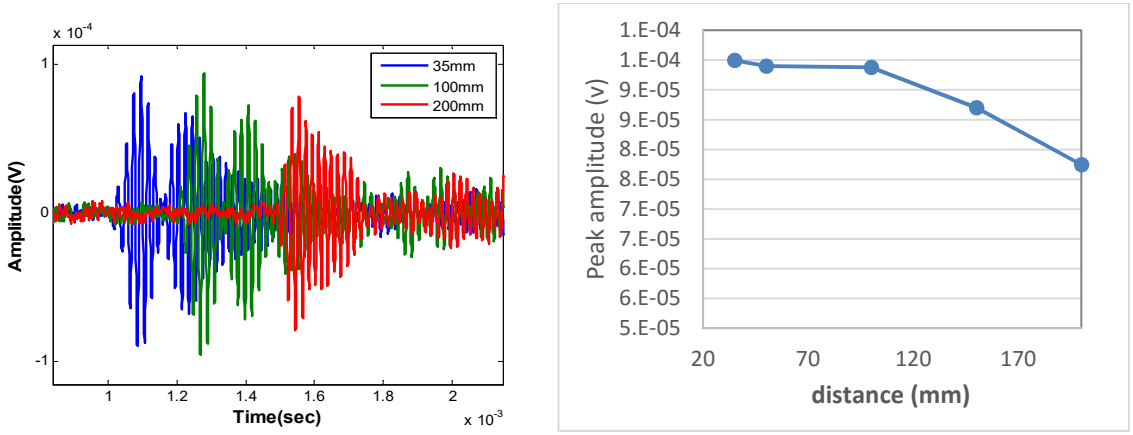

Figure 8.14 Large offset test results with varying sender offset distance: (left) 3 time signals, where the colormap indicates specific distance and (right) peak amplitude of each signal.

8.2.2 Large-Offset Configuration for Characterizing Different RSD levels

This section studies different levels of damage with long distances between senders and receivers, and large offsets between concrete surface and senders/receivers. Figure 8.15 shows three different samples: one with no damage (referred to as "R1"), and moderate damaged and severely damaged regions (referred to as "R2" and "R3" respectably), which are from the same specimen. The damage levels of the two regions cannot be distinguished by visual observation.

Figure 8.15 shows the testing configuration for scanning these three different samples. Offset distances from both receiver and sender are 250 mm, which is a safe range for clearing rail in field tests. Surface wave propagating distance between sender and receiver is 850 mm throughout the rail seat. There are 5 mm gaps between the sensors in the 2-D array as shown in the figure. These seven receivers collected surface wave signals simultaneously for rapid scanning of the entire seat area.

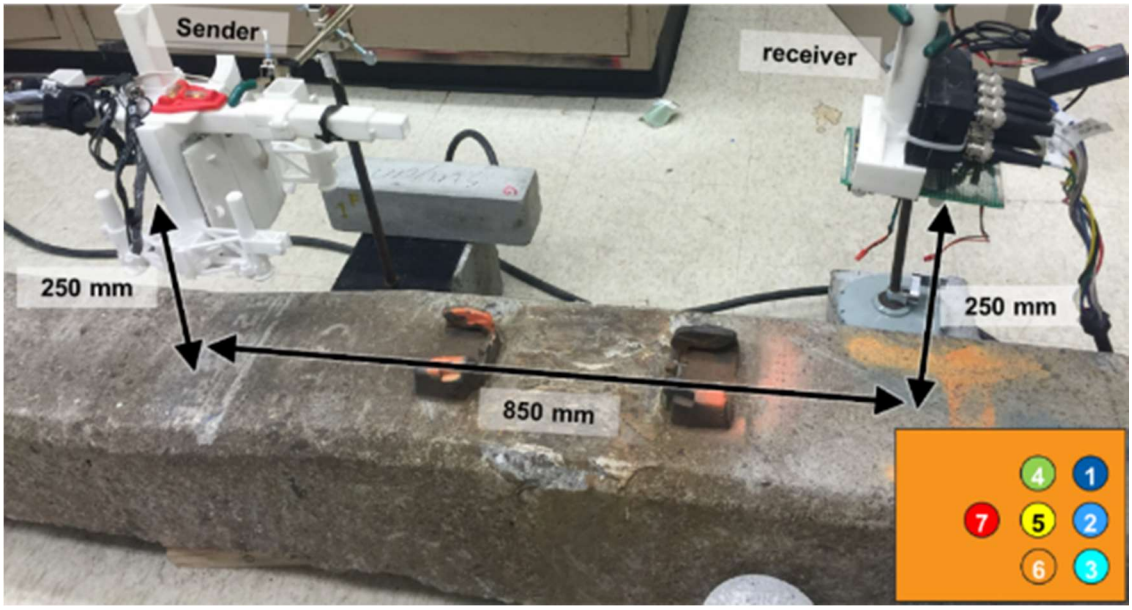

Figure 8.15 Testing configration for large offset configuration across rail seat. 2-D array configuration shown in the inset.

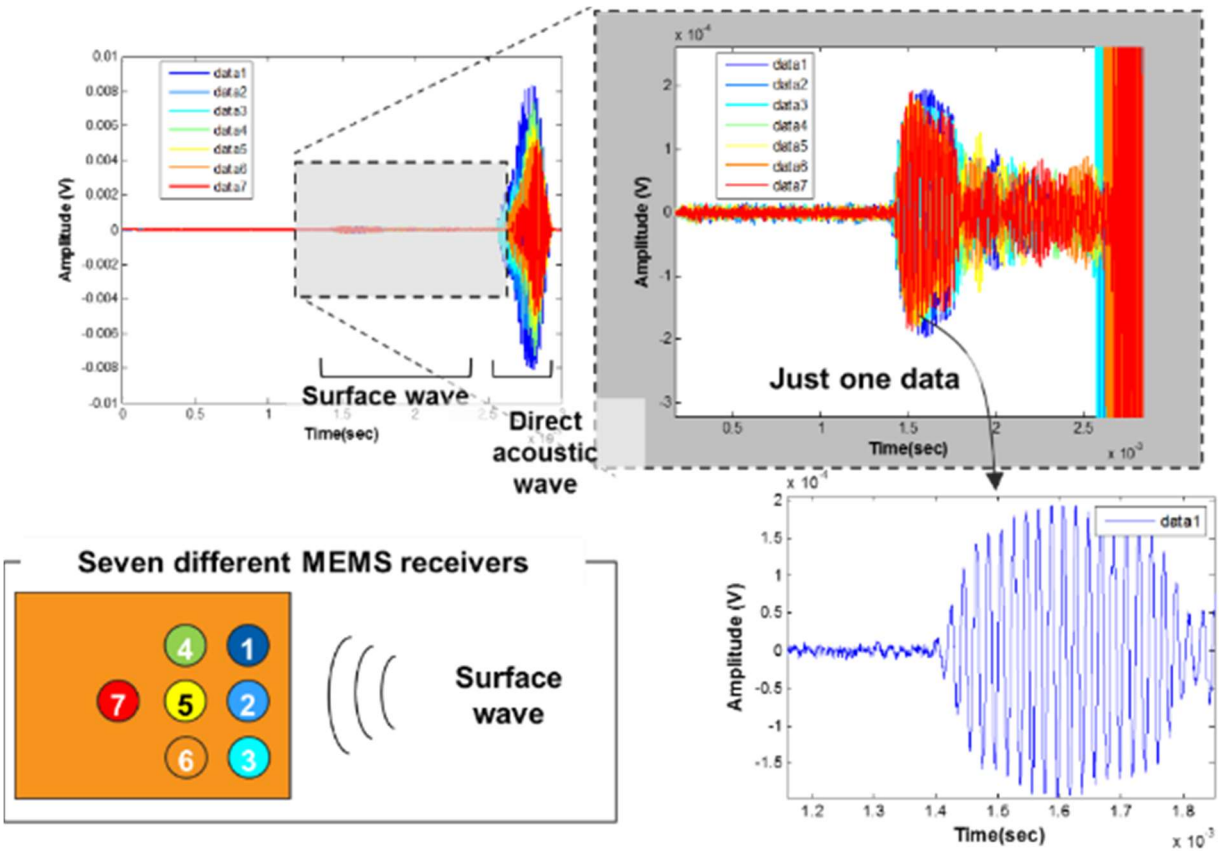

Figure 8.16 Large offet configuration results: (top row) raw time signals collected from 2-D array, (bottom left) testing configuration of 2-D array, (bottom right) typical individual surface wave signal.

The short-time integrate average signal (STIA) analysis is applied. Figure 8.17 represents how the results indicate a clear distinction between the solid and two damaged samples. E_{STIA} values are also calculated. E_{STIA} are -9.2 x 10^3, -10.7 x 10^3, and -12.2 x 10^3 for R1, R2 and R3 respectively. Smaller value indicates more energy loss due to scatterings. The value of the area of the STIA analysis shows that Solid has the highest value, which means less wave scattering by damage. R3 shows a lower value than the R2 value; however, there is no verification.

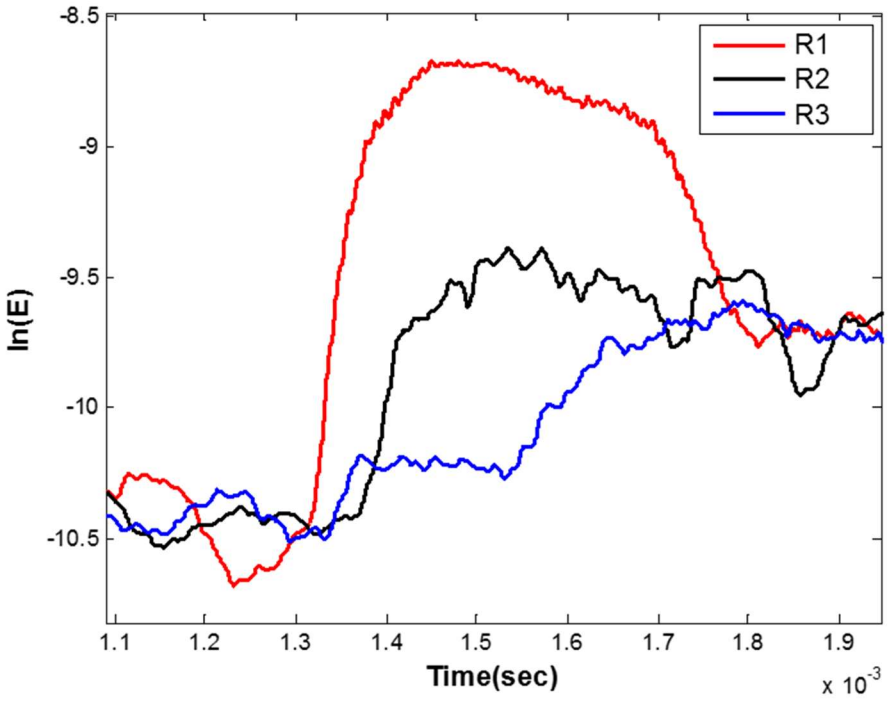

Figure 8.17 Test result from short-time integrated signal analysis using the large offset testing configuration.

Based on the data collected from the lab samples, an ultrasonic data analysis scheme was developed to reliably characterize the existence and severity of RSD *in situ*. The analysis scheme is designed in a manner by which it may be employed by a non-expert. The mobile platform will be deployed on a real concrete tie specimen with consideration for the limitations imposed by geometry and space. Thus, a large offset testing setup with SIS analysis can characterize different levels of the RSD condition.

CHAPTER 9 CONCLUSIONS

This thesis investigates the use of a fully contactless ultrasonic testing system for defect characterization in concrete structures. The following conclusions are drawn based on the conducted numerical and theoretical analyses and experiments.

9.1 Air-coupled Sensor and Hardware Development

Air-launched sending (capacitive membrane) and contactless receiving transducers are developed, along with associated necessary hardware. All hardware and software were designed and assembled by the author. Three types of contactless air-coupled sensors (condenser and dynamic type microphones and modified MEMS sensors) were evaluated to detect leaky surface wave propagation, Lamb wave propagation, and vibration resonance in concrete. Experiments indicate that suitable air-launched ultrasonic surface waves can be generated in concrete, and furthermore that all sensor types can reliably detect propagating leaky surface waves that resonate from the concrete surface and propagate in air. The following specific conclusions are drawn.

- A fully contactless ultrasonic system, comprising the contactless sending (capacitive membrane) and receiving (MEMS) transducers, provides consistent coupling conditions, allowing surface wave propagation measurements to be conducted with improved sensitivity and confidence.

- Modified air-coupled sending transducers with field-programmable-gate-arrays (FPGA) having rapid response times can be used to generate controlled signals, such as Gaussian pulses with specific center frequency and bandwidth and chirp signals.

- MEMS sensors show consistent ultrasonic leaky surface wave detection in terms of time signal amplitude and phase. The signal amplitude consistency of the air-coupled transducers is superior to that obtained with conventional contact sensors (accelerometers). Air-coupled sensors can provide suitable signals even when applied to rough surface conditions.

- MEMS sensors offer significant advantages over other sensor types, such as low cost, small size (good spatial resolution), and broad frequency bandwidth, thus better enabling implementation in multi-sensor arrays.

- Multi-sensor arrays offer testing and data collection advantages that enable powerful surface wave analysis schemes, such as seismic surface wave methods (e.g. multichannel analysis of surface waves, or MASW).

- Testing configuration parameters, such as sensor height and sender incident angle, should be well controlled in order to obtain high quality surface wave signals. Optimized testing configurations for the fully contactless UT system are recommended.

- Multiple insulation baffle layers positioned between sender and receiver improve the amplitude and signal-to-noise ratio of air-coupled signals provided by the developed testing hardware. The electronics design also reduces electrical and ambient noise content through the incorporation of shielded cables and the shielded sensors housings.

- The well-controlled scanning frame that incorporates the sensors offers rapid data collection and imaging capability and, furthermore, it provides consistent and well-controlled ultrasonic signals.

9.2 Delamination Damage Characterization

The developed air-coupled ultrasonic testing configuration was applied to detect delamination using Lamb wave interpretation of MASW-type data. 3-D plots were generated, which are built up from Lamb mode changes (phase velocity shifts), to identify regions above delamination defect. The following specific conclusions are drawn.

- The developed fully air-coupled ultrasonic testing system provides consistent data from concrete with sufficient signal to noise ratio to deploy MASW-type measurements.

- The broadband air-launched transducer modified by the author is an important component with the developed MASW approach for delamination detection because various frequency for energy shift will be observed depending on depth. Therefore, in practical issue, the broad band signals are important to investigate various or unknown depth of delamination cases.

- The Lamb wave energy-jump condition is defined by shifting of dominant energy between fundamental symmetric and antisymmetric Lamb modes. The energy shift occurs at specific frequency for a given plate (delamination) thickness. In this way, the jump condition frequencies distinguish delaminated from full thickness regions in a solid. Specifically, as the frequency at the jump condition decreases, the delamination defect thickness increases. Effect of other material properties (poison ratio, elastic modulus and density) are not significant to the jump condition.

- Multiple data can be used to construct a 3-D image comprising stacked 2-D images that identify delamination defects. The 3-D image clearly show boundary of deamination area. The performance of the 2-D slice images are comparable to those from the existing NDT method impact-echo indicating similar damage area. As such, the method shows promise for rapid and effective bridge deck evaluation.

- Excitability of the S0 mode decreases with increasing Poisson's ratio, and the energy shift will eventually disappear at large Poisson's ratio. Further studies are warranted to explore interesting aspects of this behavior.

9.3 Scatter and Microcracking Damage Characterization

Using the developed air-coupled testing configuration, ultrasonic surface wave backscatter measurements were used to characterize distributed microcracking damage in concrete. Backscatter parameters were extracted using time domain energy subtraction analysis (ESA) and spectral variance analysis (SVA). The backscatter energy measurements are sensitive to the presence of distributed microcracks, providing better performance than conventional coherent pulse UT approaches. Backscatter data enable statistically significant distinctions between moderate damage levels in concrete. The collected backscatter data are also applied to the image and identify localized regions of damage. The following specific conclusions are drawn.

- Scattered field data, extracted from time signals, can be obtained using a fully contactless ultrasonic system. Air-launched ultrasonic surface backscatter data provide distinction between several different extents of distributed microcracking damage in concrete. Thus, characterization

of sub-wavelength sized defects is possible with ultrasonic surface wave backscatter field data. Data from conventional forward propagating coherent pulse analysis are not able to distinguish those same damage states.

- Most backscatter responses arise from distributed microcracks located in front of the ultrasonic sender. Microcracks located behind the sender contribute minimally to the backscatter energy.

- The developed normalized backscatter energy parameter allows generalized measurements that appear to be independent of the testing setup, showing a monotonic increase in value as the internal cracking damage content increases.

- The proposed method offers a consistent, sensitive and practical non-destructive testing (NDT) approach to monitor actual distributed cracking in concrete, potentially enabling imaging that identifies specific distributed near-surface damaged areas in a structure.

- Overall maximum aggregate size was 2 cm. Different types of concrete with different maximum aggregate size will be compared with the backscattering energy.

9.4 Interfacial Damage Characterization (RSD) in Rail Ties

Air-launched surface waves are used to interrogate interfacial damage related to rail seat deterioration (RSD) in concrete rail ties. Results provide distinctions among different RSD levels. Close proximity and large-offset scan configurations, appropriate for application to rail structures in situ, are proposed. The following specific conclusions are drawn

- The developed fully air-coupled ultrasonic testing system, using multi-sensor MEMS array receivers, provides consistent data from rail tie structures. The configuration works across multiple ray paths and sensor heights, and is applicable to rail pad- ties interfaces with overlying rail.

- Fully UT system can characterize within different RSD condition, either through velocity or attenuation (wave energy) measurements. The attenuation of the surface wave signal

amplitude is more sensitive to the presence of damage surface than the surface wave velocity.

- Short-time-interval average signal (STIS) analysis allows for clear distinctions between RSD damage levels in concrete tie test samples from in-place measurements. The total energy loss of STIS indicates RSD damage level.

- The large (250mm) offset testing configuration provides some ability to detect among different damage levels. A testing prototype for field verification that uses this configuration is feasible.

9.5 Future work

Ultimately, the findings presented in this thesis can be used to develop a fully contactless UT scanning prototype that makes use of optimal data acquisition and advanced analysis techniques to enable large sections of bridge deck, large spatial structures such as nuclear power plants elements, and rail structures to be inspected in a timely and efficient manner. Successful implementation will provide new technology for a more resilient and sustainable infrastructure. In order to achieve the goal of successful implementation, the following issues should be addressed:

- The Lamb wave jump condition should be studied further, considering various types of material properties and delamination conditions. An analytical model that describes the jump condition behavior, especially for contactless sensing, would be helpful to guide the research.

- The development of an analytical random scattering model would be helpful to provide deeper understanding and guide future research on the surface wave backscatter approach. Furthermore, a more complete understanding of the technical basis for the spectral variance model is needed. Application of the backscatter approach to concrete with a range realistic damage types (ASR, Freezing & thawing) and extents is important in order to move toward field application of the method.

- Development of a practical testing prototype that enables moving, continuous application of the developed contactless ultrasonic testing approach to rail structures in situ is appropriate at this time and needed for field verification and implementation.

REFERENCES

Abraham, O. et al., 2012. Non-contact, automated surface wave measurements for the mechanical characterisation of concrete. *Construction and Building Materials*, 37, pp.904–915.

ACI Committee 349, 2002. Evaluation of Existing Nuclear Safety-Related Concrete Structures. *Report ACI 349.3R-02, American Concrete Institute, Farmington Hills, MI.*

Aggelis, D.G. et al., 2011. NDT approach for characterization of subsurface cracks in concrete. *Construction and Building Materials*, 25(7), pp.3089–3097.

Aggelis, D.G. & Shiotani, T., 2009. Effect of Inhomogeneity Parameters on Wave Propagation in Cementitious Material. *ACI Materials Journal*, April(105), pp.187–193.

American Concrete Institute (ACI) Committee 228, 1998. *Nondestructive Test Methods for Evaluation of Concrete in Structures*, Rep. No.ACI 228.2R-98, Farmington Hills, Mich.

Anugonda, P., Wiehn, J.S. & Turner, J. a., 2001. Diffusion of ultrasound in concrete. *Ultrasonics*, 39(6), pp.429–35.

ASTM, 2008a. *Standard Test Method for Evaluating Asphalt-Covered Concrete Bridge Decks Using Ground Penetrating Radar D6087*,

ASTM, 2008b. *Standard Test Method for Fundamental Transverse , Longitudinal , and Torsional Resonant Frequencies of Concrete Specimens C 215-08*, West Conshohocken, PA.

Becker, J., Jacobs, L.J. & Qu, J., 2003. Characterization of cement-based materials using diffuse ultrasound. *Journal of Engineering Mechanics*, 129(12), pp.1478–1484.

Bishko, A. V, Samokrutov, A.A. & Shevaldykin, V.G., 2008. Ultrasonic echo-pulse tomography of concrete using shear waves low-frequency phased antenna arrays. In *Proc17th World Conference on Nondestructive Testing*. Shanghai, China, pp. 25–28.

Bjurstrom, H. & Rydèn, N., 2013. Aircoupled detection of the S1 ZGV lamb mode in a concrete plate based on backward wave propagation. In *AIP Conf. Proc.* Denver, Colorado, USA,15-20 July 2013, pp. 1294–1300.

Carr, H. & Wykes, C., 1993. Diagnostic measurements in capacitive transducers. *Ultrason.*, 31(1), pp.13–20.

Chen, J. et al., 2010. Rapid evaluation of alkali–silica reactivity of aggregates using a nonlinear resonance spectroscopy technique. *Cement and Concrete Research*, 40(6), pp.914–923.

Chen, X.J. et al., 2008. Characterization of progressive microcracking in Portland cement mortar using nonlinear ultrasonics. *NDT & E International*, 41(2), pp.112–118.

Cowan, M. et al., 1998. Group velocity of acoustic waves in strongly scattering media: Dependence on the volume fraction of scatterers. *Physical Review E*, 58(5), pp.6626–6636.

Deroo, F. et al., 2010. Damage detection in concrete using diffuse ultrasound measurements. In *AIP Conference Proceedings*. American Institute of Physics, pp. 1509–1516.

Deroo, F., 2009. *Damage detection in concrete using diffuse ultrasound measurements and an effective medium theory for wave propagation in multi-phase materials*. MS Thesis, Georgia Institute of Technology.

Elderton, W.P., 1902. Tables for Testing the Goodness of Fit of Theory to Observation. *Biometrika*, 1(2), pp.155–163.

Ganji, B.A., 2011. *Design and Fabrication of a Novel MEMS Silicon Microphone*, Rijeka, Croatia: InTech Press.

Garnier, V. et al., 2013. Acoustic techniques for concrete evaluation: Improvements, comparisons and consistency. *Construction and Building Materials*, 43, pp.598–613.

Gaydecki, P.A. et al., 1992. The propagation and attenuation of medium-frequency ultrasonic waves in

concrete : a signal analytical approach. *Meas. Sci. Technol.*, 3, pp.126–134.
Geoffrey Baskir et. al., 2013. 2013 report card. *ASCE*, p.500. Available at: http://www.infrastructurereportcard.org/a/#p/state-facts/sources.
Gordon, E., 2010. On the rails Wooden ties common but concrete ties last. *Techachapinews*. Available at: http://www.tehachapinews.com/lifestyle/x2027236298/On-the-rails-Wooden-ties-common-but-concrete-ties-last.
Goueygou, M., Popovics, J.S., et al., 2009. Microstructure Characterization in Cement Paste Using Backscattered Diffuse Ultrasound. *AIP Conference Proceedings*, 1528, pp.1528–1535.
Goueygou, M., Lafhaj, Z. & Soltani, F., 2009. Assessment of porosity of mortar using ultrasonic Rayleigh waves. *NDT&E International*, 42(5), pp.353–360.
Graff, K.F., 1991. *Wave Motion in Elastic Solids*, New York: Dover Publications.
Green, R.E., 2004. Non-contact ultrasonic techniques. *Ultrasonics*, 42(1-9), pp.9–16.
Gros, X.E., 1997. *NDT Data Fusion*, New york: Elsevier Science.
Gross, J. et al., 2013. Evaluation of near surface material degradation in concrete using nonlinear Rayleigh surface waves. *AIP Conference Proceedings*, 1309, pp.1309–1316.
Hall, K.S., 2011. *Air-coupled ultrasonic tomographic imaging of concrete elements*. Ph.D. Dissertation, The University of Illinois at Urbana-Champaign.
Ham, S. & Popovics, J.S., 2015a. Application of Micro-Electro-Mechanical Sensors Contactless NDT of Concrete Structures. *Sensors*, 15(4), pp.9078–9096.
Ham, S. & Popovics, J.S., 2015b. Contactless ultrasonic scanning approach toward automated inspection of concrete structures. *Automation in Construction,* 58, pp.155-164.
Ham, S. & Popovics, J.S., 2014. Fast Lamb Wave Energy Shift Approach Using Fully Contactless Ultrasonic System to Characterize Concrete Structures. In *AIP Conf. Proc*. p. 10.
In, C.-W. et al., 2009. Characterization of ultrasonic Rayleigh surface waves in asphaltic concrete. *NDT&E International*, 42(7), pp.610–617.
Janberg, N., 2013. Guldborgsundbro Bridge. *International Database for Civil and Structural Engineering*, p.1. Available at: http://structurae.net/structures/guldborgsundbro.
Jensen, J.A. et al., 2006. Synthetic aperture ultrasound imaging. *Ultrasonics*, 44 Suppl 1, pp.e5–15.
Kim, G., In, C.-W., et al., 2014. Air-coupled detection of nonlinear Rayleigh surface waves in concrete-Application to microcracking detection. *NDT & E International*, 67, pp.64–70.
Kim, G., Kim, J.-Y., et al., 2014. Quantitative evaluation of carbonation in concrete using nonlinear ultrasound. *Materials and Structures,*pp.1-11.
King, D., 2012. *Collapse dynamics of ultrasound contrast agent microbubbles*. Ph.D. Dissertation, University of Illinois at Urbana-Champaign.
Knowles, 2009. Datasheet: SPM0404UD5 Mini SiSonic Ultrasonic Acoustic Sensor. *Knowles Acoustics*, pp.1–10. Available at: http://media.digikey.com/pdf/Data Sheets/Knowles Acoustics PDFs/SPM0404UD5.pdf.
Krautkramer, J. & Krautkramer, H., 1990. *Ultrasonic Testing of Materials*, Berlin Heidelberg: Springer-Verlag GmbH.
Lamb, H., 1917. On Waves in an Elastic Plate. *Proceedings of the Royal Society A: Mathematical, Physical and Engineering Sciences*, 93(648), pp.114–128.
Landis, E.N. & Shah, S.P., 1995. Frequency-dependent stress wave attenuation in cement-based materials. *Journal of Engineering Mechanics*, 121(June), pp.737–743.
Larose, E. & Hall, S., 2009. Monitoring stress related velocity variation in concrete with a 2 x 10(-5) relative resolution using diffuse ultrasound. *The Journal of the Acoustical Society of America*, 125(4), pp.1853–6.
Lobkis, O. & Weaver, R.L., 2003. Coda-wave interferometry in finite solids: Recovery of P-to-S conversion rates in an elastodynamic billiard. *Physical Review Letters*, 90(25), p.254302.

Lynnworth, L.C., 1965. Ultrasonic impedance matching from solids to gases. *IEEE Trans. Son. Ultrason.*, SU-12, pp.37–48.
Maser R, K. & Roddis, W., 1990. Principles of thermography and radar for bridge deck assessment. *Journal of Transportation Engineering*, 116(5), pp.583–601.
Maslin, G.D., 1983. A simple ultrasonic ranging system. *The Journal of the Acoustical Society of America*, 73(S1), p.S58.
Mielentz, F., 2008. Phased Arrays for Ultrasonic Investigations in Concrete Components. *Journal of Nondestructive Evaluation*, 27(1-3), pp.23–33.
Mindess, S., Young, J.F. & Darwin, D., 2002. *Concrete (2nd Edition)*, Prentice Hall.
Morse, P.M. & Ingard, K.U., 1939. *Theoretical Acoustics, Ch 8: The Scattering of Sound*, New Jersey: Princeton University Press.
Naus, D.J., 2009. *A compilation of elevated of elevated temperature concrete material property data and information for use in assessments of nuclear power plant reinforced concrete structures*, Oak Ridge, TN.
Naus, D.J., 2007. *Primer on Durability of Nuclear Power Plant Reinforced Concrete Structures - A Review of Pertinent Factors*, Oak Ridge, TN.
NRC, 2011. *Concrete Degradation by Alkali-Silica Reaction, Information Notice 2011-20*, Washington, DC.
Oh, T., Kee, S., et al., 2013. Comparison of NDT methods for assessment of a concrete bridge deck. *Journal of Engineering Mechanics*, 139(March), pp.305–314.
Oh, T., Popovics, J.S., et al., 2013. Improved interpretation of vibration responses from concrete delamination defects using air-coupled impact resonance tests. *Journal of Engineering Mechanics*, 139, pp.315–324.
Oh, T. et al., 2012. Practical finite element based simulations of nondestructive evaluation methods for concrete. *Computers & Structures*, 98-99, pp.55–65.
Oppenheim, A. V. & Schafer, R.W., 2009. *Discrete-Time Signal Processing (3rd Edition) (Prentice Hall Signal Processing)*, Prentice Hall.
Ould Naffa, S. et al., 2002. Detection of chemical damage in concrete using ultrasound. *Ultrasonics*, 40(1-8), pp.247–51.
Park, C.B., Miller, R.D. & Xia, J., 1998. Imaging dispersion curves of surface waves on multi-channel record. *In SEG Expanded Abstracts*, 17(1), pp.1377–1380.
Pedersen, M. & McClelland, J., 2005. Optimized Capacitive MEMS Microphone for Photoacoustic Spectroscopy (PAS) Applications. In M. Razeghi & G. J. Brown, eds. *Proceedings of SPIE*. pp. 108–121.
Piwakowski, B., Kaczmarek, M. & Safinowski, P., 2012. Automated non destructive testing by non-contact surface waves. In *AIP Conf. Proc*. Gdarisk, Poland, pp. 255–258.
Poupinet, G., Ellsworth, W.L. & Frechet, J., 1984. Monitoring velocity variations in the crust using earthquake doublets: An application to the Calaveras Fault, California. *Journal of Geophysical Research*, 89(B7), p.5719.
Punurai, W. et al., 2007. Characterization of multi-scale porosity in cement paste by advanced ultrasonic techniques. *Cement and Concrete Research*, 37(1), pp.38–46.
Purnell, P. et al., 2004. Noncontact ultrasonic diagnostics in concrete: A preliminary investigation. *Cement and Concrete Research*, 34(7), pp.1185–1188.
Quiviger, A. et al., 2012. Effect of the presence and size of a real macro-crack on diffuse ultrasound in concrete. *NDT & E International*, 45(1), pp.128–132.
Roesset, J.M. et al., 1990. Modulus and thickness of the pavement surface layer from SASW tests. *Transportation Research Record*, 1260, pp.53–63.
Rydèn, N. & Lowe, M.J.S., 2004. Guided wave propagation in three-layer pavement structures. *The*

Journal of the Acoustical Society of America, 116(5), p.2902.
Rydèn, N. & Park, C.B., 2004. Surface waves in inversely dispersive media. *Near Surface Geophysics*, 2, pp.187–197.
Saint-Pierre, F., Rivard, P. & Ballivy, G., 2007. Measurement of alkali–silica reaction progression by ultrasonic waves attenuation. *Cement and Concrete Research*, 37(6), pp.948–956.
Schaal, C. et al., 2015. Rayleigh to Lamb wave conversion at a delamination-like crack. *Journal of Sound and Vibration*, 353, pp.150–163.
Schickert, M., 2005. Progress in ultrasonic imaging of concrete. *Materials and Structures*, 38(283), pp.807–815.
Schickert, M., Krause, M. & Mu, W., 2003. Ultrasonic imaging of concrete elements using reconstruction by synthetic aperture focusing technique. *Journal of Materials in Civil Engineering*, (June), pp.235–246.
Schindel, D.W., Hutchins, D.A. & Sayer, M., 1995. The design and characterization of micromachined air-coupled capacitance transducers. *IEEE Transactions on Ultrasonics, Ferroelectrics and Frequency Control*, 42(1), pp.42–50.
Schurr, D.P., 2010. *Monitoring damage in concrete using diffuse ultrasonic coda wave interferometry*. MS Thesis, Georgia Institute of Technology.
Scott, M.L., 1999. *Automated characterization of bridge deck distress using pattern recognition analysis of ground penetrating radar data automated characterization of bridge deck distress using pattern recognition analysis of ground penetrating radar data*. Ph.D. Dissertation, Virginia Polytechnic Institute and State University.
Selleck, S.F. et al., 1998. Ultrasonic investigation of concrete with distributed damage. *ACI Materials Journal*, 95(95), pp.27–36.
Shah, A.A. & Ribakov, Y., 2009. Non-linear ultrasonic evaluation of damaged concrete based on higher order harmonic generation. *Materials & Design*, 30(10), pp.4095–4102.
Shokouhi, P., 2012. Monitoring of Progressive Microcracking in Concrete Using Diffuse Ultrasound. In *6th European Workshop on Structural Health Monitorin*. pp. 1–8.
Snieder, R. et al., 2002. Coda Wave Interferometry for in Seismic Velocity. *Science*, 295(March), pp.2253–2255.
Snieder, R., 1986. The influence of topography on the propagation and scattering of surface waves. *Physics of the Earth and Planetary Interiors*, 44(3), pp.226–241.
Soltani, F. et al., 2013. Relationship between ultrasonic Rayleigh wave propagation and capillary porosity in cement paste with variable water content. *NDT&E International*, 54, pp.75–83.
Suaris, W. & Fernando, V., 1987. Detection of crack growth in concrete from ultrasonic intensity measurements. *Materials and Structures*, 20, pp.214–220.
Suaris, W. & Fernando, V., 1988. Ultrasonic Pulse Attenuation as a Measure of Damage Growth during Cyclic Loading of Concrete. *ACI Materials Journal*, (84), pp.185–193.
Walraven, J.A., 2003. Introduction to applications and industries for microelectromechanical systems (MEMS). *International Test Conference, 2003. Proceedings. ITC 2003.*, 1.
Weaver, R.L., 1990. Diffusivity of ultrasound in polycrystals. *J. Mech. Phys. Solids*, 38(1), pp.55–86.
Weaver, R.L. & Sachse, W., 1995. Diffusion of ultrasound in a glass bead slurry. *The Journal of the Acoustical Society of America*, 97(April 1995), pp.2094–2102.
Weyers, R.E. et al., 1993. *Concrete bridge protection, repair, and rehabilitation relative to reinforcement corrosion: A methods application manual*, Blacksburg, Virginia.
Wilcox, P., 2004. Modeling the excitation of Lamb and SH waves by point and line sources. *AIP Conference Proceedings*, 700, pp.206–213.
Zeman, J.C. et al., 2009. Failure mode and effect analysis of concrete ties in North America. In *In Proc. of the 9th International Heavy Haul Conference*. Shanghai, China, pp. 220–277.

Zeman, J.C., 2010. *Hydraulic mechanisms of concrete-tie rail seat deterioration*. MS Thesis, University of Illinois at Urbana-Champaign.
Zhu, J., Popovics, J.S. & Schubert, F., 2004. Leaky Rayleigh and Scholte waves at the fluid–solid interface subjected to transient point loading. *The Journal of the Acoustical Society of America*, 116(4), p.2101.

.

APPENDIX A: MODULE

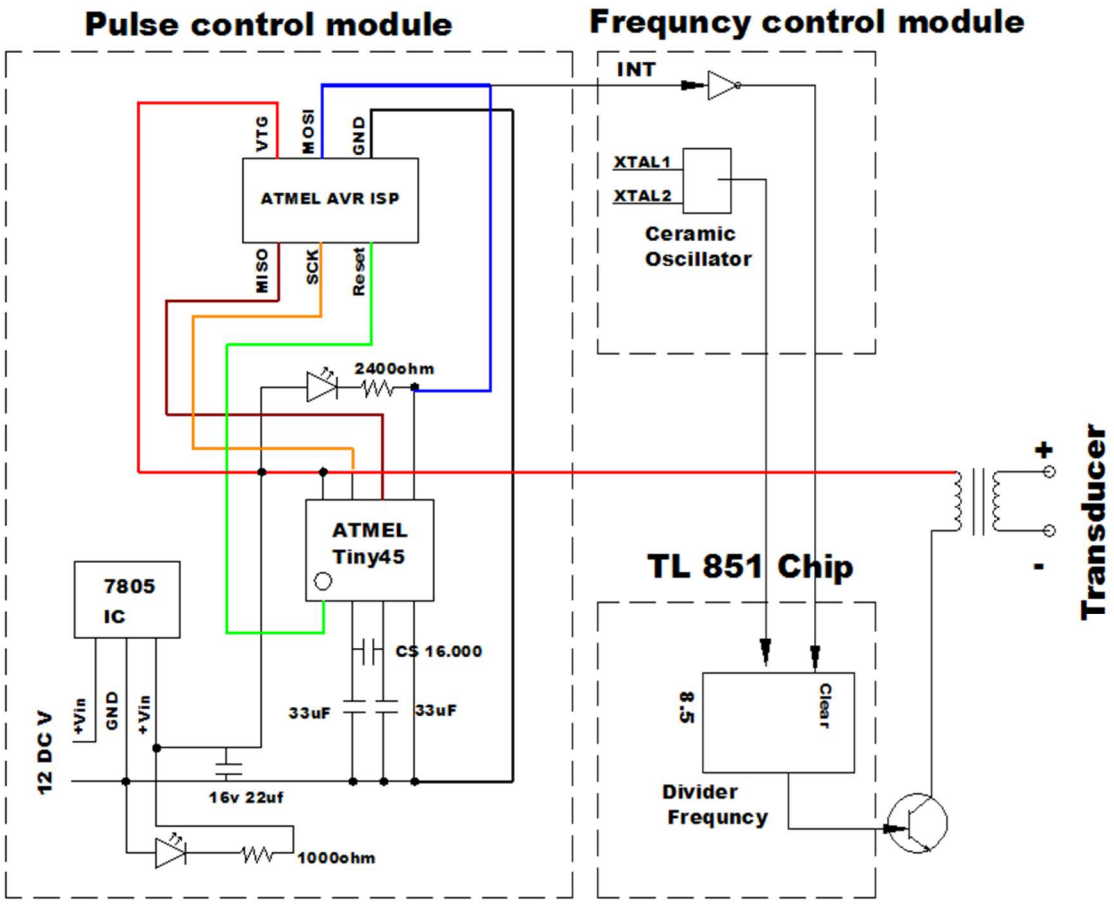

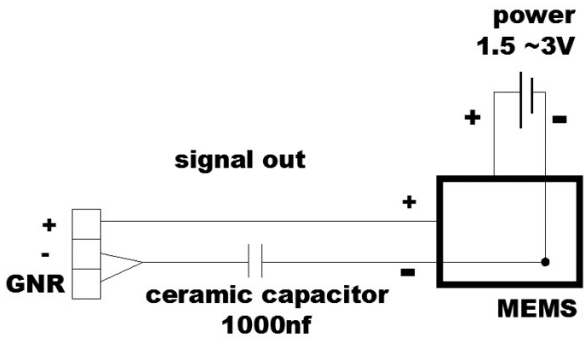

APPENDIX B: FE SIMULATION CODE FOR LAMB WAVE MODEL

```
**
** ABAQUS Input Deck Generated by HyperMesh Version  : 13.0.0.119
** Generated using HyperMesh-Abaqus Template Version : 13.0
**
**   Template:  ABAQUS/EXPLICIT
**
*NODE
    332424,  -17.8218       ,  11.6533        ,  0.0
    332425,  -17.98560833333,  10.682191666667,  0.0
    332426,  -18.14941666667,  9.7110833333333,  0.0
    332427,  -18.313225     ,  8.739975       ,  0.0
    3
   2205086,  40.379         ,  -50.0          ,  0.0
   2205087,  -560.379       ,  -50.0          ,  0.0
   2205088,  -560.379       ,  -50.0          ,  0.0
**HWCOLOR COMP          3     4
*ELEMENT,TYPE=CPE4R,ELSET=Baffle
    1250276,   1657648,   1657671,   1657668,   1657647
    1249785,   1657174,   1657173,   1657182,   1657186
    1249784,   1657129,   1657174,   1657186,   1657128
     607462,   1010739,   1010792,   1007179,   1007178
     607461,   1010738,   1010790,   1010792,   1010739

3.2300E-04,0.0
**HMNAME CURVE          1 50kHz
*AMPLITUDE, NAME =Chirp100k, DEFINITION = TABULAR
0.0       ,0.0
1.0000E-06,0.0
2.0000E-06,1.4529E-04
3.0000E-0
1.6000E-05,0.00521192
1.7000E-05,0.00512749
1.8000E-05,0.00484422
```

```
1.9000E-05,0.00434211
5.8000E-05,8.7851E-04
5.9000E-05,0.00468277
6.0000E-05,0.00779447
6.1000E-05,0.00965484
6.2000E-05,0.00987688
6.3
8.2000E-05,-0.0076268
8.3000E-05,-0.0033254
8.4000E-05,0.00175943
8.5000E-05,0.00588234
8.6
1.1800E-04,0.0
1.1900E-04,0.0
**HMNAME CURVE          2 Chirp100k
**HMNAME LOADSTEP          1 Step-1
*STEP, NAME = Step-1
*DYNAMIC, EXPLICIT, ELEMENT BY ELEMENT
        ,8.0000E-04,          ,
**HWNAME LOADCOL          1 HM_Load_Cols_1
**HWCOLOR LOADCOL          1    45
*CLOAD, AMPLITUDE = Chirp100k
   332456,2,-2.0
*OUTPUT, HISTORY, TIME INTERVAL = 1e-006
*NODE OUTPUT, NSET = nset
V1,V2,
A1,A2,
*ELEMENT OUTPUT, ELSET = eset
PRESS,
*RESTART, WRITE
*END STEP
```

APPENDIX C: FE FOR RANDOM SCATTERING MODEL

```
**
** ABAQUS Input Deck Generated by HyperMesh Version  : 13.0.0.119
** Generated using HyperMesh-Abaqus Template Version : 13.0
**
**   Template:  ABAQUS/EXPLICIT
**
*NODE
   332424,  45.5572       ,  11.6533       ,  0.0
   332425,  45.393391666667,  10.682191666667,  0.0
   332426,  45.229583333333,  9.7110833333333,  0.0
   332427,  45.065775     ,  8.739975      ,  0.0
.....
  1838939,  40.0          ,  -40.0         ,  0.0
  1838940,  40.0          ,  0.0           ,  0.0
  1838941,  0.0           ,  0.0           ,  0.0
**HWCOLOR COMP         1    13
*ELEMENT,TYPE=CPE3,ELSET=Column
   461112,    862758,    862757,    862763
**HWCOLOR COMP         2     5
*ELEMENT,TYPE=CPE3,ELSET=gap
   545446,    355216,    355215,    355282
**HWCOLOR COMP         3     4
*ELEMENT,TYPE=CPE4R,ELSET=Baffle
   236375,    572415,    572802,    572781,    572416
   236374,    572414,    572797,    572802,    572415
  1354159,   1760967,   1760969,   1760968,   1760966
  1354158,   1760943,   1760942,   1760969,   1760967
……
  1363389,   1771449,   1771438,   1771437,   1771445
  1363390,   1036731,   1771419,   1771450,   1036732
```

```
  1363391,  1036732,  1771450,  1771448,  1036733
  1363392,  1771439,  1771451,  1771418,  1771417
  1363393,  1771451,  1771450,  1771419,  1771418
  1363394,  1771438,  1771449,  1771451,  1771439
  1363395,  1771449,  1771448,  1771450,  1771451
**HWCOLOR COMP         1    13
*ELEMENT,TYPE=CPE4R,ELSET=Column
   407642,   808179,   808178,   808184,   808188
….
   405843,   806668,   806666,   806578,   806579
   405309,   806150,   806156,   806027,   806028
   405295,   806143,   806126,   806122,   806123
   405241,   806099,   806098,   806096,   806097
   406927,   807679,   807620,   807621,   807631
**HM_comp_by_property "PropAir"     6
*SOLID SECTION, ELSET=gap, MATERIAL=air
**HM_comp_by_property "property4"     3
*SOLID SECTION, ELSET=Column, MATERIAL=conc
**HM_comp_by_property "propsteel"     4
*SOLID SECTION, ELSET=Baffle, MATERIAL=steel
*ELSET, ELSET=DSSDS
   406096,   441090,   442017,   442242,   528601,   599975,   601387,   602394
*NSET, NSET=nset
   374443,   374463,   374483,   374698,   931110,  1002915,  1004213,  1005212
*NSET, NSET=defect
  1838822,  1838823,  1838824,  1838825,  1838826,  1838827,  1838828,  1838829,
  1838830,  1838831,  1838832,  1838833,  1838834,  1838835,  1838836,  1838837
*MATERIAL, NAME=air
*DENSITY
1.0000E-12,0.0
*ELASTIC, TYPE = ISOTROPIC
0.142     ,0.0       ,0.0
```

```
*MATERIAL, NAME=conc
*DENSITY
2.4000E-09,0.0
*ELASTIC, TYPE = ISOTROPIC
35570.0   ,0.2       ,0.0
*MATERIAL, NAME=steel
*DENSITY
7.8000E-09,0.0
*ELASTIC, TYPE = ISOTROPIC
200000.0  ,0.3       ,0.0
**HMNAME PLOT          1 untitled
**HMNAME PLOT CURVE          1
*AMPLITUDE, NAME =50kHz, DEFINITION = TABULAR
0.0       ,0.0
1.0000E-06,0.0
2.0000E-06,0.0
3.0000E-06,0.0
4.0000E-06,0.0
5.0000E-06,0.0
6.0000E-06,0.0
7.0000E-06,0.0
8.0000E-06,0.0
9.0000E-06,0.0
1.0000E-05,0.0
....
3.2100E-04,0.0
3.2200E-04,0.0
3.2300E-04,0.0
**HMNAME CURVE          1 50kHz
**HMNAME LOADSTEP          1 Step-1
*STEP, NAME = Step-1
*DYNAMIC, EXPLICIT, ELEMENT BY ELEMENT
```

,5.0000E-04, ,
**HWNAME LOADCOL 1 HM_Load_Cols_1
**HWCOLOR LOADCOL 1 45
*DLOAD, AMPLITUDE = 50kHz
157089, P4,-1.0
157091, P4,-1.0
157095, P2,-1.0
157100, P4,-1.0
157098, P4,-1.0
157241, P4,-1.0
157239, P4,-1.0
157245, P2,-1.0
157250, P4,-1.0
157248, P4,-1.0
157211, P4,-1.0
157209, P4,-1.0
157215, P2,-1.0
157220, P4,-1.0
157218, P4,-1.0
156641, P4,-1.0
156639, P4,-1.0
156645, P2,-1.0
156650, P4,-1.0
156648, P4,-1.0
156611, P4,-1.0
156609, P4,-1.0
156615, P2,-1.0
156620, P4,-1.0
156618, P4,-1.0
156761, P4,-1.0
156759, P4,-1.0
156765, P2,-1.0

```
   156770,   P4,-1.0
   156768,   P4,-1.0
*OUTPUT, HISTORY, TIME INTERVAL = 1e-006
*NODE OUTPUT, NSET = nset
A1,A2,
V1,V2,
*ELEMENT OUTPUT, ELSET = DSSDS
PRESS,
*RESTART, WRITE
*END STEP
```

APPENDIX D: MATLAB CODE FOR BACKSCATTER

```
asensor = 8;
nn = dataset -1; name = (num2str([0:nn]')); % name={'PMMA','0%','0.6 %'};
MEMS    = 1;
cfreq1 = 45e3 ; cfreq2  = 55e3   %
peakfr = 50; stp =  250; Nst =  650 ;Njj = [Nst; Nst; Nst; Nst; Nst ;Nst
;Nst;400]-stp+1 ;

for ii = 1:dataset;  ccc = eval(['a',num2str(ii)]);
    for jj = 1:asensor;
        for kk =1:length(kkk);
         raw = squeeze(   eval(['D3LF',ccc,'(:,jj,kk)'])    );
         NorRaw(:,jj,kk) = raw / max(raw);

 end; eval( ['D3LFNor',ccc,'=NorRaw;']) ;end;end; clearvars raw NorRaw  ii
jj kk
for ii=1:dataset;  ccc = eval(['a',num2str(ii)]);
    for jj = 1:asensor;
         raw = squeeze(   eval(['D3LFNor',ccc,'(:,jj,:)'])) ;
         matccc1(:,jj) = mean(raw');
end;  eval( ['D4meanNor',ccc,'=matccc1;']) ;end; clearvars aaa1 bbb1 ccc1
ii jj
for ii = 1:dataset; ccc = eval(['a',num2str(ii)]);
    for jj = 1:asensor;
        for kk = 1:length(kkk);
     aaa = squeeze(   eval(['D3LF',ccc,'(:,jj,kk)'])  );
     bbb = squeeze(   eval(['D4mean',ccc,'(:,jj)'])   );
     subcc(:,jj,kk) = aaa - bbb;
     end; eval( ['D5Sub',ccc,'=subcc;']) ;end; end;clearvars ii jj subcc
for ii=1:dataset;  ccc = eval(['a',num2str(ii)]);
    bbb = eval([  'D5BP',  ccc  ])     ;
    for jj = 1:asensor;
        kk = 1:length(kkk);
        area(jj,kk)  = trapz (  abs(bbb (:,jj,kk).^2)  );
        area =  squeeze (area);
        eval( ['D6area',ccc,'=area;']) ;
end;end; clearvars ii jj kk aaa bbb ccc;
```